

NASA Conference Publication 2054

NASA
CP
2054
v.1
c.1

LOAN COPY: RETURN TO
AFWL TECHNICAL
KIRTLAND AFB,



YF-12 EXPERIMENTS SYMPOSIUM

Volume 1

A conference held at
Dryden Flight Research Center
Edwards, California
September 13-15, 1978

NASA





NASA Conference Publication 2054

YF-12 EXPERIMENTS SYMPOSIUM

Volume 1

Edited by James and Associates, Lancaster, California

A conference held at
Dryden Flight Research Center
Edwards, California
September 13-15, 1978



National Aeronautics
and Space Administration

**Scientific and Technical
Information Office**

1978

FOREWORD

The YF-12 airplanes provided NASA with an opportunity to perform many research projects in a sustained high supersonic flight environment. Some of these projects investigated propulsion system performance and dynamics of mixed-compression inlets. Others studied aeroelastic effects and thermal problems present during high Mach number flight. Pressures and flow patterns around the airplane and in the inlets were mapped, and pressure and skin friction drag were measured over a wide range of Mach numbers. Many new techniques were devised to measure aerodynamic data and system operational parameters in the extreme temperature environment which was encountered.

Concurrent with the flight program, a parallel series of laboratory experiments, wind tunnel tests, and analytical studies were conducted to augment the findings of the flight program. Much of the laboratory work was involved with the development and testing of new types of instrumentation sensors that could withstand the extreme temperature environment and still provide accurate measurements. The wind tunnel studies served to provide guidelines and comparative data for the flight measurements, and several new predictive techniques for correlating high Mach number wind tunnel data with flight data were investigated. In order to compensate for minor differences in test conditions at which the flight and wind tunnel measurements were obtained, mathematical models were employed to extrapolate multivariable data sets, and statistical methods were applied to insure that such extrapolations were valid.

During the course of the program, every engineering discipline associated with structures, aerodynamics, propulsion, and controls was deeply involved. As a result of the combined efforts of personnel working in all of these research categories, an extensive data base was compiled. This data base will provide much insight for the design of future Mach 3 supersonic cruise aircraft, and it undoubtedly contains some yet undiscovered facts which will surface as research efforts continue in the future. However, it is the purpose of this symposium to disseminate findings from the most recent research projects and to stimulate the crossflow of information between government and industry personnel who may be engaged in design or research activities relating to high supersonic flight.

James A. Albers
Chairman, YF-12 Experiments Symposium

CONTENTS

FOREWORD	iii
----------------	-----

OVERVIEW OF THE NASA YF-12 PROGRAM	3
Berwin M. Kock	

SESSION I: PROPULSION SYSTEM PERFORMANCE

Chairman: Robert E. Coltrin, Lewis Research Center

AN INTRODUCTION AND SUMMARY OF THE YF-12 PROPULSION RESEARCH PROGRAM ¹	29
William G. Schweikhard and David H. Campbell	

FULL-SCALE YF-12 INLET CALIBRATION AND FLOW SYSTEM INTERACTIONS ¹	31
Robert W. Cubbison and Bobby W. Sanders	

COMPARISON OF ONE-THIRD-SCALE AND FULL-SCALE YF-12 ISOLATED INLET PERFORMANCE ¹	33
Robert W. Cubbison and Bobby W. Sanders	

MATHEMATICAL MODELING OF THE PERFORMANCE OF A YF-12 MIXED-COMPRESSION INLET BY USING MULTIPLE REGRESSION TECHNIQUES ¹	35
James D. Brownlow, Henry H. Arnaiz, and James A. Albers	

A COMPARISON OF STEADY-STATE PERFORMANCE AMONG A FLIGHT INLET ON A YF-12 AIRPLANE AND TWO WIND TUNNEL MODELS USING STATISTICAL TECHNIQUES ¹	37
Henry H. Arnaiz, James D. Brownlow, and James A. Albers	

SESSION II: INLET TIME VARYING DISTORTION

Chairman: Daniel P. Bencze, Ames Research Center

COMPARISON OF FLIGHT AND WIND TUNNEL MODEL INSTANTANEOUS DISTORTION DATA FROM A MIXED-COMPRESSION INLET ¹	41
Carol A. Bauer, Karen G. Mackall, Frederick Stoll, and Jeffrey W. Tremback	

¹ Summary only. Complete text available in volume 3 (Secret).

PREDICTED AND MEASURED MAXIMUM INSTANTANEOUS DISTORTION FOR FLIGHT AND WIND TUNNEL MODEL DATA FOR A MIXED- COMPRESSION INLET ¹	43
Howard M. Brilliant, Carol A. Bauer, and Robert A. Davis	

SESSION III: STRUCTURES

Chairman: Alan L. Carter, Dryden Flight Research Center

RECENT LOAD CALIBRATIONS EXPERIENCE WITH THE YF-12 AIRPLANE	47
Jerald M. Jenkins and Albert E. Kuhl	

FLIGHT-MEASURED AERODYNAMIC LOADS ON A 0.92 ASPECT RATIO LIFTING SURFACE	73
Robert R. Meyer, Jr. and V. Michael DeAngelis	

SESSION IV: AIRCRAFT CONTROLS

Chairman: Eldon E. Kordes, Dryden Flight Research Center

A SUMMARY OF YF-12 HANDLING QUALITIES ²	95
Donald T. Berry	

FLIGHT EXPERIENCE WITH ALTITUDE HOLD AND MACH HOLD AUTOPILOTS ON THE YF-12 AIRCRAFT AT MACH 3.....	97
Glenn B. Gilyard and John W. Smith	

PILOT WORKLOAD MEASUREMENT AND EXPERIENCE ON SUPERSONIC CRUISE AIRCRAFT.....	121
Terrence W. Rezek	

THE YF-12 GUST VELOCITY MEASURING SYSTEM	135
L. J. Ehernberger	

SESSION V: PROPULSION CONTROLS

Chairman: Frank W. Burcham, Dryden Flight Research Center

WIND TUNNEL EVALUATION OF YF-12 INLET RESPONSE TO INTERNAL AIRFLOW DISTURBANCES WITH AND WITHOUT CONTROL	157
Gary L. Cole, George H. Neiner, and Miles O. Dustin	

¹ Summary only. Complete text available in volume 3 (Secret).

² Summary only. Complete text available in volume 2 (Confidential).

FLIGHT-MEASURED TRANSIENTS RELATED TO INLET PERFORMANCE ON THE YF-12 AIRPLANE ¹	193
Paul J. Reukauf, Frank V. Olinger, L. J. Ehernberger, and Craig Yanagidate	

WIND-TUNNEL PERFORMANCE OF A THROAT-BYPASS STABILITY SYSTEM FOR THE YF-12 INLET ²	195
Gary L. Cole, Miles O. Dustin, and George H. Neiner	

FLIGHT TEST EXPERIENCE WITH A DIGITAL AIRFRAME/PROPULSION CONTROL SYSTEM ON A YF-12 AIRPLANE (Summary only)	197
Paul J. Reukauf	

SESSION VI: AERODYNAMICS

Chairman: Warner A. Robins, Langley Research Center

FLIGHT-MEASURED PRESSURE CHARACTERISTICS OF AFT-FACING STEPS IN THICK BOUNDARY LAYER FLOW FOR TRANSONIC AND SUPERSONIC MACH NUMBERS	201
Sheryll Goecke Powers	

BOUNDARY LAYER, SKIN FRICTION, AND BOATTAIL PRESSURE MEASUREMENTS FROM THE YF-12 AIRPLANE AT MACH NUMBERS UP TO 3	227
David F. Fisher	

IN-FLIGHT COMPRESSIBLE TURBULENT BOUNDARY LAYER MEASUREMENTS ON A HOLLOW CYLINDER AT A MACH NUMBER OF 3.0.	259
Robert D. Quinn and Leslie Gong	

PREDICTED AND MEASURED FLOW FIELDS UPSTREAM OF THE YF-12 INLET AND INLET INTERNAL FLOW SOLUTIONS ¹	287
L. Presley, P. Kutler, and R. Sorenson	

A PERFORMANCE MODEL OF THE YF-12C AIRPLANE ¹	289
Paul C. Redin	

¹ Summary only. Complete text available in volume 3 (Secret).

² Summary only. Complete text available in volume 2 (Confidential).

OVERVIEW

OVERVIEW OF THE NASA YF-12 PROGRAM

Berwin M. Kock
Dryden Flight Research Center

SUMMARY

An overview of the NASA YF-12 program is presented. Discussion items include a brief program history, a description of the airplane, and a review of the research program. The project organization is described. Major accomplishments are identified.

INTRODUCTION

NASA's long-standing interest in supersonic research dates back to early programs of its predecessor agency, NACA. Flight research with rocket-powered airplanes started with the historic first supersonic flight of the Bell X-1 and continued with the first Mach 2 flight made by the D-558, the first Mach 3 flight made with the X-2, and finally with the present world's record Mach 6.7 flight of the X-15.

Although these airplanes with their short duration flights provided much needed aerodynamic, stability, control, and structures data, a void still existed for information about airbreathing propulsion systems and thermal effects in the long duration supersonic cruise environment. Some of the questions were addressed to varying degrees with the advent of the F-104, B-58, and XB-70 airplanes, but of all these, only the B-58 airplane could cruise for any significant period of time at or above Mach 2.

The existence of the YF-12 airplane was announced by President Johnson in 1964, and in 1965 the airplane demonstrated its sustained Mach 3 cruise capability by setting several speed and altitude records. Originally designed as an interceptor, using a predecessor to the Phoenix Radar/Missile Armament System, the aircraft evolved into the SR-71 reconnaissance vehicle after the cancellation of the interceptor program.

The YF-12 airplane, shown in figure 1, was designed to cruise at speeds in

excess of Mach 3 and at altitudes above 24,000 meters. Since it was originally intended to serve as a long range interceptor, its design was optimized for high speed cruise, not for maneuverability. To satisfy the range objective, the airplane was rather large in size, but surprisingly light in weight, and these two factors combined to produce a very flexible airplane. Table 1 provides a list of other pertinent physical characteristics of the YF-12 airplane.

Several of the more interesting aspects of the airplane were dictated by the high-speed, high-altitude design objectives. For example, a satisfactory material had to be found that would withstand average skin temperatures in the range of 550 K, and even higher temperatures inside the inlets. Titanium was chosen but much pioneering work was required in order to work with this new material. A unique structural design concept required to handle the thermal effects led to the multispar beaded skin structure.

The high speed also necessitated a unique propulsion system design. To achieve satisfactory performance, a mixed-compression inlet (fig. 2) was required. A rather modest engine compression ratio was selected since, at cruise conditions, the inlet would provide most of the compression. A variable engine cycle was also developed. The high-speed mode of operation bled some of the air from the fourth stage compressor around the engine and directly into the afterburner (fig. 3).

Two versions of the YF-12 airplane were used in the NASA program: a YF-12A identified by its round nose and a YF-12C on which the chine is carried forward to the nose of the airplane. There are some other differences in external and internal configurations; however, there are also many similarities in the two airplanes since they share common inlet designs, structural concepts, and subsystems. In general, each of the two airplanes was dedicated to particular classes or types of research, and some of the symposium papers will refer to one or the other of the two. However, usually the distinction between them is not highly significant.

Many characteristics made the YF-12 airplanes ideal for supersonic cruise research. After removal of the radar and missile systems, a large internal volume was available for instrumentation. The mixed-compression inlet was the same type that all cruise airplanes designed for speeds in excess of Mach 2 will have to use. The larger size of the airplane made it possible to measure boundary layer behavior at realistic Reynolds numbers. The high temperature structural design was well suited to verify various analytical techniques and its titanium material will probably be used on many airplanes in the future. Its flexibility made it useful for structural dynamics studies. Finally, just flying that high and that fast advanced the state of the art in air data systems, flight controls, and even the understanding of the physics of the upper atmosphere.

NASA's involvement with the YF-12 program began during the early wind tunnel tests conducted by Lockheed in NASA facilities. Subsequently, two NASA representatives were assigned to the Category II testing of the SR-71 conducted by the U.S. Air Force. During the Category II tests, the NASA personnel were involved with the stability, control, and propulsion aspects of the tests, and in following the testing of the airplane, they recognized that much was left to be learned about the operation of Mach 3 airplanes. During the early phases of the development, many problems were "worked around" rather than being fully understood. It must be recognized that this was a very legitimate method of achieving the goal, which was

to provide a usable system to the military services. However, that approach did not necessarily provide the in-depth understanding and technology needed to build a better airplane the next time. An example of the "work around" approach was found in the autopilot. In the initial operational autopilot some modes were not usable at cruise conditions. While this did not hamper the military mission, it is almost mandatory to have a full-envelope autopilot capability for a supersonic transport.

In the late 1960's, several factors combined to provide the impetus for a YF-12 flight research program. There were a number of YF-12 airplanes in storage because of the decision against their production, and there was a strong interest in building an American supersonic transport. The XB-70 program was demonstrating that some supersonic cruise airplanes can have very serious problems. NASA was involved with the SR-71 testing, and the U.S. Air Force recognized that more information was needed about high-speed, high-altitude interceptor capabilities and limitations. These factors, combined with the vision of perceptive and dynamic people in both NASA and the U.S. Air Force, caused the joint NASA/USAF program to be undertaken.

PROGRAM ELEMENTS

As originally formulated, the major thrust of the NASA program was to have been in the area of propulsion technology, or, more specifically, inlet behavior, since the achievement of maximum inlet performance was one of the major problems encountered during the development of the airplane. In addition, concern about unstart margins, drag, distortion effects, control parameters, air data requirements, bleed system effects, and off-design behavior all suggested that the mixed-compression inlet offered a very fruitful area for research. This conclusion was further substantiated by the airframe and propulsion system interactions encountered on the XB-70 airplane. Thus, the prime objective of the YF-12 program was to be the advancement of state-of-the-art technology in mixed-compression inlets. Of necessity the effort was a combination of wind tunnel, analytical, and flight research, and at the time there were probably very few people who anticipated the difficulties involved in the task, especially the problems associated with high temperature instrumentation.

Initially, the propulsion research was delayed by flight instrumentation problems. However, researchers used this delay to advantage by also formulating a structures research program to make use of the fact that the airplane was well suited to this type of research. The structures program was intended to validate state-of-the-art analytical tools, and it presented a unique opportunity to address the problems of separating thermal stresses from aerodynamic load effects and the instrumentation problems associated with titanium structures. Many of the findings of the structures program were reported in a symposium held in 1974.

While the major program goals centered on structures research and propulsion/inlet studies, the usefulness of the airplane as an experimental test bed was becoming recognized. A wide range of aerodynamic experiments was soon formulated to address such items as flow field effects, drag, skin friction, heat transfer, boattail drag, and surface discontinuity drag.

A number of other experiments were also conducted. Although some of them are difficult to categorize into any one of the classical disciplines, they included a validation of analytical methods for predicting landing gear dynamics, the evaluation of a maintenance monitoring and recording system, the measurement of engine effluents for pollution studies, and noise suppression tests. Table 2 contains a list of the major YF-12 activities. Those activities reported in this symposium are indicated by an asterisk.

Throughout the course of the program, many assets were accumulated. These assets, listed in table 3, point out the depth of the research program. They also graphically demonstrate the fact that the airplanes were used as a research facility akin to a wind tunnel for a very wide range of activities.

PROGRAM PARTICIPATION

It is important to note that the YF-12 program was a NASA program as opposed to an Ames Research Center, Langley Research Center, Lewis Research Center, or Dryden Flight Research Center program. Every aeronautical Center participated in the program with the efforts of each Center complementing the efforts of the others (fig. 4). The program also had unique, strong, and continuing support from NASA headquarters, and the U.S. Air Force was an active partner in the program, providing logistics support and playing an active role in formulating technology experiments. Lockheed Aircraft Company also played an important role in making the program successful.

No discussion about the YF-12 program can be complete without mention of the special access security system. The agreement with the U.S. Air Force at the initiation of the program placed operations on a day-to-day basis within a special access system. Data generated from the program could be released under the conventional security classification system only after a review and approval by the U.S. Air Force. The special access requirement has had a tremendous impact on the manner in which the YF-12 program conducted its business. Maintaining a balance between the protection of sensitive material and the dissemination of technology to potential users has been and continues to be a difficult task.

CONCLUDING REMARKS

The accomplishments of the YF-12 program are difficult to analyze on a short-term basis, since the real significance of the research will be measured in its effect on airplanes built in the years from 1985 to 1990 or beyond. However, in the short term it is possible to say that over 125 reports (see bibliography) have been published, a structures symposium was conducted in 1974, and now the present symposium is consolidating much, although not all, of the other research findings of the program. Certainly the YF-12 program has been an important contribution to this nation's long-term aeronautical capabilities.

The program has now been cancelled and the last research flight will occur before

March 1979. It is unnecessary to go into the many reasons for this action; however, it is the feeling of all personnel associated with the program that the need for the capabilities of these airplanes has not disappeared. Even though circumstances have prevented active participation by industry in the program to the extent many would have wished, the objective of the program has always been to provide and update the tools and data needed to perform the numerous aeronautical design tasks.

The present symposium will document some of the technological advancements pertaining to supersonic cruise airplanes and certain other types of airplanes. All of the questions have not been answered. In fact, many of the questions have not yet been formulated. Symposium attendees are encouraged to listen to the papers and consider what more should be done. Is enough really known about inlets? What more must be learned about structural dynamics? How can drag be predicted more accurately? How can weight be reduced? These are some of the more obvious questions but there are many more as well.

Even though the YF-12 program is ending, supersonic airplane research should not end. The closing session of the symposium will focus on the direction supersonic research will take from this point. Comments from the participants are welcomed.

YF-12 BIBLIOGRAPHY

Propulsion

1. Albers, James A.: Status of the NASA YF-12 Propulsion Research Program. NASA TM X-56039, 1976.
2. Albers, James A.; and Olinger, Frank V.: YF-12 Propulsion Research Program and Results. Proceedings of the SCAR Conference, Nov. 1976, NASA CP-001, Part 1, pp. 417-456.
3. Anderson, J. Thomas; Martin, Robert K.; and Shibata, Harry H.: 1/3 Scale Inlet Model Tests Results. Vol. I — Test Definition and Steady State Data Presentation. NASA CR-114702, 1974.
4. Anderson, J. Thomas; and Edson, Ralph D.: 1/3 Scale Inlet Model Test Results. Vol. II — Dynamic Data Analysis. NASA CR-114703, 1974.
5. Anderson, J. Thomas; Martin, Robert K.; and Shibata, Harry H.: 1/3 Scale Inlet Model Test Results. Vol. III — Tabulated Steady State Data. NASA CR-114704, 1974.
6. Arnaiz, Henry H.; and Gray, Michael: In-Flight Inlet Airflow Measuring Techniques for a YF-12C Airplane. NASA TM-72850, 1977.
7. Bauer, Carol A.; and Montoya, Earl J.: Local Inlet Flow Measurements for the YF-12C Aircraft Using a Conical Spike Tip Sensor. NASA TM-72848, 1977.
8. Blausey, G. E.; Coleman, D. M.; and Harp, D. S.: Feasibility Study of Inlet Shock Stability System of YF-12. NASA CR-134594, 1972.
9. Brilliant, Howard M.; and Bauer, Carol A.: Comparison of Estimated With Measured Maximum Instantaneous Distortion Using Flight Data From an Axisymmetric Mixed Compression Inlet. AIAA Paper 77-876, July 1977.
10. Burcham, Frank W., Jr.; and Bellman, Donald R.: A Flight Investigation of Steady-State and Dynamic-Pressure Phenomena in the Air Inlets of Supersonic Aircraft. Inlets and Nozzles for Aerospace Engines, AGARD CP-91-71, Paper 24, Dec. 1971.
11. Burcham, Frank W.; Holzman, Jon K.; and Reukauf, Paul J.: Preliminary Results of Flight Tests of the Propulsion System of a YF-12 Airplane at Mach Numbers up to 3.0. AIAA Paper 73-1314, Nov. 1973.
12. Burcham, Frank W., Jr.; Montoya, Earl J.; and Lutschg, Phillip J.: Description of YF-12C Airplane, Propulsion System, and Instrumentation for Propulsion Research Flight Tests. NASA TM X-3099, 1974.
13. Campbell, D. H.: F-12 Inlet Development. SAE Paper 740831, Oct. 1974.

14. Campbell, D. H.: F-12 Series Aircraft Propulsion System Performance and Development. AIAA Paper 73-821, Aug. 1973.
15. Cole, Gary L.; Cwynar, David S.; and Geyser, Lucille C.: Wind-Tunnel Evaluation of the Response of a YF-12 Aircraft Flight Inlet to Internal Airflow Perturbations by Frequency-Response Testing. NASA TM X-3141, 1974.
16. Cole, Gary L.; Dustin, Miles O.; and Neiner, George H.: A Throat-Bypass Stability System for a YF-12 Aircraft Research Inlet Using Self-Acting Mechanical Valves. NASA TM X-71779, 1975.
17. Cole, Gary L.; Dustin, Miles O.; and Neiner, George H.: A Throat-Bypass Stability System Tested in a YF-12 Inlet. J. Aircraft, vol. 14, no. 1, Jan. 1977, pp. 15-22.
18. Cole, Gary L.; Neiner, George H.; and Dustin, Miles O.: Wind-Tunnel Steady-State Performance of a YF-12 Aircraft Flight Inlet Modified by a Throat-Bypass Stability-Bleed System. NASA TM-73802, 1979.
19. Cole, Gary L.; Sanders, Bobby W.; and Neiner, George H.: Wind-Tunnel Performance of a YF-12 Aircraft Flight Inlet Modified by Various Stability-Bypass Porous-Bleed Configurations. NASA TM-73801, 1979.
20. Cubbison, Robert W.: Effects of Angle of Attack and Flow Bypass on Wind-Tunnel Performance of an Isolated Full-Scale YF-12 Aircraft Inlet at Mach Numbers Above 2.075. NASA TM X-3140, 1978.
21. Cubbison, Robert W.: Wind-Tunnel Performance of an Isolated Full-Scale YF-12 Inlet at Mach Numbers Above 2.1. NASA TM X-3139, 1978.
22. Dustin, Miles O.; Cole, Gary L.; and Neiner, George H.: Continuous-Output Terminal-Shock-Position Sensor for Mixed-Compression Inlets Evaluated in Wind-Tunnel Tests of YF-12 Aircraft Inlet. NASA TM X-3144, 1974.
23. Dustin, Miles O.; and Neiner, George H.: Evaluation by Step Response Tests of Prototype Relief Valves Designed for YF-12 Inlet Stability Bleed System. NASA TM X-3262, 1975.
24. Duvall, Gilliam E.; and Arnaiz, Henry H.: Effects of Compressor Face Distortion on the Airflow Characteristics of a J58 Turbojet Engine. NASA TM-72847, 1977.
25. Gawienowski, John J.: Survey of Local Airflow Characteristics at the Plane of the Cowl Lip of the Left Inlet of a 1/12-Scale Model of the YF-12 Supersonic Aircraft: A Data Report, Two Volumes. NASA TM X-62483, 1975.
26. Herrick, Paul W.: J58/YF-12 Ejector Nozzle Performance. SAE Paper 740832, Oct. 1974.
27. Johnson, Harold J.; and Montoya, Earl J.: Local Flow Measurements at the Inlet Spike Tip of a Mach 3 Supersonic Cruise Airplane. NASA TN D-6987, 1973.

28. Ladd, J. M.: Airflow Calibration of a J-58 Engine at Simulated Supersonic Conditions. NASA TM X-71797, 1975.
29. Lewis Research Center: Wind-Tunnel Installation of Full-Scale Flight Inlet of YF-12 Aircraft for Steady-State and Dynamic Evaluation. NASA TM X-3138, 1974.
30. Neiner, George H.; Arpasi, Dale J.; and Dustin, Miles O.: Wind-Tunnel Evaluation of YF-12 Aircraft Inlet Control System by Frequency-Response and Transient Testing. NASA TM X-3142, 1975.
31. Neiner, George H.; Dustin, Miles O.; and Cole, Gary L.: A Throat-Bypass Stability-Bleed System Using Relief Valves to Increase the Transient Stability of a Mixed-Compression Inlet. NASA TP-1083, 1978.
32. Neiner, George H.; Dustin, Miles O.; and Cole, Gary L.: Mechanical Characteristics of Stability-Bleed Valves for a Supersonic Inlet. NASA TM X-3483, 1977.
33. Neiner, George H.; Seidel, Robert C.; and Arpasi, Dale J.: Wind-Tunnel Evaluation of Experimental Controls on YF-12 Aircraft Flight Inlet by Frequency-Response and Transient Testing. NASA TM X-3143, 1975.
34. Olinger, Frank V.; Shibata, Harry H.; and Albers, James A.: Local Flow Measurements at the Inlet Plane of a 1/12-Scale Model of the YF-12C Airplane. NASA TM X-3435, 1976.
35. Olinger, Frank V.; Taillon, Norman V.; and Reukauf, Paul J.: Some Flight-Measured YF-12 Inlet Performance Characteristics at Design and Off-Design Mach Numbers. NASA TM-72849, 1977.
36. Reukauf, Paul J.: Preliminary Flight Investigation of a YF-12A Mixed Compression Inlet. NASA TM X-56040, 1976.
37. Reukauf, Paul J.; and Burcham, Frank W., Jr.: Propulsion System/Flight Control Integration for Supersonic Aircraft. Proceedings of the SCAR Conference, Nov. 1976, NASA CP-001, Part 1, pp. 281-302.
38. Reukauf, Paul J.; Burcham, Frank W., Jr.; and Holzman, Jon K.: Status of a Digital Integrated Propulsion/Flight Control System for the YF-12 Airplane. AIAA Paper 75-1180, Sept. 1975.
39. Reukauf, Paul J.; Schweikhard, William G.; and Arnaiz, Henry H.: Flight-Test Techniques for Obtaining Valid Comparisons of Wind-Tunnel and Flight Results From Tests on a YF-12 Mixed-Compression Inlet. AIAA Paper 74-1195, Oct. 1974.
40. Schweikhard, William G.: Test Techniques, Instrumentation, and Data Processing. Distortion Induced Engine Instability, AGARD-LS-72, Oct. 1974, pp. 6-1-6-43.

41. Schweikhard, William G.; and Cubbison, Robert W.: Preliminary Results From Wind Tunnel and Flight Tests of the YF-12 Propulsion System. NASA TM X-56016, 1973.
42. Schweikhard, William G.; and Montoya, Earl J.: Research Instrumentation Requirements for Flight/Wind-Tunnel Tests of the YF-12 Propulsion System and Related Flight Experience. Instrumentation for Airbreathing Propulsion, Allen E. Fuhs and Marshall Kingery, eds., The MIT Press (Cambridge, Mass.), c. 1974, pp. 19-39.
43. Schweikhard, William G.; and Montoya, Earl J.: Research Instrumentation Requirements for Flight/Wind-Tunnel Tests of the YF-12 Propulsion System and Related Flight Experience. NASA Paper Presented at Symposium on Instrumentation for Airbreathing Propulsion, Monterey, Calif., Sept. 19-21, 1972.
44. Smeltzer, Donald B.; Smith, Ronald H.; and Cubbison, Robert W.: Wind Tunnel and Flight Performance of the YF-12 Inlet System. AIAA Paper 74-621, July 1974.
45. Smith, R. H.; and Burcham, F. W., Jr.: Instrumentation for In-Flight Determination of Steady-State and Dynamic Inlet Performance in Supersonic Aircraft. Instrumentation for Airbreathing Propulsion, Allen E. Fuhs and Marshall Kingery, eds., The MIT Press (Cambridge, Mass.), c. 1974, pp. 41-58.
46. Smith, Ronald H.; and Bauer, Carol A.: Atmospheric Effects on the Inlet System of the YF-12 Aircraft. NASA Paper Presented at the Eleventh National Conference on Environmental Effects on Aircraft and Propulsion Systems, Trenton, N.J., May 21-22, 1974.
47. Taillon, Norman V.: Steady-State Inlet Recovery and Distortion of the YF-12C Airplane. NASA TM X-3382, 1976.
48. Webb, John A., Jr.; Mehmed, Oral; and Hiller, Kirby W.: Improved Design of a High-Response Slotted-Plate Overboard Bypass Valve for Supersonic Inlets. NASA TM X-2812, 1973.
49. Webb, John A., Jr.; and Dustin, Miles O.: Analysis of a Stability Valve System for Extending the Dynamic Range of a Supersonic Inlet. NASA TM X-3219, 1975.
50. Webb, W. L.: Turbine Gas Temperature Measurement and Control System. NASA CR-140971, 1973.
51. Webb, W. L.; and Reukauf, P. J.: Development of a Turbine Inlet Gas Temperature Measurement and Control System Using a Fluidic Temperature Sensor. AIAA Paper 73-1251, Nov. 1973.
52. Webb, W. L.; and Zewski, G. J.: J58 Cooperative Control System Study. Vols. I, II, and III. NASA CR-121195, 1973.

53. Yanagidate, Craig: Tuft Study of the Local Flow Around the Nacelle of the YF-12A Airplane. NASA TM X-56035, 1975.
54. Bales, Thomas T.; Hoffman, Edward L.; Payne, Lee; and Carter, Alan L.: Fabrication and Evaluation of Advanced Titanium and Composite Structural Panels. Proceedings of the SCAR Conference, Nov. 1976, NASA CP-001, Part 2, pp. 783-797.
55. Brooks, William A., Jr.; and Dow, Marvin B.: Service Evaluation of Aircraft Composite Structural Components. NASA TM X-71944, 1973.
56. Carden, Huey D.; and McGehee, John R.: Validation of a Flexible Aircraft Takeoff and Landing Analysis/FATOLA/Computer Program Using Flight Landing Data Structures — 18th Structures, Structural Dynamics and Materials Conf., and Dynamics Specialist Conf. Technical Papers, Vol. B, American Inst. Aeronaut. and Astronaut., Inc., 1977, pp. 83-88.
57. Carter, Alan A.: Assessment of Recent Loads Analysis Methods as Applied to a Mach 3 Cruise Airplane. NASA YF-12 Flight Loads Program. NASA TM X-3061, 1974, pp. 625-645.
58. Cooper, Paul A.; and Heldenfels, Richard R.: NASA Research on Structures and Materials for Supersonic Cruise Aircraft. NASA TM X-72790, 1976.
59. Duba, R. J.; Haramis, A. C.; Marks, R. F.; Payne, L.; and Sessing, R. C.: YF-12 Lockalloy Ventral Fin Program, Vol. I., NASA CR-144971, 1976.
60. Duba, R. J.; Haramis, A. C.; Marks, R. F.; Payne, L.; and Sessing, R. C.: YF-12 Lockalloy Ventral Fin Program, Vol. II, NASA CR-144972, 1976.
61. Edinger, Lester D.; Schenk, Frederick L.; and Curtis, Alan R.: Study of Load Alleviation and Mode Suppression (LAMS) on the YF-12A Airplane. NASA CR-2158, 1972.
62. Fields, Roger A.: Strain Gage Measurement of Flight Loads at Elevated Temperature. NASA YF-12 Flight Loads Program. NASA TM X-3061, 1974, pp. 259-302.
63. Jenkins, Jerald M.: An Introduction to Thermal Effects in Strain Gage Load Measurement. NASA YF-12 Flight Loads Program. NASA TM X-3061, 1974, pp. 1-27.
64. Jenkins, Jerald M.; and Kuhl, Albert E.: A Study of the Effect of Radical Load Distribution on Calibrated Strain Gage Load Equations. NASA TM-56047, 1977.
65. Jenkins, Jerald M.; and Kuhl, Albert E.: Recent Loads Calibration Experience With a Delta Wing Airplane. NASA Paper Presented at the Fall Meeting of the Western Regional Strain Gage Committee, Society of Experimental Stress Analysis, Edwards, Calif., Sept. 28, 1977.

66. Jenkins, Jerald M.; and Kuhl, Albert E.: Summary of Recent Results Pertaining to Strain Gage Load Measurement Technology on High Speed Aircraft. NASA YF-12 Flight Loads Program. NASA TM X-3061, 1974, pp. 303-323.
67. Jenkins, Jerald M.; Kuhl, Albert E.; and Carter, Alan L.: Strain Gage Calibration of a Complex Wing. J. Aircraft, vol. 14, no. 12, Dec. 1977, pp. 1192-1196.
68. Jenkins, Jerald M.; Kuhl, Albert E.; and Carter, Alan L.: The Use of a Simplified Structural Model as an Aid in the Strain Gage Calibration of a Complex Wing. NASA TM-56046, 1977.
69. Jenkins, Jerald M.; and Lemcoe, M. M.: Problems Associated With Attaching Strain Gages to Titanium Alloy Ti-6Al-4V. NASA TM X-56044, 1977.
70. Kordes, Eldon E.; and Curtis, Alan R.: Results of NASTRAN Modal Analyses and Ground Vibration Tests on the YF-12 Airplane. ASME Paper 75-WA/Aero-8, Dec. 1975.
71. Olinger, Frank V.; Sefic, Walter J.; and Rosecrans, Richard J.: Laboratory Heating Tests of the Airplane. NASA YF-12 Flight Loads Program. NASA TM X-3061, 1974, pp. 207-257.
72. Quinn, Robert D.; and Olinger, Frank V.: Flight Temperatures and Thermal Simulation Requirements. NASA YF-12 Flight Loads Program. NASA TM X-3061, 1974, pp. 145-183.
73. Sefic, Walter J.; and Reardon, Lawrence F.: Loads Calibration of the Airplane. NASA YF-12 Flight Loads Program. NASA TM X-3061, 1974, pp. 61-107.
74. Vano, Andrew; and Steel, Jon L.: Measurement of Aircraft Structural Deflections in Flight. NASA YF-12 Flight Loads Program. NASA TM X-3061, 1974, pp. 109-143.
75. Wheaton, Duane L.; and Anderson, Karl F.: Laboratory Digital Data Acquisition and Control System for Aircraft Structural Loading and Heating Tests. NASA YF-12 Flight Loads Program. NASA TM X-3061, 1974, pp. 185-206.
76. Wilson, Ronald J.; Cazier, Frank W., Jr.; and Larson, Richard R.: Results of Ground Vibration Tests on a YF-12 Airplane. NASA TM X-2880, 1973.
77. Wilson, E. J.: Strain Gage Installation on the YF-12 Aircraft. NASA Paper Presented at Meeting of the Soc. of Exp. Stress Analysis, Los Angeles, Calif., May 13-18, 1973.
78. Wilson, Earl J.; Cook, Clarence E.; and Anderson, Karl F.: Strain and Temperature Measurement Techniques. NASA YF-12 Flight Loads Program. NASA TM X-3061, 1974, pp. 29-59.

79. Wilson, Ronald J.; Cazier, Frank W., Jr.; and Larson, Richard R.: Results of Ground Vibration Tests on a YF-12 Airplane. NASA TM X-2880, 1973.

Aerodynamic Performance

80. Lamb, Milton; Stallings, Robert L., Jr.; and Richardson, Celia S.: Aerodynamic Characteristics of 1/25 Scale Model of YF-12 Airplane at Mach 1.80 to 2.96 With and Without External Instrument Packages and Flow Field Surveys at Mach 2.96. NASA TM X-2524, 1972.
81. Larson, Terry J.; and Ehernberger, L. J.: Techniques Used for Determination of Static Source Position Error of a High Altitude Supersonic Airplane. NASA TM X-3152, 1975.
82. Larson, Terry J.: Compensated and Uncompensated Nose Boom Static Pressures Measured From Two Air Data Systems on a Supersonic Airplane. NASA TM X-3132, 1974.
83. Montoya, Earl J.: Wind-Tunnel Calibration and Requirements for In-Flight Use of Fixed Hemispherical Head Angle-of-Attack and Angle-of-Sideslip Sensors. NASA TN D-6986, 1973.
84. Powers, Sheryll Goecke: Flight-Measured Pressure Characteristics of Aft-Facing Steps in High Reynolds Number Flow at Mach Numbers of 2.20, 2.50, and 2.80 and Comparison With Other Data. NASA TM-72855, 1978.
85. Redin, Paul C.: Optimization of Transonic Acceleration Performance for the YF-12C Airplane Using the Climb-Dive Maneuver. NASA TM X-2694, 1973.
86. Schweikhard, William G.; and Redin, Paul C.: Altimetry, Performance, and Propulsion Problems of High-Altitude Supersonic Cruise Aircraft. Proceedings of NASA Aircraft Safety and Operating Problems Conf., May 1971, Vol. II, NASA SP-270, pp. 7-23.

Stability and Control

87. Bailey, Rodney O.; Petroff, Daniel N.; and Shibata, Harry H.: Effect of Inlet/Airframe Interactions of High Mach Numbers on Aircraft Static Stability and Control Effectiveness. NASA TM X-62467, 1975.
88. Berry, Donald T.: Some Handling-Qualities Problems of High-Altitude Supersonic Cruise Aircraft. Proceedings of NASA Aircraft Safety and Operating Problems Conf., May 1971, Vol. II, NASA SP-270, pp. 25-38.
89. Berry, D. T.; and Gilyard, G. B.: Some Stability and Control Aspects of Airframe/Propulsion System Interactions on the YF-12 Airplane. ASME Paper 73-WA/Aero-4, Am. Soc. Mech. Eng., Nov. 1973.

90. Berry, Donald T.; and Gilyard, Glenn B.: Airframe/Propulsion System Interactions — An Important Factor in Supersonic Aircraft Flight Control. AIAA Paper 73-831, Aug. 1973.
91. Berry, Donald T.; and Gilyard, Glenn B.: A Review of Supersonic Cruise Flight Path Control Experience With the YF-12 Aircraft. Proceedings of NASA Aircraft Safety and Operating Problems Conf., NASA SP-416, 1976, pp. 147-163.
92. Berry, Donald T.; Mallick, Donald L.; and Gilyard, Glenn B.: Handling Qualities Aspects of NASA YF-12 Flight Experience. Proceedings of the SCAR Conf., NASA CP-001, Part 1, 1976, pp. 193-213.
93. Brown, Stuart C.: Computer Simulation of Aircraft Motions and Propulsion System Dynamics for the YF-12 Aircraft at Supersonic Cruise Conditions. NASA TM X-62245, 1973.
94. Gilyard, Glenn B.; and Belte, Daumants: Flight-Determined Lag of Angle-of-Attack and Angle-of-Sideslip Sensors in the YF-12A Airplane From Analysis of Dynamic Maneuvers. NASA TN D-3819, 1974.
95. Gilyard, Glenn B.; Berry, Donald T.; and Belte, Daumants: Analysis of a Lateral-Directional Airframe/Propulsion System Interaction. NASA TM X-2829, 1973.
96. Gilyard, Glenn B.; Berry, Donald T.; and Belte, Daumants: Analysis of a Lateral-Directional Airframe/Propulsion System Interaction of a Mach 3 Cruise Aircraft. AIAA Paper 72-961, Sept. 1972.
97. Gilyard, Glenn B.; and Hill, Donald K.: Flight-Determined Longitudinal and Lateral-Directional Derivatives of the YF-12A Airplane. NASA TM-72852, 1978.
98. Gilyard, Glenn B.; Smith, John W.; and Falkner, Victor L.: Flight Evaluation of a Mach 3 Cruise Longitudinal Autopilot. AIAA Paper 74-910, Aug. 1974.
99. McMaster, John R.; and Schenk, Frederick L.: The Development of the F-12 Aircraft Flight Control System. AIAA Paper 73-822, Aug. 1973.
100. Powers, Bruce G.: Phugoid Characteristics of a YF-12 Airplane With Variable-Geometry Inlets Obtained in Flight Tests at a Mach Number of 2.9. NASA TP-1107, 1977.
101. Schweikhard, William G.; and Berry, Donald T.: Cooperative Airframe/Propulsion Control for Supersonic Cruise Aircraft. SAE Paper 740748, Apr. 1974.
102. Schweikhard, William G.; Gilyard, Glenn B.; Talbot, J. E.; and Brown, T. W.: Effects of Atmospheric Conditions on the Operating Characteristics of Supersonic Cruise Aircraft. I.A.F. Paper 76-112, Internat. Astronaut. Fed., Oct. 1976.

103. Scoggins, James R.; Clark, Terry L.; and Possiel, Norman C.: Relationships Between Stratospheric Clear Air Turbulence and Synoptic Meteorological Parameters Over the Western United States Between 12-20 km Altitude. NASA CR-143837, 1975.
104. Smith, John W.; and Berry, Donald T.: Analysis of Longitudinal Pilot-Induced Oscillation Tendencies of YF-12 Aircraft. NASA TN D-7900, 1975.

Environmental Factors

105. Ehernberger, L. J.: High Altitude Turbulence Encountered by the Supersonic YF-12A Airplane. NASA Paper Presented at AMS Sixth Conference on Aerospace and Aeronautical Meteorology, Nov. 1974.
106. Ehernberger, L. J.; and Love, Betty J.: High Altitude Gust Acceleration Environment as Experienced by a Supersonic Airplane. NASA TN D-7868, 1975.
107. Farlow, N. H.; Watson, V. R.; Loewenstein, M.; Chan, K. L.; Hoshizaki, H.; Conti, R. J.; and Meyer, J. W.: Measurements of Supersonic Jet Aircraft Wakes in the Stratosphere. NASA Paper Presented at Second Intern. Conf. on the Environmental Impact of Aerospace Operations in High Atmosphere, Am. Meteorology Soc., 1974, pp. 53-58.
108. Holdeman, James D.: Dispersion of Turbojet Engine Exhaust in Flight. NASA TN D-7382, 1973.
109. Holdeman, J. D.: Dispersion and Dilution of Jet Aircraft Exhaust at High-Altitude Flight Conditions. J. Aircraft, vol. 11, no. 8, Aug. 1974, pp. 483-487.
110. Holdeman, James D.: Emission Calibration of a J-58 Afterburning Turbojet Engine at Simulated Supersonic Stratosphere Flight Conditions. TM X-71571, 1974.
111. Holdeman, J. D.: Emission Calibration of a J-58 Afterburning Turbojet Engine at Simulated Supersonic, Stratospheric Flight Conditions. Second Intern. Conf. on the Environmental Impact of Aerospace Operations in the High Atmosphere, Am. Meteorology Soc., 1974, pp. 66-72.
112. Holdeman, James D.: Exhaust Emission Calibration of Two J-58 Afterburning Turbojet Engines at Simulated High-Altitude, Supersonic Flight Conditions. NASA TN D-8173, 1976.
113. Holdeman, James D.: Gaseous Exhaust Emission From a J-58 Engine at Simulated Supersonic Flight Conditions. NASA TM X-71532, 1974.

114. Holdeman, James D.: Measurement of Exhaust Emissions From Two J-58 Engines at Simulated Supersonic Cruise Flight Conditions. NASA TM X-71826, 1976.
115. Maglieri, Domenic J.; Huckel, Vera; and Henderson, Herbert R.: Sonic-Boom Measurements for SR-71 Aircraft Operating at Mach Numbers to 3.0 and Altitudes to 24,384 Meters. NASA TN D-6823, 1972.

Human Factors

116. Muckler, Fred; Obermayer, Richard W.; and Nicklas, Douglass R.: Pilot Performance Measurement Study. Final Technical Report. Manned Systems Sciences. NASA CR-143842, 1977.
117. Nicklas, Douglass R.: Pilot Performance Measurement Study, I. YF-12 Mission Evaluation and Task Analysis. Manned System Sciences, June 1973.
118. Obermayer, Richard W.: Pilot Performance Measurement Study, II. Data Collecting and Processing. Manned Systems Sciences, Feb. 1973.
119. Obermayer, Richard W.: Pilot Performance Study, III. Measurement Development. Manned Systems Sciences, May 1973.

General

120. Johnson, Clarence L.: Some Development Aspects of the YF-12A Interceptor Aircraft. AIAA Paper 69-757, July 1969.
121. Love, James: Flight Test Results of an Automatic Support System Onboard a YF-12A Airplane. Automatic Support Systems for Advanced Maintainability. Inst. Elec. and Electron. Eng., 1974, pp. 211-220.
122. Love, James E.; Fox, William J.; and Wicklund, Edward J.: Flight Study of a Vehicle Operational Status and Monitoring System. NASA TN D-7546, 1974.
123. Matranga, Gene J.: Background Information on Operating Problems of High-Altitude Supersonic Cruise Aircraft. Proceedings of NASA Aircraft Safety and Operating Problems Conf., May 1971, Vol. II, NASA SP-270, pp. 1-5.
124. Matranga, Gene J.; and Fox, William J.: YF-12A Development and Operational Experience. Design Conference Proceedings, Feb. 1976, AFWAL, Vol. I.
125. McMaster, John R.; and Schenk, Frederick L.: The Development of the F-12 Series Aircraft Manual and Automatic Flight Control System. AIAA Paper 73-822, Aug. 1973.
126. Miller, Richmond L., Jr.: Flight Testing the F-12 Series Aircraft. AIAA Paper 73-823, Aug. 1973.

127. Rich, Ben R.: F-12 Series Aircraft Aerodynamic and Thermodynamic Design in Retrospect. AIAA Paper 73-820, Aug. 1973.
128. Rich, Ben R.: F-12 Series Aircraft Aerodynamic and Thermodynamic Design in Retrospect. J. Aircraft, vol. 11, no. 7, July 1974, pp. 401-406.

TABLE 1.—YF-12 SPECIFICATIONS

Wing —	
Area, m ²	166.761
Aspect ratio	1.939
Root chord, m	18.542
Tip chord, m	0
Span, m	17.983
Dihedral, deg	0
Incidence, deg	1.20
Airfoil (modified biconvex), percent	2.5
Sweep, deg	52.629
Mean aerodynamic chord at W.S. 118.0, m	12.361
Inboard elevon —	
Area (each), m ²	3.63
Travel up, deg	35
Travel down, deg	20
Outboard elevon —	
Area (each), m ²	4.877
Travel up, deg	35
Travel down, deg	20
Total vertical tail —	
Area, m ²	14.006
Aspect ratio	0.778
Taper ratio	0.392
Root chord, m	6.096
Tip chord, m	2.387
Span, m	3.302
Airfoil (modified biconvex), percent	2.5
Sweep, deg	32.207
Mean aerodynamic chord, m	4.511
Movable vertical tail —	
Area (each), m ²	6.526
Root chord, m	4.512
Tip chord, m	2.387
Mean aerodynamic chord, m	3.559
Span, m	1.892
Travel, deg	±20
Fuselage ventral fin —	
Area, m ²	6.735
Root chord, m	4.178
Tip chord, m	2.616
Aspect ratio	0.61
Airfoil (modified biconvex), percent	3.5 to 2.0

TABLE 1.—CONCLUDED

Nacelle ventral fin —	
Area, m ²	2.044
Root chord, m	4.248
Tip chord, m	3.266
Airfoil (modified biconvex), percent	2.5
Fuselage —	
Diameter, m	1.626
Overall length, m	30.986

TABLE 2.—MAJOR YF-12 ACTIVITIES

Propulsion	Structures and materials	Other
<u>Inlet</u> <i>Steady-state performance</i> *Distortion *Pressure recovery Airflows Pressure distributions *Forebody flow field effects <i>Dynamics</i> *Duct dynamics *Inlet transients *Dynamic distortion *Instrumentation techniques *Atmospheric effects <u>Engine</u> Turbine inlet temperature system Inlet/engine interactions Airflow calibration <u>Controls</u> Shock position sensors *Shock stability valves *Digital inlet control *Frequency response testing	Fuel tank sealants Composite structural components Advanced metallic components Landing gear dynamics Strain gage installation techniques *Strain gage calibration methods NASTRAN model analysis Deflection measurements *Low aspect ratio load prediction Thermal stress Structural dynamics Temperature measurements <u>Aerodynamics</u> *Forebody flow field *Aircraft performance modeling *Heat transfer *Skin friction measurement *Boattail drag Flow field mapping *Boundary layer profiles *Boundary layer noise *Discontinuity drag (aft step)	Noise suppressor tests Maintenance recorder system Exhaust wake constituents *Upper atmosphere characteristics Sonic boom measurements Military support experiments *Altitude hold autopilot *Autothrottle systems Air data measurements *Propulsion/airframe integration *Man/machine interface Shuttle landing studies *Handling qualities criteria

TABLE 3.—YF-12 RESEARCH ASSETS

Two highly instrumented aircraft
 NASTRAN model
 FLEXSTAB model
 1/12-scale force model tests
1/12-scale oil flow and tuft model tests
 1/12-scale pressure model tests
 1/25-scale flow survey model tests
 Full-scale inlet wind tunnel tests
One-third-scale inlet wind tunnel tests
 1/12-scale model inlet flow survey
Airplane/inlet/engine computer model
 Inlet/engine computer model
 Engine computer model
 Engine airflow calibration tests
Engine product of combustion tests in Propulsion Systems Laboratory
 Noise tests
 Wealth of flight test data
 Operational experience

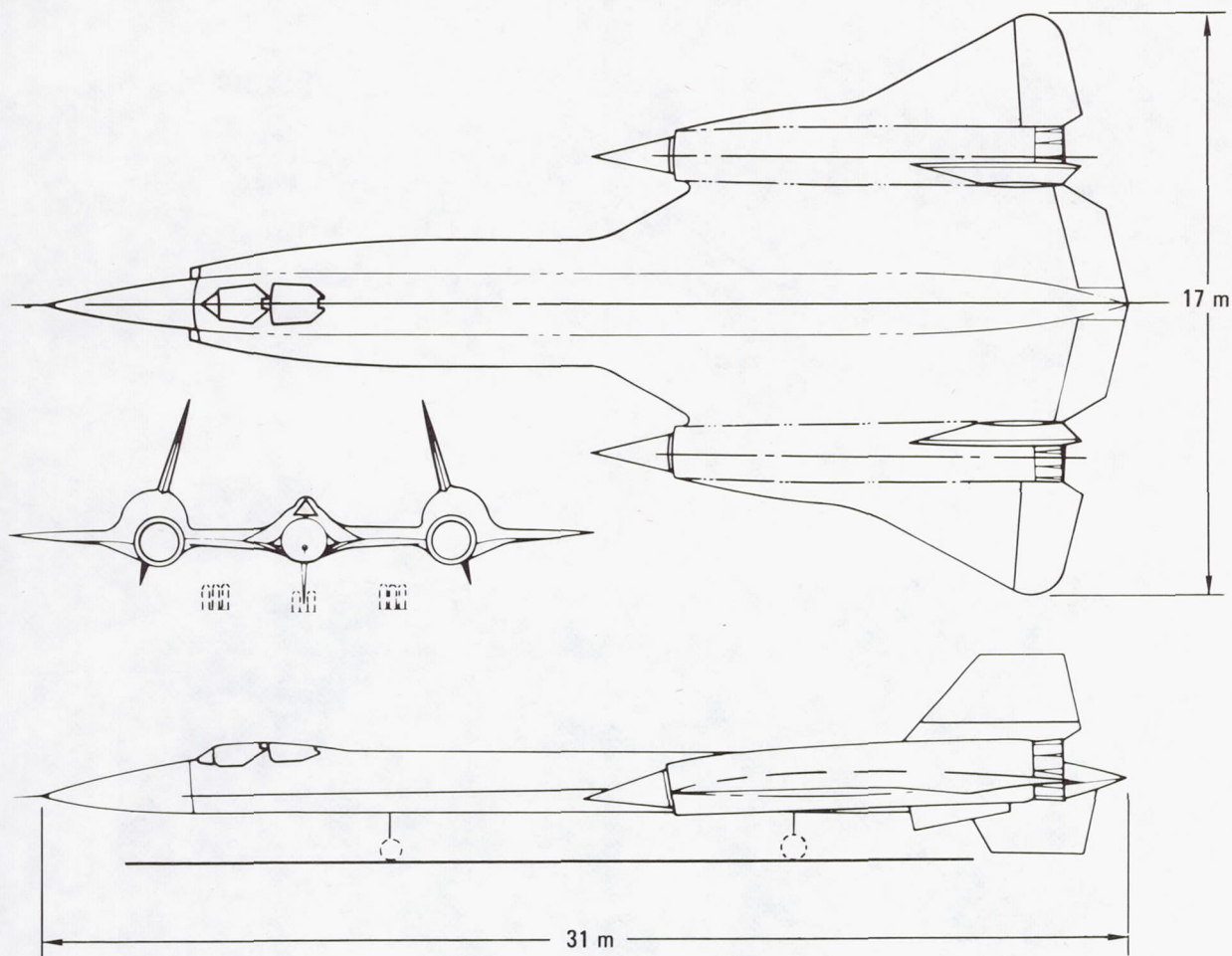


Figure 1.—YF-12A airplane.

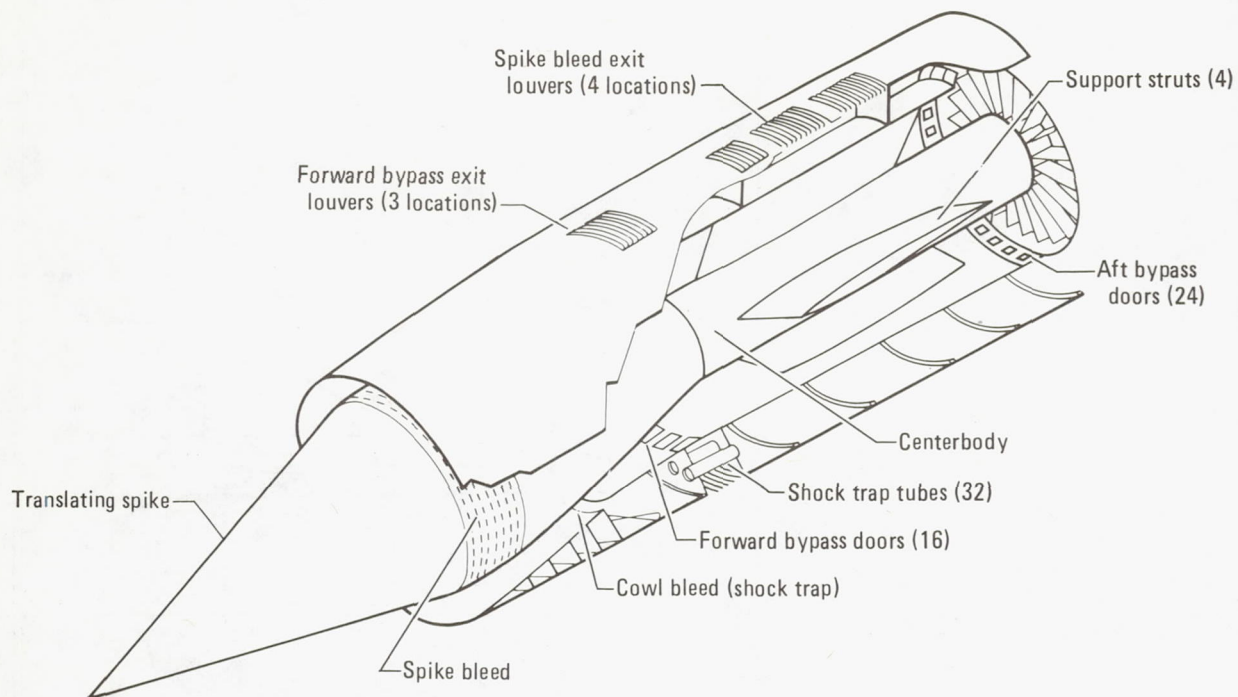


Figure 2.—Cutaway view of the inlet.

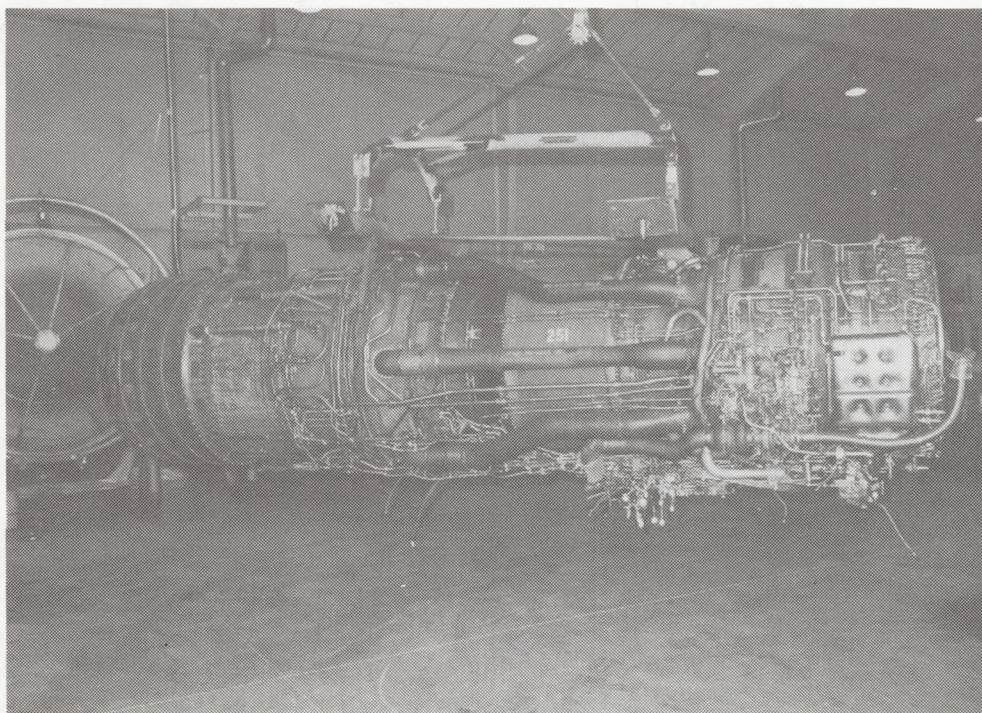


Figure 3.—J58 engine.

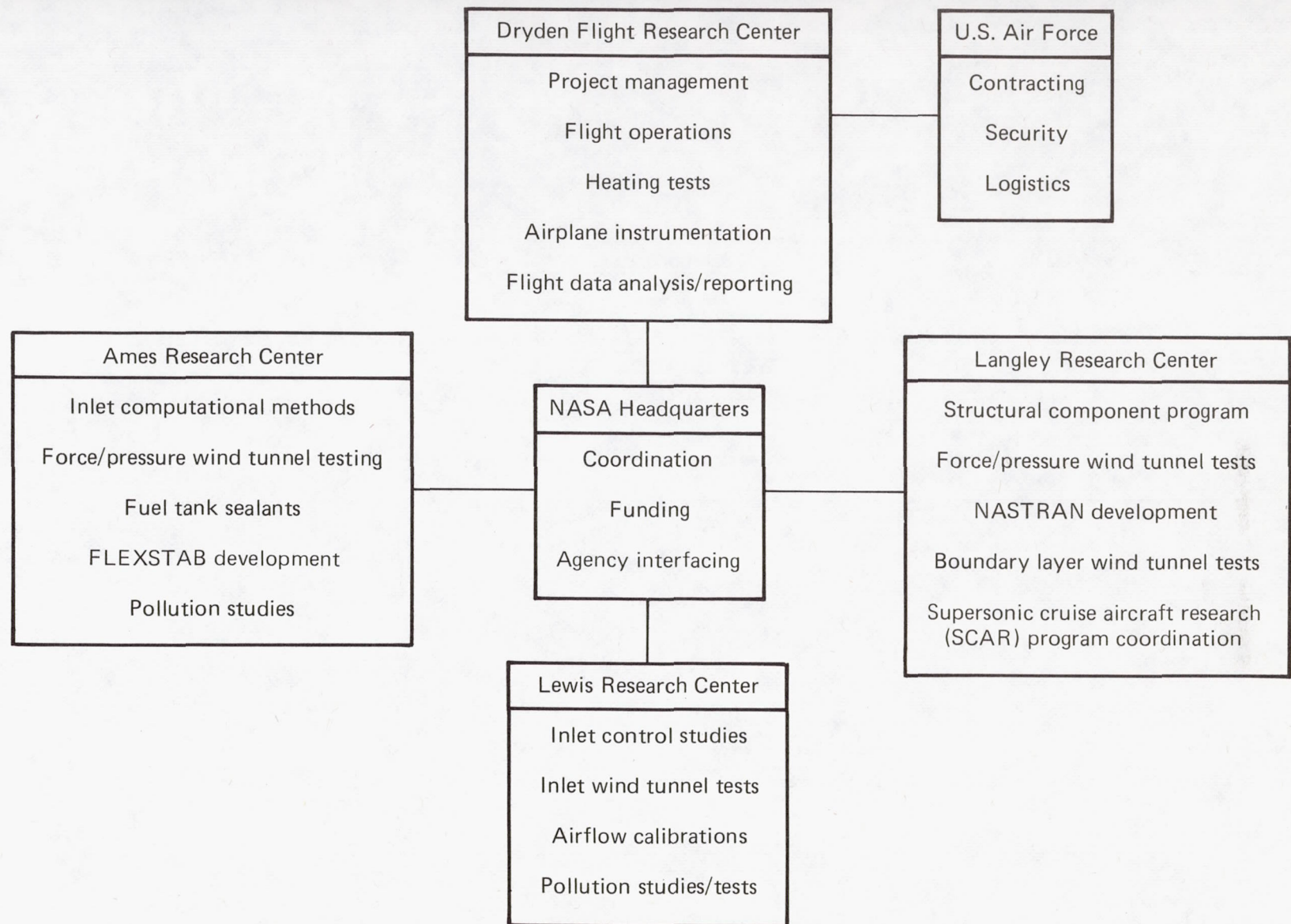


Figure 4.—YF-12 project organization.

SESSION I: PROPULSION SYSTEM PERFORMANCE

Chairman: Robert E. Coltrin, Lewis Research Center

AN INTRODUCTION AND SUMMARY OF THE YF-12
PROPULSION RESEARCH PROGRAM

William Schweikhard and David H. Campbell
Dryden Flight Research Center

SUMMARY

An overview of the YF-12 propulsion research program, its objectives, and some of the considerations and obstacles involved in carrying it out are presented. A description of the propulsion system, its controls and operating characteristics, and some highlights of previously unpublished results are included. Insights and pitfalls associated with a program whose prime objective was the correlation of analytical, wind tunnel, and flight results are presented. In addition, findings associated with the development of high temperature flight instrumentation, the measurement of local flows in and around the inlet, and the measurement of airflows and pressures through the bleed and bypass regions are discussed.

FULL-SCALE YF-12 INLET CALIBRATION
AND FLOW SYSTEM INTERACTIONS

Robert W. Cubbison and Bobby W. Sanders
Lewis Research Center

SUMMARY

The isolated, full-scale, flight hardware inlet was tested in the Lewis Research Center 10- by 10-Foot Supersonic Wind Tunnel to provide the calibrations necessary for flight data reduction and to establish inlet operating boundaries which in turn determined the flight test conditions. The scope and results of the calibration are presented as well as the inlet flow system interactions. The inlet operating envelope showing the unstart-restart boundaries is presented along with a discussion of the operational anomalies encountered.

COMPARISON OF ONE-THIRD-SCALE AND FULL-SCALE
YF-12 ISOLATED INLET PERFORMANCE

Robert W. Cubbison and Bobby W. Sanders
Lewis Research Center

SUMMARY

Steady-state data obtained on a one-third-scale isolated inlet model tested in the Ames Research Center Unitary Plan Wind Tunnel Complex 9- by 7-Foot and 8- by 7-Foot Supersonic Wind Tunnels and on a full-scale flight inlet tested in the Lewis Research Center 10- by 10-Foot Supersonic Wind Tunnel are presented for Mach numbers above 2.0. Performance levels are compared for nominal standard day and peak operating conditions. Unstart boundaries and the effect of angle of attack are discussed.

MATHEMATICAL MODELING OF THE PERFORMANCE
OF A YF-12 MIXED-COMPRESSION INLET BY
USING MULTIPLE REGRESSION TECHNIQUES

James D. Brownlow , Henry H. Arnaiz , and James A. Albers
Dryden Flight Research Center

SUMMARY

A mathematical model to correlate wind tunnel and flight performance data of a high-speed, mixed-compression inlet was derived from a set of wind tunnel test data. A multiple regression technique, which basically uses a least-squares method to fit equations to the data, was used to derive the model. The mathematical model was evaluated using both a mathematical (statistical) and an engineering approach. Results of the evaluation indicated that the model could generally predict the wind tunnel results within the accuracy of the wind tunnel measurements.

A COMPARISON OF STEADY-STATE PERFORMANCE AMONG A FLIGHT INLET
ON A YF-12 AIRPLANE AND TWO WIND TUNNEL MODELS
USING STATISTICAL TECHNIQUES

Henry H. Arnaiz, James D. Brownlow, and James A. Albers
Dryden Flight Research Center

SUMMARY

A comparison was made between the steady-state performance of a flight inlet on a YF-12 airplane and a full-scale and a one-third-scale wind tunnel model of the same inlet. The purpose of the comparison was to determine if performance differences were present between flight and wind tunnel models when operated over a Mach number range where the inlets were in the mixed-compression mode. Although the comparison was to have been made at identical test conditions, it was found that identical test conditions could not be obtained because of limitations encountered in the testing of the three inlets. Therefore, the comparison was made by applying statistical techniques, such as the analysis of covariance, to the test data. The results of these analyses indicated that, with minor exceptions, little or no differences were present between the performance of the flight inlet and the two wind tunnel models.

SESSION II: INLET TIME VARYING DISTORTION

Chairman: Daniel P. Bencze, Ames Research Center

COMPARISON OF FLIGHT AND WIND TUNNEL MODEL
INSTANTANEOUS DISTORTION DATA FROM A
MIXED-COMPRESSION INLET

Carol A. Bauer, Karen G. Mackall,
Frederick Stoll, and Jeffrey W. Tremback
Dryden Flight Research Center

SUMMARY

Comparisons were made between flight and wind tunnel distortion data to determine if values of instantaneous distortion obtained from wind tunnel models could be used to predict instantaneous distortion values present in flight. In this study data from a mixed-compression inlet on a YF-12C airplane were compared with data obtained from both a full-scale and a one-third-scale wind tunnel model of the same inlet, all operating at nearly identical test conditions for two supersonic Mach numbers. Steady-state and instantaneous values of radial, circumferential, and maximum-minus-minimum distortion descriptors were used for the analysis. Strouhal number scaling techniques were used so that the properties of the fluctuating components of the descriptors, such as the mean value, the standard deviation, an inlet turbulence term, and the maximum value of instantaneous distortion could be compared.

Some of the results of the analysis showed that although steady-state distortion levels may be significantly different, several relationships existed between the wind tunnel and flight data. For example, a linear relationship existed between the maximum value of instantaneous distortion and the steady-state distortion value. This relationship was found to be independent of both the inlet and the test condition and could be used for both flight and wind tunnel model data. This indicates that, using these wind tunnel derived relationships and the flight value of steady-state distortion, the maximum value of instantaneous distortion in flight can generally be predicted within ± 10 percent.

Inlet turbulence levels on all three inlets were found to agree very well at each test condition. This indicates that the inlet turbulence level measured on wind tunnel models is representative of that measured in flight.

PREDICTED AND MEASURED MAXIMUM INSTANTANEOUS DISTORTION
FOR FLIGHT AND WIND TUNNEL MODEL DATA
FOR A MIXED-COMPRESSION INLET

Howard M. Brilliant
U.S. Air Force Academy


Carol A. Bauer and Robert A. Davis
Dryden Flight Research Center

SUMMARY

A method was recently developed for estimating probable maximum instantaneous compressor face total pressure distortion. The advantage of this method is that it requires fewer total pressure measurements to be made. In the present study, the same method was applied to the YF-12C mixed-compression inlet using data obtained from YF-12C flight tests and from wind tunnel tests of both full-scale and one-third-scale inlet models. Values estimated by the method investigated were found to be within 20 percent of the measured values for the three sets of data examined.

SESSION III: STRUCTURES

Chairman: Alan L. Carter, Dryden Flight Research Center



RECENT LOAD CALIBRATIONS EXPERIENCE

WITH THE YF-12 AIRPLANE

Jerald M. Jenkins and Albert E. Kuhl
Dryden Flight Research Center

SUMMARY

The results of recent experience using calibrated strain gages to measure wing loads on the YF-12A airplane are presented. Structural configurations relative to the thermal environment and resulting thermal stresses are discussed. A thermal calibration of the YF-12A is described to illustrate how contaminating thermal effects can be removed from loads equations. The relationship between ground load calibrations and flight measurements is examined for possible errors, and an analytical approach to accommodate such errors is presented.

INTRODUCTION

The measurement of structural loads is an important part of the flight test program on any new aircraft. In the past, these loads have been effectively measured by the use of calibrated strain gage systems (ref. 1). However, new supersonic and hypersonic aircraft often use complex delta-wing designs (refs. 2 to 4) and operate in higher temperature environments. This makes the measurement of structural loads more difficult. In addition to the fact that the delta-wing structure is harder to calibrate because of its structural complexities, the thermal effects present at the higher speeds (refs. 5 and 6) also cause contamination of the strain gage measurements necessary to deduce flight loads (ref. 7).

To obtain valid measurements of loads from aircraft operating in higher temperature environments, the use of thermally calibrated strain gage systems was investigated using the YF-12A aircraft as a typical delta-wing design (refs. 8 to 10). The errors which resulted from the induced thermal effects were determined. A simple computer model (ref. 11) was developed to predict strain patterns which would assist in placing strain gages and in developing load equations.

This report deals with the general philosophy used to calibrate the strain gage system and to determine the accuracy of the load equations when applied to a typical delta-wing configuration.

SYMBOLS

Physical quantities in this report are given in the International System of Units.

g	acceleration due to gravity, m-N/sec^2
L_A	wing loading due to aerodynamic forces, N or m-N
L_I	wing loading due to inertial forces, N or m-N
L_M	total measured wing loading, N or m-N
L_T	wing loading induced by thermal effects, N or m-N
T	temperature, K
t	time, min

STRUCTURAL CONFIGURATIONS

Supersonic and hypersonic wing designs (ref. 12) consider both aerodynamic and structural factors. The frequent use of the delta-wing shape reflects the obvious need for aerodynamic efficiency. However, structural considerations are more latent and require considerable explanation. Figure 1 shows a structural skeleton of the YF-12A airplane. The wing surfaces are built up of a beaded outer skin and a corrugated inner skin. These surfaces are supported by 28 closely-spaced spanwise beams and by four chordwise ribs. The wing beams are continuous through the fuselage. The engine nacelle is an integral part of the wing and the nacelle rings provide continuity between the inner and outer wing beams. A factor to be considered in the structural design of a supersonic wing is the presence of elevated structural temperatures and temperature gradients when operating in the higher Mach number range. Differential temperatures among structural elements, the effects of dissimilar materials, and nonlinear temperature distributions result in thermal stresses that can be very large.

There is little documented information about state-of-the-art methods for calculating thermal stresses in complex structures. This lack of information has probably led to avoidance design philosophies in which the designer configures the structure to avoid thermal stresses as much as possible. An example of avoidance design is illustrated in figure 2. In this case, the skin structure is corrugated to allow expansion in one direction. Skins of this type are generally attached to the substructure using a standoff-type clip which allows the expansion to be absorbed in an accordian-like manner. The standoff clips provide the structural continuity,

creating a heat shield effect. It is very likely that future designs will also include avoidance techniques similar to those used on the YF-12A airplane; however, while these designs reduce the magnitudes of thermal stresses, they do not eliminate them, as will be shown later.

THERMAL ENVIRONMENT

The primary problems arising from elevated structural temperatures concern the structure itself. There are two important factors which must be considered: the absolute magnitude of the temperature and the manner in which the temperature is distributed. The absolute magnitude of the temperature affects such things as the strength of the material, its stiffness, and the interactions between dissimilar materials. The temperature gradients and the nature of the gradients primarily affect the severity of the thermal stresses. Both of these factors influence measurements of flight loads using strain gages.

The isotherms shown in figure 3 illustrate how steady-state temperatures are distributed on the YF-12A airplane when cruising at Mach 3. Under these conditions maximum temperatures reach 589 K. The manner in which these temperatures increase is shown in figure 4 for different skin locations. It can be seen that, as the airplane increases speed to its Mach 3 cruise, the skin temperatures rise quickly to their steady-state values.

Although the skin areas generally reach steady-state temperatures quickly, this is not true of the substructure. The time history shown in figure 5 illustrates that the substructure spar cap and spar web are slow to reach steady-state temperature. In this case the airplane is at a Mach 3 cruise for 15 minutes before the substructure temperatures begin to stabilize. The same effect can be seen more graphically in figure 6 where the temperatures are plotted for four different time segments during a Mach 3 cruise flight. At the 8-minute time segment, the temperature gradients are large and the distribution of temperature is highly nonlinear. After about 32 minutes, the temperature reaches steady state. At that time, the gradients are not large and the nonlinearity is significantly reduced.

The nature of these gradients and the characteristics of nonlinearities have a large influence on the thermal stress patterns induced in the aircraft structure by the temperature field. Transient thermal stresses will be a major design concern in any future supersonic aircraft capable of speeds much above Mach 2. The presence of these thermal stresses can also cause errors in strain gage measurements of aerodynamic, inertial, or dynamic loads unless the thermal stresses are considered in the strain gage calibration procedures.

THERMAL STRESS

Two types of thermal stress result from the supersonic flight environment. The first type (ref. 13) results from the forces that arise in a system of mutually connected members as a result of their combined effect on one another. This may be caused by the use of materials having different coefficients of expansion, or it may

be caused by nonuniform temperatures in the bodies making up the system. A second type (ref. 13) results from nonlinearities in the temperature field or in the material properties of the body. This type of stress might occur if a single spar has a nonlinear temperature gradient through its depth. For example, consider the structural element in figure 7. If the temperature distribution shown is imposed on this skin/substructure element, thermal stresses arise due to the nonlinear nature of the temperature distribution. Thermal stresses in this case may be computed using elementary beam theory (ref. 14). The results of this type of thermal stress analysis are shown in figure 8.

The stress pattern in the skin reflects the heat sink effect of the substructure. Tensile stresses exist in the cooler areas near the substructure and compressive stresses exist in the hotter areas. A widely varying stress pattern is also present through the depth of the substructure. In this case, large tensile stresses exist in the web area, while the lower cap has compressive stresses. This demonstrates the need for a thorough analysis as part of any design or testing endeavor in which thermal stresses are a factor.

It is important to understand that the distribution of thermal stress shown in figure 8 is for a single instant in time. Thermal stresses are generally time-dependent and vary in direct relation to the manner in which the temperature field varies with time. Because the temperatures are constantly changing, thermal stresses in any one discrete element may vary from large compressive values to large tensile values during a flight.

The data presented in figure 9 were developed from laboratory heating tests on the YF-12A airplane. These ground heating tests determined the strain gage outputs due to the effects of heat alone. These outputs could then be put into the load equations, which are linear equations that relate several strain gage outputs to a set of calibration loads. From these equations the thermal load can be calculated. The transient behavior of strain gages can be seen indirectly in figure 9, which is a time history of the thermal errors for a set of shear, bending, and torsion equations. In this case, the thermal load is shown as a ratio with respect to a reference load. The reference load is the approximate wing loading under 1g flight conditions. The ratio values are used to provide a more meaningful measure of the relative magnitude of the thermal effects.

It was found that the outputs of the strain gages used in the shear and torque equations maximize near the time when the Mach 3 cruise begins. At that time, the value approaches half of the reference load. This correlates with the nonlinear distributions of temperature shown in figure 6. The nonlinearity of the temperature distribution has its greatest effect on the web thermal stresses which are primarily used to develop shear and torsion equations.

The time history of the bending equation is quite different. The value slowly builds to around 10 percent of the reference load near the end of the cruise. The bending gages, which are usually located on the caps or skins, were found to be more sensitive to the temperature rise than to the thermal stress levels.

THERMAL CALIBRATION

The presence of thermal stresses of unknown magnitudes in the region where strain gages are located causes measurement errors, since the strain gages sense both aerodynamic forces and thermal effects. This problem is similar to the situation that arises when loads are measured during conventional subsonic maneuvering flight. In this case, the strain gages sense a combination of aerodynamic and inertial loads. The total measured load, L_M , is mathematically represented as:

$$L_M = L_A + L_I \quad (1)$$

where L_A is the total aerodynamic force and L_I is the total inertial force.

Since inertial loads can be calculated quite accurately if the mass characteristics of a wing are known, the aerodynamic load can be calculated by deducting the calculated inertial load from the total measured load:

$$L_A = L_M - L_I \quad (2)$$

This approach is commonly used to remove the inertial loads from flight data. The same type of relationship is valid for removing thermal effects for supersonic and hypersonic maneuvering flight. In this case the equation is:

$$L_A = L_M - L_T - L_I \quad (3)$$

where L_T is the fictitious load induced by the thermal effects. The philosophy of the correction is straightforward; however, implementing the correction is not so direct because determining the value of L_T is difficult. Frequently, the thermal load is large and must be determined with substantial accuracy. The ideal way to determine thermal effects would be to calculate the thermal stresses. Unfortunately, there is very little state-of-the-art information available about calculating thermal stresses in complex structures. The limited information (ref. 15) that is available indicates that large deviations exist between predicted and measured values. Precise calculations of thermal stresses also require a thorough and detailed definition of structural temperatures and such calculations would be awesome in size. Therefore, it does not appear that calculating the thermal stresses is a viable way to provide the load corrections unless considerable progress is made in calculative techniques.

A more direct approach to this problem uses a procedure known as a thermal calibration. In this procedure, the structure of the airplane is heated in a ground-based facility to obtain conditions identical to those experienced in flight. The objective of this procedure is to obtain the output from each of the strain gages that is due to heating effects only. In the laboratory environment, there are no aerodynamic or other external forces present (gravity excepted) to contaminate the determination of the thermal effects. This type of calibration was performed on the YF-12A airplane and the results are presented in reference 15. The thermal calibration procedure has proven to be feasible; however, the task of performing a thermal calibration is difficult. Duplicating an in-flight temperature time history for a complex airplane

structure is time consuming, costly, and technically complicated.

The facilities used to heat the airplane to obtain the thermal calibration are shown in figure 10. The airplane's surface temperatures were controlled by using thermocouples linked to a digital computer which commanded heating inputs from banks of radiant heat lamps. The surface of the airplane was divided into approximately 1000 zones which were independently controlled during the thermal calibration. The heating time histories of several flight profiles were simulated to provide corrections for several high Mach number conditions. The laboratory data were then used to correct the flight data.

Certain characteristics of thermal behavior should be known when thermal calibrations are necessary. Figure 11 shows temperature time histories of typical skin and web responses during three distinct phases of a flight: (A) increasing Mach number, (B) cruise at constant Mach number, and (C) decreasing Mach number. For the majority of the flight, the structure is in a state of changing temperature. The largest thermal stresses, and therefore the largest thermal corrections, occur during the transient portion of the flight, as indicated in figures 4 to 9. This means that when the temperatures are near steady state, as depicted in figure 12, the thermal corrections are at their smallest values. Early in the flight, the thermal component is large compared to the aerodynamic component of load. More possibility of error exists when the ratio of L_T/L_A is large because the correction value is large.

When the ratio of L_T/L_A is small, such as for maneuver B, shown in figure 12, the errors present in the correction are also small and the aerodynamic component can be determined more accurately. Because of this, it is preferable to conduct load maneuvers near equilibrium conditions where the thermal gradients are small. However, sometimes special test requirements may be imposed that prevent the data from being obtained at the optimum thermal conditions. For example, if the data must be obtained for high airplane gross weights, this information cannot be obtained during the latter part of a flight. As a flight progresses, the constant- g wing loads decrease as the gross weight decreases due to fuel consumption, and this can affect the L_T/L_A ratio. Therefore, although it is preferable to get data late in the flight, there are instances in which exceptions must be made.

LOAD CALIBRATIONS

The traditional approach used to obtain wing loads data using calibrated strain gages has followed a sequence that includes: (1) locating strain gage bridges on pertinent structural members, (2) applying point loads to the wing in a grid pattern, (3) linearly relating the applied loads to the strain gage bridge outputs by means of a load equation, and (4) computing the equation error by using the strain gage bridge outputs in the equations, and then calculating the difference between the result and the known applied load. This approach has been used with great success for many years on high-aspect-ratio wings; however, the delta-wing shapes are not so amenable to this approach, and there is little additional information available regarding the calibration of delta-wing airplanes. Fortunately, recent experience has provided some additional information on the subject.

The basic problem arises from the fact that delta wings usually have multispar configurations with large chord dimensions relative to the span dimensions. With this configuration, a high degree of structural redundancy exists, which makes it difficult to determine how well a system can measure various load distributions. A study was conducted with two objectives: (1) to investigate a method to evaluate the accuracy of the load equations in deducing the true flight loads being measured and (2) to examine how well a simple computer structural model can be used to predict load response characteristics.

Mathematical Loadings

In order to develop a technique to evaluate the accuracy with which a load equation can compute various load distributions, it is necessary to identify a range of load distributions to serve as a standard. The three load distributions shown in figure 13 represent a reasonable cross section of expected loadings. Included are a loading with a forward center of pressure (typical of a subsonic load distribution), a loading with a central center of pressure (typical of a supersonic load distribution), and a loading with an aft center of pressure (typical of a loading induced by a large control surface deflection).

A method for interfacing the three mathematical loadings with the information developed from the load calibration is shown in figure 14. The load calibration provides influence coefficients and load equations. By subdividing the three mathematical loadings into local area loadings corresponding to the calibration load points, the strain gage bridge output can be calculated by multiplying the local area loading by the influence coefficient for that area. If this is done for all the local area loadings, and if all of the resulting outputs are summed, the result is the total output for each strain gage bridge due to the total mathematical wing loading. If these outputs are used appropriately in the load equations, a load may be calculated for comparison with the mathematically applied loading. This provides a functional check on how the load measuring system responds to varying load distributions.

This approach was used to examine the load calibration, and the subsequently developed load equations for the YF-12A airplane. A mathematical loading of 44,482 newtons was distributed over the surface of the wing according to the three load distributions described in references 16 to 18 and shown in figure 13. The procedures outlined in figure 14 were then used to calculate the loads from the superimposed strain gage outputs and the available load equations. The results are shown in figures 15 to 17.

As shown in figure 15, eight shear equations were checked using the procedure described. It was found that many of the equations calculated a load less than that mathematically applied. This implies a deficiency in the equations' ability to account for all the load on the surface. The worst cases occurred when the center of pressure was aft. Deficiencies of 20 percent or more were common for this condition.

The bending moment results (fig. 16) show a different trend. The greatest deficiency, between 5 and 10 percent, occurred in the central center-of-pressure case. In general, the bending moment equations seemed quite consistent and able to accommodate load variations well.

Six torsion equations are examined in figure 17. It is important to exercise caution when examining torsion data, since the reference axis location is arbitrary and this affects the magnitude of the results. It is also important to note that the vertical scales are different for the three cases. Although the equations provided reasonably accurate load calculations in two of the cases, a large discrepancy existed between the calculated load and the applied load for the aft center-of-pressure case.

There are two basic conclusions that can be drawn from this study: (1) There is still much that is not understood about calibrating low-aspect-ratio wings, and (2) computational procedures can be very helpful in selecting equations and in evaluating system errors.

Another interesting feature is apparent in figure 18, which shows the location of the calibration loads. The lengths of the vectors represent the magnitude of the loads. It is interesting to note that there is little correlation between the location of the large calibration loads and the location of the large flight loads depicted in figure 13. The magnitude of the calibration loads is usually a function of substructure bearing strength, and it does not necessarily correspond to the manner in which flight loads are distributed on the wing surface. This is a common condition, particularly on delta-wing structures.

Structural Computer Models

It is advantageous to know the nature of the structural response of various wing spars prior to developing a load calibration plan. A study was conducted to determine if a relatively simple structural model could be used to predict spar strain responses to load and to develop predicted influence coefficient plots of a general nature. Since the point of diminishing returns is quickly reached when the expense of modeling is considered, the study was limited to a simple structural model.

A bar element NASTRAN model of the wing of the YF-12A airplane was developed for this study. The ability of the model to predict strains along the root of the wing is shown in figures 19 and 20. In figure 19, the calculated and measured shear strains are shown at the wing root spars for loads applied to the wing at the locations and in the directions indicated by the arrows. It can be seen that the correlation between the measured shear strains and the strains calculated using the simple computer model is good. A similar comparison for bending strains is made in figure 20, and the correlation between the measured and predicted strains is also good.

In figures 21 and 22, influence coefficients have been calculated using the structural model, and they have been calculated from the laboratory load calibration data. The influence coefficients represent the strain that exists per unit of applied load. In the figures, the influence coefficient is plotted against the span on the basis of constant chord lines. The measured and calculated influence coefficients are compared in figure 21 for three different shear bridges located strategically along the wing root. The characteristic shapes of the measured and calculated curves are quite similar. In the first case the magnitude of the calculated data exceeds that of the measured data considerably; however, the general correlation is good. A similar comparison is shown in figure 22 for a bending bridge. The correlation for the bending bridges is also good and this plot is typical.

The results of this study indicate that considerable information can be gained from a simple structural computer model of a supersonic wing. This type of information is also extremely helpful in locating strain gages and in identifying potential strain gage combinations for use in load equations.

CONCLUDING REMARKS

Generally, wing configurations for supersonic, and even hypersonic airplanes, are low-aspect-ratio structures, with delta-wing shapes occurring most frequently. Present design trends configure the structure to avoid large thermal stresses. However, since there is no practical way to eliminate thermal stresses entirely, they must be considered in the design, testing, and operation of supersonic and hypersonic airplanes.

All aircraft which operate in the high supersonic and hypersonic speed ranges experience the effects of aerodynamic heating. Both high temperatures and large thermal gradients affect the validity of load measurements using calibrated strain gages. Structural temperature levels may even become high enough to alter spar stiffness, which could result in load path changes that might subsequently invalidate the wing strain gage calibration. Nonuniform temperature distributions also induce thermal stresses which can be very large and which can contaminate flight measurements of loads using strain gages.

Thermal effects which prevent valid high Mach number strain gage data from being obtained can be determined by thermally calibrating supersonic airplanes. Therefore, a ground laboratory heating simulation is a necessary part of the flight test program if valid loads data are to be obtained. The magnitudes of thermally induced loads vary in the supersonic environment, but they are large enough to require consideration in all cases.

A study to examine the adaptability of a set of load equations selected solely on the basis of the load calibrations revealed that discrepancies can exist if the loads to be measured are not considered in the overall selection process. The study also indicated that a relatively simple structural computer model can be very useful in predicting strain response to external loads with relatively good accuracy. This capability provides considerable foresight in locating strain gages and in identifying possible strain gage combinations for use in load equations.

REFERENCES

1. Skopinski, T. H.; Aiken, William S., Jr.; and Huston, Wilber B.: Calibration of Strain-Gage Installations in Aircraft Structures for the Measurement of Flight Loads. NACA Rept. 1178, 1954.
2. Jenkins, Jerald M.; DeAngelis, V. Michael; Friend, Edward L.; and Monaghan, Richard C.: Flight Measurements of Canard Loads, Canard Buffeting, and Elevon and Wing-Tip Hinge Moments on the XB-70 Aircraft Including Comparisons with Predictions. NASA TN D-5359, 1969.
3. Rich, Ben R.: The F-12 Series Aircraft Aerodynamic and Thermodynamic Design in Retrospect. AIAA Paper 73-820, Aug. 1973.
4. Ripley, E. L.: Structural Tests for the Supersonic Transport Aircraft. Technical Report 70121, Royal Aircraft Establishment (Farnborough, Hants., England), July 1970.
5. Quinn, Robert D.; and Olinger, Frank V.: Flight Temperatures and Thermal Simulation Requirements. NASA YF-12 Flight Loads Program. NASA TM X-3061, 1974, pp. 145-183.
6. Olinger, Frank V.; Sefic, Walter J.; and Rosecrans, Richard J.: Laboratory Heating Tests of the Airplane. NASA YF-12 Flight Loads Program. NASA TM X-3061, 1974, pp. 207-257.
7. Jenkins, Jerald M.: Some Views on the Use of Strain Gages for Flight Loads Measurements on Future High Performance Aircraft. Proceedings of Western Regional Strain Gage Committee, —1969 Spring Meeting, Philip Q. Vulliet, ed., pp. 1-2. (Available from Soc. for Exp. Stress Analysis, 21 Bridge Sq., Westport, Conn. 06880.)
8. Fields, Roger A.: Strain Gage Measurement of Flight Loads at Elevated Temperature. NASA YF-12 Flight Loads Program. NASA TM X-3061, 1974, pp. 259-302.
9. Sefic, Walter J.; and Reardon, Lawrence F.: Loads Calibration of the Airplane. NASA YF-12 Flight Loads Program. NASA TM X-3061, 1974, pp. 61-107.
10. Jenkins, Jerald M.; and Kuhl, Albert E.: Summary of Recent Results Pertaining to Strain Gage Load Measurement Technology on High Speed Aircraft. NASA YF-12 Flight Loads Program. NASA TM X-3061, 1974, pp. 303-323.
11. Jenkins, Jerald M.; Kuhl, Albert E.; and Carter, Alan L.: The Use of a Simplified Structural Model as an Aid in the Strain Gage Calibration of a Complex Wing. NASA TM-56046, 1977.
12. Plank, P. P.; and Pennings, F. A.: Hypersonic Wing Test Structure Design, Analysis, and Fabrication. NASA CR-127490, 1973.

13. Fridman, Ya. B., ed.: Strength and Deformation in Nonuniform Temperature Fields. Authorized translation from the Russian, Consultants Bureau, New York, 1964.
14. Boley, Bruno A.; and Weiner, Jerome H.: Theory of Thermal Stresses. New York. John Wiley & Sons, Inc., 1962.
15. Carter, Alan L.: Assessment of Recent Loads Analysis Methods as Applied to a Mach 3 Cruise Airplane. NASA YF-12 Flight Loads Program. NASA TM X-3061, 1974, pp. 625-645.
16. Allen, H. Julian: General Theory of Airfoil Sections Having Arbitrary Shape or Pressure Distribution. NACA Rept. 833, 1945.
17. DeYoung, John; and Harper, Charles W.: Theoretical Symmetric Span Loading at Subsonic Speeds for Wings Having Arbitrary Plan Form. NACA Rept. 921, 1948.
18. Tucker, Warren A.; and Nelson, Robert L.: Theoretical Characteristics in Supersonic Flow of Two Types of Control Surfaces on Triangular Wings. NACA Rept. 939, 1949.

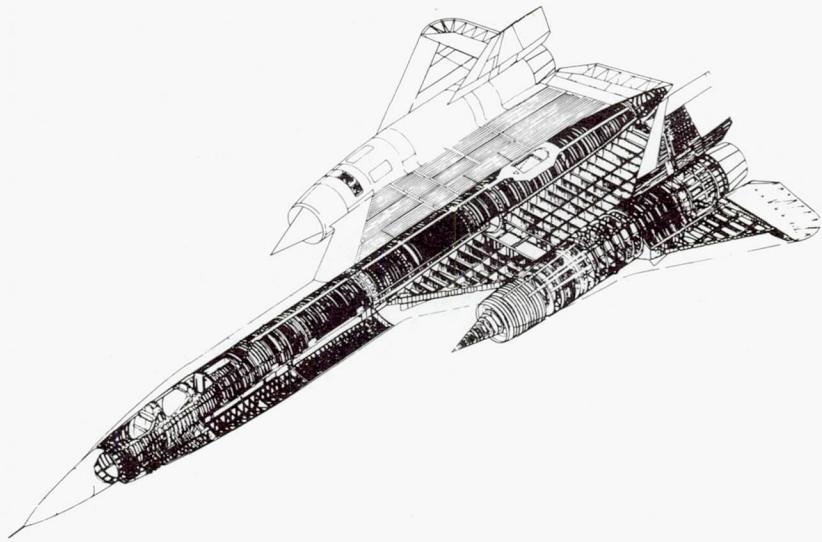


Figure 1.—Structural skeleton of a complex delta-wing aircraft.

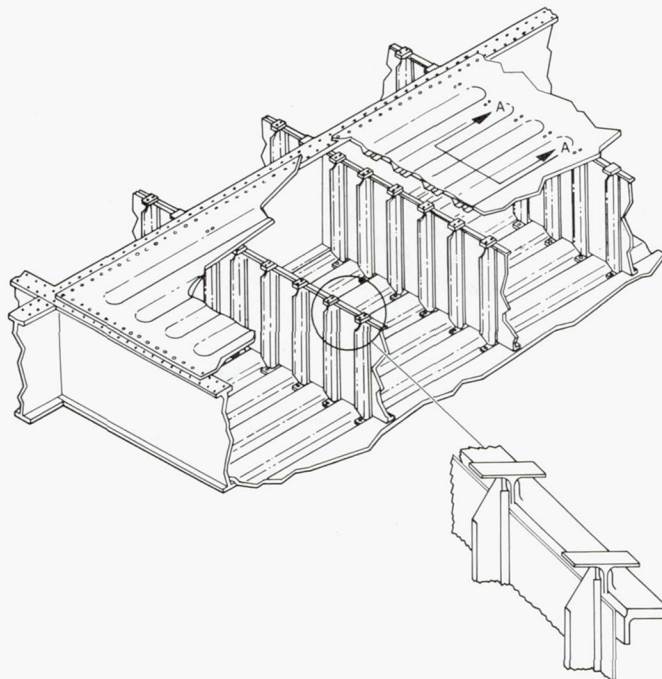


Figure 2.—Wing design used to minimize thermal stress.

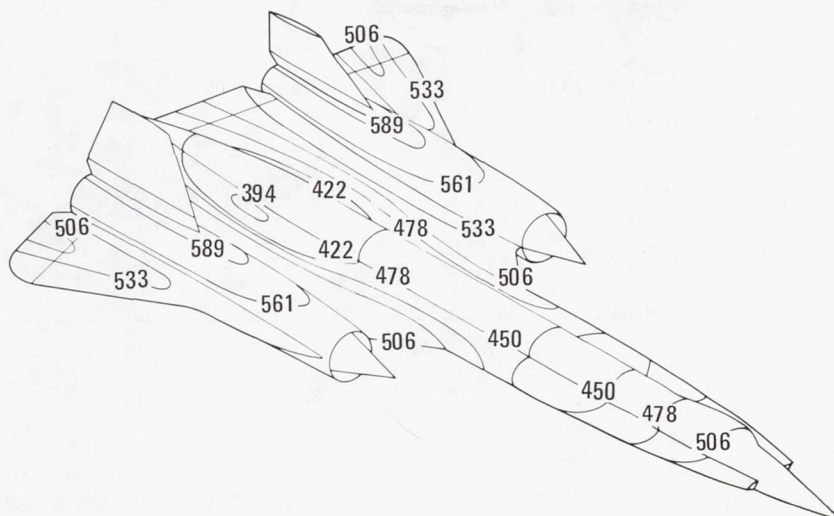


Figure 3.—Surface temperatures at high-Mach-number cruise condition.

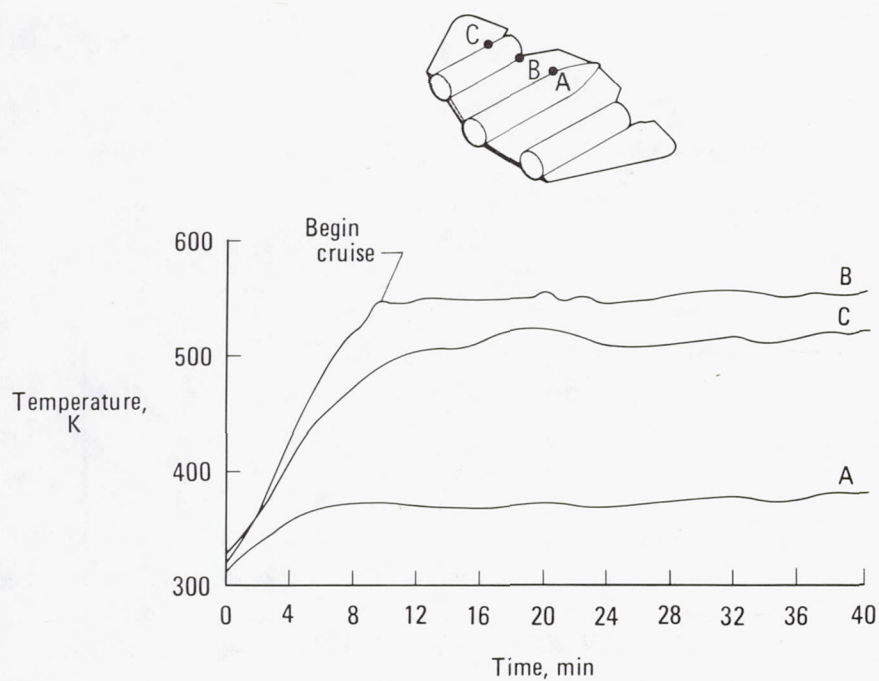


Figure 4.—Time history of typical wing skin surface temperatures.

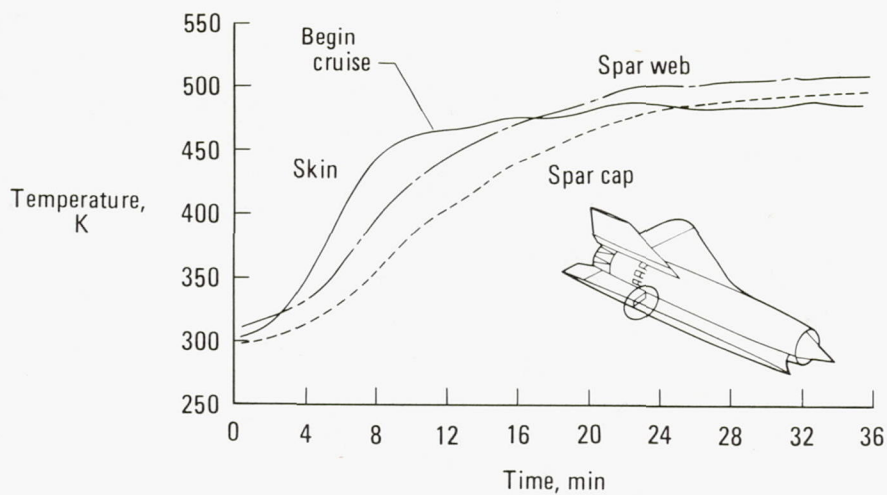


Figure 5.—Time history of typical wing spar temperature distribution.

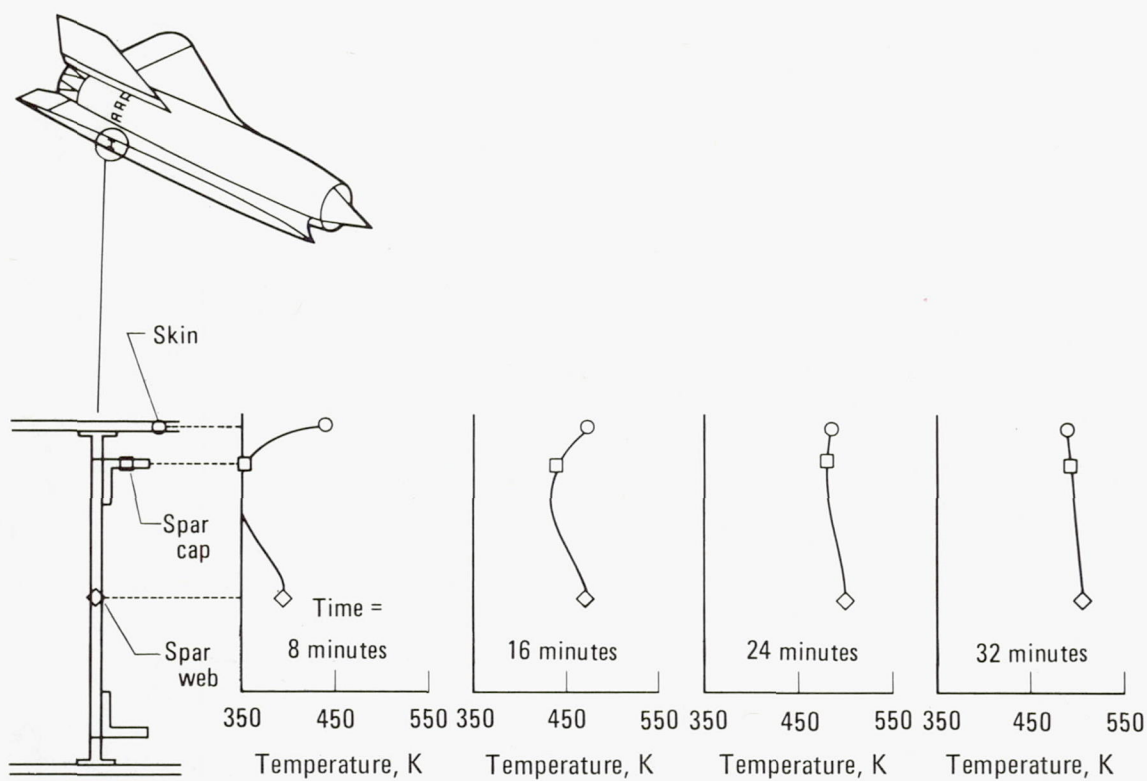


Figure 6.—Distribution of typical temperatures in wing spar.

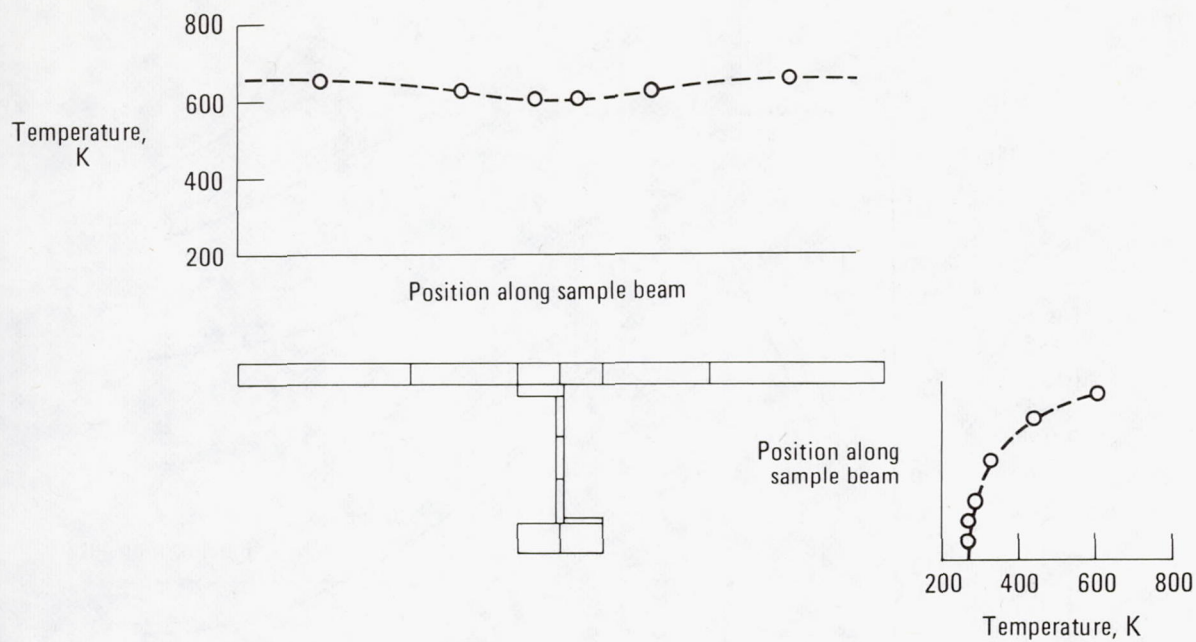


Figure 7.—Temperature distribution for analysis of sample beam.

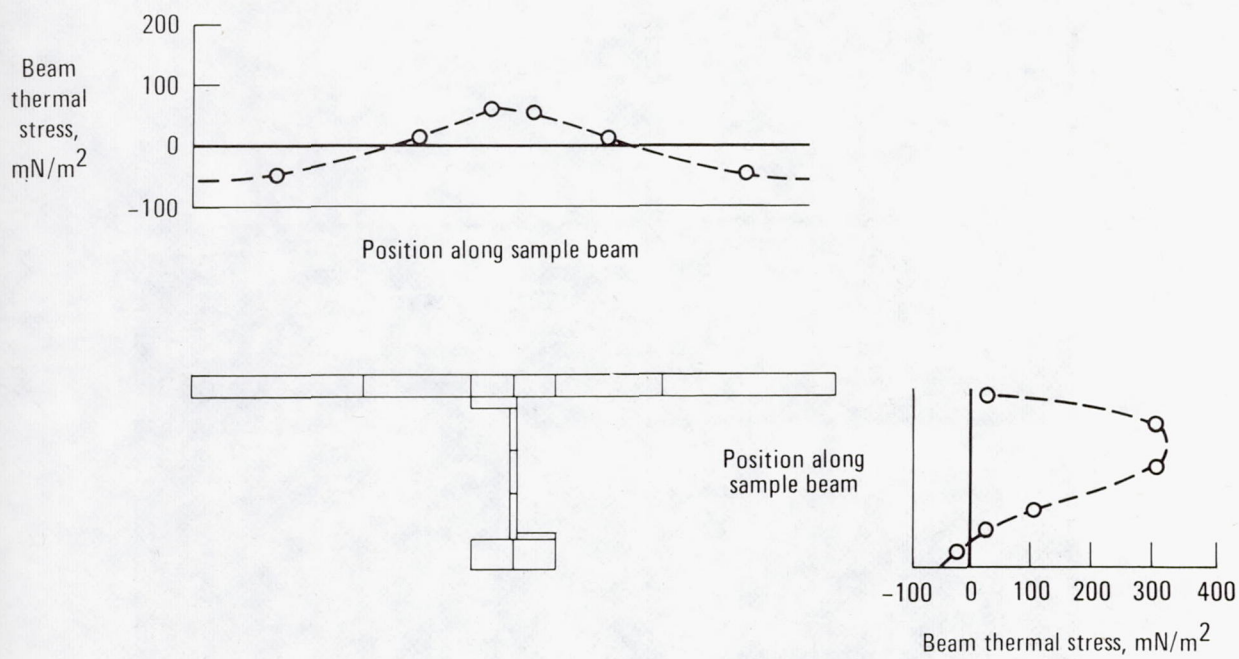


Figure 8.—Thermal stress distribution for analysis of sample beam.

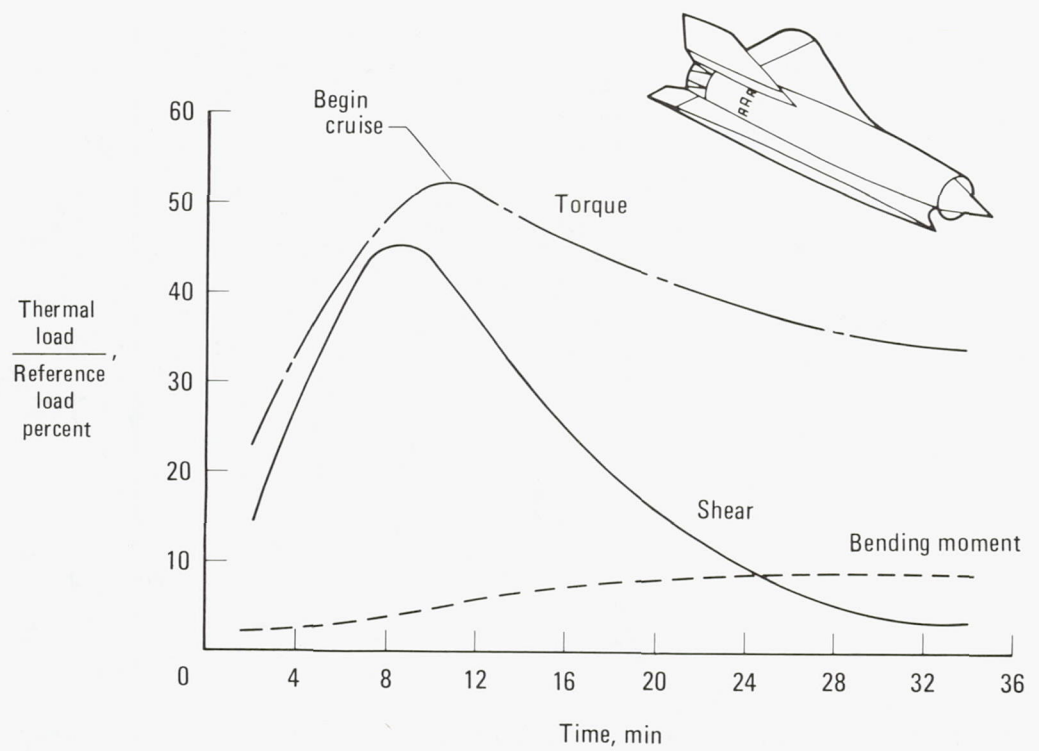


Figure 9.—Thermal effects on strain gage load equations.

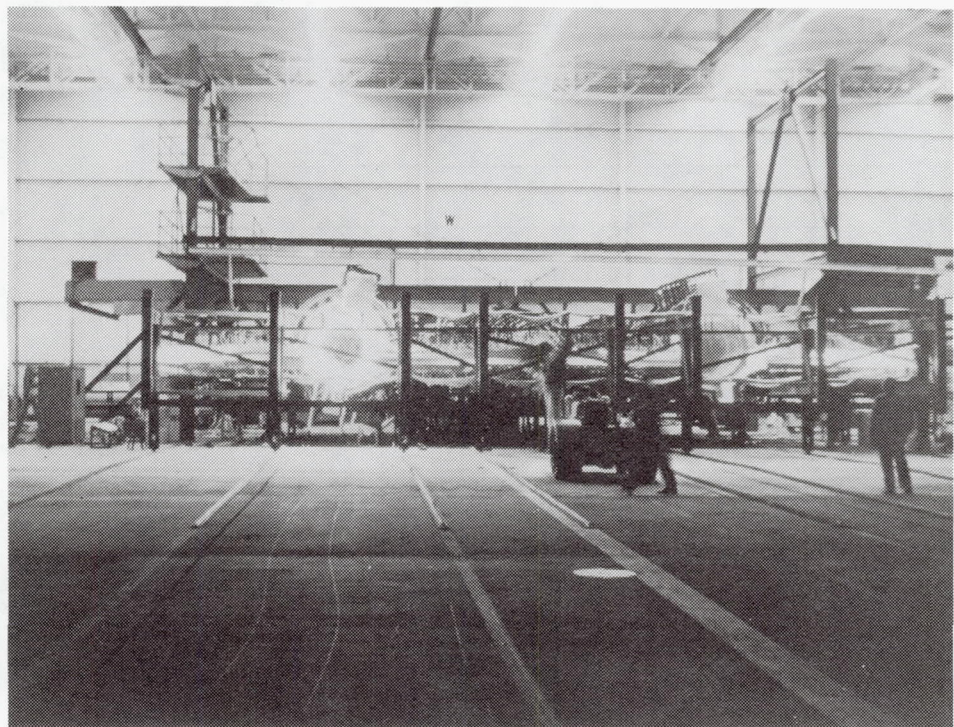


Figure 10.—Radiant heating of the airplane during the thermal calibration.

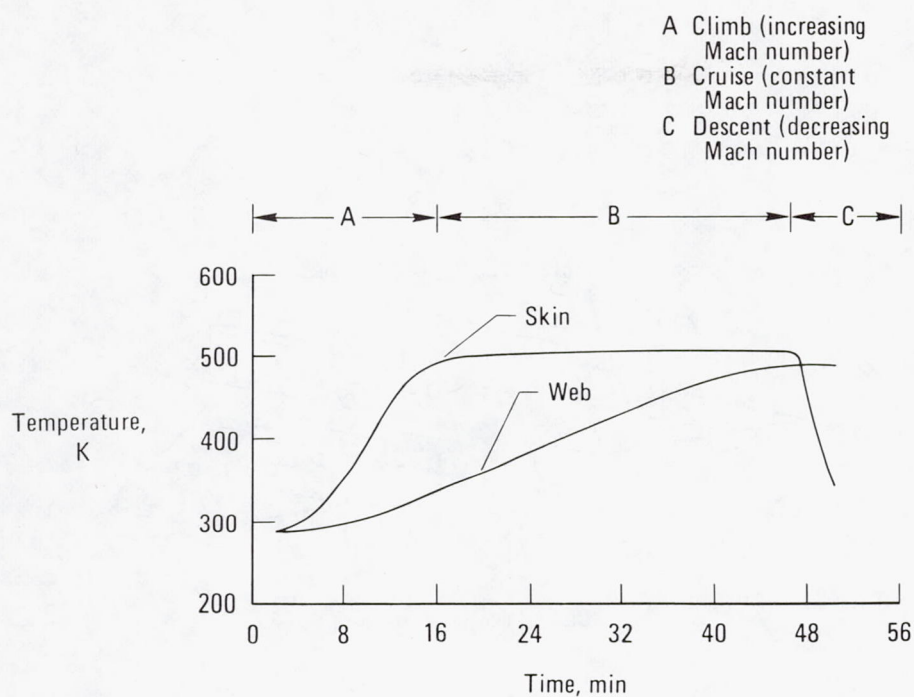


Figure 11.—Thermal profile of a supersonic flight.

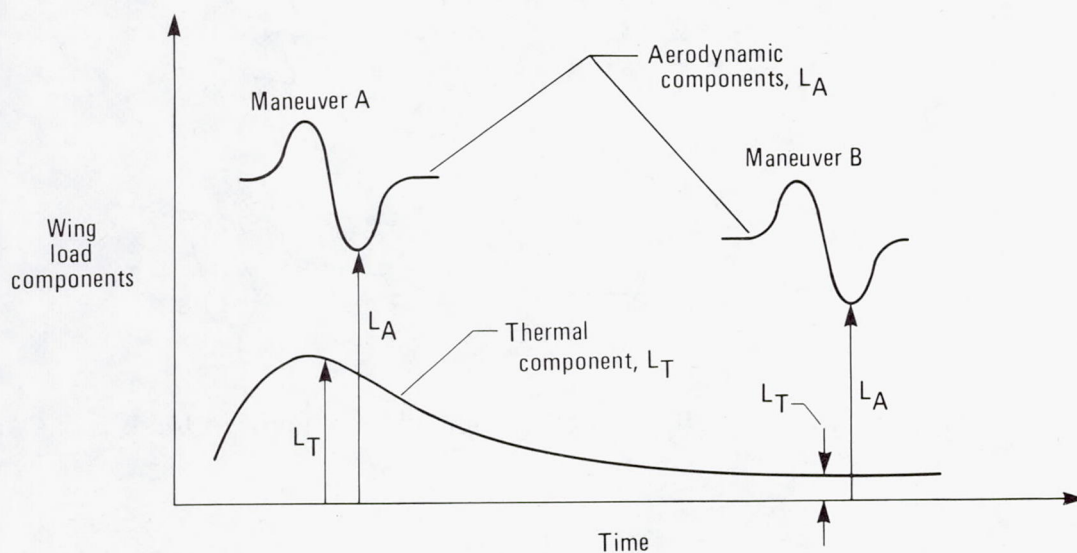
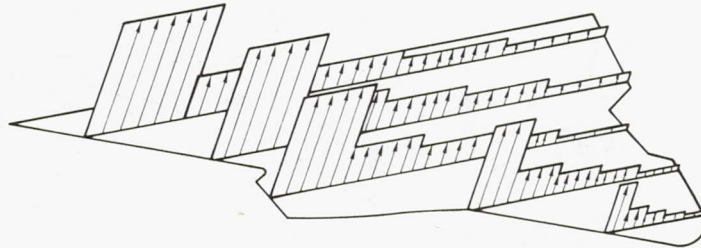
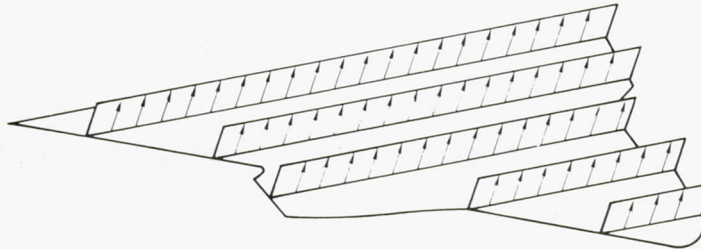


Figure 12.—Aerodynamic and thermal components of load relative to flight profile.

Forward center of pressure



Central center of pressure



Aft center of pressure

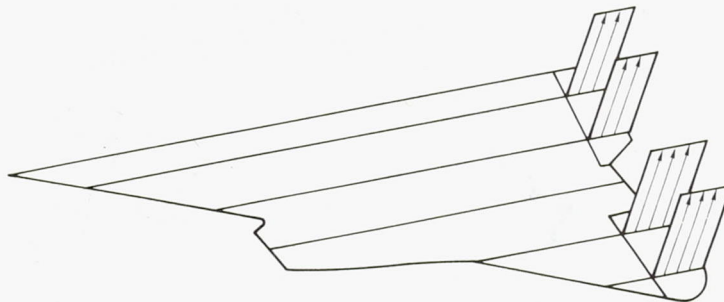


Figure 13.—Distribution of mathematically applied loads .

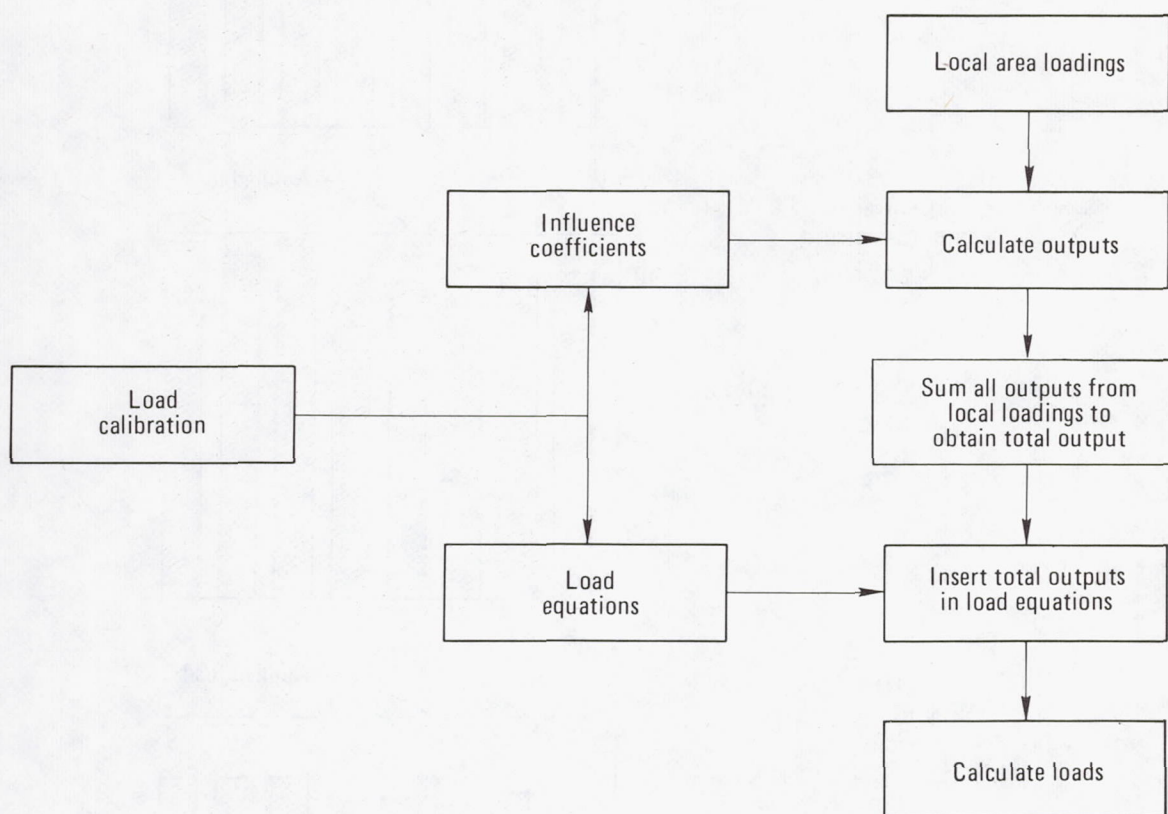


Figure 14.—Schematic showing computation of mathematically applied loads.

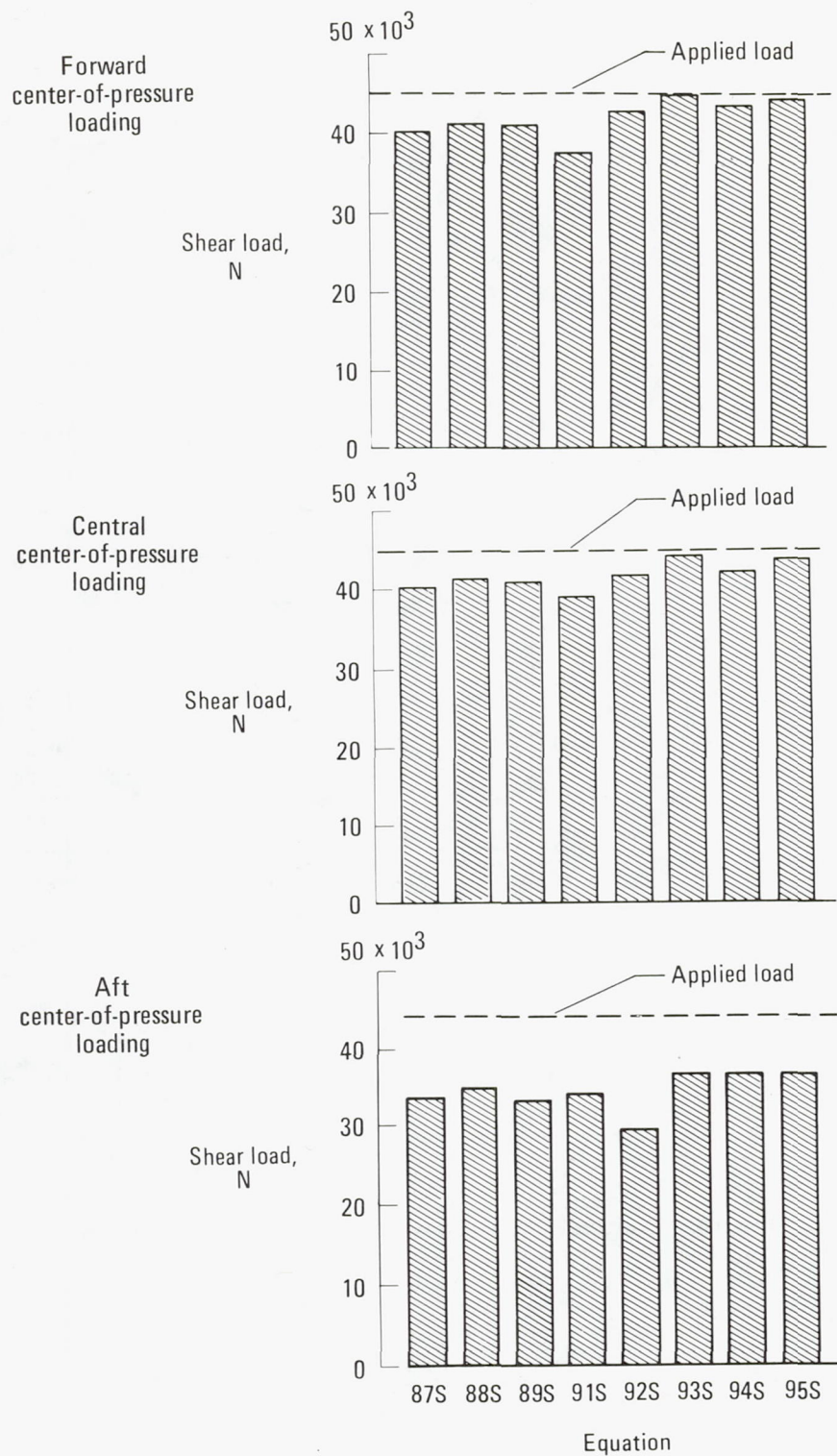


Figure 15.—Comparison of calculated and mathematically applied shear loads.

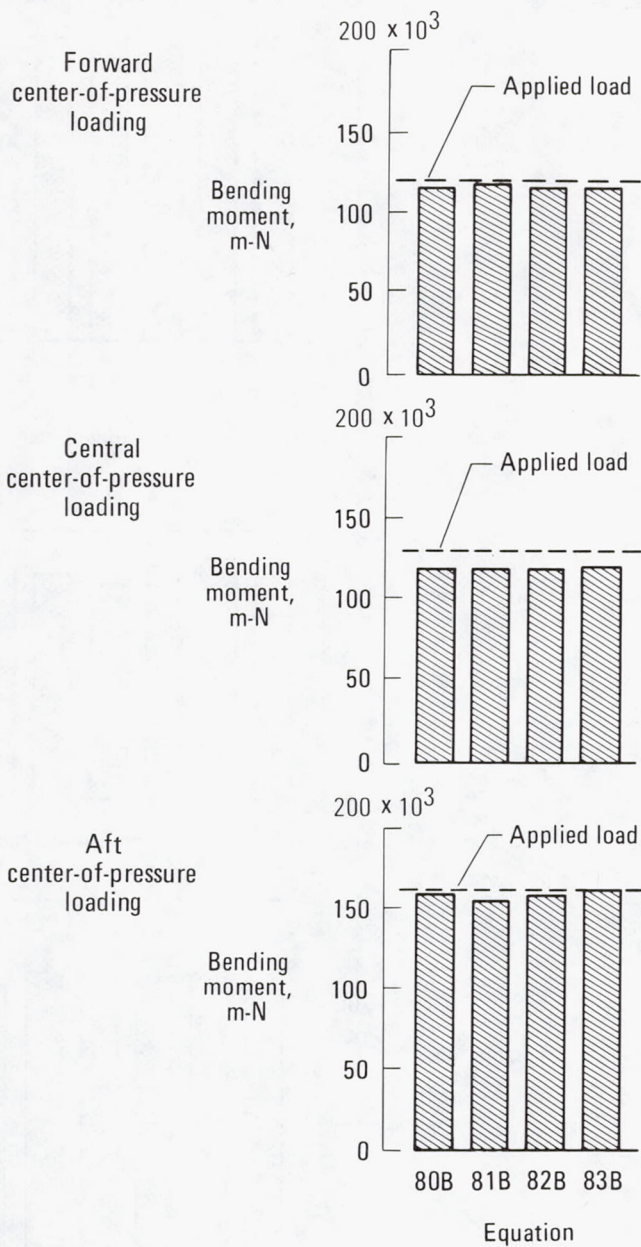
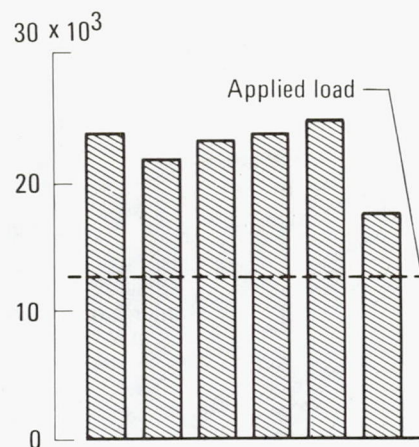


Figure 16.—Comparison of calculated and mathematically applied bending moments.

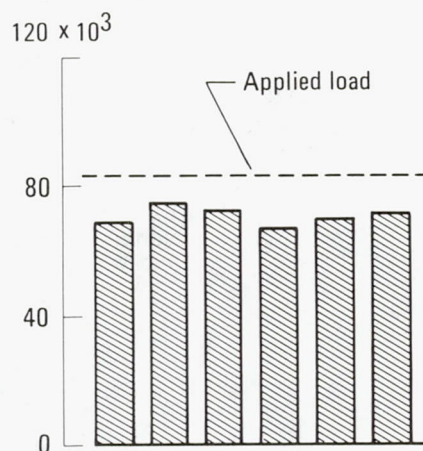
Forward
center-of-pressure
loading

Torsion load,
m-N



Central
center-of-pressure
loading

Torsion load,
m-N



Aft
center-of-pressure
loading

Torsion load,
m-N

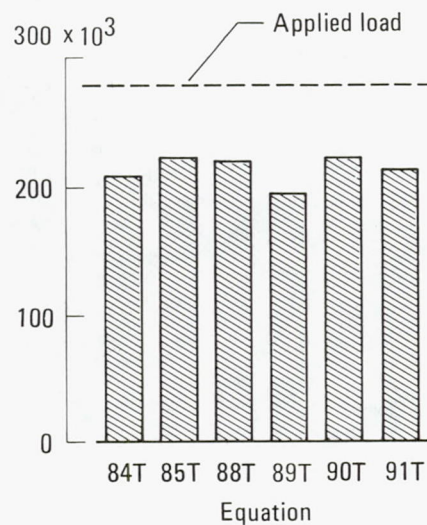


Figure 17.—Comparison of calculated and mathematically applied torsion loads.

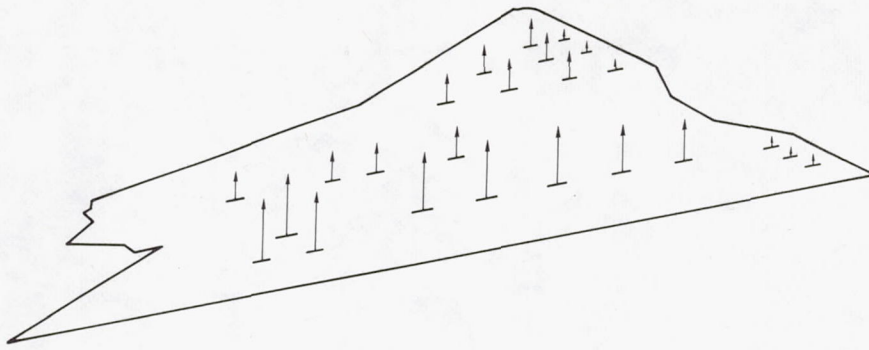


Figure 18.—Location and relative magnitude of loads applied during load calibration.

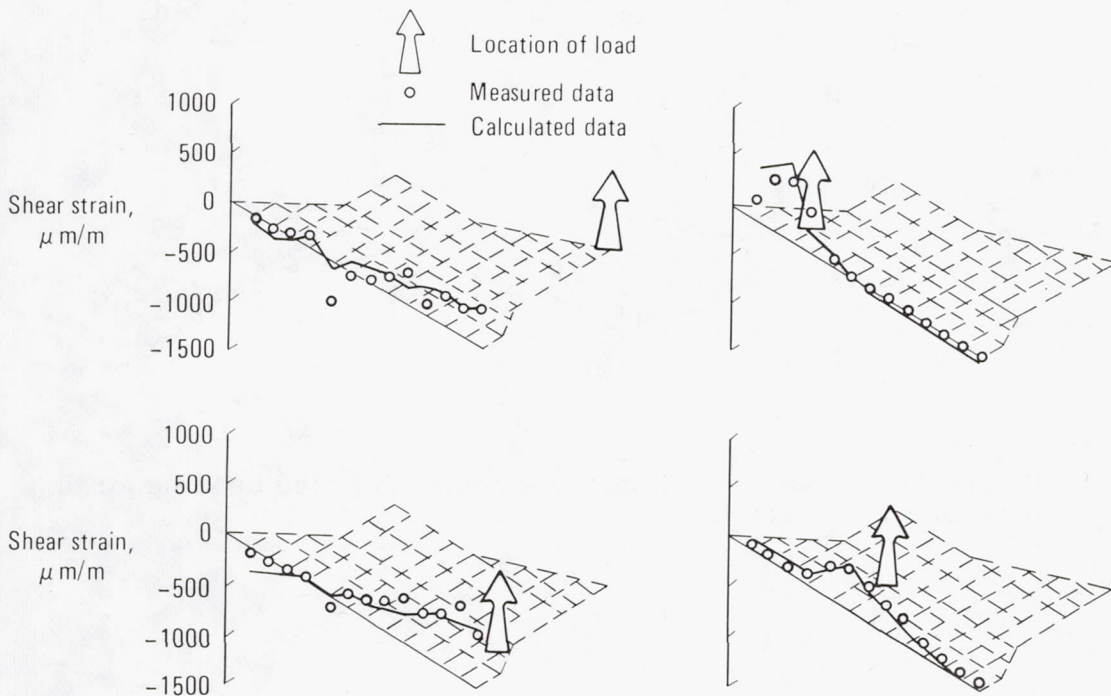


Figure 19.—Comparison of measured and calculated shear strains for several discrete loads.

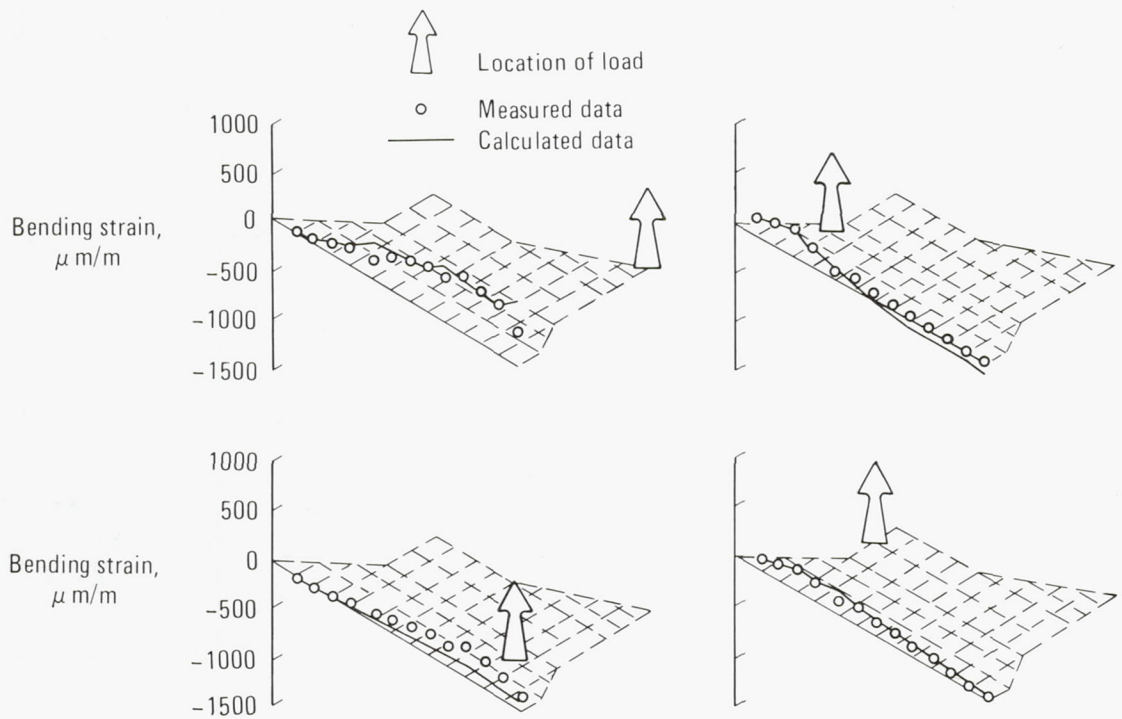


Figure 20.—Comparison of measured and calculated bending strains for several discrete loads.

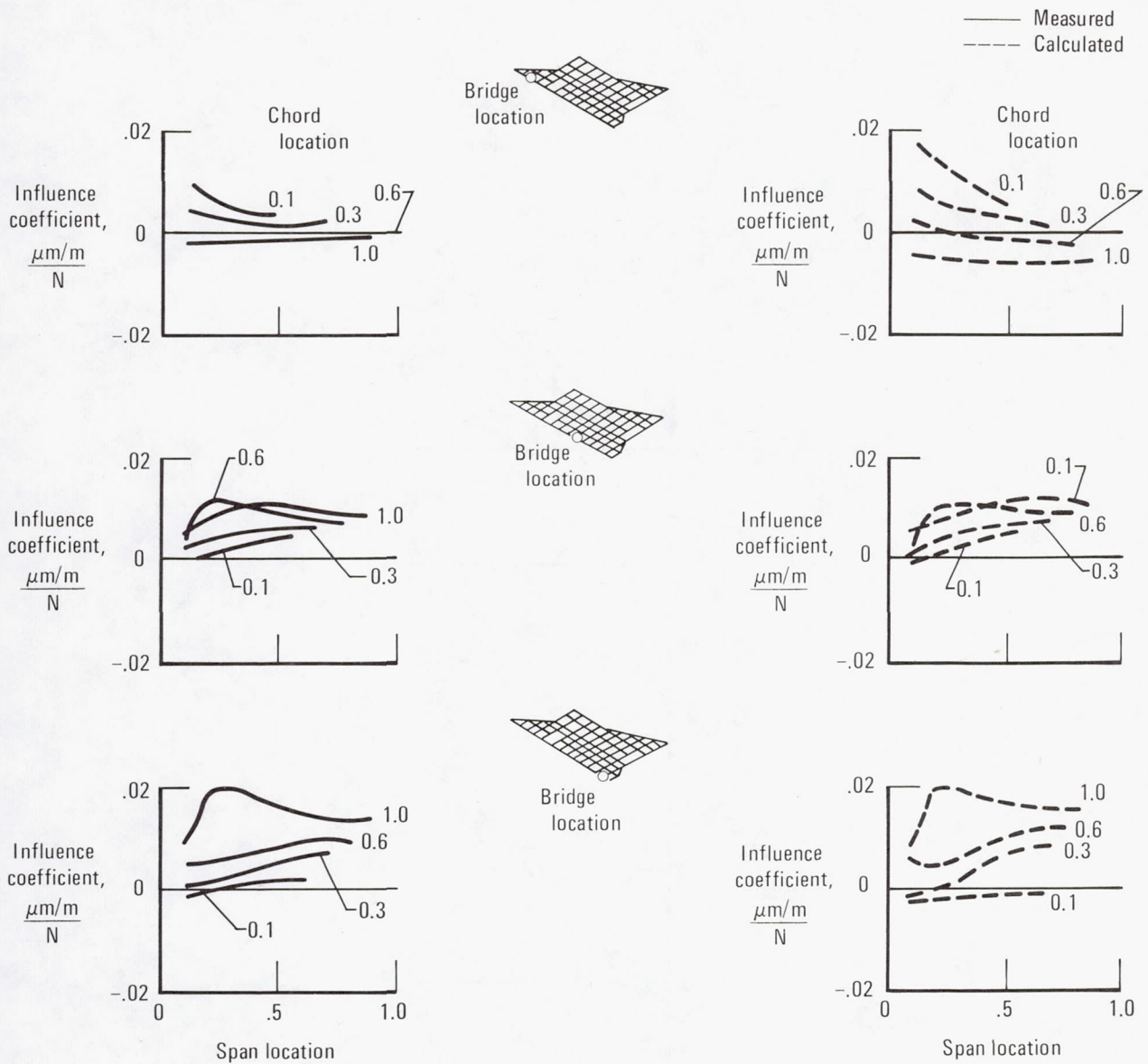


Figure 21.—Comparison of measured and calculated influence coefficient plots for shear strain.

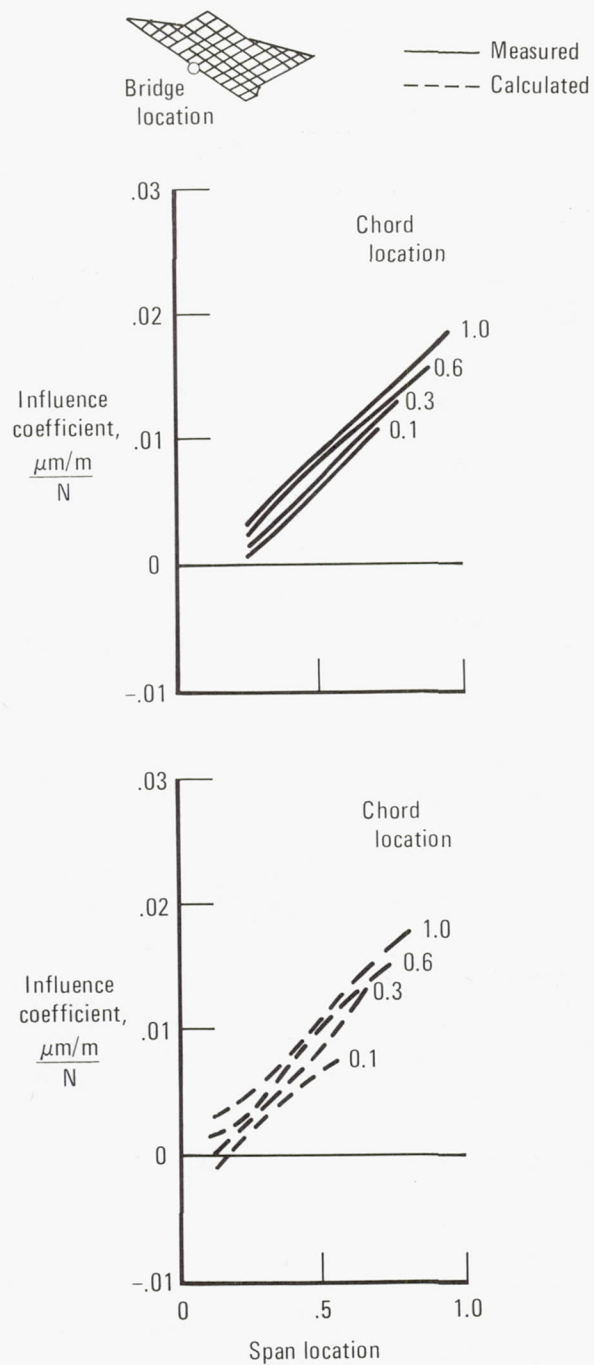


Figure 22.—Comparison of measured and calculated influence coefficient plots for bending strain.

FLIGHT-MEASURED AERODYNAMIC LOADS ON A 0.92 ASPECT RATIO LIFTING SURFACE

Robert R. Meyer, Jr. and V. Michael DeAngelis
Dryden Flight Research Center

SUMMARY

Ventral fin loads, expressed as normal force coefficients, bending moment coefficients, and torque coefficients, were measured during flight tests of a YF-12A airplane. Because of the proximity of the ventral fin to the ailerons, the aerodynamic loads presented were the result of both sideslip loads and aileron crossflow loads. Aerodynamic data obtained from strain gage loads instrumentation and some flight pressure measurements are presented for several Mach numbers ranging from 0.70 to 2.00. Selected wind tunnel data and results of linear theoretical aerodynamic calculations are presented for comparison.

INTRODUCTION

Because of their lower aerodynamic drag, low-aspect-ratio lifting surfaces are becoming more prevalent in high-speed aircraft designs. Typical examples are the low-aspect-ratio stabilizing surfaces used on both the XB-70 and YF-12 airplanes. Literature searches revealed very little experimental data to support recent advances in theoretical methods for predicting aerodynamic loads on very low-aspect-ratio lifting surfaces. References 1 to 3 present flight-measured aerodynamic loads data on the low-aspect-ratio lifting surfaces of trapezoidal planforms shown in figure 1. Of these three lifting surfaces, the XB-70 canard has the lowest aspect ratio at 1.65. For comparison, the YF-12 ventral fin with a 0.92 aspect ratio is also shown.

The change in lift curve slope and chordwise center-of-pressure location with Mach number is shown in figure 2 for the four planforms presented in figure 1. The three planforms with aspect ratios greater than 1.5 have similar characteristics in terms of the magnitude of the lift curve slope, the chordwise center-of-pressure location, and the variation of these two parameters with Mach number. However, for Mach numbers in the transonic region, the YF-12 ventral fin with an aspect ratio less than 1 shows distinct differences in the magnitude of the lift curve slope and

in the location of the chordwise center of pressure. Because the YF-12 ventral fin data differed significantly from data on the planforms with aspect ratios greater than 1.5, the centerline ventral fin of the YF-12A airplane was studied to add to the available data on low-aspect-ratio lifting surfaces at transonic speeds where the aerodynamic loads tend to be most severe.

The YF-12 ventral fin structure was found to be very rigid during ground tests and was considered to remain rigid throughout the flight envelope investigated. This rigidity made the flight data obtained from the ventral fin ideal for comparison with wind tunnel data and with theoretical aerodynamic calculations for rigid structures.

Aerodynamic data obtained from strain gage loads instrumentation and some flight pressure measurements are presented for several Mach numbers ranging from 0.70 to 2.00. Selected wind tunnel data and results from theoretical aerodynamic calculations are presented for comparison. Because of the proximity of the ventral fin to the ailerons, the measured aerodynamic loads resulted from a combination of sideslip loads and aileron crossflow loads.

SYMBOLS

Physical quantities in this report are given in the International System of Units (SI). The measurements were taken and calculations were made in U.S. Customary Units. Factors relating the two systems are presented in reference 4.

The results of this investigation were derived from data obtained using the reference ventral-fin-panel planform defined in figure 3. The bending moment reference axis is the strain gage instrumentation axis. This axis is located at the 62.62-centimeter ventral fin station and is oriented normal to the 69.5-percent chord line. For clarification, the reference dimensions and areas used to nondimensionalize the flight data are included in the symbols list.

B	reference ventral fin bending moment, m-N
$b/2$	reference ventral fin semispan measured from the strain gage instrumentation station, 135.5 cm
C_B	aerodynamic bending moment coefficient of the reference ventral fin, $\frac{B}{qSb/2}$
$C_{B_\beta} =$	$\frac{\partial C_B}{\partial \beta}$, per deg
$C_{B_{\delta_a}} =$	$\frac{\partial C_B}{\partial \delta_a}$, per deg
$C_L =$	lift coefficient, $\frac{L}{qS}$

C_{L_α}	$= \frac{\partial C_L}{\partial \alpha}$, per deg
C_N	aerodynamic normal force coefficient of the reference ventral fin, $\frac{N}{qS}$
C_{N_β}	$= \frac{\partial C_N}{\partial \beta}$, per deg
$C_{N_{\delta_a}}$	$= \frac{\partial C_N}{\partial \delta_a}$, per deg
ΔC_p	differential pressure coefficient, $\frac{p_1 - p_r}{q}$
C_T	aerodynamic torque coefficient of the reference ventral fin, $\frac{T}{qS\bar{c}}$
C_{T_β}	$= \frac{\partial C_T}{\partial \beta}$, per deg
$C_{T_{\delta_a}}$	$= \frac{\partial C_T}{\partial \delta_a}$, per deg
c	reference ventral fin local chord, cm
\bar{c}	reference ventral fin mean aerodynamic chord measured normal to 69.5-percent chord at ventral station 125.48 cm, 299.59 cm
M	Mach number
MAC	mean aerodynamic chord
N	reference ventral fin aerodynamic normal force, N
p_l	local static pressure on left surface of ventral fin, N/m^2
p_r	local static pressure on right surface of ventral fin, N/m^2
q	free stream dynamic pressure, N/m^2
S	reference ventral fin area, $4.00 m^2$
T	reference ventral fin torque, m-N
x	chordwise distance rearward of leading edge of local chord, cm

$\left(\frac{x}{c}\right)_{cp}$	reference ventral fin chordwise center of pressure location, $\frac{C_{T\beta}}{C_{N\beta}}$
$\left(\frac{2y}{b}\right)_{cp}$	reference ventral fin spanwise center of pressure location, $\frac{C_{B\beta}}{C_{N\beta}}$
α	airplane angle of attack, deg
β	airplane angle of sideslip, deg
δ_a	differential aileron deflection, left aileron position minus right aileron position, deg

FLIGHT TEST VENTRAL FIN DESCRIPTION

The ventral fin, located on the aft fuselage of the YF-12A aircraft (fig. 4), is hinged along the root axis at the front spar (40-percent chord) and at the aft spar (75-percent chord) and is folded parallel to the wing for takeoff and landing clearance. The fin, which incorporates a hexagonal airfoil shape with a thickness-to-chord ratio of 0.03, was designed to increase lateral-directional stability at high speeds. The 4.0-m² area is based on the defined ventral-fin-panel planform, with an aspect ratio of 0.92 (fig. 3). As shown in figure 4, the ventral fin is located near the inboard ailerons where it is subject to loads induced by the differential deflection of the ailerons.

The substructure of the ventral fin is constructed of titanium. The leading and trailing edges and the skin panels are constructed from a beryllium-aluminum alloy. The stiffness of the fin, determined from static loadings, precluded measuring any aeroelastic effects throughout the flight envelope investigated.

FLIGHT INSTRUMENTATION AND ACCURACIES

The ventral fin was instrumented with strain gages located at its root and with four chordwise rows of static pressure orifices. To measure shear or normal force, bending moment, and torque on the ventral fin, the strain gages were calibrated using the method described in reference 5. Most of the static pressure orifices were holes drilled through the center of skin fasteners, with the exception of the leading edge orifices which were holes drilled in the leading edge. Two types of pressure sensing instrumentation were used. The first type, intended to obtain data only during steady-state flight maneuvers, was scanning valves plumbed to chordwise pressure orifice rows at the 93.98-centimeter, 119.18-centimeter, and 173.48-centimeter ventral stations. The second type, intended to obtain data during both steady state and dynamic flight maneuvers, was individual pressure transducers plumbed to a chordwise pressure orifice row at the 144.53-centimeter ventral station. The location of the pressure orifices and strain gage instrumentation is shown in figure

The measurement of aircraft parameters such as Mach number, angle of attack, and angle of sideslip have been documented in other reports, such as reference 6. The estimated accuracies of all measured quantities used in this report are presented in table 1.

WIND TUNNEL TESTS

Transonic pressure measurements were obtained from tests of the 1/12-scale sting-mounted model of the YF-12A airplane in the NASA Ames 11-Foot Wind Tunnel. The wind tunnel model ventral fin was instrumented with four chordwise rows of static pressure orifices which corresponded closely to the relative locations of the pressure orifices on the ventral fin of the flight vehicle. Most of the pressure data were obtained at a Reynolds number of 7.62×10^6 per meter, and a few selected points were run at a Reynolds number of 20.32×10^6 per meter. Since no apparent differences were noted in the data, the wind tunnel data obtained at the lower Reynolds number were used. These data were integrated to obtain the ventral fin aerodynamic loads.

THEORETICAL ANALYSIS

The theoretical data were obtained from the FLEXSTAB computer program (ref. 7). FLEXSTAB is a system of digital computer programs based on linear theories for evaluating the static and dynamic stability, trim state, structural loading, and elastic deformations of arbitrary aircraft configurations in subsonic and supersonic flight. The linear aerodynamic analytical method used in FLEXSTAB is essentially that developed by Woodward (refs. 8 and 9) for representing supersonic flow about wing-body combinations. The method has been extended to include subsonic flow with arbitrary wing-body, nacelle, and tail arrangements.

When using the FLEXSTAB program to calculate the ventral fin loads, no attempt was made to incorporate boundary layer effects. Since ground static loadings showed the ventral fin to be very rigid, all theoretical aerodynamic data presented for comparison with flight-measured data and wind tunnel data are for a rigid fin configuration.

RESULTS AND DISCUSSION

The flight loads were obtained from two types of maneuvers: (1) a dynamic aileron pulse maneuver which imposed essentially pure aileron crossflow loads on the fin, and (2) a steady-sideslip maneuver which imposed a combination of sideslip and aileron crossflow loads on the fin. Pressure load distributions of wind tunnel aileron crossflow loads and flight-derived steady-sideslip loads for a Mach number of 0.90 are presented in figures 6 and 7, respectively.

Figure 6 presents a representative wind tunnel pressure load distribution due to aileron deflection along the four chordwise rows of pressure orifices. It appears

that the effect of aileron deflection on bending moment is negligible because the load is concentrated at the root of the fin. However, the torque load is notable due to the long moment arm about the quarter chord point of the MAC. In this case the load is concentrated toward the trailing edge of the ventral fin from about 70 percent to 100 percent of the MAC depending on Mach number.

Figure 7 shows a flight ventral fin pressure distribution during a steady-state sideslip maneuver. It suggests that the increase in angle of sideslip loads the leading edge of the fin while the aileron deflection loads the aft portion of the fin in the opposite direction. While this combination tends to cancel normal and bending moment loads, it tends to increase torque loads about the quarter chord point of the MAC. This could cause an excessive torque load during certain flight conditions. Figure 7 shows the differential surface pressures, ΔC_p . For the flight condition presented, the ΔC_p distribution in the vicinity of the leading edge is representative of the distribution of the pressures on the surface with the low pressure field. Therefore, the high leading edge pressures of rows 2, 3, and 4, followed by the large pressure gradient, suggest that a leading edge vortex is present.

Figure 8 presents flight-measured aerodynamic normal force coefficient data, bending moment coefficient data, and torque coefficient data plotted against angle of sideslip. These data are compared with wind tunnel measurements and theoretical calculations for a Mach number of 0.90. The flight data were obtained from the strain gage loads instrumentation during steady sideslip maneuvers and were corrected for the presence of the aileron crossflow loads by subtracting the aileron crossflow component loads ($C_{N_{\delta_a}}$, $C_{B_{\delta_a}}$, and $C_{T_{\delta_a}}$) which were determined

from the aileron pulse maneuvers. A least-squares straight line was fitted to the wind tunnel data for the data points above -2° angle of sideslip. It was felt that below -2° angle of sideslip, the leading edge vortex would affect the linearity of the curve. From the C_N and C_B data for -5° and -6° angle of sideslip, the presence of a leading edge vortex condition appears to have influenced the integrated pressure data. By indicating a decrease in torque at the lower sideslip angles, the C_T data do not appear to substantiate the vortex effects shown by the C_N and C_B data. However, because of the leading edge sweep and the idealized geometric planform shape, and because the effect of the vortex seems to be most pronounced at the outboard rows of pressure orifices, the effect of the vortex should be more pronounced on the integrated coefficients of C_N and C_B than on C_T . Also, since the large pressure gradients at the leading edge are defined by only a few pressure orifices, the effect of the leading edge vortex on the C_T data is probably lost in the resolution of the data and in the mechanics of the integration. The theoretical calculations are based on linear theory and do not account for the presence of a leading edge vortex.

Slopes were obtained from the data presented in figure 8 and from similar data obtained at other Mach numbers. These computations presented in figure 9 show the normal force coefficient slopes as well as the spanwise and chordwise center-of-pressure locations. The flight-derived C_{N_β} data show that the maximum value of

C_{N_β} occurs at low supersonic speeds around Mach 1.2 to Mach 1.4. The wind tunnel C_{N_β} data agree with the flight data at Mach 0.70 and Mach 0.90, but underpredict the normal force curve slope at Mach 0.95. The disagreement at Mach 0.95 may be due to the problem of defining the large leading edge pressure gradient with only a few pressure orifices. The theoretical calculations show similar trends in the variation of C_{N_β} with Mach number, but slightly underpredict C_{N_β} at transonic speeds.

At transonic conditions the strain gage flight-measured spanwise center-of-pressure locations vary from 52 percent to 58 percent of the semispan. The wind tunnel data and theoretical calculations place the spanwise center-of-pressure location between 42 percent and 48 percent of the semispan. At supersonic conditions, the flight-measured spanwise center of pressure shifts substantially inboard.

An analysis of the strain gage calibration data indicates that a larger than actual bending moment is obtained from the bending moment equation when the load is applied to the leading edge of the ventral fin, and a smaller than actual bending moment is obtained from the bending moment equation when the load is applied to the center and aft portions of the fin. Hence, the flight data show a more outboard position for the spanwise center-of-pressure location than do the wind tunnel or theoretical data, particularly for the transonic Mach numbers where the leading edge is most highly loaded.

Transonically, the flight data show that the chordwise center of pressure moves from 22 percent of the MAC at Mach 0.70 to 10 percent of the MAC at Mach 0.95. The wind tunnel data show a similar trend with Mach number, but indicate that the center of pressure is located slightly farther aft.

The theory shows a forward located center of pressure at about 14 percent of the MAC but predicts little movement in the center of pressure with changes in Mach number. The forward moving location of the chordwise center of pressure contrasts with the center-of-pressure movement for higher-aspect-ratio planforms. This could have a significant impact on the structural design of very low-aspect-ratio lifting surfaces. Supersonically, the chordwise center-of-pressure location moves aft and approaches 50 percent of the MAC at Mach 2.

Figure 10 shows the aileron crossflow loads which were obtained from aileron pulse maneuvers. At Mach numbers of 0.98 and above, aileron deflections do not affect the ventral fin loads; however, for transonic Mach numbers less than 0.98, aileron deflections do affect the ventral fin loads, most notably the torque loads, $C_{T_{\delta_a}}$. Transonically, $C_{N_{\delta_a}}$ and $C_{B_{\delta_a}}$ are fairly constant with change in Mach number, but $C_{T_{\delta_a}}$ varies in level from -0.0016 at Mach 0.7 to -0.0027 at Mach 0.95.

Although the effects of $C_{N_{\delta_a}}$ and $C_{B_{\delta_a}}$ are small or even negligible when compared with the loads imposed on the ventral fin from sideslip (figs. 8 and 9), torque loads due to aileron deflection, $C_{T_{\delta_a}}$, are significant when compared with torque loads

due to sideslip, $C_{T\beta}$. The wind tunnel data show good agreement with the flight data, and the theoretical calculations at Mach 0.90 show good agreement with the flight data for $C_{T\delta_a}$ but overestimate $C_{N\delta_a}$ and $C_{B\delta_a}$. The discrepancies may be attributed to the idealization of the airplane's configuration for computer modeling in the linear aerodynamic theory.

CONCLUDING REMARKS

The aerodynamic loads of a 0.92-aspect-ratio ventral fin were measured during a flight test program of the YF-12A airplane. These data, which cover the Mach number range from 0.70 to 2.00, are presented in coefficient form and are compared with data obtained from wind tunnel tests and with the results obtained from application of a linear aerodynamic theory.

The loads induced on the ventral fin were found to result from (1) the load due to change in the angle of sideslip and (2) the load due to aileron deflection because of the proximity of the fin to the ailerons.

The flight data show that the slope of the normal force curve peaks at a Mach number of about 1.2 to 1.4 instead of about Mach 1.0, as is the case with slightly higher aspect-ratio planforms. Also, as the Mach number increases transonically, the chordwise center-of-pressure location moves forward from 22 percent of the MAC at Mach 0.7 to 10 percent of the MAC at Mach 0.95 before moving aft as Mach number increases supersonically.

Wind tunnel and flight pressure data suggest the presence of a leading edge vortex which adds an increment of load to the ventral fin and which results in a nonlinear normal force curve.

The wind tunnel data and theoretical calculations were in fair agreement with the flight data although the data from the theoretical calculations were not as sensitive to change in Mach number as were the flight-measured data and the wind tunnel data.

The deflection of the ailerons affected the ventral fin loads up to a Mach number of 0.98. Although aileron deflections had little effect on the normal force and bending moment coefficients, they had a pronounced effect on the torque coefficient since the aileron crossflow load was concentrated on the aft portion of the fin. At airspeeds greater than Mach 0.98 there were no aileron-induced loads on the ventral fin.

The forward center-of-pressure location of the additional airload could influence the structural design of very low-aspect-ratio lifting surfaces, and the combination of the additional airload and the aileron crossflow loads could result in large torque loads on this type of fin.

REFERENCES

1. Keener, Earl R.; and Jordan, Gareth H.: Wing Loads and Load Distributions Throughout the Lift Range of the Douglas X-3 Research Airplane at Transonic Speeds. NACA RM H56G13, 1956.
2. Pyle, Jon S.: Flight-Measured Wing Surface Pressures and Loads for the X-15 Airplane at Mach Numbers From 1.2 to 6.0. NASA TN D-2602, 1965.
3. Jenkins, Jerald M.; DeAngelis, V. Michael; Friend, Edward L.; and Monaghan, Richard C.: Flight Measurements of Canard Loads, Canard Buffeting, and Elevon and Wing-Tip Hinge Moments on the XB-70 Aircraft Including Comparisons With Predictions. NASA TN D-5359, 1969.
4. Mechtly, E. A.: The International System of Units - Physical Constants and Conversion Factors. Second Revision. NASA SP-7012, 1973.
5. Skopinski, T. H.; Aiken, William S., Jr.; and Huston, Wilber B.: Calibration of Strain-Gage Installations in Aircraft Structures for the Measurement of Flight Loads. NACA Rept. 1178, 1954.
6. Larson, Terry J.: Compensated and Uncompensated Nose Boom Static Pressures Measured From Two Air Data Systems on a Supersonic Airplane. NASA TM X-3132, 1974.
7. Dusto, A. R.; Brune, G. W.; Dornfeld, G. M.; Mercer, J. E.; Pilet, S. C.; Rubbert, P. E.; Schwanz, R. C.; Smutny, P.; Tinoco, E. N.; and Weber, J. A.: A Method for Predicting the Stability Characteristics of an Elastic Airplane. Volume 1-FLEXSTAB Theoretical Description. NASA CR-114712, 1974.
8. Woodward, F. A.; Tinoco, E. N.; and Larsen, J. W.: Analysis and Design of Supersonic Wing-Body Combinations, Including Flow Properties in Near Field. Part I: Theory and Application. NASA CR-73106, 1967.
9. LaRowe, E.; and Love, J. E.: Analysis and Design of Supersonic Wing-Body Combinations, Including Flow Properties in Near Field. Part II: Digital Computer Program Description. NASA CR-73107, 1967.

TABLE 1.—YF-12A FLIGHT INSTRUMENTATION ACCURACY

Parameter	Estimated accuracy
Mach number—	
Supersonic	± 0.012
Subsonic	± 0.004
Airspeed, m/sec—	
Supersonic	± 0.3
Subsonic	± 0.5
Altitude, m—	
Subsonic, supersonic	± 46
Transonic	± 67
Dynamic pressure, N/m ²	
Supersonic	± 72
Subsonic	± 287
Angle of attack, deg—	
Subsonic, supersonic	± 0.25
Transonic	± 0.50
Angle of sideslip, deg.	± 0.25
Elevon position, deg	± 0.1
Fuel quantities, N	± 1334
Accelerations, g—	
Vertical	± 0.04
Lateral	± 0.01
Longitudinal	± 0.06
Attitudes, deg—	
Pitch	± 0.4
Roll	± 1.2
Yaw	± 0.4
Rates, deg/sec—	
Pitch	± 0.1
Roll	± 0.1
Yaw	± 0.1
Pressure coefficient	± 0.01
Normal force coefficient, percent	5
Bending moment coefficient, percent	15
Torque coefficient, percent	8

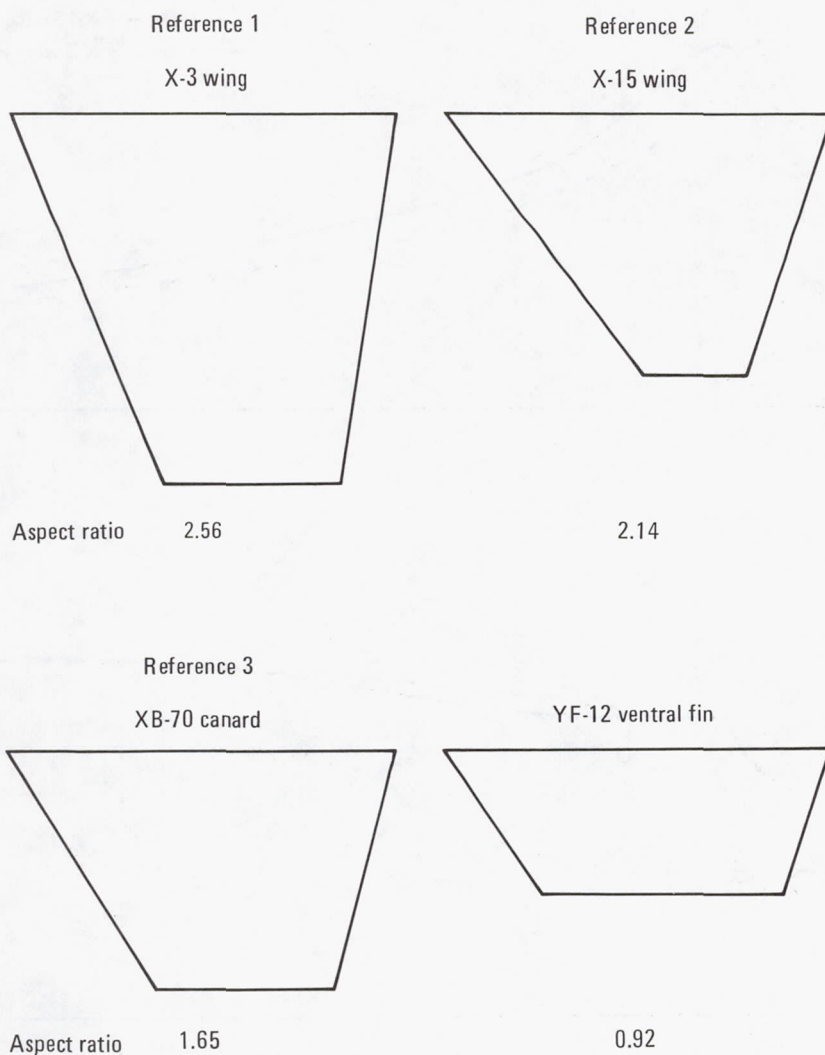


Figure 1.—Some low-aspect-ratio lifting surfaces for which experimental aerodynamic loads data are available. Planforms not drawn to scale.

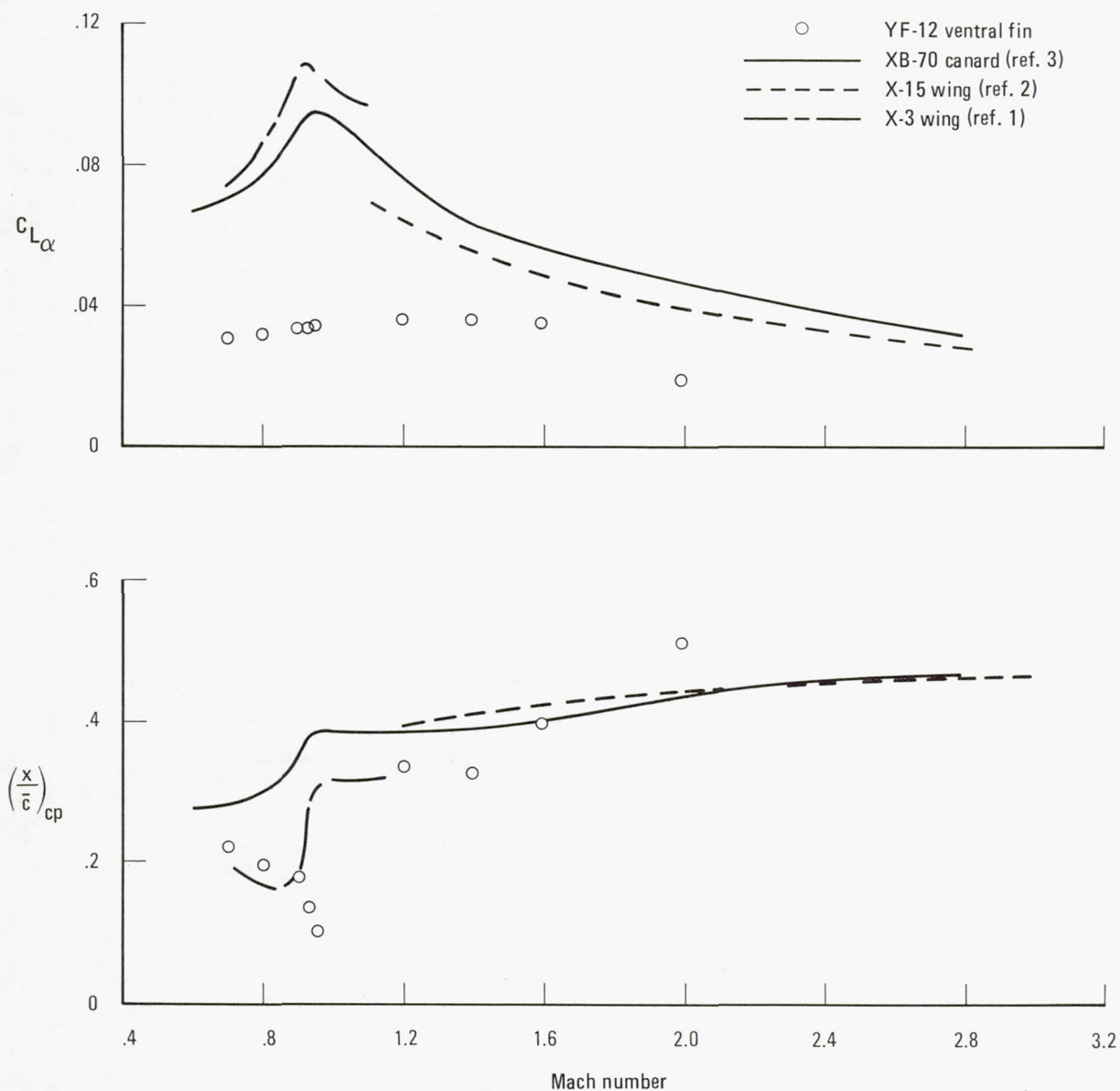


Figure 2.—Variation of flight-determined lift curve slope and chordwise center-of-pressure location with Mach number for several low-aspect-ratio lifting surfaces.

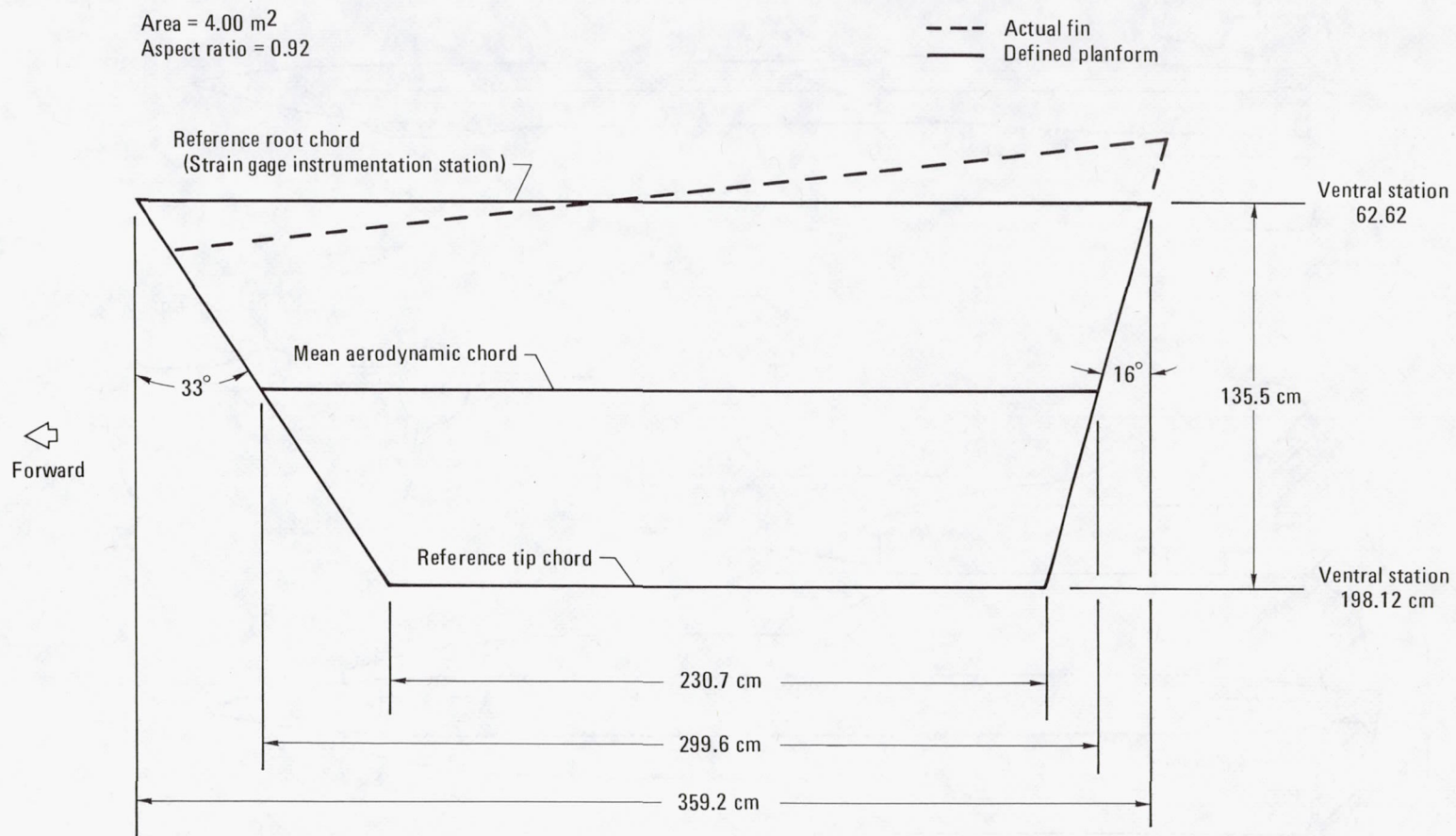


Figure 3.—Defined planform of flight test ventral fin, YF-12A airplane.

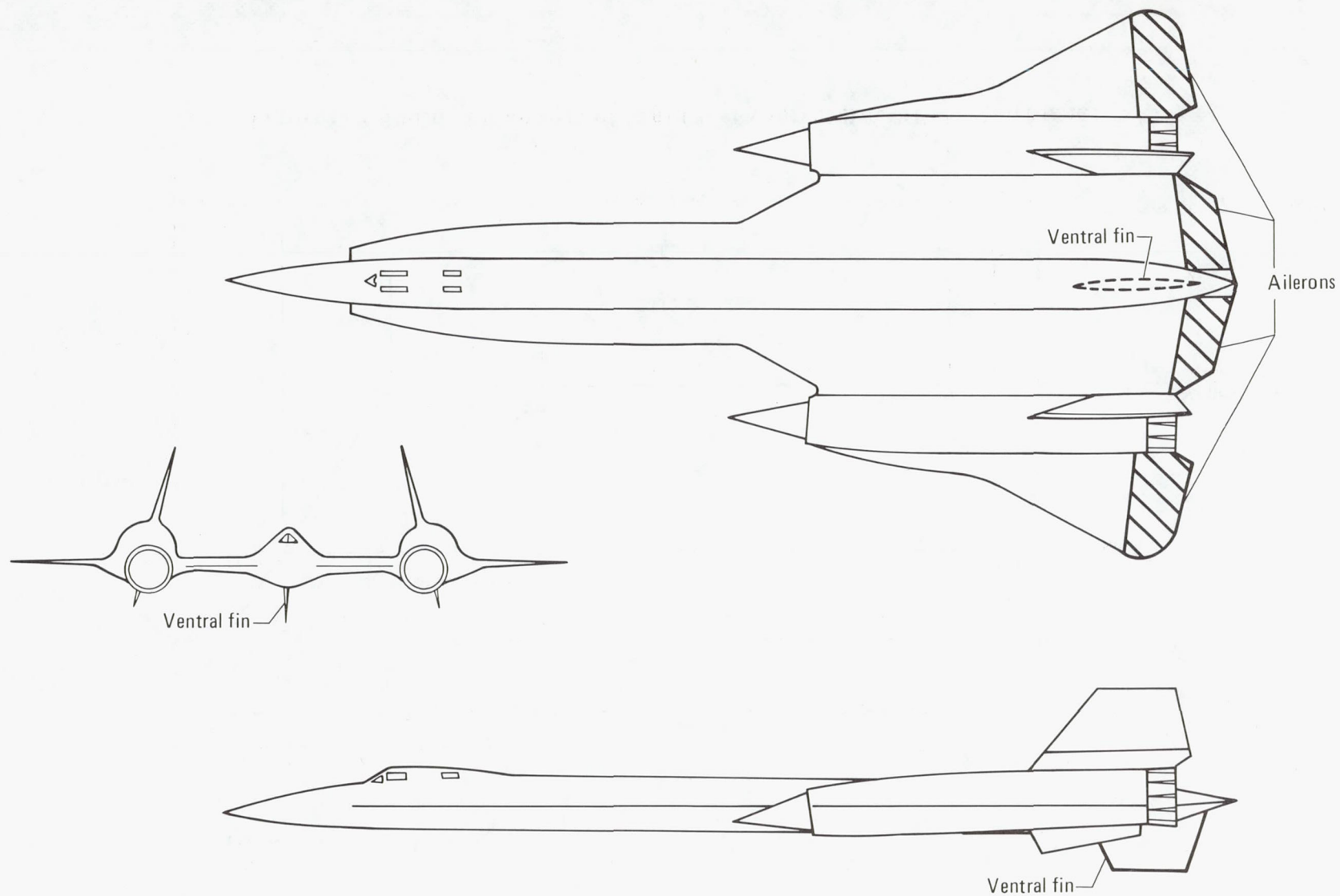


Figure 4.—Three views of YF-12A airplane showing proximity of ailerons to ventral fin.

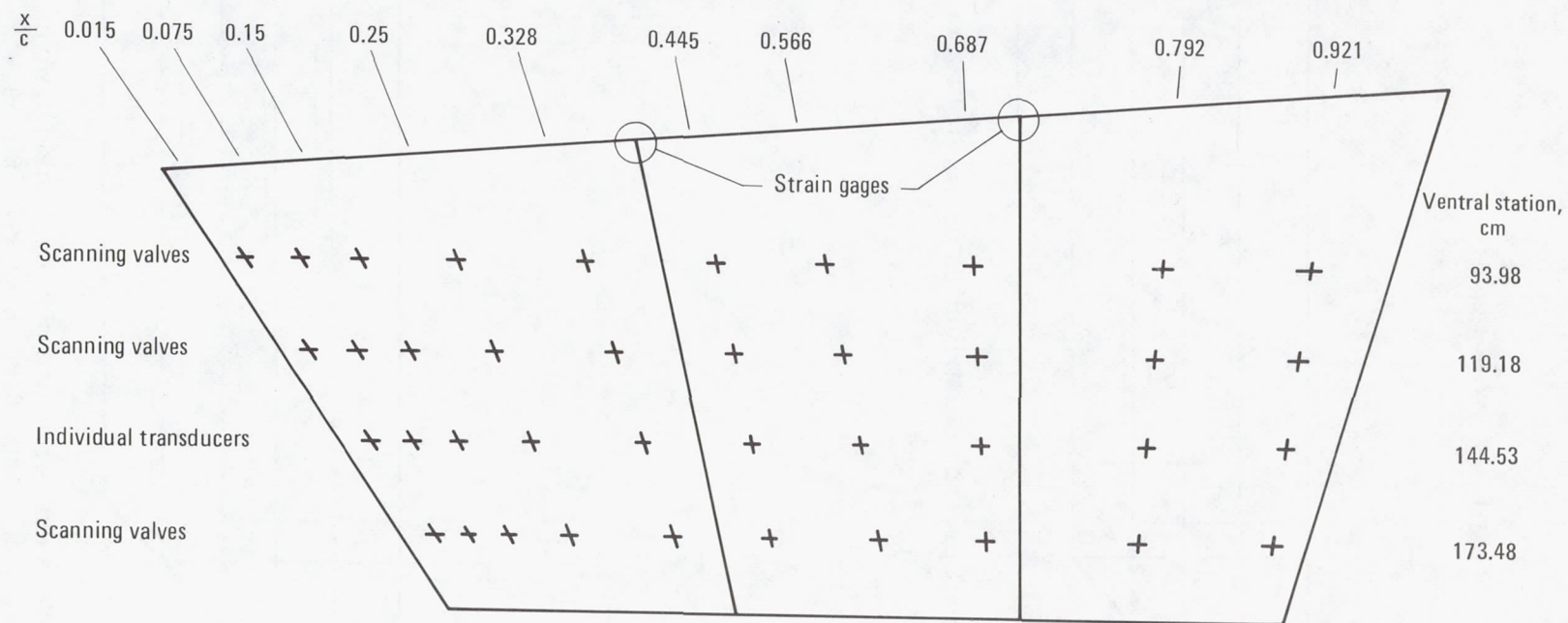


Figure 5.—Ventral fin instrumentation.

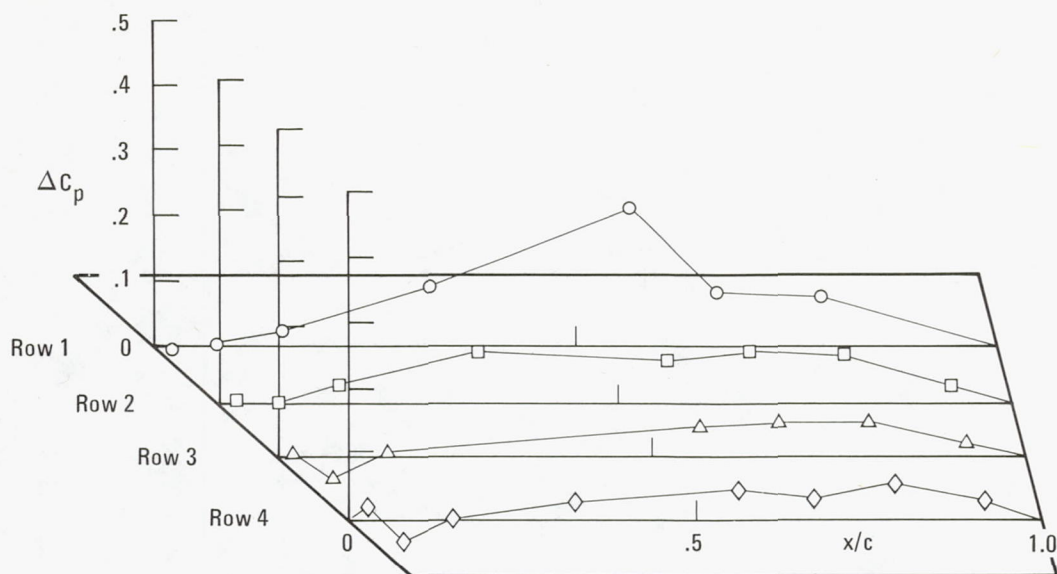


Figure 6.—Wind tunnel pressure distribution on ventral fin due to aileron deflection. $M = 0.90$, $\delta_a = 10^\circ$, $\beta = 0^\circ$.

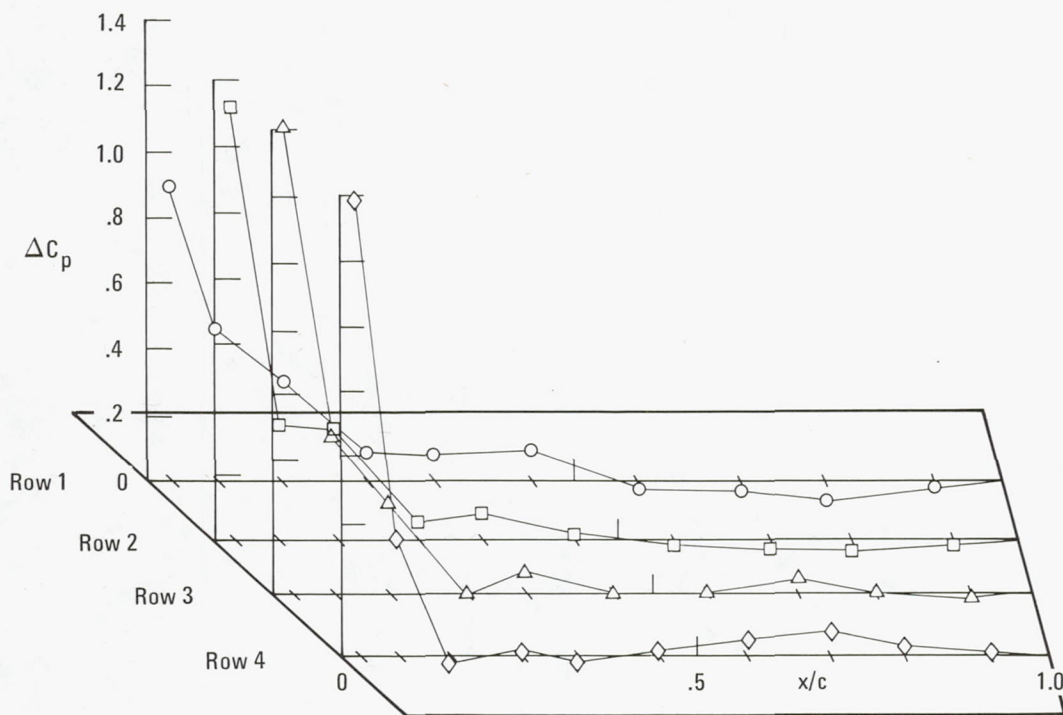


Figure 7.—Flight-measured pressure distribution on ventral fin due to steady-state sideslip loads. $M = 0.90$, $\delta_a = 3.7^\circ$, $\beta = -3.8^\circ$.

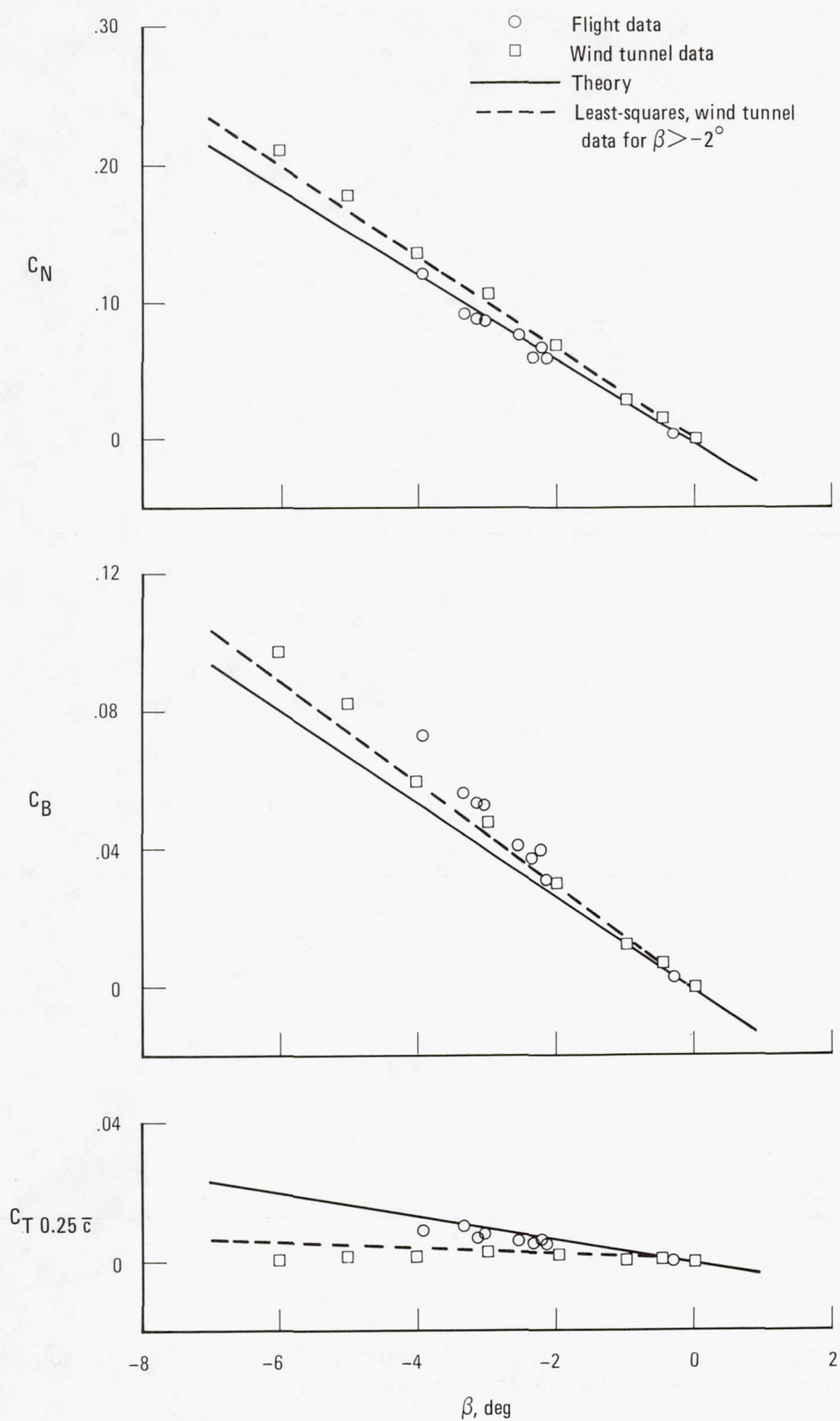


Figure 8.—Ventral fin load coefficients for flight, wind tunnel, and theoretical data shown as a function of angle of sideslip at Mach 0.90.

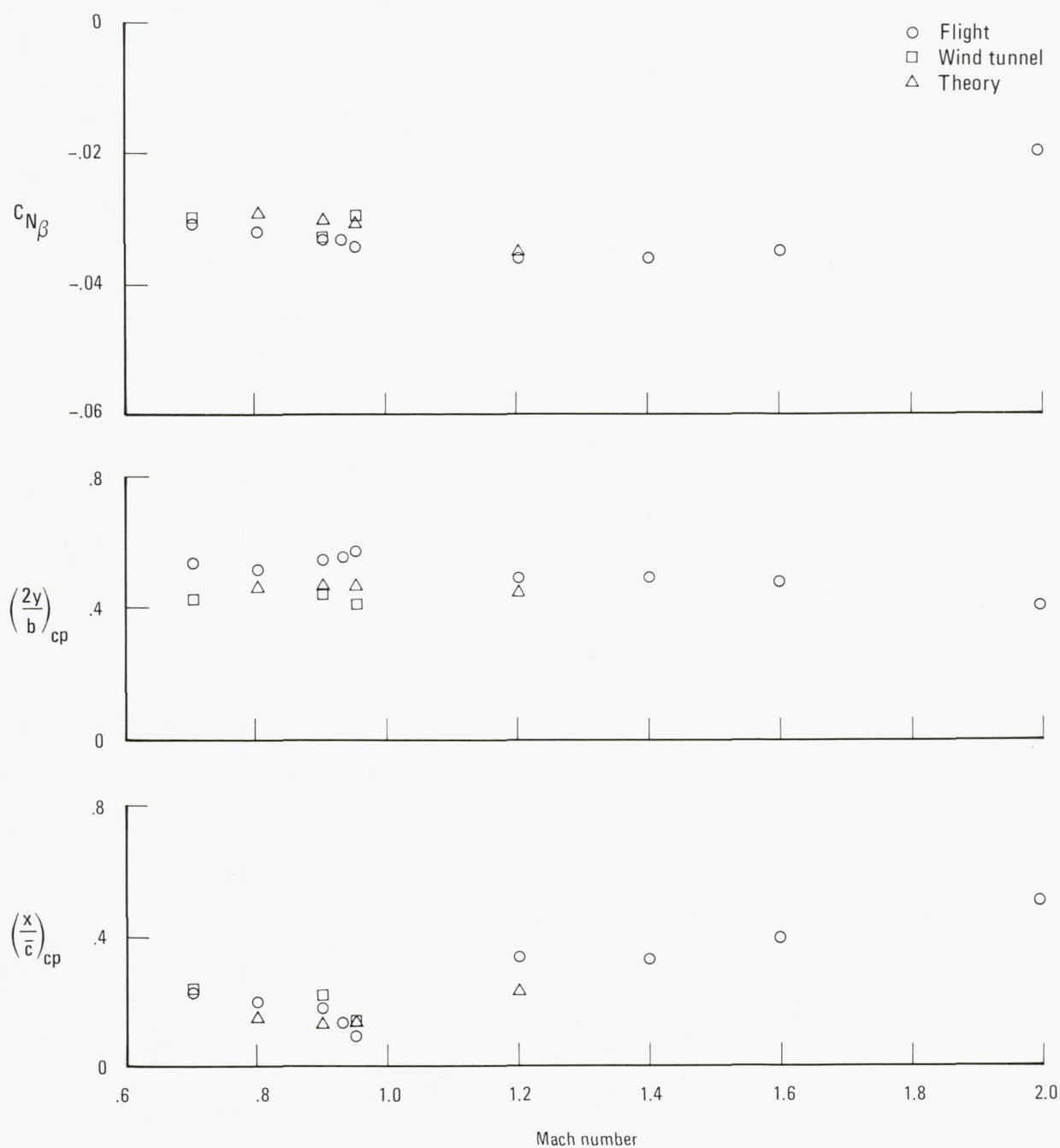


Figure 9.—Variation of ventral fin normal force coefficient slopes and center-of-pressure locations with Mach number.

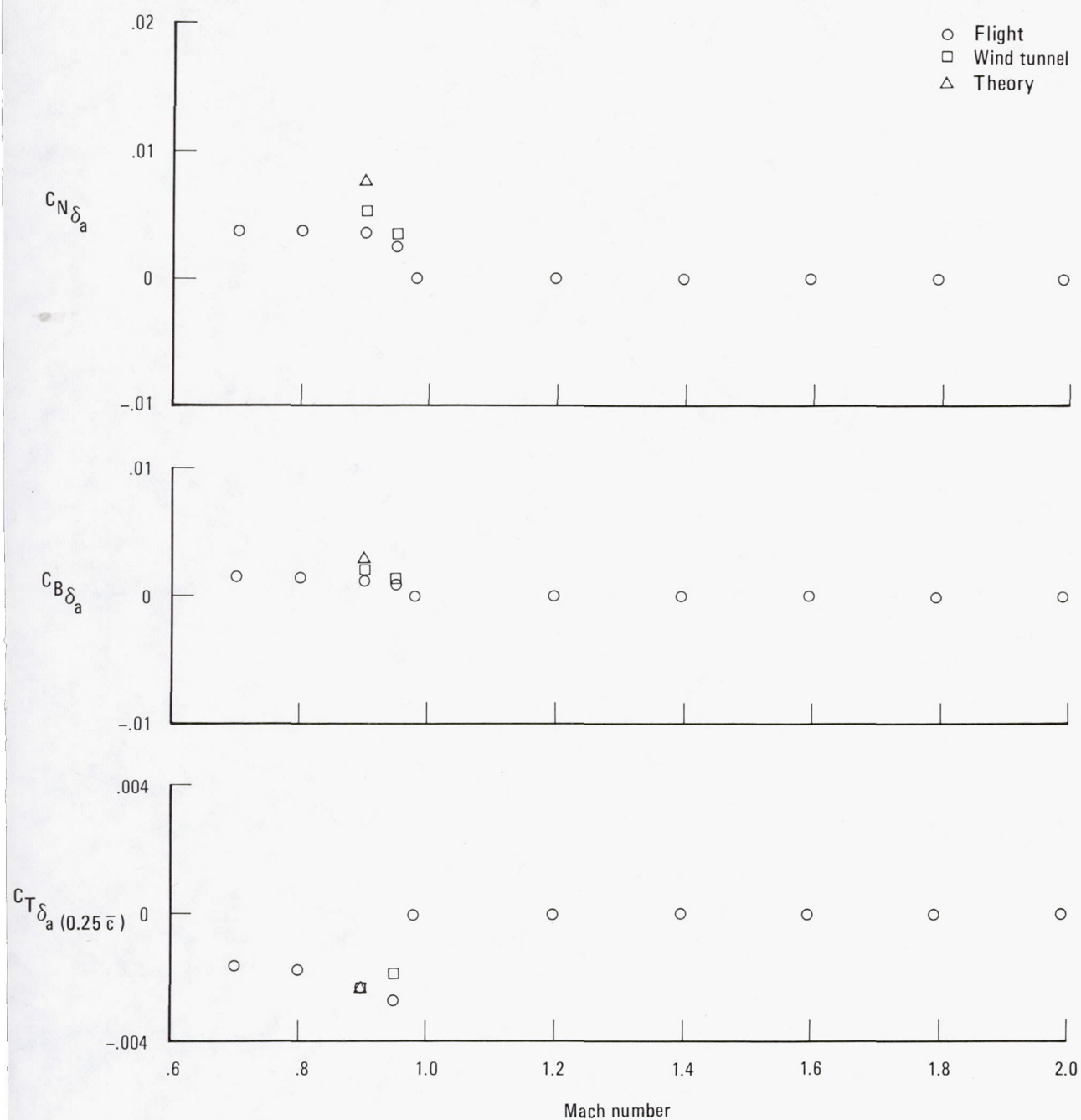


Figure 10.—Variation of ventral fin load coefficients due to aileron deflection with Mach number.

SESSION IV: AIRCRAFT CONTROLS

Chairman: Eldon E. Kordes, Dryden Flight Research Center

A SUMMARY OF YF-12 HANDLING QUALITIES

Donald T. Berry
Dryden Flight Research Center

SUMMARY

Handling quality observations made during the YF-12 flight research program are summarized. Emphasis is placed on characteristics generic to supersonic cruise vehicles, particularly those characteristics associated with longitudinal control during high-altitude, supersonic cruise. During these conditions, low levels of longitudinal short period damping are acceptable to the pilot; however, control of Mach number and altitude can be a problem because of decreased control effectiveness, sluggish propulsion system response, and atmospheric disturbances, accentuated by an unfavorable balance between kinetic and potential energy. Although total alleviation of the problem will require advancements in propulsion and control system characteristics, it was found that marked improvements could be immediately obtained through the use of better cockpit displays.

YF-12 ride qualities during takeoff and during certain propulsion system disturbances are harsh and could be unacceptable for passengers if present in a commercial supersonic cruise airplane.

FLIGHT EXPERIENCE WITH ALTITUDE HOLD AND MACH HOLD AUTOPILOTS ON THE YF-12 AIRCRAFT AT MACH 3

Glenn B. Gilyard and John W. Smith
Dryden Flight Research Center

SUMMARY

In order to obtain maximum range when operating aircraft at high altitude and high Mach number conditions, precise control of both flightpath and speed is necessary. However, experience with the XB-70, YF-12, and Concorde airplanes has shown that simultaneous control of flightpath and speed is extremely difficult at these flight conditions. Therefore, one aspect of the YF-12 program was to investigate methods to improve the altitude and Mach hold capabilities for high supersonic and hypersonic aircraft.

In this study, the altitude hold mode of the YF-12A airplane was modified to include a high-pass-filtered pitch rate feedback along with optimized inner loop altitude rate proportional and integral gains. An autothrottle control system was also developed to control either Mach number or KEAS at the high-speed flight conditions.

Flight tests indicated that, with the modified system, significant improvements were obtained in both altitude and speed control, and the combination of altitude and autothrottle hold modes provides the most stable aircraft platform thus far demonstrated at Mach 3 conditions.

INTRODUCTION

Although accurate control of altitude and Mach number becomes increasingly important in achieving maximum range performance at high altitude, high Mach number flight conditions, experience with the XB-70 (ref. 1), YF-12 (ref. 2), and Concorde (ref. 3) airplanes has shown that precise control of flightpath and speed become more difficult at these conditions. Decreased aircraft stability, low static pressures, and the presence of atmospheric disturbances are all factors that contribute to this degraded control. The combination of high altitude and high speed also contributes to an unfavorable balance between kinetic and potential energy, thereby requiring large altitude changes to correct for small Mach number

errors when flying a Mach hold mode using the elevator control.

This report covers one aspect of the YF-12 program directed at developing satisfactory altitude-hold and autothrottle-Mach-hold autopilot modes for operation at high altitude, Mach 3 flight conditions. Both flight-test results and simulator studies (ref. 4) are presented and comparisons are made using various control schemes.

SYMBOLS

Physical quantities in this report are given in the International System of Units.

a_n normal acceleration at center of gravity, g

h pressure altitude, m

KEAS knots equivalent airspeed

M Mach number

PLA power lever angle, deg

p_s static pressure, N/m^2

p_{t_2} stagnation pressure, N/m^2

s Laplace operator

α angle of attack, deg

Δ incremental change

ΔT temperature change, K

δ_e average elevon deflection, deg

θ pitch angle, deg

φ roll angle, deg

Subscripts:

e error

2 compensated location on nose boom

3 location 0.2667 meter aft of stagnation pressure port on nose boom

A dot over a quantity denotes the time derivative of that quantity.

FLIGHT SYSTEM

Aircraft Description

The YF-12 airplane (figs. 1 and 2) is an advanced, twin-engine, delta-wing aircraft designed for long-range cruise at speeds greater than Mach 3 and altitudes greater than 24,000 meters.

The airplane has two axisymmetric, variable-geometry, mixed-compression inlets, which supply air to two J58 engines. Each inlet has a translating spike and forward bypass doors to control the position of the normal shock in the inlet. An automatic inlet control system varies the spike and bypass door positions to keep the normal shock in the optimum location. The pilot may also manually control the spike and bypass doors.

Two nacelle-mounted, all-movable vertical tails (rudders) provide directional stability and control. Each rudder is canted inward and pivots on a small stub section attached directly to the top of the nacelle. Two elevons on each wing, one inboard and one outboard of each nacelle, perform the combined functions of ailerons and elevators.

The airplane is normally operated with the stability augmentation system (SAS) engaged to provide artificial stability in pitch and yaw and to provide damping in pitch, yaw, and roll.

A more complete description of the aircraft is given in reference 5.

Air Data Computer

The autopilot obtains Mach number and altitude information from an electro-mechanical air data computer (ADC). The ADC, described more completely in reference 4, receives static and total pressure data from a compensated nose boom installation. The static pressure threshold of the ADC is approximately 1.676 N-m^2 , which corresponds to an altitude change of 3.67 meters at a flight altitude of 23,662 meters. The effective lag of the static pressure system is approximately 1.5 seconds at this flight condition.

ALTITUDE AND MACH HOLD CONTROL SYSTEM

The original altitude hold control system, shown in figure 3, was designed around a pitch SAS and an attitude hold loop. The altitude hold outer loop commands attitude changes that are proportional to altitude rate, altitude error, and the integral of altitude error. Both the pitch SAS and attitude hold loops perform satisfactorily.

Since the altitude hold mode of the autopilot receives altitude information from the ADC, any peculiarities in the air data parameter, p_s , show up in the altitude

hold capabilities of the autopilot. The location of the nose boom static pressure source can have a significant effect on the altitude hold operation. The static pressure source, p_{s_2} (fig. 4), which is on the compensated portion of the nose boom, is used by the ADC. Compensated static pressure ports are located to minimize static pressure position errors in the transonic region, but they are sensitive to angle of attack, as shown in figure 5. At a trim angle of attack of 3° , the $\Delta p_{s_2} / \Delta \alpha$ ratio is zero, but at 5° a typical value of $\Delta p_{s_2} / \Delta \alpha$ is -22.02 N/m^2 . The variation in the $\Delta p_{s_2} / \Delta \alpha$ ratio and resulting variation in indicated altitude is caused by angle of attack changes.

The conventional Mach hold control system (fig. 6) is an outer loop of the basic pitch SAS and attitude hold loop. The Mach hold autopilot receives Mach number information from the ADC and commands attitude changes proportional to the sum of Mach error plus the integral of Mach error.

The Mach hold mode of the autopilot receives Mach number information from the ADC; therefore, the same static pressure angle-of-attack effects previously discussed also affect the Mach number information. At an airspeed of Mach 3.0 and an altitude of 23,000 meters, the Mach number sensitivity, $\Delta M / \Delta \alpha$, is approximately 0.01 Mach per degree angle of attack.

SIMULATION SYSTEM

A combined analog/digital computer simulation was first used to duplicate and analyze problems with the original autopilot and then to investigate the effects of system modifications or new system designs. A perturbation model representing the aerodynamics and aircraft performance characteristics was programed for a flight condition of Mach 3.0 and altitudes greater than 21,336 meters. The simulation was a modification of that described in reference 6 and included the three longitudinal degrees of freedom, the inlet geometry effects on aircraft motion, inlet operation characteristics up to the unstart boundary, the characteristics of the afterburning mode of the engines, and the variation of density with altitude. An aircraft model with quasi-static flexibility corrections was used. No structural modes were simulated and all control system dynamics above 5 hertz were eliminated. The simulation could accept a variety of continuous and discrete input disturbances and could prove time histories of any quantity in real time.

Altitude Hold

The baseline altitude hold mode of the YF-12A autopilot was designed to operate at altitudes less than 18,288 meters. Preliminary evaluations of the altitude hold mode at altitudes exceeding 21,336 meters found that its operation varied from day to day. Occasionally, altitude could be held reasonably constant; at other times, it diverged in an unacceptable manner.

Figure 7 illustrates good altitude control at approximately Mach 3.0 and 23,622 meters. The pilot described the atmosphere as stable, as evidenced by the ease of holding the Mach number and altitude conditions. The low frequency limit cycle in altitude is due to the ADC static pressure threshold. The high frequency oscillatory characteristics in δ_e were due to the sensitivity of static pressure to angle of attack.

An example of unacceptable altitude hold control at Mach 3.0 and 23,622 meters is presented in figure 8. The pilot described the atmosphere as unstable, as evidenced by the difficulty in holding altitude and by the jumps in the indicated Mach number. Although atmospheric disturbances apparently induced the erratic altitude behavior on this occasion, other types of disturbances or untrimmed conditions could also initiate the altitude instability. The high frequency oscillations were due to the sensitivity of static pressure to angle of attack. As angle of attack increased in proportion to a_n , $\Delta p_{s_2} / \Delta \alpha$ increased negatively and the short period motion became divergent. When angle of attack decreased, $\Delta p_{s_2} / \Delta \alpha$ decreased and the short period motion damped.

Parametric studies of static pressure sensitivity to angle of attack, as well as the effect of autopilot gains on altitude hold performance, are provided in reference 4.

Improved Altitude Hold

The first phase of the autopilot improvement program involved tuning the baseline autopilot to see if satisfactory performance could be obtained at altitudes greater than 21,336 meters.

The simulator altitude hold gain optimization studies were initially performed with $\Delta p_{s_2} / \Delta \alpha$ set at zero. In this configuration, good altitude hold was obtained on the simulator with the original altitude rate gain, one-half the original altitude error gain, and one-fourth the original integral of the altitude error gain. In subsequent simulation studies, compensation in the static pressure angle-of-attack sensitivity was achieved by including the high-pass-filtered pitch rate feedback shown in figure 9. Bending compensation was added to eliminate structural interaction, and high frequencies were cut off before the signal was summed with $\Delta \theta$ and sent to the autopilot.

Typical flight-test data with the modified autopilot are shown in figure 10. After engagement, the autopilot kept altitude constant to within ± 7.62 meters for the 4-minute duration of the run. The long period, 35-second, low amplitude oscillation was due to the threshold of the ADC. As illustrated, there was no degradation of altitude hold, even though 0.4 Mach was lost.

The high frequency (one cycle per second) low amplitude ($\pm 0.2^\circ$) oscillation of the elevon was a short period limit cycle produced by the nonlinear characteristics of the rate gyro used in the high-pass-filtered pitch rate autopilot loop. (The gyro used is noted for reliability, not for resolution or linearity.)

A typical YF-12 experimental flight, made for purposes other than control systems research, consists of brief 1- to 2-minute periods of flight at stabilized

Mach numbers and altitudes for as many conditions as can be fitted into the flight plan. For these flights, pilots have found the modified autopilot valuable for rapidly obtaining and holding altitude. Figure 11 illustrates a typical engagement of the modified autopilot with an initial rate of descent of approximately 400 meters per minute.

The atmosphere was stable for both modified autopilot examples. However, any latent aircraft control system instabilities would probably have been excited by the deceleration shown in figure 10 or by the initial rate of descent condition shown in figure 11.

With the altitude hold mode engaged, the pilot's Mach hold task was easy. In addition to improving the quality of each run, it was estimated that, because of the time saved in establishing and maintaining altitude, using the modified autopilot, 10 percent additional data could be obtained on each flight. Reference 4 provides a more complete evaluation of the altitude hold autopilot program.

Mach Hold

Conventional Mach hold.—The conventional Mach hold mode of the YF-12C autopilot (fig. 6) was designed to operate over the entire Mach number range of the aircraft. At speeds greater than Mach 2.0, the desired Mach number could be held quite accurately to within ± 0.02 Mach for wings-level conditions. In turns, the quality of Mach control was generally reduced, particularly at the higher Mach numbers. Although the problem of holding Mach in the turn did not receive much attention, it appears that the primary cause is related to the automatic navigation mode of the autopilot, which operates through the ailerons and couples with the longitudinal axis in turning flight. An example of the performance of the conventional Mach hold mode at Mach 2.85 is presented in figure 12. The first 7 minutes were flown with wings level and the speed was held to within ± 0.02 Mach of its value at engagement. However, the ride was quite rough, as evidenced by the $\pm 0.2g$ normal acceleration levels and by the peak-to-peak altitude change of 1066 meters. Seven minutes of data were obtained in turning flight with a bank of approximately 34° . In the turn, the quality of Mach hold was slightly degraded ($\Delta M \approx \pm 0.025$) as were the ride qualities ($\pm 0.35g$ normal acceleration). A peak-to-peak altitude change of 610 meters was encountered during the turn.

It is obvious from the Mach hold example in figure 12 that although the Mach number control was fairly good, the associated ride qualities in terms of normal accelerations were unacceptable. Furthermore, the altitude changes could be unacceptable from an air traffic control standpoint.

The effect of static pressure source sensitivity to angle of attack in the Mach hold mode is presented in reference 4 for the YF-12A aircraft, which has a slightly different Mach hold control scheme.

Autothrottle Mach and KEAS hold.—The second major objective of the autopilot improvement program was to develop an autothrottle control system which could control either Mach or KEAS and which would be compatible with the improved altitude hold control system. The initial autothrottle control studies were evaluated on the previously discussed NASA simulation system. A functional diagram of the

autothrottle control system implemented on the aircraft is presented in figure 13.

Either Mach or KEAS from the ADC and pitch attitude are gain-adjusted and summed to provide the control reference signal. The input signals were filtered to reduce noise, and additional lead was provided by the high-pass filter. The output of a proportional-plus-integral logic network was used for the actuator command signal. In turn, throttle control was accomplished by a constant rate actuator moved in a discrete fashion by the switching relay commands.

Figure 14 provides a simulation comparison of various autopilot control modes at Mach 3.0 and 22,100 meters for a mild temperature variation of no more than 2.4 K peak to peak over a period of 9 minutes (ref. 7).

The response of the attitude hold mode to such a temperature variation is shown in figure 14(a). Attitude, which is not shown, is essentially constant ($\Delta\theta = \pm 0.03^\circ$), but altitude drifted off significantly, and Mach number was uncontrolled. The ride was smooth for this control mode.

Attitude hold is the inner loop for both the altitude hold and conventional Mach hold modes. The altitude hold simulation run is presented in figure 14(b) which shows that altitude was held accurately to within 15 meters peak to peak. The ride was good, but Mach number drifted off.

The conventional Mach hold simulation run is presented in figure 14(c). Airspeed was held reasonably accurately to within ± 0.01 Mach, although control of the high frequency Mach variations was slight. The associated altitude variation was large (336 meters peak to peak), especially in view of current air traffic control altitude assignments. The resulting variations in normal accelerations were $0.12g$ peak to peak. Although this level was probably not disturbing in terms of ride qualities, it was significant in view of the mildness of the temperature variation.

The simulation run of altitude hold combined with the autothrottle Mach hold system is shown in figure 14(d). Mach number was held well, but not noticeably better than with the conventional Mach hold. However, with the autothrottle, altitude was controlled accurately and ride qualities improved. Accurate control of the high frequency Mach number error was dependent on the thrust modulation capability of the autothrottle system, which is low for this airplane.

Figure 15 shows the flight-test data obtained at Mach 3.0 and 22,100 meters with the autothrottle in Mach hold and the pitch autopilot in altitude hold. The atmospheric conditions during this run were stable or smooth. The systems capabilities were tested a number of ways in this example. The autothrottle was engaged in Mach hold while stabilized in a 36° bank turn. Shortly after engagement, the aircraft was rolled to wings level. Approximately 2 minutes into the autothrottle run, the pilot commanded a 0.023 Mach reduction; however, Mach was not controlled as rapidly because the power levers were at their minimum authority. During the stabilized portions of the time history, speed was held to within approximately ± 0.01 Mach of its desired value. The altitude hold mode was on throughout the autothrottle run. The desired altitude was perfectly maintained prior to and after the rollout, although 24.4 meters were gained during the rollout transition. It should be noted that the altitude was held accurately even though rather large power changes were commanded by the autothrottle Mach hold system. The ride qualities, indicated by the normal acceleration, were good.

A second example of Mach hold autothrottle is presented in figure 16. In this case, the altitude hold and autothrottle Mach hold were engaged with wings level. After approximately 1.5 minutes, the aircraft was rolled into a 30° bank turn and remained in the turn for the duration of the autothrottle run. Speed was controlled to approximately ± 0.01 Mach, and altitude was controlled to within 16 meters peak to peak after the initial engage transient.

The autothrottle also has a KEAS hold mode which, when used in conjunction with altitude hold, theoretically should have been equivalent to Mach hold. In this configuration, KEAS could be controlled to within ± 2 knots of the desired airspeed.

Thus far, pilots' comments on autothrottle experience have been quite favorable. Except for short intervals, the autothrottle system could control Mach or KEAS more accurately than the pilot.

The autothrottle was evaluated with two different speed actuators. The slow and fast actuators covered the same throttle range in 20.5 seconds and 3.48 seconds, respectively. No significant difference in control quality was apparent; however, the slow actuator was desirable since it was much less active than the fast actuator.

To date, our flight experience has demonstrated that the combination of altitude hold and autothrottle Mach hold provides the most stable aircraft platform capability ever demonstrated at high altitude, Mach 3 conditions.

CONCLUSIONS

Good altitude hold was demonstrated at high altitudes using existing autopilot concepts and hardware with only minor modifications. These modifications added a high-pass-filtered pitch rate feedback to compensate for angle-of-attack sensitivity and to improve the blend of altitude rate, error, and integral gains. Static pressure source sensitivity to angle of attack was found to have a significantly adverse effect on altitude hold.

Accurate Mach control was demonstrated at high speeds using an autothrottle control system. The combination of altitude hold and autothrottle Mach hold provided the most stable aircraft platform ever demonstrated at high altitude, Mach 3 conditions.

REFERENCES

1. Berry, Donald T.; and Powers, Bruce G.: Flying Qualities of a Large, Supersonic Aircraft in Cruise and Landing Approach. AIAA Paper 70-566, May 1970.
2. Berry, D. T.; and Gilyard, G. B.: Some Stability and Control Aspects of Airframe/Propulsion System Interactions on the YF-12 Airplane. ASME Paper 73-WA/Aero-4, Am. Soc. Mech. Eng., Nov. 1973.
3. Coleman, Herbert J.: Concorde Tour Adds to Operations Data. Aviation Week & Space Technology, vol. 97, no. 6, Aug. 1972, pp. 31-32.
4. Gilyard, Glenn B.; and Smith, John W.: Flight Results and Simulator Studies of a Mach 3 Cruise Longitudinal Autopilot. NASA TP-1180, 1978.
5. Gilyard, Glenn B.; Berry, Donald T.; and Belte, Daumants: Analysis of a Lateral-Directional Airframe/Propulsion System Interaction. NASA TM X-2829, 1973.
6. Brown, Stuart C.: Computer Simulation of Aircraft Motions and Propulsion System Dynamics for the YF-12 Aircraft at Supersonic Cruise Conditions. NASA TM X-62245, 1973.
7. Schweikhard, W. G.; Gilyard, Glenn B.; Talbot, J. E.; and Brown, T. W: Effects of Atmospheric Conditions of the Operating Characteristics of Supersonic Cruise Aircraft. I.A.F. Paper 76-112, Internat. Astronaut. Fed., Oct. 1976.

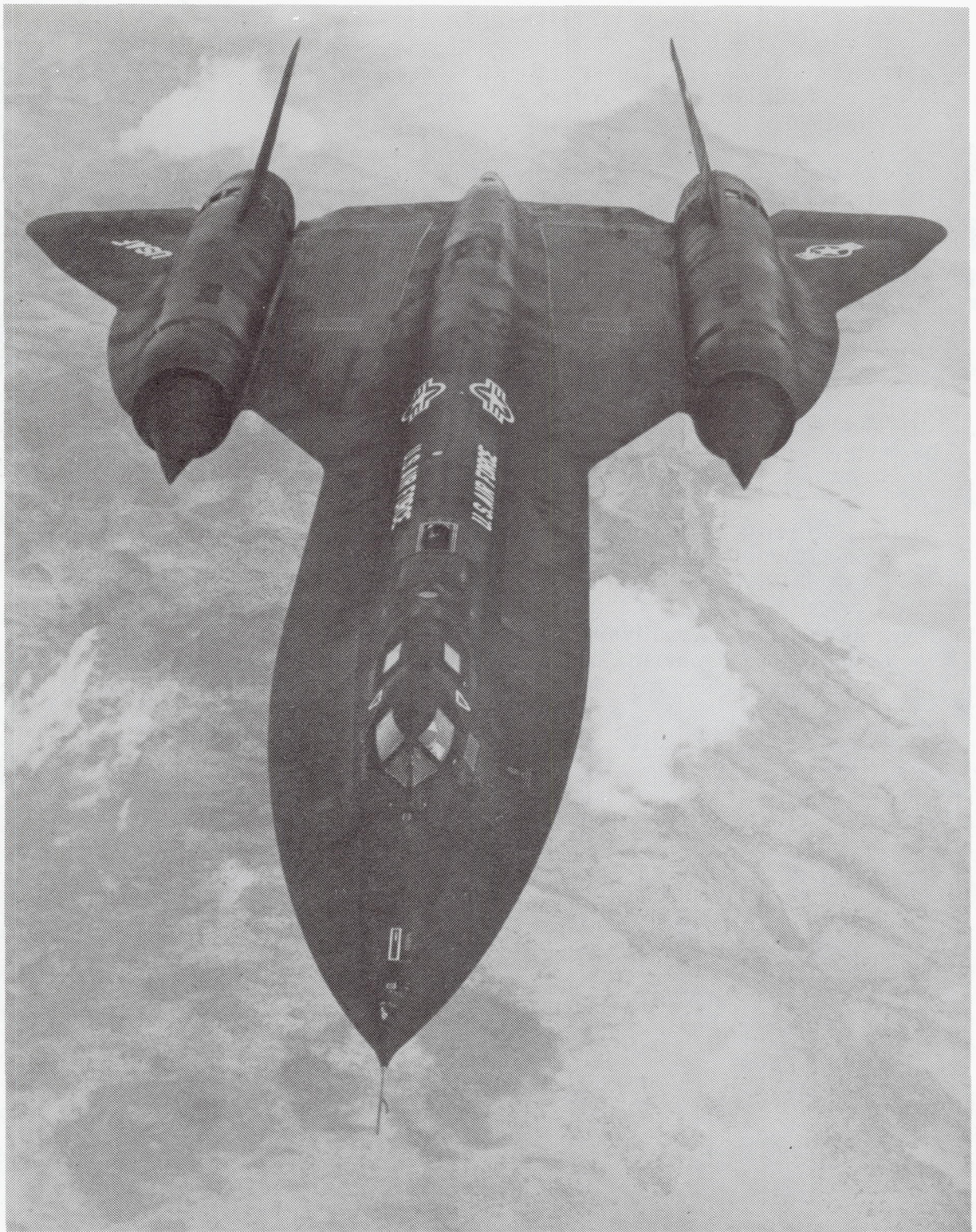


Figure 1.—YF-12C airplane.

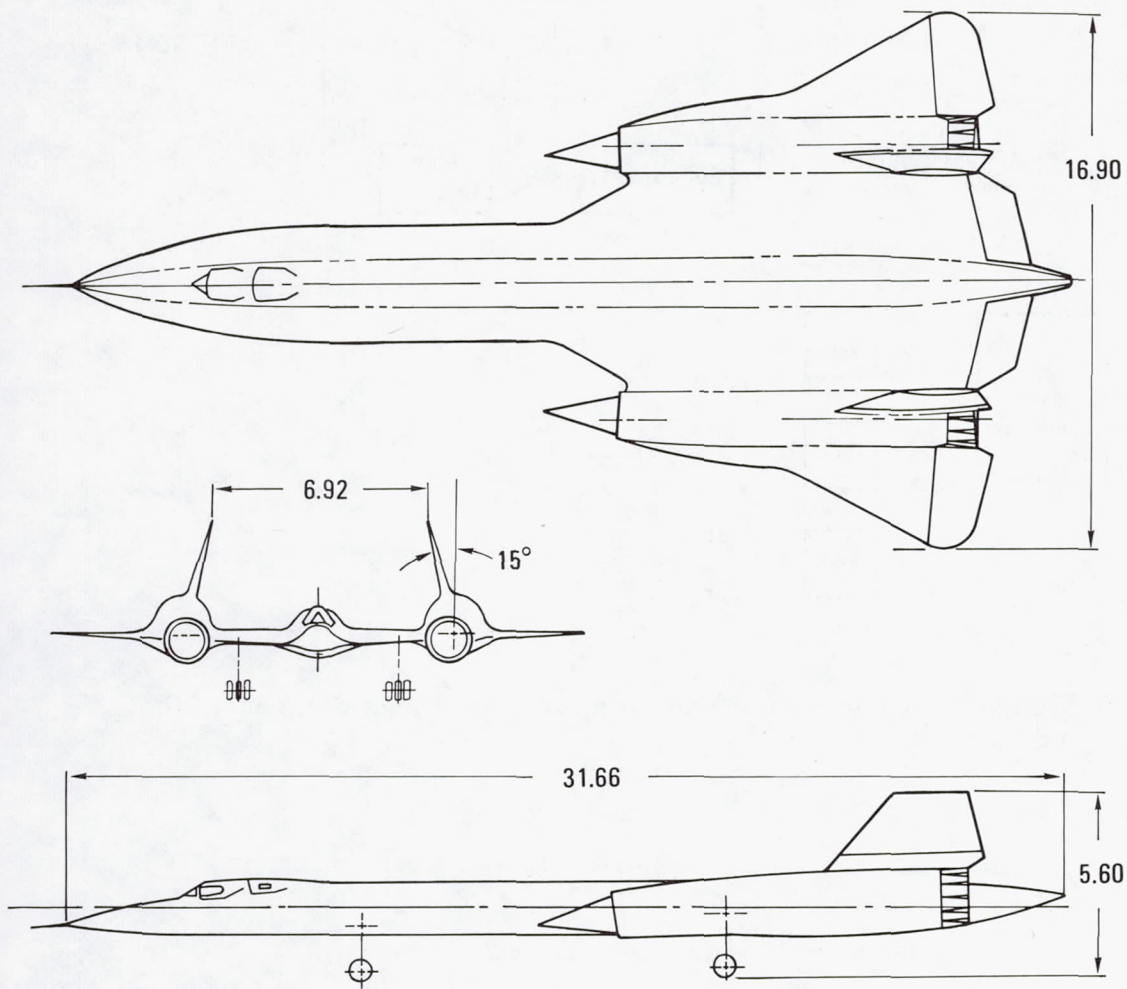
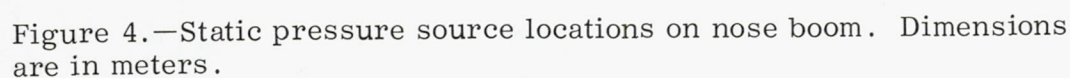
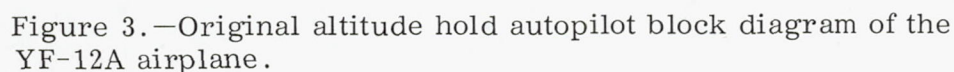


Figure 2.—Three-view drawing of the airplane. Dimensions are in meters.



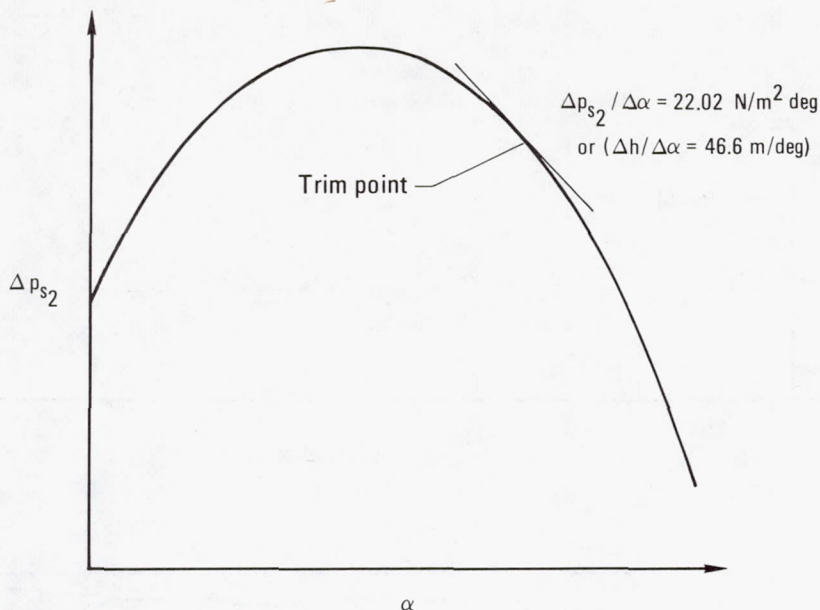


Figure 5.—Variation of static pressure error with angle of attack.
 $M \approx 3$, $h \approx 23,622$ meters.

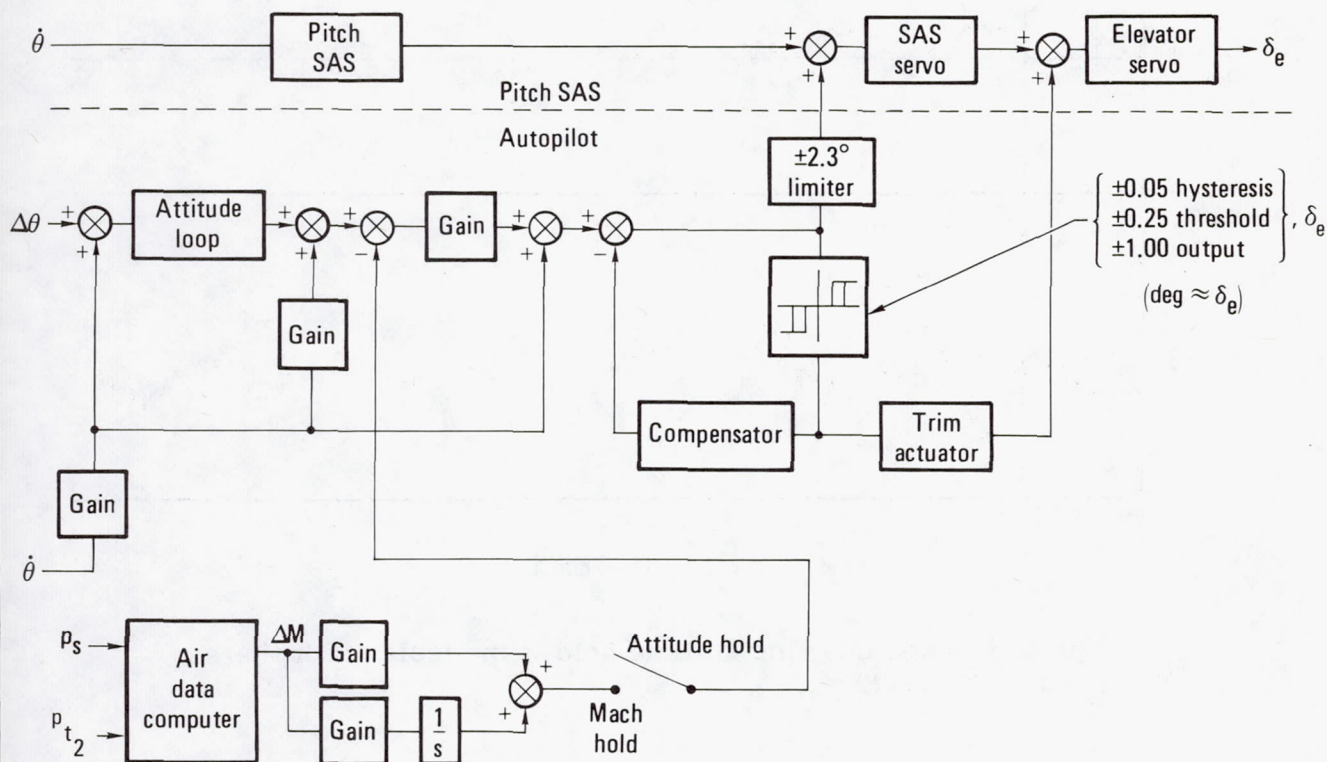


Figure 6.—YF-12C Mach hold control system. $h > 15,240$ m.

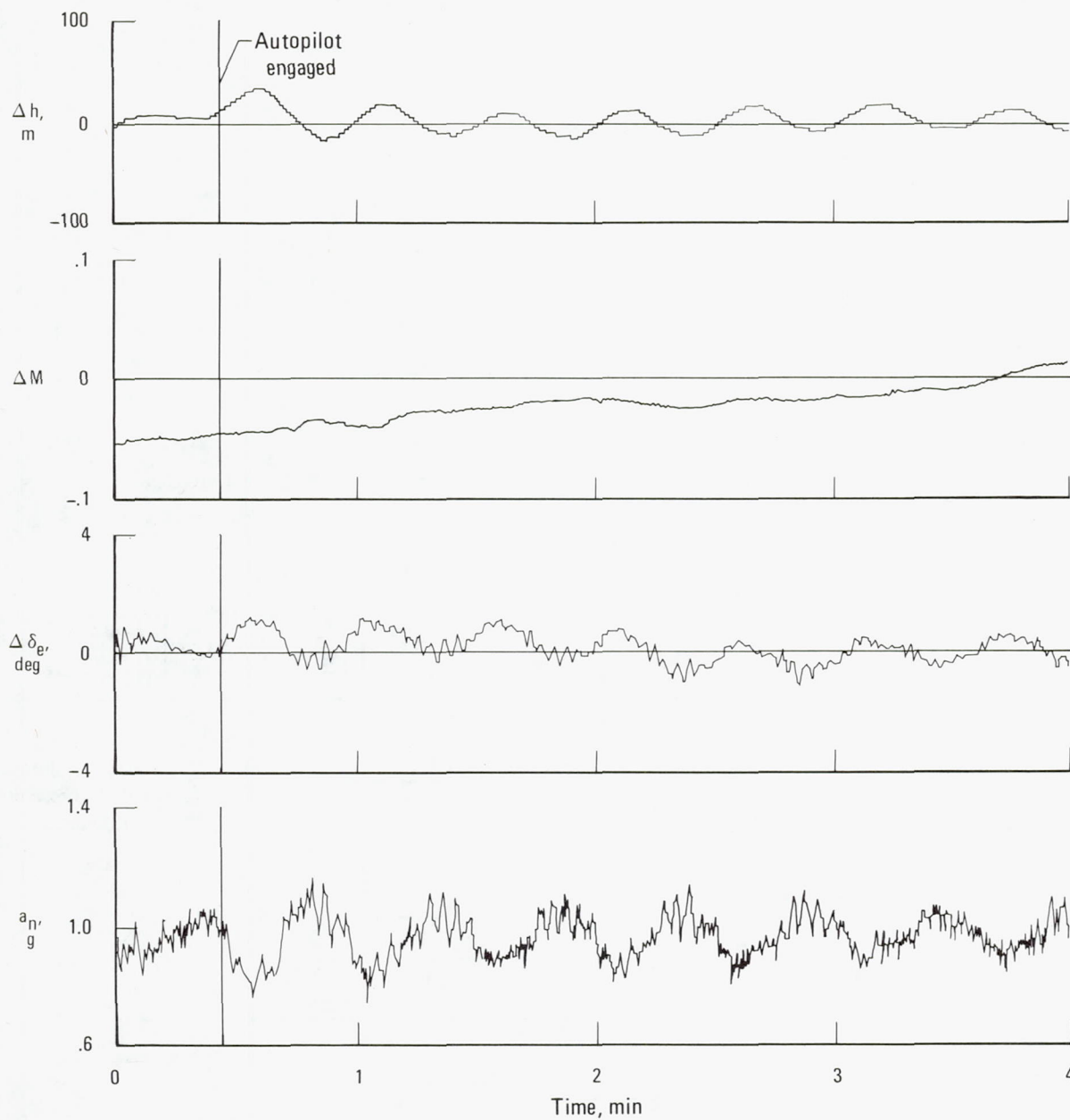


Figure 7.—Good baseline altitude hold with stable atmosphere.
 $M \approx 3$, $h \approx 23,622$ m.

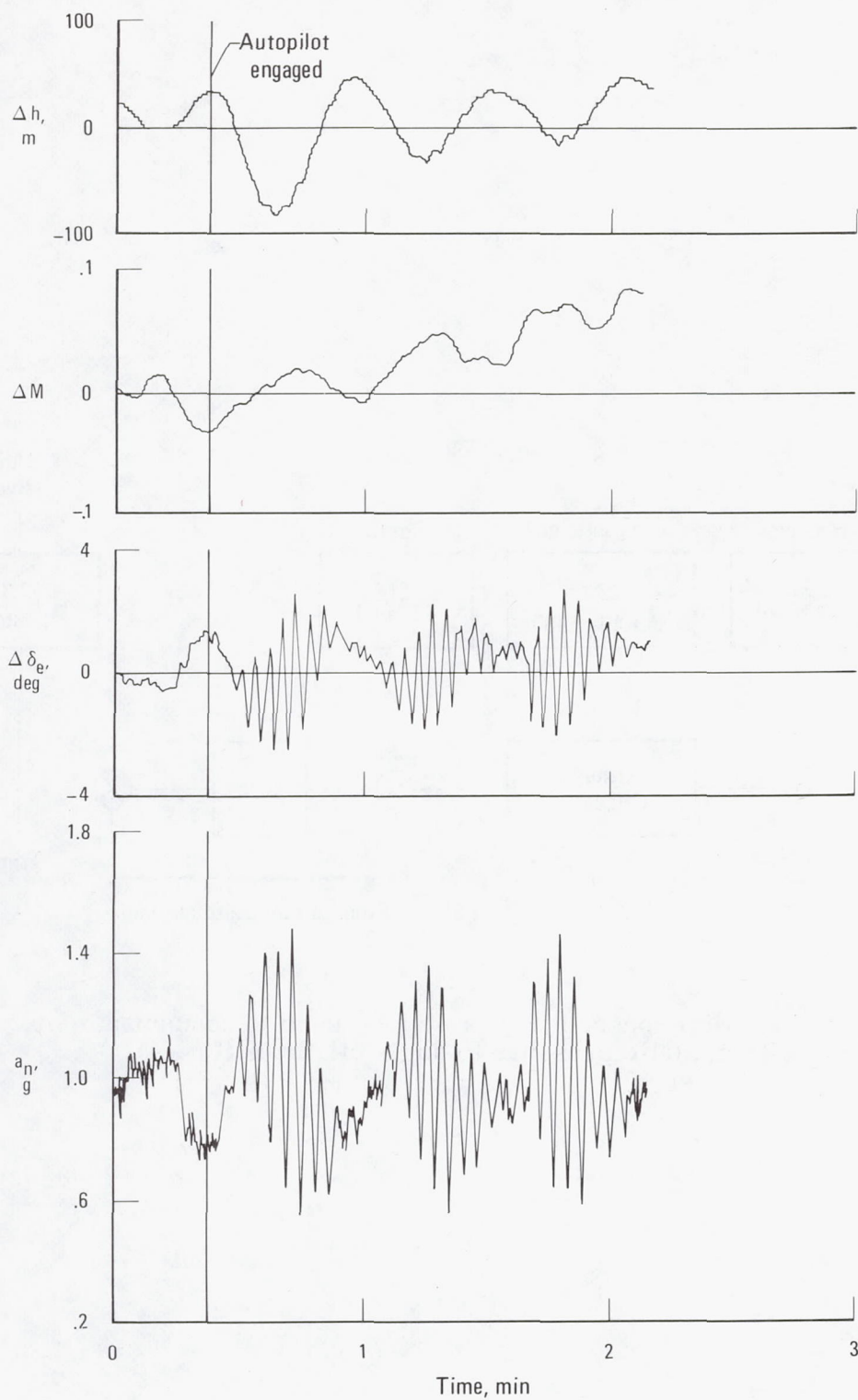


Figure 8.—Unacceptable baseline hold with unstable atmosphere.
 $M \approx 3$, $h \approx 23,622$ m.

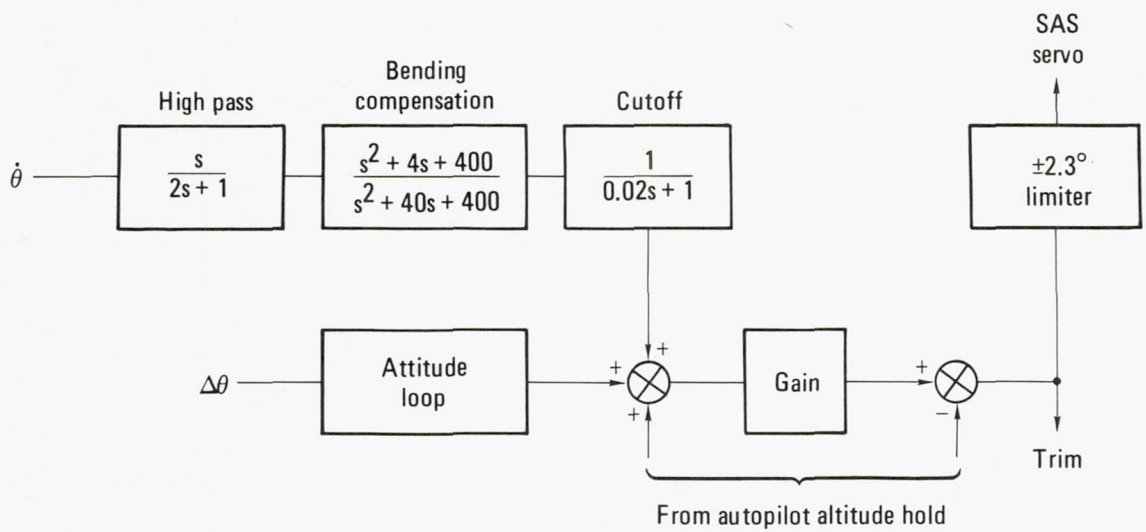


Figure 9.—High-passed pitch rate loop used to compensate for sensitivity of static pressure to angle of attack (fig. 4).

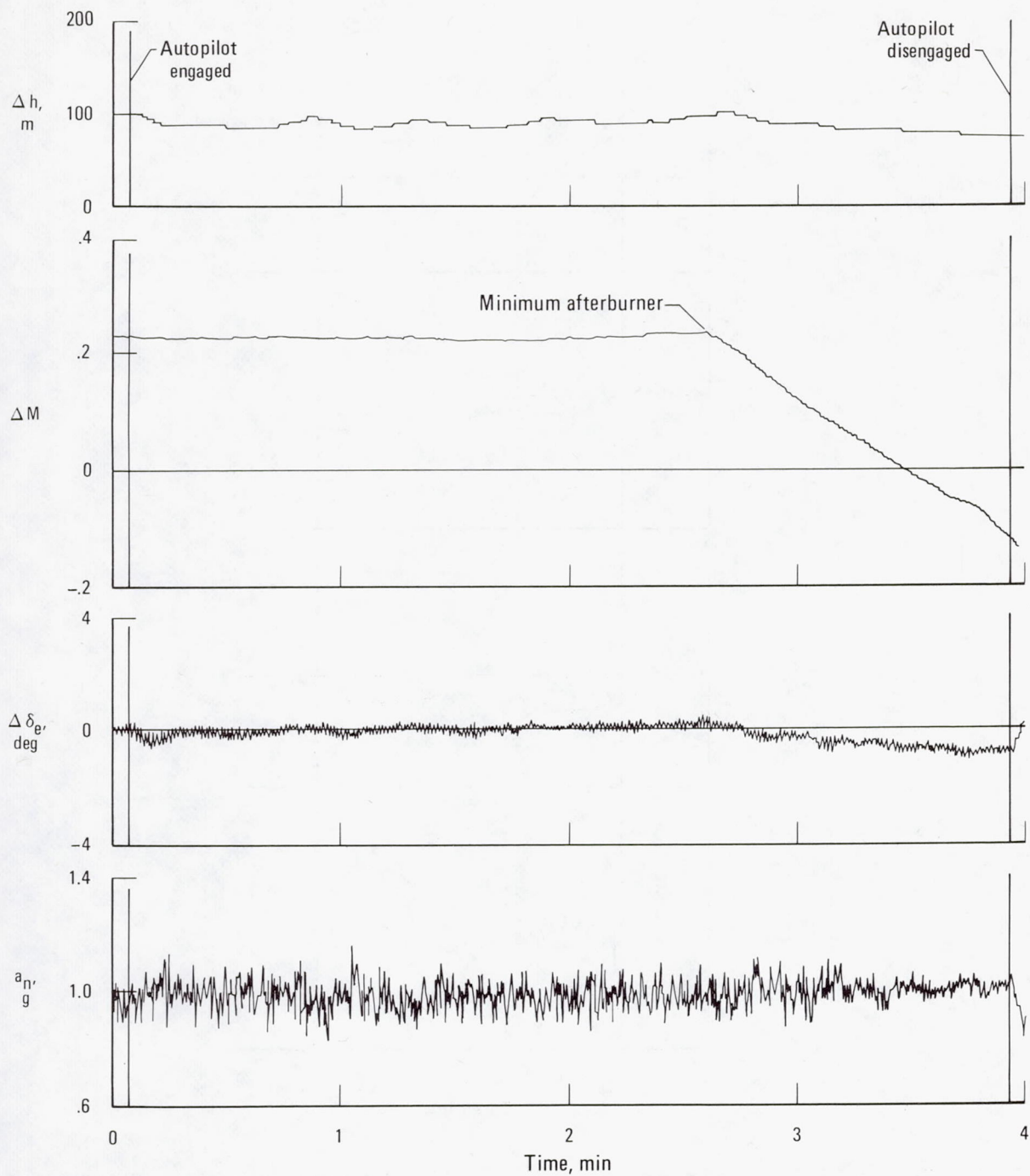


Figure 10.—Performance of modified autopilot. $M \approx 3$, $h \approx 23,622$ m.

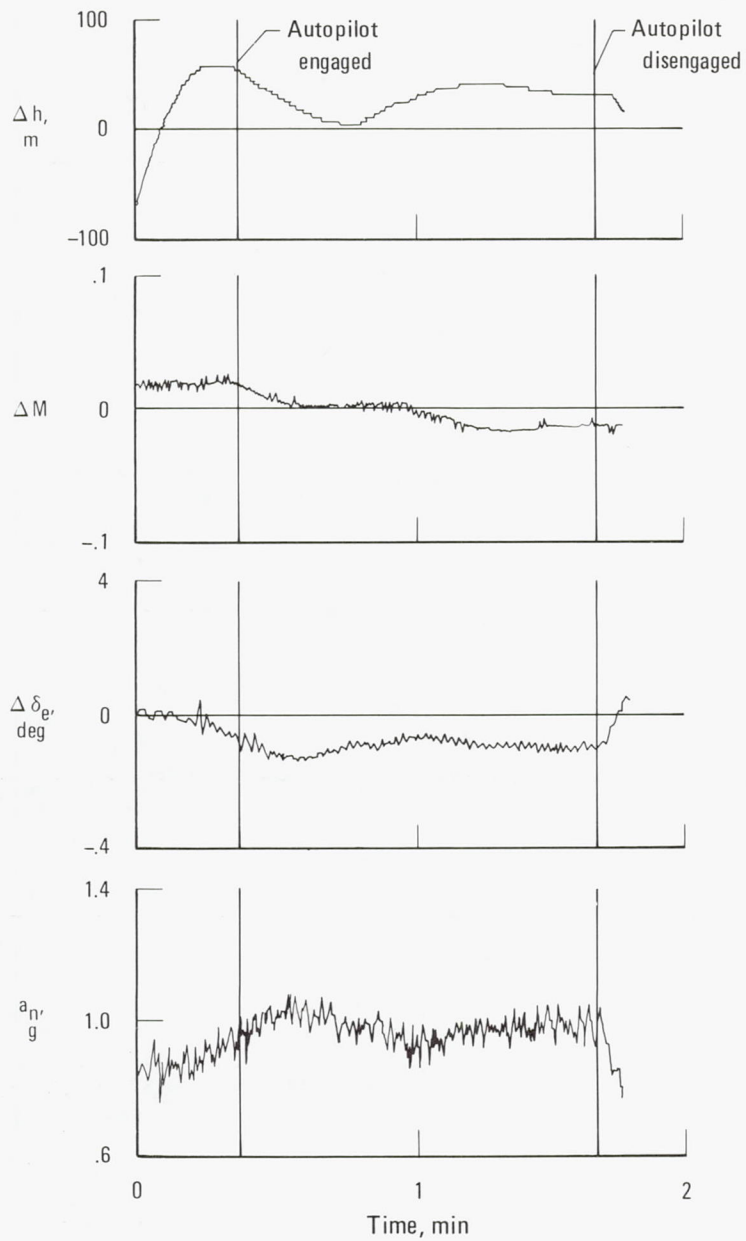


Figure 11.—Performance of modified autopilot with an initial rate of descent. $M \approx 3$, $h \approx 23,622 \text{ m}$.

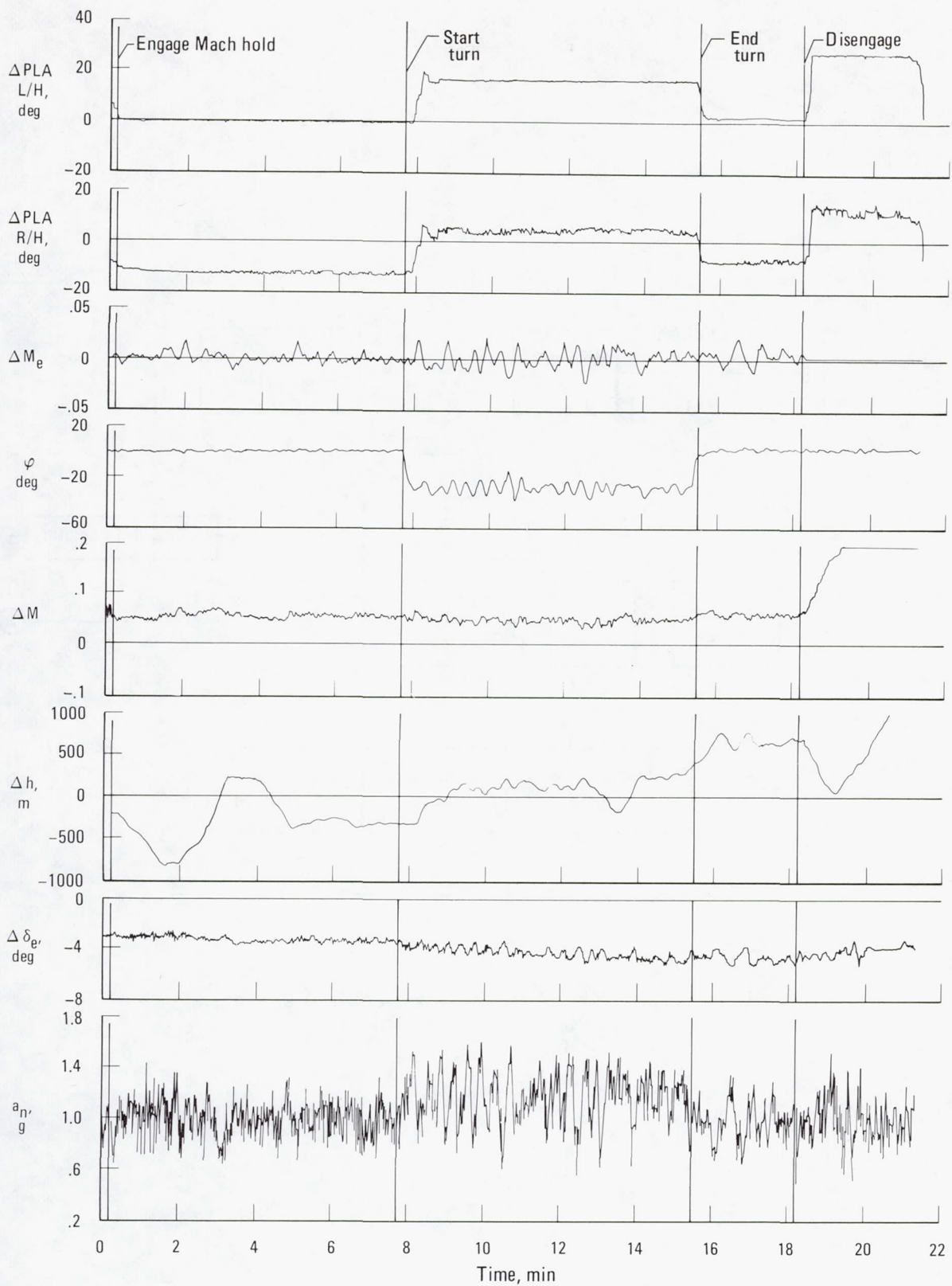


Figure 12.—Conventional Mach hold of the YF-12C airplane. Mach 2.85.

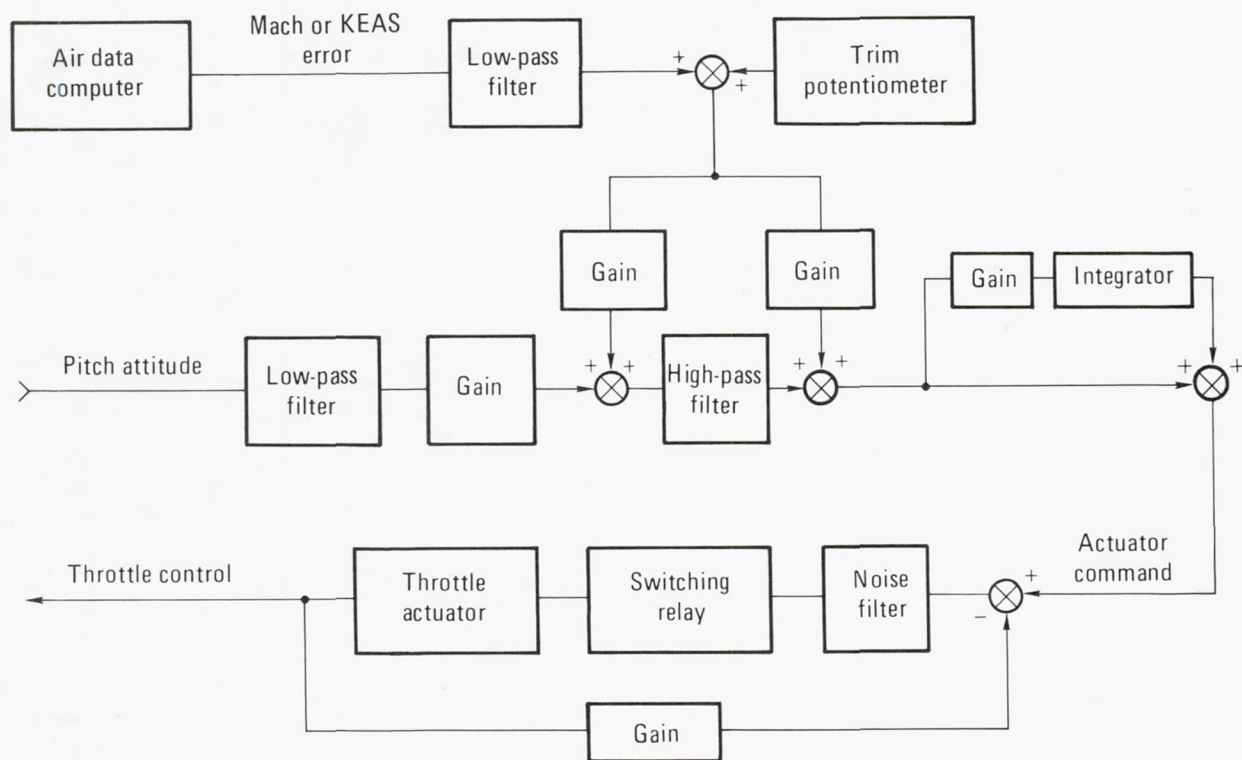
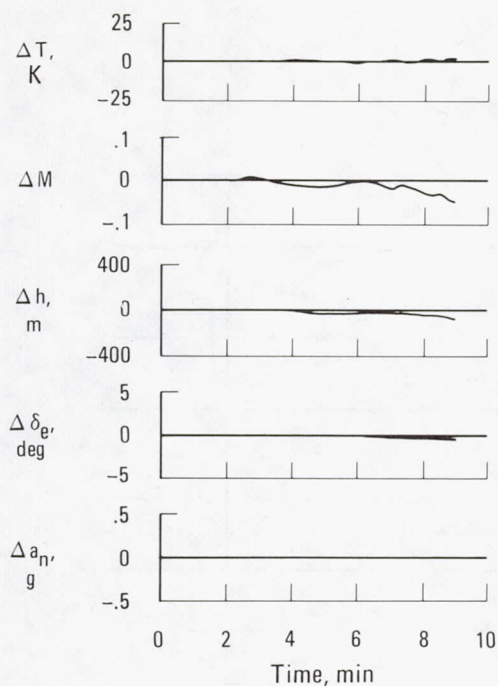
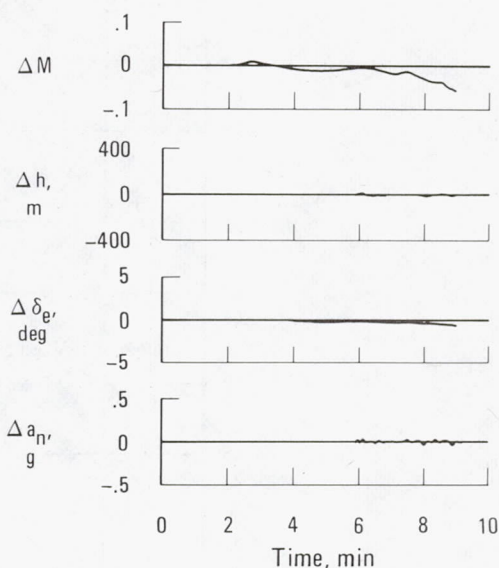


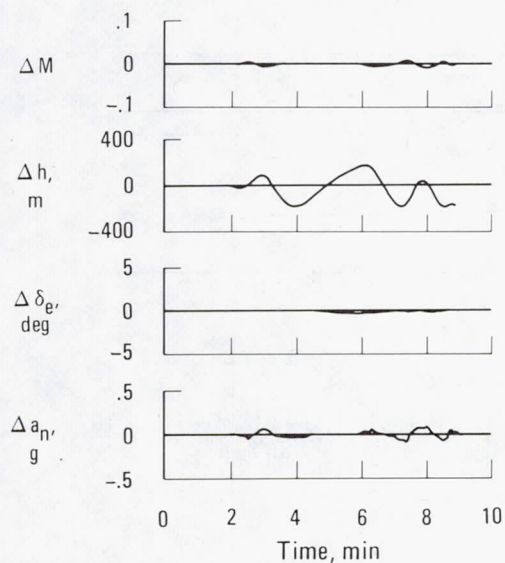
Figure 13.—YF-12 autothrottle control system.



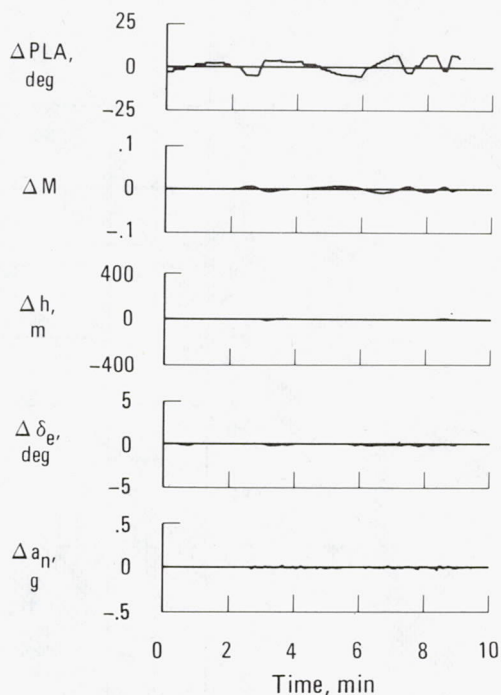
(a) Attitude hold.



(b) Altitude hold.



(c) Mach hold.



(d) Altitude hold and autothrottle Mach hold.

Figure 14.—Simulated aircraft response to nominal temperature variations with different types of control. $M \approx 3.0$.

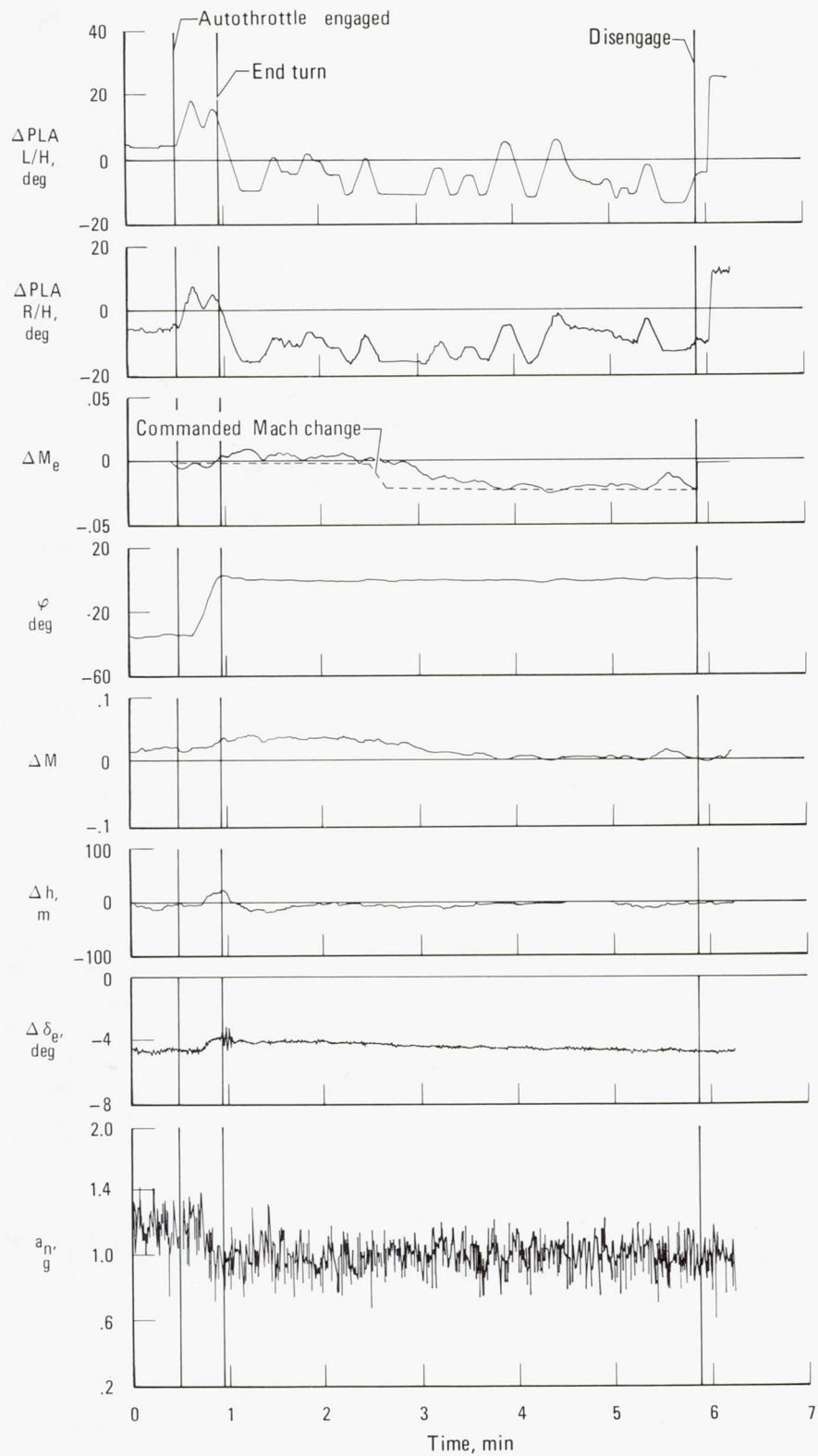


Figure 15.—Autothrottle Mach hold and altitude hold. $M \approx 3.0$, $h \approx 22,100$ m.

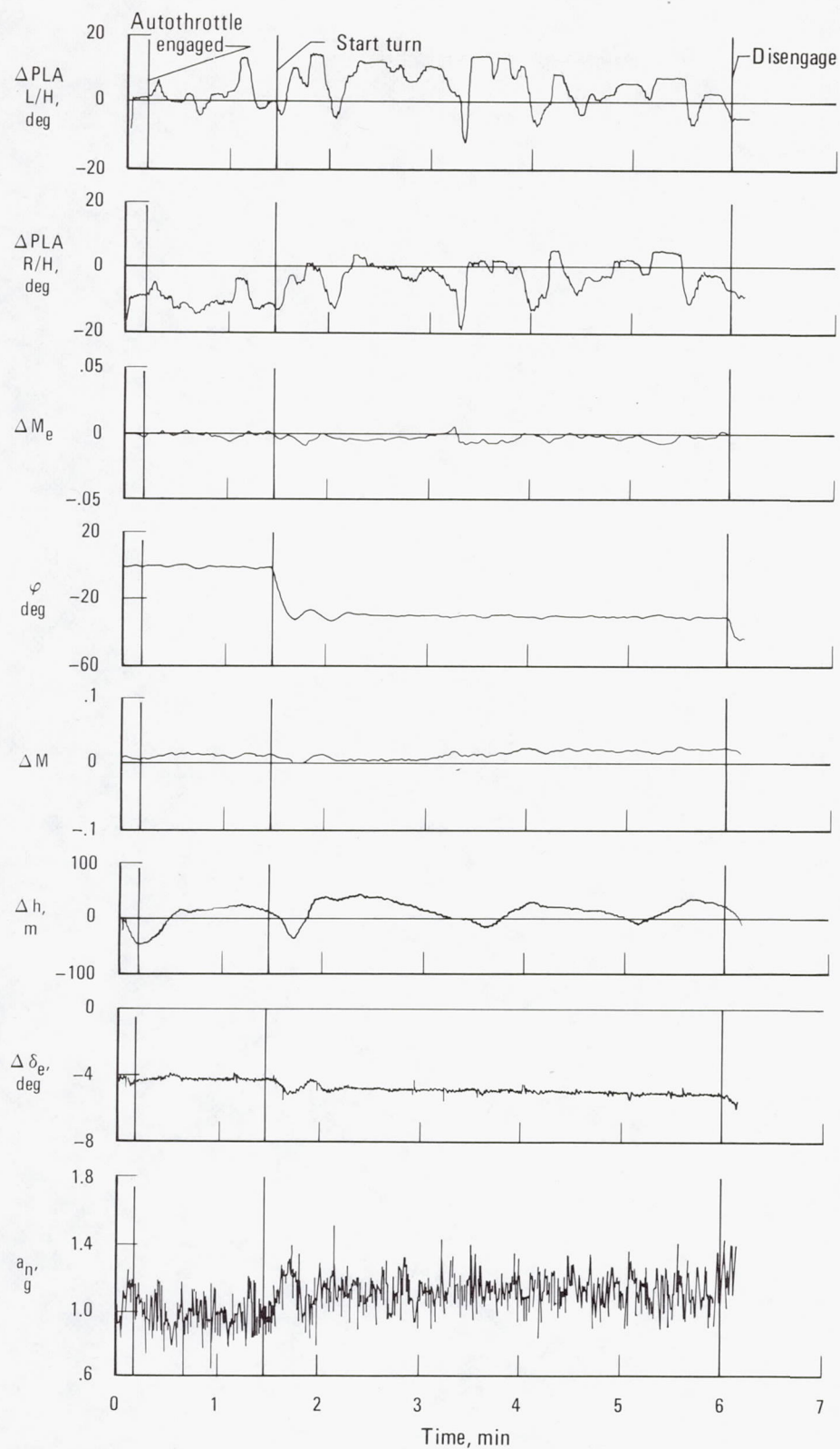


Figure 16.—Autothrottle Mach hold and altitude hold. $M \approx 2.8$, $h \approx 21,030$ m.

PILOT WORKLOAD MEASUREMENT AND EXPERIENCE ON SUPERSONIC CRUISE AIRCRAFT

Terrence W. Rezek
Dryden Flight Research Center

SUMMARY

The YF-12 aircraft is considered as representative of high workload supersonic cruise aircraft. A study was performed to determine which aircraft parameters and which physiological parameters would be most indicative of crew workload. This study is summarized and the recommendations formed a basis for a continuing study in which variations of the interval between heart beats is examined as a measure of nonphysical workload. Preliminary results of this work are presented. Current efforts in further defining this physiological measure are outlined.

INTRODUCTION

The need to understand the limits of human capability in all areas of aeronautical flight has spawned a large number of physiological studies of the human operator of flight vehicles. Each aeronautical system has a unique set of characteristics which impact the operator, but all modern systems exhibit steadily increasing operator workload demands. These demands take two forms; the physical, that is, extremes of heat, cold, noise, vibration, pressure and g forces; and the nonphysical, that is, personal risk, mission responsibility, and the large amount of information needing to be perceived, thought about, and acted upon in short time spans. The effects of the aeronautics environment on the operator are well documented (ref. 1) and some studies have demonstrated physiological effects in the absence of physical work (refs. 2 and 3). There have even been some attempts to quantify the effects of mental workload, albeit in a clinical atmosphere (refs. 4 to 6). From all this has come the realization that certain physiological phenomena accompany nonphysical workload. One objective of NASA's human factors research is the quantification of these nonphysical effects and their separation from physical effects.

In any mechanical-human interactive system, operation is achieved through an exchange of energies. This exchange and the resulting work can easily be measured

quantitatively with regards to the mechanical system. This is not the case with the human system. The total workload imposed on the human organism by any given task has two sources, the physical and the nonphysical, which may interact over a range from 0 to 100 percent. The purely physical, such as the labor involved in ditch-digging, can be measured in terms of both cause (weight of dirt thrown through a given height against a force of 1g) and effect (oxygen consumed, calories burned, and so forth). The nonphysical workload is much more difficult to measure. But as anyone knows who has come home exhausted after a day during which the most strenuous activity was the sharpening of a pencil, nonphysical work is very real.

The physiological monitoring effort at Dryden Flight Research Center (DFRC) has produced many hours of heart rate information from a large number of subjects in a variety of aircraft. However, correlative data concerning pilot activity occurring at given heart rates were not available. At the time the heart rate data were acquired, the possibility of assessing nonphysical workload through physiological measures was not fully appreciated.

The addition of the YF-12 aircraft to the DFRC research vehicles offered an opportunity to study nonphysical workload in a high-demand system. The high performance capabilities of this aircraft and its unique handling characteristics suggested such high demands but also implied that using secondary tasks to augment ambient workload might be hazardous. To avoid any possibility of compromising mission performance or flight safety, the studies would have to be conducted on a noninterference basis; consequently, a three-part program was conceived. First, a contract was let with a company specializing in mission evaluation and task analysis. The results and recommendations from this study are summarized. Second, those parameters from both the aircraft and the pilot which showed sensitivity to workload and were amenable to recording were selected for long-term monitoring, and the resulting data were analyzed. Finally, a possible method was devised for separating the effects of physical from nonphysical workload on a select physiological parameter.

PILOT PERFORMANCE MEASUREMENT STUDY

The principal objective of the study contract was to investigate pilot performance measurement in theory and practice during high-performance aircraft research at DFRC. The best approach was felt to be a study of realistic pilot and vehicle tasks. The study involved: (1) the development of measurement sets for system and pilot performance, (2) the investigation of objective, subjective, and physiological pilot performance measures, (3) the development of measures for such applications as pilot workload and crew control display effectiveness, and (4) the development of practical and feasible automatic and semiautomatic data processing techniques.

Flight Crew Task Analysis

Information collected from the aircraft, engines, and avionics is listed in table 1. This list covers the conditions of vehicle control, attitudes, systems, and engine thought to be most indicative of the pilot's control and performance. This information

was needed to permit the evaluation of operational pilot tasks and system performance in lieu of imposing a secondary task. The choice of these parameters resulted from an extensive task analysis specific to the YF-12 airplane and associated missions. A different set of parameters is likely to result when different aircraft, missions, or both are considered.

In this study it had to be recognized that the crew operations were already established. The aircraft, the test program, the crews, the missions, and the tests were given. The task at hand was to learn how the operations were conducted, and how to develop quantitative and qualitative measures of crew performance.

The Pilot's Duties

As aircraft commander, the pilot is ultimately responsible for flight planning and execution. He maintains the aircraft attitude and airspace position in a specified mission profile. He divides his attention between attitude and position instruments, outside visual references, and air traffic in the maintenance of attitude and position. To follow the mission profile precisely, he must monitor and adjust all aircraft systems for normal and emergency conditions. In the performance of a test maneuver, he establishes the pretest conditions for the aircraft systems, attitude, and position. During the tests, he alters aircraft systems, attitudes, and positions in the prescribed way. Upon recovery to a posttest condition, he reestablishes pretest conditions or proceeds to a point in the flight profile for the next test. The pilot also is required to monitor such housekeeping items as fuel, center of gravity, oxygen suit, and environment. In terms of communications, he is responsible for contact with the flight test engineer (FTE), control tower, ground radar, the chase pilot, the tanker boom operator, and other air-to-air communications. He shares responsibility with the FTE for communications with ground control, the tanker commander, air traffic centers, and other flight test supporting units on the ground.

Flight Test Engineer's Duties

Despite the ultimate responsibility of the pilot for the mission, a flight could not be successfully completed without the full-time participation of the flight test engineer. One of his primary duties is navigation. He is responsible for setting up, monitoring, and updating all navigation equipment en route. He provides the pilot with headings and distances to checkpoints and turns; he takes tactical air navigation (TACAN) fixes and communicates with air traffic centers and ground control for clearances and confirmation of position fixes.

The FTE assists the pilot in timing and maintaining the flight profile. He provides the information the pilot needs before, during, and after the test. He signals the start of the test and intermediate event points during and at the end of a test, or both. He records his own and the pilot's parametric observations before, during, and after each test.

From entry into the cockpit to leaving the cockpit he performs all checklist items of procedures; he also serves as a source of detailed information concerning subsystem operations. He monitors fuel consumption and computes the center of gravity to check the semiautomatic-to-automatic center of gravity computation during flight.

The FTE observes, communicates, and records all unusual events such as turbulence and unstarts. He shares responsibility with the pilot for communication with ground control, the tanker and commander, air traffic centers, and other flight test support units on the ground.

DEVELOPMENT OF MEASUREMENT DATA SETS

Mission and task analyses were made to establish measurement requirements. All subsystem functions and maneuvers were included, and critical tasks were analyzed in more detail, using timeline analysis techniques. Data collection procedures were examined, and a prototype data reduction and processing system was developed.

Human Performance Measurement

There are at least five ways to acquire information about human performance: system performance, secondary task workload, physiological activity, pilot control models, and statements of subjective opinion.

System performance measurements.—System performance measurement includes the comparison of all system and subsystem parameters with mission requirements. Such comparisons are often most relevant to the solution of system design problems, but are perhaps only obliquely related to human performance, since system performance reflects the combined performance of human and machine. System performance measurement may be a necessary part of the total measurement set, but it is not likely to be sufficient in and of itself.

Secondary task workload measurement.—A common measurement technique for the purpose of workload assessment calls for the measurement of performance on an added secondary task; the human operator is instructed to attend to the secondary task only to the degree that performance on the principal, or primary, task will permit. Measurement of the performance of only the secondary task indicates the level of performance for an unloaded operator; poorest performance on the secondary task (no attention given to it) may indicate the level of performance for a completely loaded operator. In this way, a workload scale can be constructed that indicates the percentage of loading of an operator with a given primary task. Unfortunately, the secondary task may interfere with the performance of the primary task, that is, the human operator may adopt a strategy for performing both tasks simultaneously in a way which is no longer relevant to the study of the primary task. Further, in such operational settings as the YF-12 airplane, a secondary task may compromise flight safety. Nevertheless, it may be possible to employ the secondary task concept. For example, in some circumstances the control of aircraft pitch attitude may be considered the primary task, and roll control may be considered the secondary task; under heavily loaded situations the pilot may be able to prevent pitch performance from deteriorating only if roll control is sacrificed (therefore, pitch control would indicate the presence of a high degree of operator loading). This and other adaptations of the secondary task measurement concept may be suitable for measurement in the YF-12 flight test

program. As a rule, in an operational setting, measurement must be accomplished on subordinate tasks embedded in the normal task structure.

Physiological parameter measurement.—As the human operator can often maintain a fixed level of performance until the actual point of overload, it was felt that an earlier indication of loading might be obtained through physiological measurement. Many physiological parameters have been measured in relation to human work capacity and reserve. However, this study was confined to a consideration of electrocardiograph (ECG) signals. Recent literature has related heart rate variability to mental workload (refs. 4 to 6). Heart rate variability, often termed sinus arrhythmia, is a variation in the time interval between successive heart beats. The variability has been shown to decrease when a subject is given a mental task and to increase when the subject is not noticeably occupied; however, some variation is also attributable to dynamic and static physical workload, respiration rate, emotion, and age. The evidence is so encouraging that sinus arrhythmia measurement must be considered a candidate for measurement system development.

Pilot control model measurement.—A significant aspect of the pilot's duties is the direct manual control of the aircraft. The manner in which the pilot controls various parameters can be mathematically modeled in a manner consistent with total vehicle control analysis. One form of mathematical model can be derived from spectral analyses of the input information to pilot's display and pilot's control signals. Depending on the nature of the control task, such a model may have from one to four parameters. These parameters vary as pilot control performance levels change, and in particular as the nature of pilot control changes. For example, from such a model, the pilot's gain or sensitivity is apparent, and also the degree to which course changes and smoothing disturbances are anticipated. In short, the manner in which the pilot controls is quantified so that changes in control activity may be apparent even though the level of performance error in relation to mission requirement does not change. Such modeling should, therefore, be considered for part of the preliminary candidate measurement set.

Statement of subjective opinion.—The pilot is the only available source of some kinds of information, and information may be volunteered by the pilot or crew which the investigator would not have known to ask about. Subjective opinion is perhaps the easiest of all information to obtain, but it is difficult to obtain in quantitative form. Perhaps the most widely known technique for the quantification of pilot opinion of vehicle handling qualities is the Cooper-Harper scale.

The flight crew may be the best, and it is sometimes the only source of some types of information, such as details of the crew tasks, task performance criteria, the nature of performance tradeoffs, the dimensions of task difficulty, and unplanned or unmentioned flight events. Examples of such subjective data are shown in figure 1. At the suggestion of the crew, the events in any flight were classified into four workload categories: communications, vehicle control, time sharing, or busy (induced by flight stresses). The crew identified instances of most, routine, or least workload during each monitored flight. They also offered comments on specific events as they happened and the time when each occurred. Subjective measurement, then, must be considered in the attempt to create a comprehensive measurement set.

Audio and Time Recording

In the flight test setting, completed performance measures are meaningful only if the exact times and conditions of the events are known. Many events and their corresponding times can be gleaned only from adequately transcribed and timed communication recordings (flight test engineer's log, flight test engineer-to-pilot intercom, and crew-to-ground).

PHYSICAL AND NONPHYSICAL WORKLOAD CORRELATION TECHNIQUES

Flight Tests

This early study gave some indication of what was possible in the way of performance measurement of the crew of a high performance aircraft. Unfortunately, the major question was still unanswered: How can a measurement of nonphysical workload be extracted from ECG, the single available physiological parameter? As suggested above, as this study was concluding, new literature appeared which suggested that sinus arrhythmia was a reliable indicator of nonphysical workload. Since this literature was the product of several independent researchers, the schemes devised to score the amount of level of arrhythmia varied widely. When examined, the only measure which produced consistent results was standard deviation. NASA's programing efforts were therefore directed towards producing a computer program to determine the sensitivity of variation statistics, especially standard deviation, to nonphysical workload. Data reduction limitations at DFRC prevented the digitization of early YF-12 physiological data. While this problem is being resolved, the concepts were applied to data from some of DFRC's remotely piloted research vehicle programs.

The normal human ECG is a tracing of an electric potential function driving a muscular pump. As with any pump, the activity is cyclic and the driving function must be basically rhythmic. Left to itself, this rhythmic function would seem to originate in a free-running oscillator with a relaxed regulatory system. Under no other load than basic life sustenance, an average resting heart rate, on a minute-by-minute basis, remains fairly constant. If examined closely by measuring the interval between each beat and calculating the heart rate for that interval, a wide variation becomes evident. As either physical or nonphysical workload (or both) increases, this variation dramatically decreases, almost as if the oscillator becomes more stable under stress.

DFRC had developed a method for obtaining ECG under a wide variety of human activities. Originally intended to collect the ECG in analog form aboard high performance aircraft, the method and equipment have proved adaptable to the collection of physiological data in digital form. The data are transmitted directly to ground-based computers as in the remotely piloted vehicle program, or to in-flight recorders, as used on the YF-12 airplane. What happens to the heart's cyclic activity during a time of nonphysical flight stress is shown in figure 2. These data were taken during a remotely piloted flight of the 3/8-scale F-15 airplane. In this series of flights a scale model of the F-15 with full onboard avionics and a single forward-looking video camera for visual data was dropped from beneath another

aircraft and flown through unpowered maneuvers to a lakebed landing. The pilot performing these maneuvers was on the ground in the remote piloting facility. The top graph shows heart rate as a 15-second average; that is, each point is an average of the instantaneous rate of every beat occurring in the preceding 15 seconds. There is the gradual climb to launch, a dramatic jump at launch, and a decline after drogue chute deployment. The bottom graph shows one method of displaying heart rate variability. Over the same 15-second intervals discussed above, the instantaneous rates of each beat are compared to find the minimum and maximum in milliseconds. The difference between these two measures is found and plotted against the same time scale as used in the top graph. The variation in these numbers is wide throughout most of the flight, and the variation is very small during the portions most demanding of the pilot.

Clinical Tests

Since both physical and nonphysical workloads have stabilizing influences on the function generator, it is important to know how much influence each has. A series of clinical tests is being constructed to attempt to separate these factors. In these tests, the pilots at DFRC and some volunteers from the employee population are to be tested in the DFRC stress physiology laboratory. First, heart rate variability is to be measured under carefully quantified physical workloads. Then, on the assumption that nonphysical workload can be adequately simulated by increasing demands on the subject's information-processing capability, a simple decision task with minimal physical involvement is being devised. If an individual's saturation point under nonphysical demand can be successfully measured, the two tasks can be combined and the total effect, including any synergism, can be measured.

YF-12 Cold Wall Tests

As of this date, data handling techniques have evolved to a reliable stage. A physiological indicator of nonphysical workload has been developed but requires proof. The YF-12 test missions have recently included the type of scheduled partitioning of flight (cold wall experiments) which have shown the most pronounced ECG variability on other programs. During these flights, the aircraft had to be maneuvered to a precise point in space and had to maintain a specified altitude and airspeed through the experiment. At the moment when all conditions were met, a pod suspended below the aircraft was blown open, uncovering a cryogenically cooled cylinder. As might be expected, this greatly disturbed the airflow about the aircraft, which occasionally disturbed the pilots.

Some preliminary results from these flights are shown in figure 3. This started out as a sequential histogram, that is, the rate at which each heart beat occurred was plotted sequentially against time for a period which began just before the cold wall experiment and ended about 10 minutes after it. For the figure as shown, a line was drawn through the minimum and maximum points to create a graphic envelope of heart rate. Again, the variability narrows dramatically as the cold wall test approaches. Figure 4 shows the same data presented in a manner similar to the remotely piloted vehicle data discussed above.

ONGOING RESEARCH: THE YF-12 AIRCRAFT AS A RESEARCH VEHICLE

The initial study demonstrated a potential measurement system for workload comparisons and indicated the direction further research might take towards the development of a complete theory of flight workload. The YF-12 aircraft is nearly ideal for the study of pilot workload. The measurements that can be produced are not likely to be exceeded in a laboratory or simulated environment; in fact, the simulation of the YF-12 environment is not within the current state of the art. Therefore, the continued use of the workload measurement system during the conduct of the ongoing YF-12 program is recommended.

Electrocardiograph Recordings

Information to be collected from the aircraft, engines, and avionics is listed in table 1. This information supports the measurement of pilot tasks and system performance. The large number of recorded measurements is a direct result of the extensive task analysis made on this class of vehicles and the projected flight test missions. A different set of parameters is likely to result when different aircraft, missions, or both are considered.

Audio and Time Recordings

In the flight test setting, most applications of computed measures depend on knowing the times and the conditions corresponding to measured performance. Many events and their corresponding time can be gleaned from the flight test engineer's log, but some are not available from this source. The primary source of information is the set of communication recordings after careful transcription and timing.

Subjective Measures

Subjective measures depend on direct access to the crew's knowledge, opinions, and ratings through postflight interview sessions in addition to information obtained from flight briefings and debriefings.

Minimum Parameter Set

The minimum parameter set consists of the ECG recordings, the parameters listed in table 1, communications recordings, and crew interviews. Other information relevant to the conduct of an experiment is to be obtained from briefings, debriefings, and flight monitoring.

The YF-12 airplane is an excellent stressor for the human operator. This research with it may help to establish a quantifiable measure of workload, and, perhaps, a system saturation point. Overloaded systems suffer breakdowns; when the system includes human operators, the cost of breakdown may be measured in lives.

REFERENCES

1. Bioastronautics Data Book. NASA SP-3006, 1964.
2. Roman, James; Perry, John J.; Carpenter, Lewis R.; and Awni, Shaiban A.: Flight Research Program — VI. Heart Rate and Landing Error in Restricted Field of View Landings. Aerospace Medicine, vol. 38, no. 2, Feb. 1967, pp. 128-132.
3. Roman, James: Risk and Responsibility as Factors Affecting Heart Rate in Test Pilots. The Flight Research Program — II. Aerosp. Medicine, vol. 36, no. 6, June 1965, pp. 518-523.
4. Kalsbeck, J. W. H.: Sinus Arrhythmia and the Dual Task Method in Measuring Mental Load. Measurement of Man at Work; an Appraisal of Physiological and Psychological Criteria in Man-Machine Systems, W. T. Singleton, J. G. Fox, and D. Whitfield, eds., van Nostrand Reinhold Co., 1971, pp. 101-113.
5. Rohmert, W.; Laurig, W.; Phillip, U.; and Luczak, H.: Heart Rate Variability and Work-Load Measurement. Ergonomics, 1973, vol. 16, no. 1, pp. 33-44.
6. Mulder, G.; Mulder, W. R. E. H.; and van der Meulen, Hajonides: Mental Load and the Measurement of Heart Rate Variability. Ergonomics, 1973, vol. 16, no. 1, pp. 69-83.
7. Muckler, Fred; Obermayer, Richard W.; and Nicklas, Douglass R.: Pilot Performance Measurement Study — Final Technical Report. NASA CR-143842, 1977.

TABLE 1.—AIRCRAFT PARAMETERS

Spike position
Forward bypass position
Aft bypass position
Engine
Coarse pitch rate
Fine pitch rate
Coarse roll rate
Fine roll rate
Coarse yaw rate
Fine yaw rate
Pitch attitude
Roll attitude
Center-of-gravity normal acceleration
Center-of-gravity lateral acceleration
Duct pressure ratio
Right rudder position
Longitudinal stick position
Lateral stick position
Event
Right power lever position
Left power lever position
Computed angle of attack
Computed angle of sideslip
Altitude
Inlet system condition
Spike tip total pressure
Time (hr, min, sec, msec)

FLIGHT 015 CREW POS. Pilot

BUSY, TIME-SHARING

Least/Most	Time	Nature of Event/Comments
Routine	102045-102400	TP #1
Most	102400-102800	TP #2 - Off schedule on α ; missed sideslip points; four times as difficult
Routine	102900-103300	Item 10
Most	114850-115600	TP #5 - Busy (also an unstart at 115508)

VEHICLE/EQUIPMENT CONTROL DIFFICULTY

Most	102400-102800	TP #2 - (See explanation above).
Most	103328 - 103800	Items 11 & 27 - difficult to
	120310 - 120800	control
Least	104018 - 104435	TP #3 - Easy (used autopilot)
Most	121136 - 121155	TP #6 - Wasn't satisfied with 1st one (performed again); had trouble on 1st one with trim; had autopilot on and was cross- controlling against it.
Least	121520 - 122300	TP #7 - Used autopilot; went well (flt eng. did not turn tape on until 122137)
Least	122500 - 122900	Did another TP #2 - "Went real well"

Figure 1.—Subjective data.

FLIGHT 015 CREW POS. Pilot

COMMUNICATION

Least/Most	Time	Nature of Event/Comments
Most	121630 - 122900 (get more off tape)	Went well - no saturation
		except
		Trying to get in touch with
		NASA southbound off of second
		loop

STRESSFUL

Most	110206 - 110648	Item 15 & 16 - trying to find the tanker
Most	104556 - 104915	TP #4 - know you're going to get an unstart - but don't know when or how bad (unstart about 104840)
Most	115022 - 115600	TP #5 - Looking for unstarts (unstart 115508)

Figure 1.—Concluded.

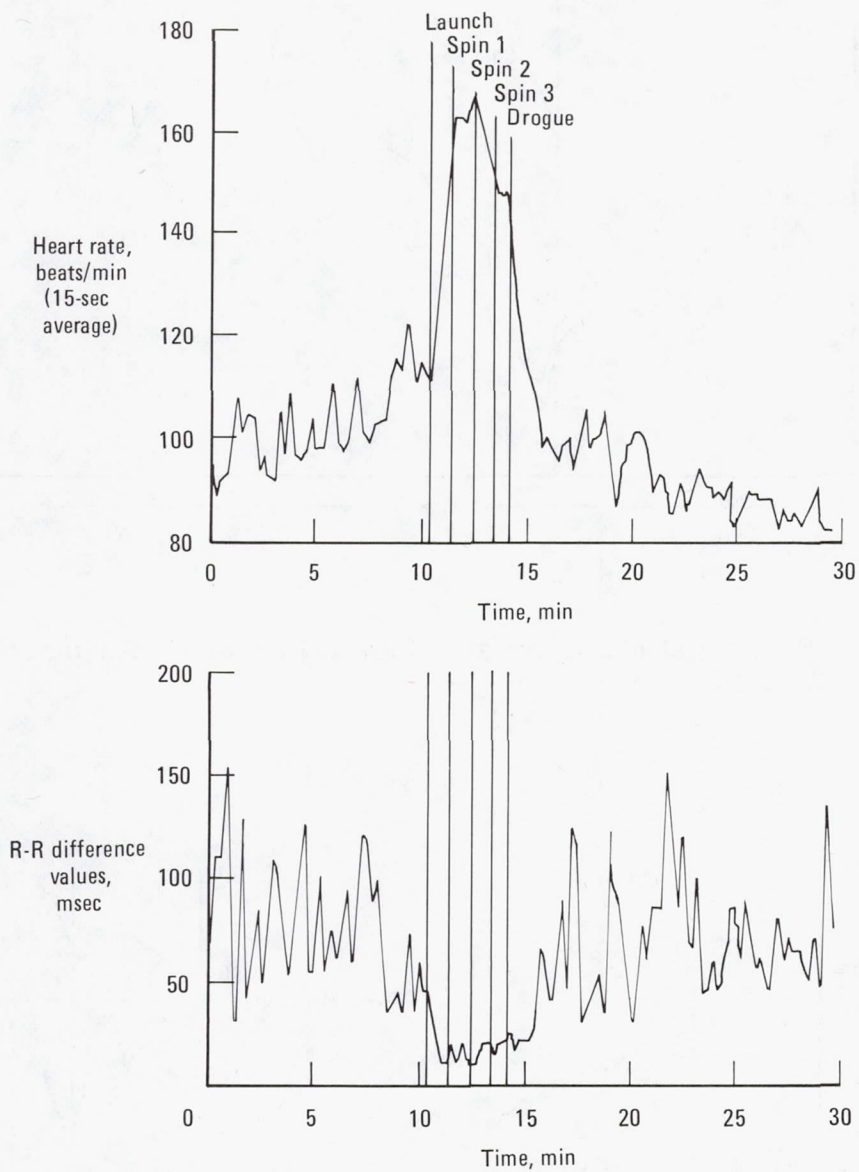


Figure 2.—Electrocardiograph data from the F-15 remotely piloted vehicle.

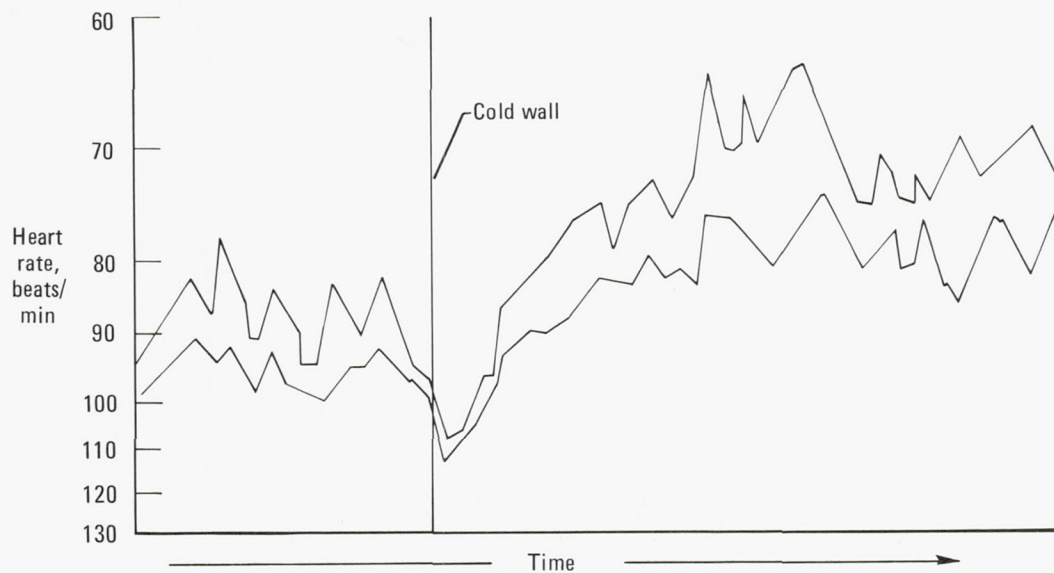


Figure 3.—Sequential histogram showing ECG envelope during cold wall experiment.

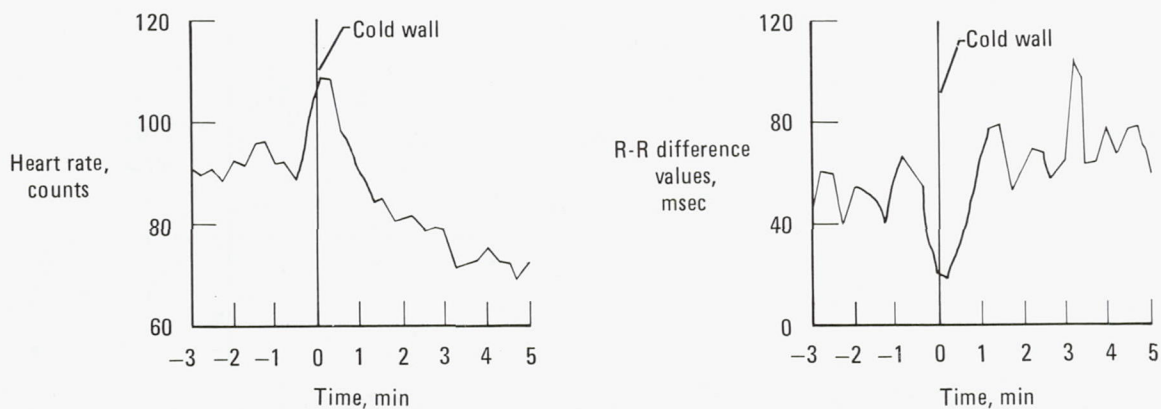


Figure 4.—Electrocardiograph data from YF-12 cold wall experiment showing R-R variation.

THE YF-12 GUST VELOCITY MEASURING SYSTEM

L. J. Ehernberger
Dryden Flight Research Center

SUMMARY

A true gust velocity measuring system designed to alleviate complications resulting from airframe flexibility and from the high-speed, high-temperature environment of supersonic cruise aircraft was evaluated on a YF-12 airplane. A unique feature of the system is the use of fixed vanes on which airflow direction changes produce differential pressure variations that are measured. Airframe motions, obtained by postflight integration of recorded angular rate and linear acceleration data, are removed from the flow angle data.

An example of turbulence data obtained at high-altitude, supersonic flight conditions is presented. Comparisons are made with previous high-altitude turbulence measurements obtained with subsonic aircraft and with turbulence criteria contained in both military and civil design specifications for supersonic cruise vehicles. Results of these comparisons indicate that the YF-12 turbulence sample is representative of turbulence present in the supersonic cruise environment.

INTRODUCTION

Turbulence characteristics in the supersonic cruise environment have been measured by subsonic aircraft up to an altitude of 22 kilometers. References 1 to 3 present subsonic aircraft data for true gust velocity measurements and for derived equivalent gust velocities based on airplane gust acceleration loads. These data have been verified to a limited extent by supersonic measurements reported in references 4 to 6. However, as supersonic airframe and system designs become more refined, the need arises to obtain true gust velocity measurements to evaluate the effects of turbulence on aircraft and flight systems designed to operate in the supersonic flight environment (ref. 7).

A variety of instrument configurations has proven practical for gust measurements on subsonic aircraft. However, the gust velocity errors due to flow angle measurement errors increase in direct proportion to speed. Therefore, the angular resolution requirements for supersonic cruise measurements are increasingly more stringent as the flight speed increases. Additional complications are also encountered in the separation of sensor motions due to aircraft maneuvering from the gust flow

direction measurements. This is due to the combined effects of structural flexibility and the higher flight speeds.

In general, the magnitude of airframe bending is greater at the lower frequencies. At high speeds, the structural frequencies are superimposed on longer gust wavelengths having greater turbulent energy. This contrasts with conditions encountered in subsonic flight, where significant bending is usually limited to the shorter gust wavelengths with less turbulent energy and with highly repeatable spectral patterns. Thus, at supersonic cruise conditions, the measurement of airflow motion at the structural bending frequencies requires the use of sensors having greatly improved amplitude resolution and phase matching capabilities. An additional complication results from aerodynamic heating which can deteriorate the performance of movable, low-inertia flow direction vanes at the higher Mach numbers (ref. 6). The presence of heating also requires special consideration in the selection and installation of transducers.

A true gust velocity measurement concept designed to alleviate these complications is being evaluated in the supersonic cruise environment using the YF-12 airplane. This report describes the system used to obtain measurements of longitudinal, vertical, and lateral components of gust velocity. It also presents a preliminary example of turbulence data obtained during supersonic cruise at approximately 19.8 kilometers altitude. These data are compared with measurements obtained with subsonic aircraft and with turbulence criteria contained in current civil and military design specifications applicable to supersonic cruise vehicles.

SYMBOLS

Physical quantities in this report are given in the International System of Units (SI).

a_x	lateral acceleration
a_y	longitudinal acceleration
a_n	vertical acceleration
C_{p_α}	pressure coefficient for gust vane angle of attack
C_{p_β}	pressure coefficient for gust vane angle of sideslip
l_x	linear longitudinal distance from gust vane to reference instruments
l_y	linear lateral distance from gust vane to reference instruments
l_z	linear vertical distance from gust vane to reference instruments
M	free stream Mach number
p	roll attitude angular rate

p_{dl}	differential pressure between the dog-leg total pressure source and p_{t_2}
p_{t_2}	measured nose boom total pressure
p_α	differential pressure between lower and upper ports of the angle-of-attack vane
q	pitch attitude angular rate
q_∞	incompressible dynamic pressure
R_t	ratio of dog-leg total pressure to p_{t_2}
r	yaw attitude angular rate
u	longitudinal gust velocity
V	true airspeed
v	lateral gust velocity
w	vertical gust velocity
\dot{z}	airplane vertical velocity (positive down)
α	free stream angle of attack
β	free stream angle of sideslip
Δ	incremental change
θ	pitch attitude
ϕ	roll attitude

INSTRUMENTATION

The primary components of the true gust velocity system are the sensors used to measure airflow angle changes and true airspeed variations. Differential pressures across four fixed-flow direction vanes near the base of the nose boom are used to determine airflow direction. The vanes are arranged in a cruciform configuration, as shown in figure 1. Two of the vanes independently measure angle of sideslip, while the remaining two vanes independently measure angle of attack. This configuration provides measurement redundancy and minimizes asymmetric aerodynamic interference between the vanes.

The vanes are constructed of stainless steel in a triangular planform. They have a leading edge sweep angle of 66.5° and a thickness of 3.18 centimeters. Each vane is tapered with a 30° semiwedge angle (fig. 1(c)) to prevent oblique shock attachment. This enhances its pressure sensitivity to flow angle changes at high Mach numbers.

Figure 1(c) shows the slotted pressure sources on either side of each vane. The differential pressures across each of the vanes are measured by transducers located in the nose section of the aircraft. Insulation and air conditioning are used to maintain instrument temperatures below 313 K. The sensitivity of the vane differential pressure is also increased by the wing-body effect of the vanes attached to the boom. Positioning the vanes near the base of the boom avoids interference with the airplane's flow direction sensor and static sources located on the forward portion of the boom. It also minimizes the length of tubing and resulting pressure lag so that phase and amplitude errors are negligible below about 20 hertz.

In addition to gust inputs, the measured flow direction is also a function of the motion of the fixed vane and its nose boom mounting. Translational and rotational inputs are sensed with three-axis linear accelerometers and angular rate gyros aligned to the nose boom axis and mounted adjacent to the vane pressure sensors.

Although normally it would have been desirable to use the nose boom pressure source to determine longitudinal gust velocities, the length of the YF-12 nose boom would have caused excessive tubing lag. It was not possible to install a transducer in the forward portion of the boom since all available space was already occupied by tubing used for the primary airplane instruments. However, even if space had been available, the elevated temperatures present in the boom during high-speed flight made the location unsuited for transducer use. Therefore, the longitudinal gust velocity was sensed by means of a dog-leg pitot probe that was attached to the lower surface of the nose, approximately 3.5 meters aft of the nose boom (fig. 2). A differential pressure transducer using the nose boom total pressure as a reference measured the local pitot pressure at the probe. Using the dog-leg pitot probe, the length of the pitot lines was kept to less than one meter. This provided good frequency response up to approximately 20 hertz and permitted the transducer to be installed in the air conditioned instrument compartment in the nose of the aircraft.

To avoid phase errors and minimize mechanically induced signal errors, sensor dynamic characteristics were carefully scrutinized in the selection process. Resolution and phase errors were also minimized using a special 13-bit analog-to-digital encoder. Signals digitized by the encoder were synchronously read and recorded in each PCM time frame. The data acquisition system acquired each parameter measurement at the rate of 200 samples per second. Parameter characteristics are provided in table 1.

Auxiliary data parameters used in the gust calculations included airplane Mach number, airspeed, altitude, free stream ambient temperature, roll attitude, and pitch attitude. The instruments and systems used to measure these parameters are described in references 8 and 9.

DATA ANALYSIS PROCEDURES

Lateral and Vertical Gust Velocities

The true gust velocity calculations were based primarily on the angle-of-attack and angle-of-sideslip changes caused by the turbulence. The measured flow angles were corrected for aircraft motion and then the gust time history was calculated by multiplying the sine of the incremental flow angle by the true airspeed. To accomplish this, the gust vane pressure data were first normalized to coefficient form and converted to flow angle information. The gust vane flow angle pressure coefficients were obtained using the incompressible dynamic pressure, q_∞ , as shown in the following equation:

$$C_{p_\alpha} = \frac{p_\alpha}{q_\infty} \quad (1)$$

where C_{p_α} is the gust angle-of-attack pressure coefficient and p_α is the differential pressure between the lower and upper sources of the angle-of-attack vane. Calibration of the gust vane pressure coefficients in terms of airplane free stream flow direction was accomplished by fitting data obtained for in-flight maneuvers at several Mach numbers using fifth order polynomials. The polynomial curves resulting from the calibration maneuvers for the Mach number range from 2.2 to 2.8 are shown in figure 3(a).

To calculate the lateral and vertical gust velocities, the flow angle changes and rates were corrected for angular attitude changes and rates as shown by the equation for the vertical gust component, w .

$$w = V \sin \left[\left(\Delta\alpha + \frac{q}{V} l_x - \frac{p}{V} l_y \right) \cos \varphi + \left(\Delta\beta - \frac{r}{V} l_x - \frac{p}{V} l_z \right) \sin \varphi - \Delta\theta \right] - \Delta\dot{z} \quad (2)$$

The angular rate effect on the flow angles was removed by using the measured roll, pitch, and yaw attitude rates, p , q , and r , respectively. The true airspeed, V , and the linear distances from the reference instruments, l_x , l_y , and l_z , measured along the longitudinal, lateral, and vertical axes were used in the form $\frac{q}{V} l_x$, as shown in equation (2). Next, the incremental flow angles, $\Delta\alpha$ and $\Delta\beta$, were resolved into components along the earth reference axes using the sine and cosine functions of the nose roll attitude, φ . To complete the vertical gust velocity calculation, the incremental pitch attitude changes, $\Delta\theta$, were subtracted from the incremental earth referenced angle of attack. The sine of the resulting angle was multiplied by the true airspeed, and the incremental vertical translation velocity, $\Delta\dot{z}$, was subtracted from the resulting term.

The nose roll attitude, φ , used in the gust velocity equation, was obtained by transforming the airplane inertial platform attitude data from airframe reference coordinates to the nose boom axes. Frequency-response and phase shift problems associated with direct attitude measurements were circumvented by integrating

angular rate data from a special high response, low drift gyro to obtain the incremental pitch and yaw attitude changes of the gust vanes. The rate data were first transformed to earth reference coordinates and then integrated. Incremental vertical and lateral translation velocity changes were determined in a similar manner. The linear acceleration measurements were corrected for the earth's gravitational component and transformed to earth referenced coordinates using the inertial platform attitude data. Then, after the mean values of each component were determined and removed to minimize drift, the data were integrated to obtain the velocity changes.

Longitudinal Gust Velocity

The longitudinal component of gust velocity was obtained by using the ratio of the local total pressure at the dog leg to the nose boom total pressure. In equation form this is given by

$$R_t = \frac{p_{dl} + p_{t_2}}{p_{t_2}} \quad (3)$$

where the differential pressure measured between the dog leg and the nose boom is designated as p_{dl} and the nose boom total pressure is designated p_{t_2} . At supersonic

Mach numbers, R_t becomes sensitive to angle of attack, so a correction was applied.

The correction increased linearly with C_{p_α} and with the parameter $\sqrt{M^2 - 1}$, where

M is the free stream Mach number. A Mach number which includes the gust input was obtained from the corrected R_t by means of a fifth order polynomial determined from flight data for Mach number acceleration and deceleration runs. The polynomial curve for the Mach numbers from 2.0 to 2.8 is shown in figure 3(b). This Mach number, which is responsive to gusts, was then multiplied by the speed of sound to give the true velocity units. The longitudinal gust velocity time history was then computed using first order regression analysis to remove the mean value and the trend from the true airspeed time history.

In contrast to the airplane reference used for longitudinal velocity, the lateral and vertical velocity components were resolved into earth referenced components as described. Differences due to the referencing convention were negligible for the gust data presented because airplane attitude and ground speed changes were minimal. However, the differences would be significant in the case of maneuvering flight.

Statistical Analyses

Spectral and statistical analyses of the data were used to eliminate errors caused by electrical transients in the instrumentation or by bit errors accumulated during the recording and processing of the digital data. This was accomplished by screening parameters of interest for sample-to-sample changes that were larger than values which were specified to discriminate between physically realistic measurement changes and extraneous data points. When found, such values were replaced with

the last valid data value. While this procedure did not restore the true values to the time history data, it did eliminate significant spectral and statistical distortion from most data records.

The spectral and statistical analyses were accomplished by a library program which uses a fast Fourier transform. The analysis routine included detrending the parameters and filtering with a fourth order Butterworth filter having a 3-decibel break point at 16 hertz. As with the spike removal, the detrending and filtering eliminated unwanted spectral content that would have otherwise concealed gust or transient spectral phenomena of interest.

RESULTS AND DISCUSSION

To illustrate the type of turbulence data encountered on the YF-12 flights, one of the stronger turbulence encounters was selected. This encounter, rated as having a light-to-moderate intensity by the aircrew, occurred during a deceleration from Mach 2.75 to Mach 2.69, between altitudes of 19.8 and 19.9 kilometers. A steady wings level condition was held throughout the encounter and the pitch attitude change was less than 0.3° . The longitudinal, lateral, and vertical gust velocity time histories were obtained using calculations previously described and are shown in figure 4. Their intensity appears to be stationary in a statistical sense; however, at the lower frequencies or longer wavelengths, the longitudinal component exhibits noticeably stronger quasi-periodic variations than do the lateral and vertical components.

Probability density plots for these data may be compared to normal probability density functions having the same mean and variance values, as shown in figure 5. It was assumed that the deviations from the plots of the normal curves were due to the relatively short record length.

The power spectra shown in figure 6 were obtained using eight degrees of freedom and a seven-point Hann-Tukey smoothing window. The relatively higher spectral density amplitudes of the longitudinal component at long wavelengths are indicative of the quasi-periodic long period characteristics noted in the time histories. The differences in the spectral densities of the component gust velocities at the longer wavelengths also significantly influence the comparison of the component root-mean-squared (rms) velocities. The rms velocity for the total spectral range was 2.15 meters per second for the longitudinal component in contrast to rms gust velocities of about 1.21 and 1.16 meters per second for the lateral and vertical components. However, for the spectral range limited to wavelengths less than 667 meters, which was selected for comparison with other data, the rms velocities for the three components were close, with 0.82 meter per second for the longitudinal component compared to 0.67 and 0.83 meters per second for the lateral and vertical components. Thus, both the rms gust velocities and the spectral density properties are important measures of the turbulence intensity.

Inaccuracies in the gust data may be attributed to three sources: system noise errors, dynamic matching and response errors, and calibration inaccuracies. Although a thorough analysis of the errors present in the preliminary data sample has not yet been completed, preliminary studies of the data for several turbulence

encounters indicate that the rms noise level is probably on the order of 0.2 meter per second or less. Over the measurement ranges used, calibration precision of the fast response Mach number and flow direction sensors is high relative to the basic airplane Mach number and flow angle measurements. However, the gust sensor calibrations are nonlinear and gust measurement accuracy can be affected by slope changes occurring within small measurement ranges. In addition, instrument drift may not be linear with time and thus may not be completely eliminated by subtracting the mean values or by detrending. The combination of calibration and drift errors are estimated to cause about 10-percent error in the measured gust velocities. Resultant rms gust velocity errors in the preliminary data appear to be on the order of 0.3 to 0.4 meter per second.

The intensity of the preliminary YF-12 turbulence data was compared to previous data obtained using subsonic aircraft and to intensity factors contained in established design criteria. Presented in figure 7 are the widely depicted examples of clear air turbulence, cumulus turbulence, and thunderstorm turbulence (ref. 10). For comparison, the spectral density amplitudes for the vertical, lateral, and longitudinal time histories for the YF-12 data are indicated by shaded regions on the figure, which can be seen to lie close to the amplitude of the clear air turbulence (ref. 10) based on lower altitude measurements.

Reference 11 contains the probability distributions for the rms gust velocities for wavelengths less than 667 meters obtained from the HICAT (high altitude clean air turbulence) project using the U-2 airplane at altitudes between 14 and 22 kilometers. Data from the U-2 measurements indicated a 1.0-percent probability for rms gust velocities of 0.65, 0.69, and 0.59 meters per second or greater (longitudinal, lateral, and vertical). The same data indicated a 0.1-percent probability for rms gust velocities of 1.12, 1.15, and 0.96 meters per second or greater in the same axes. For the YF-12 turbulence sample, the measured longitudinal, lateral, and vertical rms gust velocities were 0.82, 0.67, and 0.83 meters per second. This comparison is shown in tabular form below:

HICAT probability, percent	Rms gust velocity, m/sec (wavelengths < 667 m)		
	u	v	w
1.0	0.65	0.69	0.59
0.1	1.12	1.15	0.96
YF-12 data	0.82	0.67	0.83

During the HICAT project less turbulence was experienced at altitudes near 20 kilometers than at altitudes below 19 kilometers; therefore, the rms gust velocities from the HICAT data are probably greater than they would have been had they been obtained only at the altitude of the YF-12 sample. Thus, based on the reference 11 data, the probability of encountering turbulence equal to or greater than the intensity of the YF-12 sample at 19.8 kilometers altitude is estimated at about 0.1 percent or less.

A similar comparison may be made between the intensity of the high-altitude turbulence sample and current turbulence design criteria for civil and military aircraft. For nonstorm turbulence at altitudes corresponding to that of the YF-12 sample, reference 12 specifies that turbulence having an rms gust velocity of 1.05 meters per second will be present 0.09 percent of the time. This is close to the estimated 0.1-percent probability values for measured YF-12 intensities having an rms vertical gust velocity over the total spectral range of 1.16 meters per second.

The military specification (ref. 13) establishing intensity design criteria for the YF-12 flight level is essentially the same as the civil specification. However, reference 13 also specifies discrete gust magnitudes as a function of normalized discrete gust length for the simulation of gusts or ramps having a "one-minus-cosine" shape. The magnitudes specified increase with wavelength to a maximum peak-to-peak value of 5.2 times the rms gust velocity. A comparison of the specification values with maximum peak-to-peak values contained in the YF-12 time histories (fig. 4) is shown below:

Gust velocity component	Rms gust velocity, m/sec	YF-12 peak-to-peak value, m/sec	5.2 criteria peak-to-peak value, m/sec
Longitudinal	2.15	7.0	11.2
Lateral	1.21	5.8	6.3
Vertical	1.16	4.9 to 9.7	6.0

The observed maximum amplitudes generally fall within the reference 13 criteria, as would be expected for the nominally short time histories. The higher value for the YF-12 vertical component had large velocity excursions in both the positive and negative directions, as shown at 9.3 seconds in figure 4. This is characteristic of a vortex core associated with a breaking wave and, in such cases, where turbulence is originating, neither the reference 13 criteria nor any other ensemble process statistics could be expected to apply precisely for homogeneous turbulence.

On the basis of the comparisons between the gust velocities of the YF-12 turbulence sample and those of references 11 to 13, it can be concluded that the intensity of the YF-12 sample is strong and, therefore, can appropriately represent high-altitude turbulence for supersonic cruise aircraft system response studies.

CONCLUDING REMARKS

A preliminary sample of gust data obtained using the YF-12 airplane has demonstrated the feasibility of using fixed, differential pressure flow vanes for turbulence measurements in the high-speed flight environment. The turbulence measurement system design considered the dynamic response of the instruments necessary to accurately sense the reference motion of the instrument platform as well as to accurately sense the free stream turbulence inputs. Spectra of the preliminary turbulence time histories indicate that system characteristics are adequate over a frequency range from less than 1 hertz to greater than 10 hertz, a

range which covers most of the turbulence inputs and aircraft system responses of interest. Comparisons with current design criteria and previously obtained data indicate that the intensity of turbulence measured by the YF-12 airplane is representative of strong high-altitude turbulence and is appropriate for use in system response studies for the supersonic cruise environment.

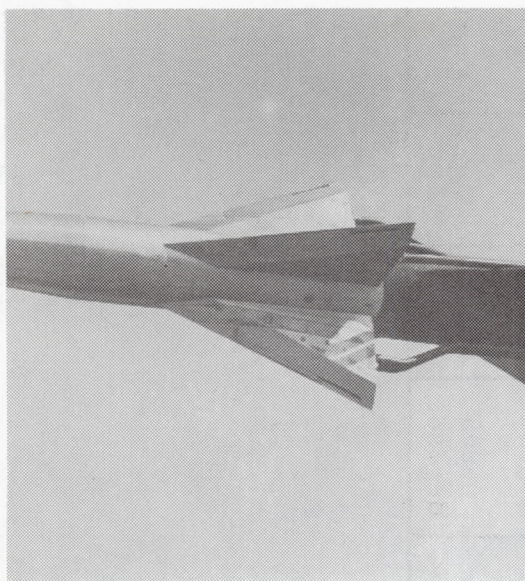
REFERENCES

1. Press, Harry; and Steiner, Roy: An Approach to the Problem of Estimating Severe and Repeated Gust Loads for Missile Operations. NACA TN 4332, 1958.
2. Coleman, Thomas L.; and Steiner, Roy: Atmospheric Turbulence Measurements Obtained From Airplane Operations at Altitudes Between 20,000 and 75,000 Feet for Several Areas in the Northern Hemisphere. NASA TN D-548, 1960.
3. Waco, David E.; and Ashburn, Edward V.: Turbulence Variations During the High Altitude Clear Air Turbulence (HICAT) Program. J. Aircraft, vol. 10, no. 1, Jan. 1973, pp. 56-58.
4. Kordes, Eldon E.; and Love, Betty J.: Preliminary Evaluation of XB-70 Airplane Encounters With High-Altitude Turbulence. NASA TN D-4209, 1967.
5. Ehernberger, L. J.; and Love, Betty J.: High Altitude Gust Acceleration Environment as Experienced by a Supersonic Airplane. NASA TN D-7868, 1975.
6. Wilson, Ronald J.; Love, Betty J.; and Larson, Richard R.: Evaluation of Effects of High-Altitude Turbulence Encounters on the XB-70 Airplane. NASA TN D-6457, 1971.
7. Boeing Commercial Airplane Company: Supersonic Cruise Research Airplane Study. NASA CR-145212, 1977.
8. Larson, Terry J.; and Ehernberger, L. J.: Techniques Used for Determination of Static Source Position Error of a High Altitude Supersonic Airplane. NASA TM X-3152, 1975.
9. Burcham, Frank W.; Montoya, Earl J.; and Lutschg, Phillip J.: Description of the YF-12 Airplane, Propulsion System, and Instrumentation for Propulsion Research Flight Tests. NASA TM X-3009, 1974.
10. Rhyne, Richard H.; and Steiner, Roy: Power Spectral Measurement of Atmospheric Turbulence in Severe Storms and Cumulus Clouds. NASA TN D-2469, 1964.
11. Crooks, Walter M.; Hoblit, Frederic M.; Mitchel, Finis A.; et. al.: Project HICAT — High Altitude Turbulence Measurements and Meteorological Correlations. AFFDL-TR-68-127, Air Force Flight Dynamics Lab., Nov. 1968.
12. Hoblit, Frederick M.; Paul, Neil; Shelton, Jerry D.; and Ashford, Frances E.: Development of a Power-Spectral Gust Design Procedure for Civil Aircraft. FAA-ADS-53, Federal Aviation Admin., 1966.

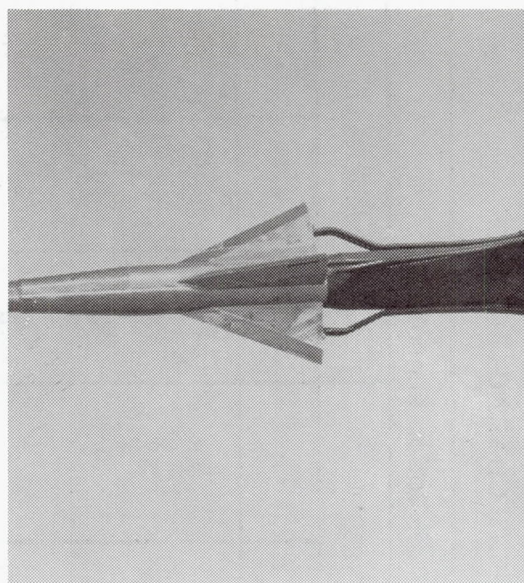
13. Military Specification: Flying Qualities of Piloted Airplanes.
MIL-F-8785B (ASG), 7 Aug. 1969.

TABLE 1.—GUST MEASURING SYSTEM INSTRUMENT CHARACTERISTICS

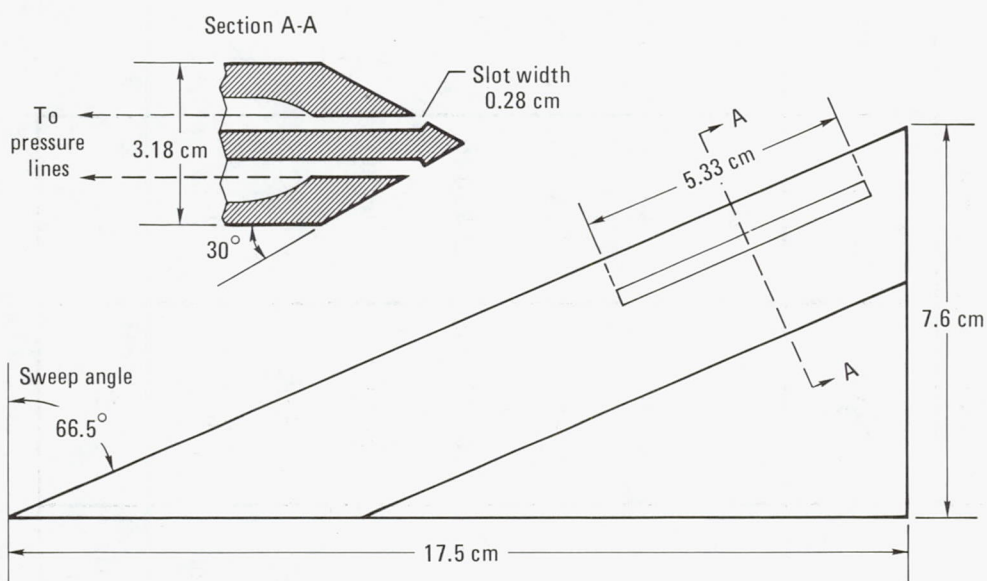
	Pressure measurements		Motion sensors					
	Gust vanes	Dog-leg	Angular rate gyros			Linear accelerometers		
			p	q	r	a_x	a_y	a_n
Natural frequency, Hz	>100	>2000	40	40	40	118	118	118
Presample filter 3 dB break, Hz	40	40	40	40	40	40	40	40
Filter slope, dB/octave	18	18	6	18	18	6	6	6
Encoded range	$\pm 13,800$ Pa	$\pm 20,700$ Pa	± 20 deg/sec	± 20 deg/sec	± 20 deg/sec	$\pm 1g$	$\pm 1g$	-1, +3g
Encoding increment	3.4 Pa	5.0 Pa	0.08 deg/sec	0.005 deg/sec	0.005 deg/sec	0.004g	0.004g	0.008g
Line length, m	1.3	1.0						
Inside diameter, cm	0.8	0.4						
Natural frequency, Hz (pneumatic)	>55	>70						



(a) Forward quarter view .



(b) Side view .



(c) Vane planform and cross section .

Figure 1.—Gust flow direction vanes .

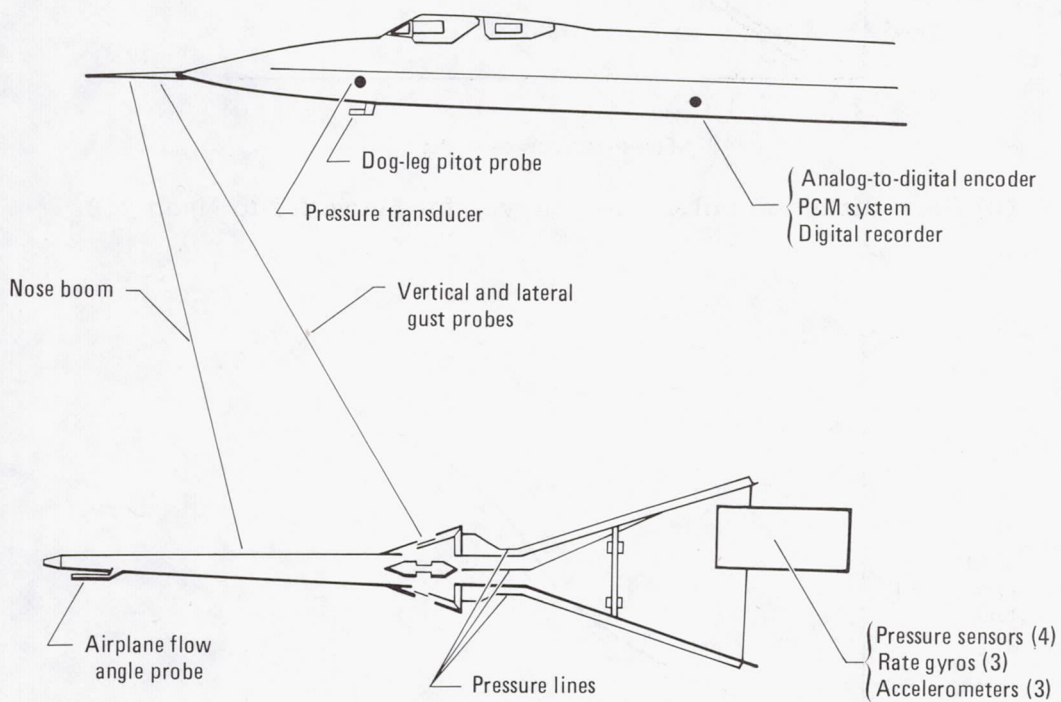
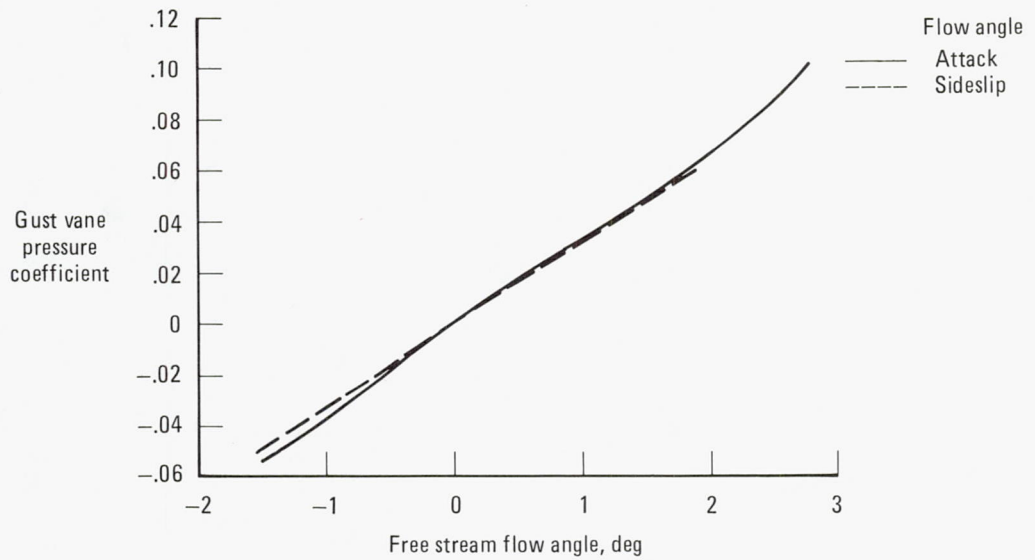
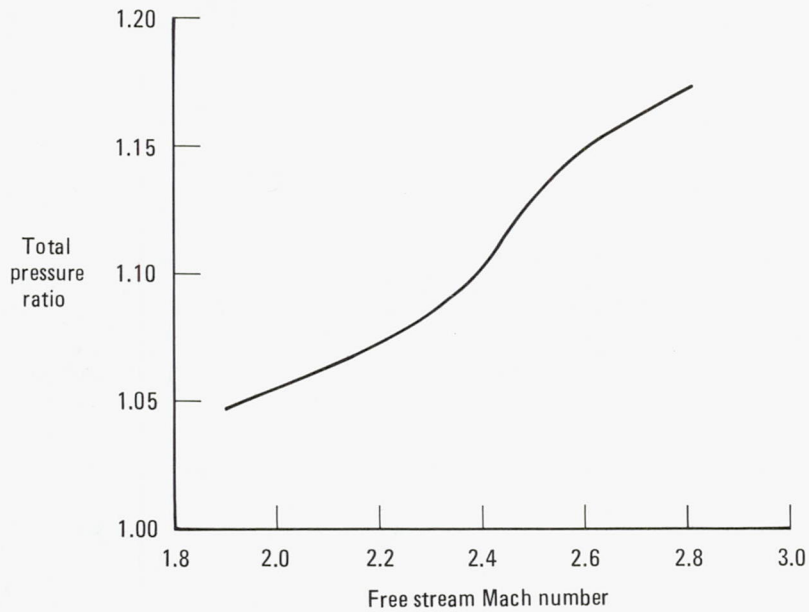


Figure 2.—Locations of gust measurement instrumentation.



(a) Flow direction polynomial curves for Mach 2.2 to Mach 2.8.



(b) Dog-leg Mach number polynomial curve, $C_{p_\alpha} = 0$.

Figure 3.—Gust probe calibration curves.

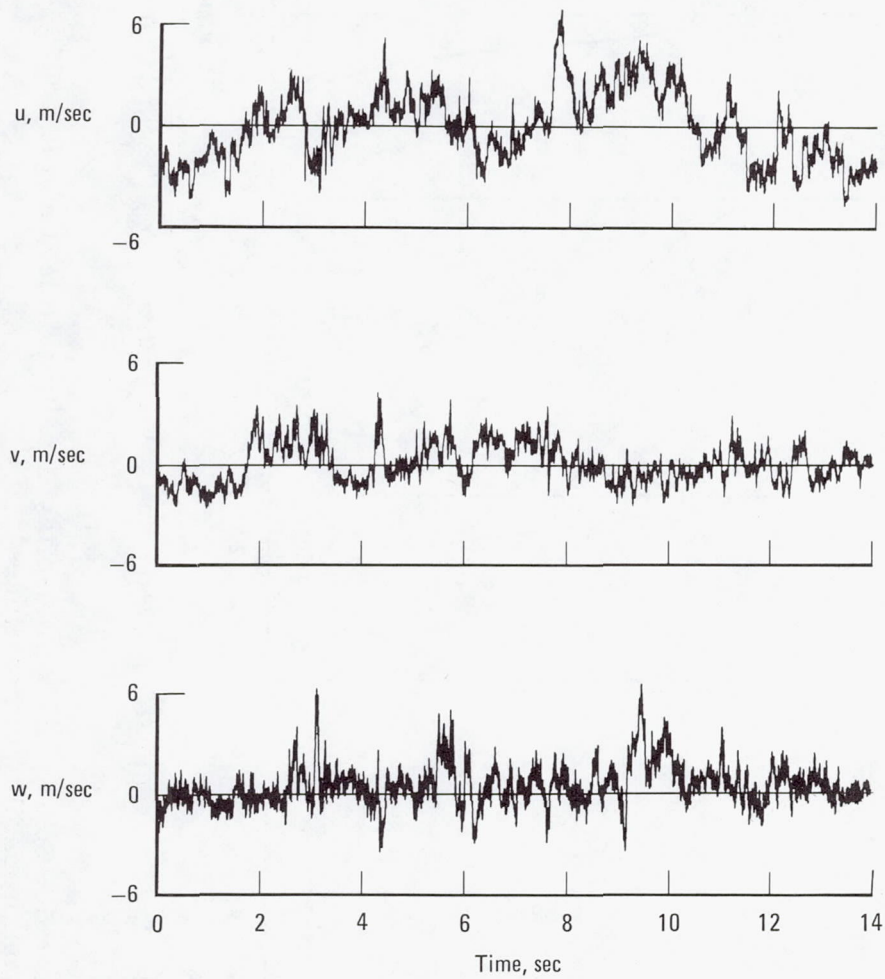
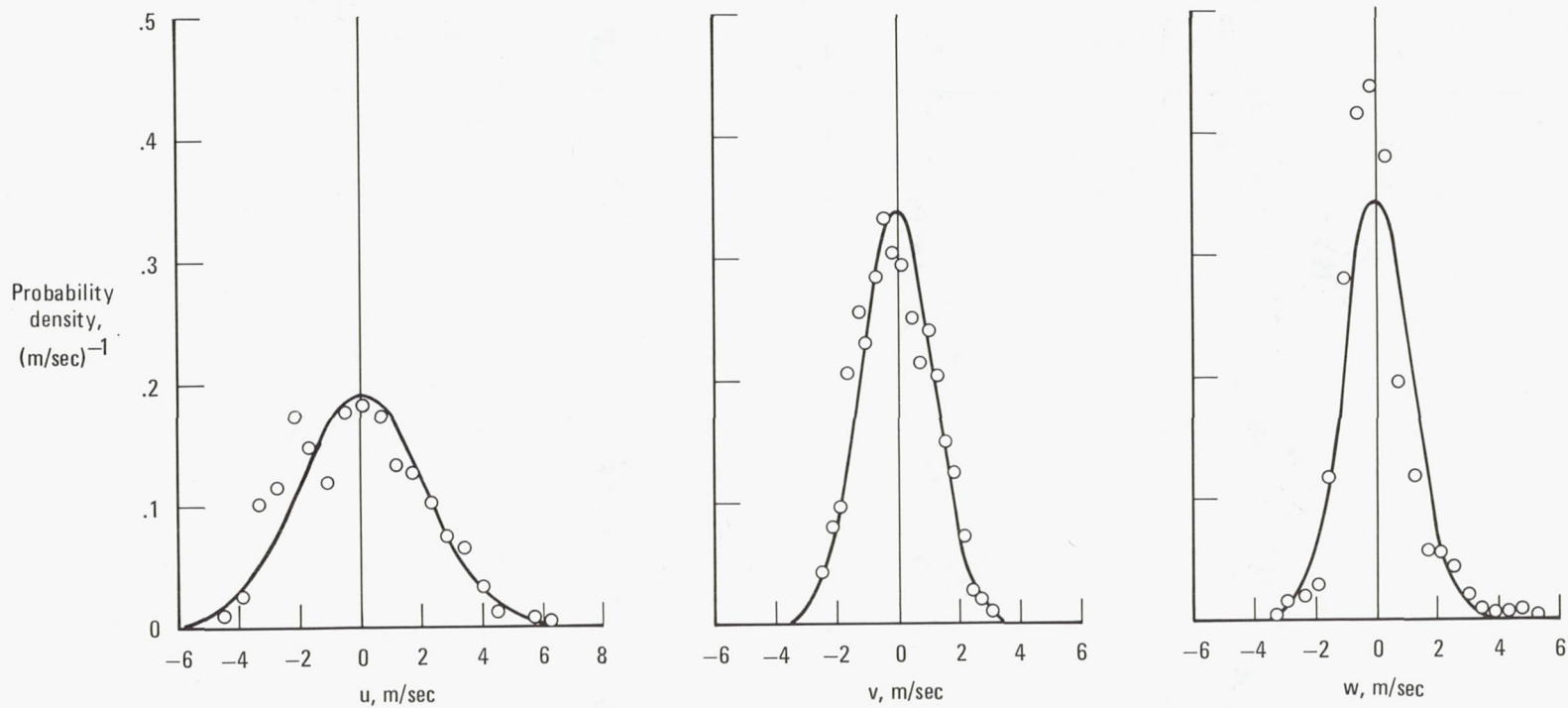


Figure 4.—YF-12 longitudinal, u ; lateral, v ; and vertical, w ; gust velocity time histories measured at 19.8 km altitude.



(a) Longitudinal, rms = 2.15 m/sec. (b) Lateral, rms = 1.17 m/sec. (c) Vertical, rms = 1.15 m/sec.

Figure 5.—Gust velocity probability density (circles) and fitted normal probability curves (lines).

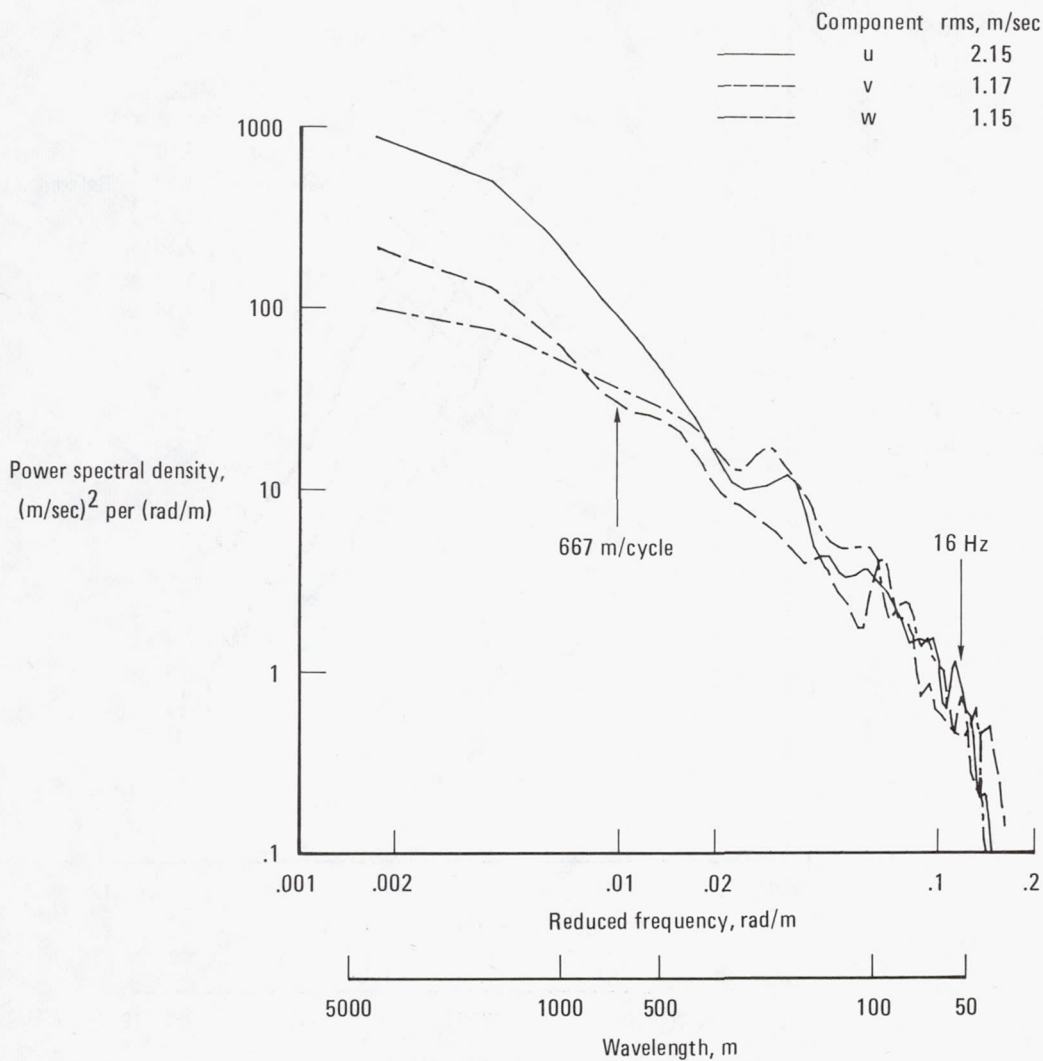


Figure 6.—Gust velocity spectral density (14-second record length, 200 samples per second, 8 degrees of freedom, 7-point Hann-Tukey window).

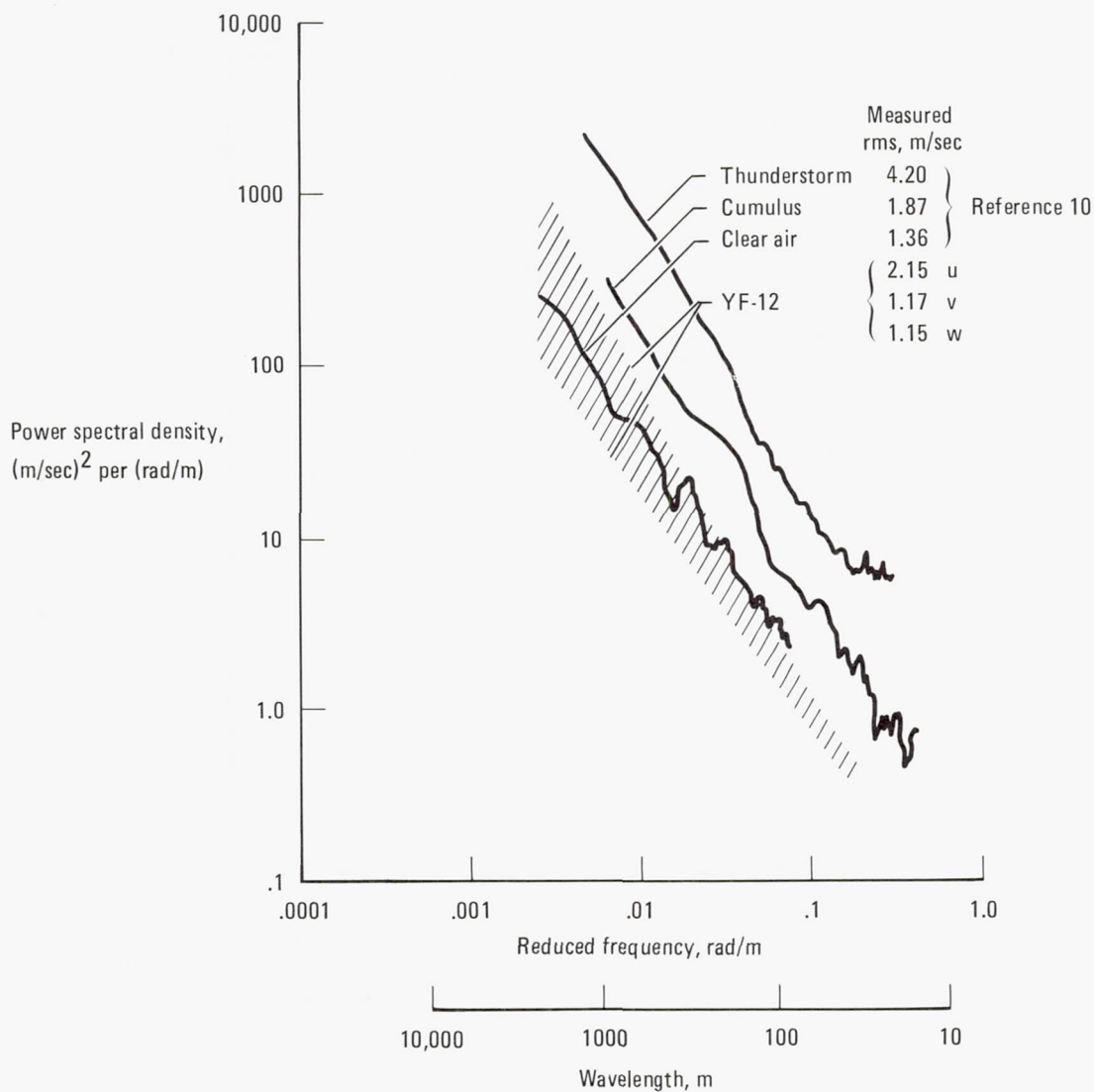


Figure 7.—Spectral densities obtained from lower altitude turbulence phenomena and from the YF-12 at high altitude.

SESSION V: PROPULSION CONTROLS

Chairman: Frank W. Burcham, Dryden Flight Research Center

WIND TUNNEL EVALUATION OF YF-12 INLET RESPONSE TO INTERNAL

AIRFLOW DISTURBANCES WITH AND WITHOUT CONTROL

Gary L. Cole, George H. Neiner, and Miles O. Dustin
Lewis Research Center

SUMMARY

Experimental responses of the inlet's terminal shock and subsonic duct static pressures to internal airflow disturbances were obtained. The disturbances were produced by the aft bypass or a specially designed disturbance generator located at the diffuser exit. Transient and frequency responses were obtained from square wave and sinusoidal wave disturbances respectively. The main objective of this program was to determine the inlet responses with the inlet's duct-pressure-ratio control system active and to investigate ways of improving those responses within the limitations of the flight actuation hardware. Frequency response data were obtained first with inlet controls inactive. This indicated the general nature of the inherent inlet dynamics, assisted in the design of controls, and provided a baseline reference for responses with active controls. In addition, the data helped to validate a NASA-Lewis small-perturbation analysis of inlet dynamics.

All the control laws were implemented by means of a digital computer that could be programmed to behave like the flight inlet's existing analog control. The experimental controls were designed using an analytical optimization technique. The capabilities of the controls were limited primarily by the actuation hardware. The experimental controls provided somewhat better attenuation of terminal shock excursions than did the YF-12 inlet control. Controls using both the forward and aft bypass systems also provided somewhat better attenuation than those using just the forward bypass. However, the main advantage of using both bypasses is in the greater control flexibility that is achieved, allowing the inlet to have a more efficient (i.e., lower drag) operating point.

INTRODUCTION

An efficient propulsion system will be a key factor in the development of an economically viable commercial supersonic cruise aircraft. Propulsion studies (ref. 1) for the NASA supersonic cruise aircraft research (SCAR) program have identified new variable cycle engine concepts that offer potential performance gains over current engines. Studies also indicate that mixed-compression inlets will be used for cruise Mach numbers of about 2.2 and above. Such inlets offer lower cowl drag and higher total pressure recovery than do all external compression inlets. However, mixed-compression inlets are subject to an undesirable phenomenon known as unstart, which would be unacceptable on a

commercial transport. Unfortunately, the chances of a disturbance induced unstart increase as the inlet operates closer to its peak performance. Thus, a challenging problem is to design a control system that will allow the inlet to operate near its peak performance without unstart.

In general, control system design requires a dynamic model (measured experimentally or determined analytically) of the plant to be controlled. In the case of an inlet, it is necessary to know the response of duct pressures and terminal shock position to engine and atmospheric induced disturbances. Numerous experimental programs (e.g., refs. 2 to 14) have been conducted by NASA and industry to obtain inlet dynamics and control information for both real and simulated engine disturbances. Except for the program described in reference 14, the inlets were generally small scale and controls were implemented using analog computers.

Considerably less information is available relating to effects of atmospheric-type disturbances on mixed-compression inlets. Simulation of atmospheric disturbances in supersonic wind tunnels is extremely difficult, but some data have been obtained by oscillating flat plates and wedge shaped airfoils upstream of inlets (refs. 4 and 8). A recent analytical study (ref. 15) indicates that control of inlet terminal shock position against atmospheric disturbances may be of more concern than control against engine disturbances.

As part of the NASA program to investigate scale and flight effects on the steady-state and dynamic performance of the YF-12 aircraft inlet, a flight inlet from a YF-12 aircraft was tested in the Lewis 10- by 10-Foot Supersonic Wind Tunnel. The fact that the inlet was a flight article allowed the test to be unique. It was the first time that the dynamic response characteristics of a flight hardware mixed-compression inlet to simulated engine disturbances were evaluated in a wind tunnel (ref. 16). It provided an opportunity to systematically evaluate the bill-of-material inlet control system, including the control laws and actuation hardware (ref. 17). For convenience the inlet control laws were programed on the digital system described in reference 18 rather than in an analog mode like the actual aircraft system. With the trend being toward the use of digital computers for control, this also provided an opportunity to gain experience in the digital implementation of an actual flight control system. The success of this program provided some impetus and justification for the cooperative control program, planned for the YF-12 airplane (ref. 19). In addition, the YF-12 inlet program provided a timely application for a controller design method that uses the parameter optimization technique described in reference 20. Results using experimental shock position controllers and comparisons to results using the bill-of-material control are given in reference 21.

This paper summarizes the wind tunnel aspects of the YF-12 inlet dynamics and control program as detailed in references 16, 17, and 21. Experimental data, selected from those references, are presented showing the inlet normal shock and subsonic duct static-pressure responses to simulated engine disturbances, with and without control. For data shown in this paper the inlet angles of attack and sideslip were zero degrees and the Mach number was either 2.956 or 2.474.

SYMBOLS

Values are given in SI units. The measurements and calculations were made in U.S. customary units.

DPR	duct-pressure ratio (P_{sD8}/P_{pLM})
E	error signal between a set-point commanded signal and the corresponding feedback signal, V
F	cost function
H	transfer function of feedback element $H = \left[\frac{\left(K_c \frac{s}{\omega_c} + 1 \right)}{s} \right]$
K_c	gain of shock-position controller
M_∞	Mach number measured at nose boom
NAR	normalized amplitude ratio, $\frac{\left(\frac{ Output }{ Input } \right)_{\text{at input frequency}}}{\left(\frac{ Output }{ Input } \right)_{\text{at lowest frequency shown, without control}}}$
$P_{p,A}$	throat total-pressure probe (see fig. 6)
P_{pLM}	external cowl pitot-pressure measurement for YF-12 aircraft inlet DPR control signal, N/cm ²
$\left. \begin{matrix} P_{s,A}, \\ P_{s,B}, \dots, P_{s,J}, \\ P_{s,L}, P_{s,Q} \end{matrix} \right\}$	static-pressure taps (see fig. 6)
P_{sD8}	static-pressure measurement for YF-12 aircraft inlet DPR control signal, N/cm ²
Q_n	noise-penalty weighting factor used in controller-gain optimization program
s	Laplace variable, 1/sec
U	control bypass door area, cm ²

α_{∞} angle of attack measured at nose boom, deg
 β_{∞} angle of sideslip measured at nose boom, deg
 ω_c controller corner frequency, rad/sec

Superscripts:

$\overline{(\quad)}$ mean value of ()
 \cdot derivative with respect to time

Subscripts:

D disturbance
V random measurement noise

APPARATUS

Inlet Model

A flight inlet from a YF-12 aircraft was used for this investigation in the 10- by 10-Foot Supersonic Wind Tunnel at Lewis Research Center. It is the same inlet that was used in the steady-state inlet performance investigations reported in references 22 and 23. Figure 1 is a schematic of the inlet showing variable geometry features and locations of bleeds and bypasses. The inlet is an axisymmetric, mixed-compression type and is sized at the design Mach number of 3+ to supply a J58 afterburning turbojet engine. The spike translates for inlet restart capability and operation at off-design Mach numbers.

Bleed regions for boundary layer control and shock stability are located on both the spike and cowl. Spike boundary-layer bleed is accomplished by a slotted surface on the spike. Cowl-boundary-layer bleed is provided by a combination flush slot and ram scoop referred to as the shock trap.

The inlet has two bypass systems. The forward bypass is used to position the terminal shock by means of a duct-pressure-ratio (DPR) control, to be described later. It is also used to bypass large amounts of airflow during an inlet restart cycle. The aft bypass provides air for some engine cooling and aids the forward bypass in matching the inlet airflow to the engine requirement at Mach numbers below 3.0. In flight, the aft-bypass is set by the pilot at one of three discrete positions. For the wind-tunnel tests, the discrete positioning mechanism was replaced with an electrohydraulic servomechanism to provide continuous position control like that of the forward bypass. Frequency responses of forward and aft bypass position to position commands are shown in figure 2. The amplitude ratio responses were normalized by dividing by the respective amplitude ratios at 0.1 hertz.

The inlet was attached to a boiler-plate nacelle and the complete assembly was strut-mounted in the wind tunnel (fig. 3). Inside the nacelle was a cold-

pipe assembly. An airflow-disturbance generator was strut-mounted in the cold pipe near the diffuser exit (fig. 3). The assembly, shown in more detail in figure 4, consisted of five sliding plate valves that were hinged so that they could expand like an umbrella. The amount of assembly expansion and the position of each sliding valve was remotely controlled by electrohydraulic servomechanisms. Airflow across the assembly was choked. Thus, actuation of the sliding plate valves provided a means of simulating perturbations in engine corrected airflow. The frequency response of sliding-valve position to position command is shown in figure 5. The amplitude response was normalized by dividing by the amplitude at 1 hertz. Note that its response has a much wider frequency range than that of the two bypass systems. Details of the sliding valve servosystem design are given in reference 24.

Inlet angle of attack could be remotely adjusted by means of the strut during a tunnel run. Inlet angle of sideslip could be adjusted only between runs. The angles of attack and sideslip were 0° for all data shown in this paper.

Additional details concerning the inlet systems and wind tunnel installation are given in reference 25. Reference 26 also gives additional information regarding the F-12 series aircraft propulsion system.

Instrumentation

The pressure instrumentation consisted of high-response strain-gage pressure transducers closely coupled to static taps and total probes located on the inlet internal-cowl surface. Relative locations of the pressure measuring stations are shown in figure 6. Exact axial locations are given in figure 11 of reference 16. The response of each transducer and its connecting line was flat within 0 to +0.5 decibel and had negligible phase shift in the frequency range of 0 to 100 hertz.

Duct static pressure, P_{sD8} , is a measurement of the pressure from eight manifolded static-pressure taps, shown in figure 6. A high-response pressure transducer of the type described previously also was used to measure the duct static pressure. The duct static pressure is of interest because it is one of two pressures used to determine duct pressure ratio DPR, the feedback signal for the YF-12 forward bypass control. The DPR system was implemented so that its response would be nearly identical to that of the flight YF-12 system. However the ratio was computed electronically rather than by the aircraft mechanical sensor.

The outputs of the pressure transducers connected to static-pressure taps $P_{s,A}$ to $P_{s,J}$ were used as inputs to an electronic terminal-shock-position sensor. The shock sensor was used to obtain a measure of the response of inlet terminal-shock position to airflow perturbations. The frequency response of terminal-shock position as measured by the sensor to actual shock position was found to be essentially flat with no more than 15° phase lag for frequencies in the range of 0 to 40 hertz. A detailed description of the sensor design and

performance is given in reference 27. Additional details regarding instrumentation are given in reference 25.

EXPERIMENTAL SETUP AND CONDITIONS

Figure 7 is a schematic of the wind-tunnel experimental setup. Shown are the inlet, the flow paths of the command signals to the servomechanisms, the flow paths of the measured inlet signals, and a general-purpose digital system. The digital system was used to program both the aircraft and experimental inlet terminal-shock-position controllers that will be described later. It also controlled the sequencing of the experiment and performed calculations to provide an immediate on-line display of results at the completion of each frequency response test. Some characteristics and capabilities of the digital computer system are given in table I and additional details of the overall system are provided in reference 18.

The inlet geometry configuration and terminal shock operating point were generally about the same as those that would be set by the YF-12 aircraft inlet-control system for corresponding flight conditions. Average free-stream wind tunnel conditions, at which data shown in this paper were taken, were as follows: Mach number, 2.956; total temperature, 373 K; Reynolds number per meter, 4.01×10^6 or Mach number, 2.474; total temperature, 310 K; Reynolds number per meter, 4.91×10^6 . The Reynolds numbers correspond to values within the flight envelope of the aircraft.

RESULTS AND DISCUSSION

Responses without Inlet Control

Responses of several inlet variables to simulated engine airflow perturbations without inlet control were obtained first. This indicated the general nature of the inherent inlet dynamics, assisted in the design of controls and provided a baseline reference for responses with active controls. In addition, the data helped to validate a NASA-Lewis small-perturbation analysis of inlet dynamics.

Experimental responses of terminal shock position and three subsonic duct static pressures to the airflow disturbance generator, at the Mach 2.956 condition, are shown in figure 8. Responses based on the small-perturbation analysis of reference 28 are also shown for comparison. The equations governing terminal-shock position were derived by taking continuity, momentum, and energy balances across the shock and accounting for a moving shock. The subsonic duct is represented by sets of one-dimensional wave equations. In general, the amplitude experimental responses have an initial rolloff followed by one or more resonances. A particularly prominent peak occurs at about 40 hertz, except for P_{sD8} . The greater attenuation of P_{sD8} is due to its measuring system line and volume dynamics. The phase data are generally dom-

inated by a delay time. This was demonstrated in reference 16 which showed phase angle to be linear with frequency above frequencies of 20 to 40 hertz, depending on signal location. The characteristics of the YF-12 inlet are similar to those of the inlets of references 8, 11, and 13. However, scale effects on the dynamics of the inlets cannot be determined explicitly because none of the inlets are the same geometrically. Also, overboard bypasses (holes in the side of the subsonic duct) were not similarly located and disturbances occurred at different locations which would modify the organ pipe frequency of the ducts. In general, the rolloff of the YF-12 inlet is more rapid than for the other inlets because of its greater subsonic-duct volume and it resonates at a lower frequency because of its greater subsonic-duct length. Although corresponding frequency response data were not available from flight for comparison, the results would be expected to be the same for a corresponding inlet operating point condition, except for a modification due to temperature. In flight, the stagnation temperature for the Mach 2.956 condition would be approximately 1.6 times the wind-tunnel value. Therefore, the duct delay and fill times would be shorter in flight than in the tunnel because the speed of sound is higher. The approximate inlet response expected for the flight condition can be determined by multiplying the tunnel disturbance frequencies by the square root of the ratio of flight temperature to tunnel temperature. For example, the resonant peak that occurs at 40 hertz in the tunnel should occur at approximately 51 hertz in flight.

Before discussing the comparison of the analytical and experimental responses in figure 8, a few observations will be made concerning the inlet analysis. Calculation of parameters used in the analysis can generally be determined analytically with satisfactory accuracy. One exception is an area parameter common to most inlet analyses. The parameter, A'/A , is defined as the ratio of the axial rate of change of duct area A' to the duct area A , evaluated at the shock operating point. The steady state gain of shock position to an airflow disturbance in the subsonic duct is a strong function of A'/A . It has been found that if the value of A'/A used in the analysis is based on inlet geometry the analytical value of the gain is always higher than the value measured experimentally. This is believed to be due to effects of shock/boundary-layer interaction that are unaccounted for and to inadequate modeling of the boundary layer bleed systems. By knowing the experimental value of the gain, an effective value of A'/A can be calculated so that the steady-state gains will match exactly. For the inlet of reference 8 the effective value of A'/A was found to range from 2 to 4 times the geometric value, depending on the boundary-layer bleed configuration. For the case of figure 8, the effective value was 2.5 times the geometric value.

A similar difficulty exists in matching the steady-state gains of static pressures in the subsonic portion of the duct to the airflow disturbance. In this case the analytically-determined value of the gain is lower if the analysis is based strictly on inlet geometric areas. The major parameter affecting this mismatch of gains is the duct Mach number at the pressure measuring station. The duct Mach number, of course, depends on the boundary layer. Experimental steady state data can also be used to make the gains match. This was not done in the case of figure 8. In general, the phase response data of

the terminal shock and the static pressures are not significantly affected by these parameters.

The agreement between the experimental and analytical responses shown in figure 8 is generally typical of that obtained with the smaller scale inlets of references 8 and 11. Agreement in phase angle is usually excellent. Amplitude ratio agreement, although not as good as phase in an absolute sense over the entire frequency range, is generally good in terms of the rolloff and resonant frequencies.

Reference 16 also presents amplitude ratio data showing how YF-12 inlet response varies with free-stream Mach number, angle of attack, shock operating point and amount of forward bypass opening. The most significant variations in initial rolloff and resonant frequency conditions were found at different free-stream Mach number conditions. The different results are attributed to combinations of changes in tunnel total temperature, spike position, forward and aft bypass opening, terminal shock operating point, and simulated-engine corrected airflow. The inlet also exhibited an extreme resonant condition with the inlet operating at a higher than normal value of duct pressure ratio, DPR. In that case the shock was near or in the shock trap, which acts in a nonlinear manner. Also, this test may have excited a resonance in the secondary airflow duct (behind the shock trap).

Frequency responses of inlet signals to both the forward and aft bypasses were also obtained. However, there is less confidence in those data because bypass motion did not remain sinusoidal above a frequency of about 1 hertz.

Responses With Inlet Control

YF-12 aircraft inlet control system. - A simplified diagram of the YF-12 aircraft inlet control system is shown for normal started-inlet conditions in figure 9. The system manipulates the spike and forward bypass positions. An air data computer converts pressures measured at the airplane nose boom to aircraft flight Mach number and angles of attack and sideslip. These flight parameters are then used as inputs to the control system. The spike is translated to provide the necessary contraction ratio at each Mach number. The purpose of the control that manipulates the forward bypass is to maintain the terminal shock at the desired location. Shock position is sensed indirectly by means of the duct-pressure-ratio, DPR. Both spike position and commanded value of DPR are scheduled as functions of Mach number and both are biased by angles of attack and sideslip and aircraft normal acceleration. In flight the schedules are implemented by means of cams, and associated filtering and compensation are accomplished electronically by analog equipment.

During the wind-tunnel program the inlet-control schedules and associated filtering and compensation were implemented on the general purpose digital system (fig. 7). This will also be done in the cooperative control program of reference 19. Since an isolated inlet was tested, the airplane air data computer and normal acceleration terms were unavailable. Therefore, the digital system was also used to calculate the airplane flight conditions that would

correspond to the measured local inlet conditions. The calculations were based on data obtained from the YF-12 flight program and from wind tunnel tests of a YF-12 scale model. The acceleration term was omitted.

The digital computer program was performed on a priority-interrupt basis at seven levels. About 25 percent of the time was spent checking the priority-interrupt structure to determine what should be calculated next and where its data should come from. About 50 percent of the time was spent calculating the spike and DPR setpoints (commanded values) and the forward bypass control. The remaining 25 percent of the time was spent on auxiliary routines, such as frequency response calculations. Updates of the setpoint values and the forward bypass control occurred every 9 milliseconds and 2 milliseconds, respectively. The control update time was faster than necessary, since the forward bypass can't respond to commands much beyond 1 hertz. According to sampled-data theory, the setpoint update time of 9 milliseconds would allow recognition of signals with frequency content of about 50 hertz or less. This was more than adequate for the wind tunnel tests, since conditions were constant. However, in flight, rapid variation of atmospheric conditions (e.g., ambient temperature and pressure and relative velocity due to gusts) can cause an undesirable response of the inlet's terminal shock (ref. 15). Hence, a more rapid update rate of the setpoint values to the control might be required. One consequence of inadequate sampling is that the bypass system will drive the inlet shock at a frequency that is different from the disturbance frequency (ref. 29). Controller dynamics were programmed using the advanced Z-transform representation of the transfer-function.

Closed-loop amplitude responses of P_{gD8} and the output of the terminal-shock-position sensor to the airflow disturbance generator at Mach 2.474 conditions are compared to the open loop responses in figure 10. (The response of DPR would be the same as that for P_{gD8} , since P_{pLM} was constant.) The closed-loop responses show that the control system is able to attenuate disturbance induced shock motions, relative to the open-loop, for disturbance frequencies only below 1 to 1.5 hertz. The control is limited primarily by the speed of response of the forward bypass system. In the frequency range of 1.5 to 10 hertz the P_{gD8} response shows considerable amplification relative to the open-loop, with a peak amplitude ratio of about 2.5 at 2 hertz. This indicates that the control is reinforcing the disturbance. The extent of the peaking can be reduced by decreasing the controller gain, but then the attenuation at the low frequencies (0.2 Hz) would not be as great. Also the speed of response would be slower. The closed-loop response eventually rejoins the open-loop response, indicating that the control system has become ineffective. Closed-loop frequency responses were also obtained at higher Mach numbers (ref. 17). The response at Mach 2.956 (ref. 17) showed very little peaking above the open-loop response. Therefore, for the operating conditions in the wind tunnel, the inlet closed-loop response was more stable at Mach 2.956 than at Mach 2.474.

Open and closed-loop transient responses to a step change in the airflow disturbance generator are shown in figure 11 for the same operating condition as that for the frequency response of figure 10. The uncontrolled change in shock position (fig. 11(a)) is approximately 13.7 centimeters. The noise-free

portion of the shock sensor trace occurs when the shock has moved upstream of pressure tap $P_{s,A}$ (fig. 6). The shape of the response of pressure $P_{s,I}$ is very similar to the shock response. The closed-loop transient (fig. 11(b)) shows that the control system responds rather unstably to the disturbance. The forward bypass oscillates at about 2 hertz with no evidence that the oscillation will die out. The frequency of the oscillation corresponds to the frequency at which peaking occurs (fig. 10). After the disturbance occurs, the control system drives the shock through some peak-to-peak excursions that are actually greater (about 16 cm) than without control. This response is undesirable and indicates a need for a controller gain adjustment at the Mach 2.474 condition.

Figure 12 shows the transient response at the Mach 2.474 condition with the loop gain reduced to about one-third of its value for the transient of figure 11. The forward bypass still exhibits an overshoot followed by some ringing which tends to die out, but the oscillations are not nearly as severe as for the case of figure 11. The forward bypass is seen to open more rapidly than it closes - an observation not quite so apparent in figure 11. The system was designed that way to allow the inlet to move quickly away from an unstart condition.

Transient responses were also obtained for the Mach 2.956 condition and are shown in reference 17. The closed-loop transient response was similar to that for the reduced gain case at Mach 2.474, indicating a better choice of gain for the Mach 2.956 condition. However, the transient response was more oscillatory than would have been expected from the closed-loop frequency response. This may be due, in part, to nonlinearities in the system.

The frequency response and transient data just discussed indicate that both types of testing are valuable. As will be discussed later, the open-loop frequency response data can be used for designing controllers. However, the closed-loop frequency response may not indicate potential problems that are revealed by transient tests. In simulating the control system, the actuation hardware should be accurately simulated including nonlinearities like hysteresis and friction. Or better yet, actual flight hardware should be used. Care must be taken to be sure that closed-loop responses are sufficiently stable at all conditions.

The closed-loop transient response of the inlet to an aft-bypass disturbance is shown in figure 13. The response is seen to be basically the same as that of figure 12. However, this transient revealed an oscillation of the aft bypass system that did not occur during transients when the DPR control system was inactive. A similar action occurred at the Mach 2.956 condition (ref. 17). This indicates that a coupling, although small, does exist between the aft-bypass servosystem and the DPR control system. The origin of the coupling is unknown, but could be due to either an aerodynamic flow force or a structural vibration. It should be kept in mind that the aft-bypass actuator used in the wind tunnel tests is not the same as the standard one used on the aircraft. However, as will be discussed later, it may be beneficial to use both overboard bypass and secondary bypass servo-driven systems for inlet control. Hence, the potential for interaction exists that may only be revealed by experimental tests.

Experimental inlet control systems. - An investigation was conducted to determine if control of the YF-12 inlet terminal shock could be improved by improving the controller dynamics and/or by using the aft bypass system or engine speed (simulated) to augment the forward bypass system (ref. 21). These tests were all conducted at the Mach 2.956 condition.

Figure 14 shows block diagrams of the four types of experimental controls that were tested. The type I system is like the aircraft inlet system except that it uses a different feedback signal and controller. Types I and II used either $P_{s,I}$ or the shock-position sensor output as the feedback signal. The closed-loop responses using either variable were not significantly different, so, unless noted otherwise, only results with $P_{s,I}$ feedback will be shown. Types III and IV controls used $P_{s,I}$ as the feedback signal. For types III and IV, a second loop causes reset action of the forward bypass by means of either the aft-bypass or the sliding-valves of the airflow-disturbance generator. The action of the sliding valves was slowed down to simulate realistic changes in engine speed. The controller for all four types was a proportional-plus-integral filter function having the general form

$$H = \frac{K_c \left(\frac{s}{\omega_c} + 1 \right)}{s}$$

Optimal fixed-form controller parameters (K_c and ω_c) were determined by using a computerized frequency-domain technique described in reference 20 as opposed to an optimal time-domain technique (e.g., ref. 30). The technique is based on minimization of a cost function which included the system regulation error (E_D) due to the disturbance and the control power (\dot{U}_V^2) due to measurement noise. The cost function can be stated in equation form as

$$F = \overline{E_D^2} + Q_n \overline{\dot{U}_V^2}$$

where Q_n is a noise-penalty weighting factor. The computer technique requires as input the transfer function for the uncontrolled inlet dynamics and actuation hardware dynamics. The computer then calculates the expected closed-loop frequency response and the cost function while searching for the optimum gains. The optimum controller gains, determined for various values of Q_n , were evaluated experimentally to find the most acceptable values of K_c and ω_c . This method provided a simpler and quicker means of arriving at controller parameters than do the classical methods such as the root locus approach that was used in reference 9. This would be especially true if more than two controller parameters were involved. The optimization approach would be even more useful in a case like the experimental program of reference 12 where the inlet had a high response (100 Hz) overboard bypass system and the control feedback signals were very noisy due to an inlet instability.

A comparison of computed analytical and experimentally measured closed-loop frequency responses for type-I controls are shown in figure 15. Results are presented for a range of values of the noise-penalty weighting factor Q_n . All of the results exhibit similar characteristics. The increase in amplitude

ratio with frequency below 1 hertz is expected because of the integral control action. As Q_n decreases the noise penalty decreases and there is a corresponding increase in controller gain. Therefore the control loop-gain increases, accounting for the greater attenuation at disturbance frequencies of about 1.5 hertz and below. The agreement between analytical and experimental results is quite good except in the vicinity of 2 hertz, when Q_n was 0.01. The same kind of discrepancy has been observed before when control system loop gains were high (e.g., ref. 9). This phenomenon was investigated more thoroughly in another test as shown in figure 16. In this case data were taken at closer frequency intervals in the vicinity of a peak like the one that occurred in figure 15. As for the results of figure 15, the sudden increase in amplitude ratio occurred only when Q_n was 0.01. The sudden change in the frequency response is characteristic of a jump resonance and indicates that the loop gain finally became large enough so that nonlinearities in the system had a significant effect on the closed-loop response. The inlet response is certainly not linear for large excursions of the terminal shock. A linearized inlet model will predict higher allowable gains than can be achieved in the real system. Thus, care must be exercised in interpreting control results from a linearized inlet model, or alternately the system nonlinearities must be accurately simulated.

Generally, it was found that a noise-penalty weighting factor, Q_n , of 0.1 resulted in good performance for the type I and II controllers. The closed-loop frequency responses generally showed good attenuation of disturbance induced shock motion at the low end of the frequency scale. At the same time, the jump resonance phenomenon of figures 15 and 16 was avoided. These controllers were also tested with the reset action of the type III and IV controls. These types of control had been investigated earlier using an actual engine (refs. 31 and 32). Figure 17 shows a comparison of the closed-loop responses for the four types of experimental control systems along with the YF-12 aircraft inlet duct-pressure-ratio control. The results indicate that, although the experimental controls gave somewhat better performance (greater attenuation), the airplane control was pretty well optimized for the Mach 2.956 condition. The optimization procedure couldn't produce a control that was significantly better than the airplane control because the forward bypass actuation hardware was the major limiting factor. Note that the addition of the reset action had a stabilizing effect on the control as evidenced by the decrease in peaking at the resonant frequency for the type III and IV controls. Additional frequency response data are given in reference 21.

Transient responses were obtained for the type I, III, and IV controls (ref. 21). No significant differences between the type I and airplane controls were observed. Figure 18 shows a transient response that illustrates the reset action of the type III control system. Just after the disturbance occurs (point 1) the forward-bypass opens (point 2) to bring the shock back to its desired position (point 3). The aft-bypass is then slowly opened by the controller reset action (point 4), which allows the forward-bypass to go closed again (point 5) to a lower drag condition. The same sequence of events occurs (points 6, 7, 8, 9, and 10) when the disturbance-generator area opens. The different rates of reset are due to the fact that the aft-bypass actuator moves faster in the closing direction than in the opening direction. The action of

the type IV control system is similar except that the reset of the forward bypass was caused by a change in engine speed simulated by the airflow-disturbance generator. Neither the type III or type IV control systems offer a response that is much faster than the type I and II or airplane control systems. The advantage is in the greater control flexibility that is achieved, allowing the inlet to have a more efficient (i.e., lower drag) operating point. This would be especially desirable for a commercial supersonic cruise aircraft. Rapid reset of the forward bypass might also be used to minimize the effects of propulsion system interaction with the lateral and longitudinal directional-control characteristics that have been noted in references 33 and 34. It is hoped that this kind of control can be demonstrated during the cooperative control flight program of reference 19.

SUMMARY OF RESULTS

The response of terminal-shock position and static pressures in the subsonic duct of a YF-12 aircraft flight-hardware inlet to perturbations in simulated engine corrected airflow were obtained with and without inlet control. Both the YF-12 duct-pressure-ratio DPR control and experimental controls which had optimal, fixed-form terminal-shock-position controllers were used. In some cases the experimental controls reset the forward bypass to the desired position by trading either aft-bypass area or a change in simulated engine speed for forward-bypass area.

The open-loop frequency-response amplitude ratio data generally exhibited a rolloff characteristic followed by one or more resonances. The results were similar to those obtained for small scale inlets except that the rolloff and first resonance occurs at lower frequencies for the YF-12 inlet. This is due to the larger volume and greater length of the YF-12 inlet subsonic duct. Phase data were found to be dominated by a delay time at frequencies above 20 to 40 hertz depending on signal location. The responses in in-flight should be similar except for a shift in the frequency scale due to a difference in temperature. Closed-loop frequency responses, calculated from open-loop transfer functions of the individual components of the system, generally gave good agreement with experimentally measured results. However, when controller gains were too high, agreement was poor in the vicinity of a resonance because nonlinearities in the system had a large effect.

Frequency responses with the YF-12 DPR control system active showed attenuation of disturbance-induced shock excursions for frequencies of about 1 hertz and below. Above 1 hertz the control was either ineffective or made the shock excursion worse. Both frequency and transient response data indicated that the inlet closed-loop response was less stable at some Mach numbers than at others. In cases where the aft bypass was used to disturb the inlet, with the DPR control system active, an undesirable coupling of unexplained origin caused the aft-bypass servosystem to oscillate. Although the aft-bypass actuator used for these tests is not the same as the standard one used on the airplane, it is important to recognize that the potential for such a coupling does exist.

The experimental terminal-shock-position controls did not perform significantly better than the YF-12 DPR control. In general, the speed of response of the forward bypass is a major limiting factor for all of the controls. The controls that reset the forward bypass were found to operate more stably than the others. Another advantage of the controls with reset is the greater degree of control flexibility, allowing the inlet to operate at a more efficient (i.e., lower drag) operating point.

REFERENCES

1. Willis, E.; and Welliver, A. D.: Variable-Cycle Engines for Supersonic Cruise Aircraft. AIAA Paper 76-759, July 1976.
2. Chun, K. S.; and Burr, R. H.: A Control System Concept for an Axisymmetric Supersonic Inlet. J. Aircr., vol. 6, no. 4, July-Aug. 1969, pp. 306-311.
3. Schweikhardt, R. G.; and Grippe, R. P.: Investigations in the Design and Development of a Bypass Door Control System for an SST Axisymmetric Intake Operating in the External Compression Mode. AIAA Paper 70-695, June 1970.
4. Investigations of Supersonic Transport Engine Inlet Configurations. (LAC-603220, Lockheed Aircraft Corp.; NASA Contract NAS2-2363.) NASA CR-68399, 1965.
5. Inlet-Exhaust-Thrust Reverser Program for the Commercial Supersonic Transport. LAC-596884, Lockheed Aircraft Corp., Aug. 1964; ASD Contract No. AF33(657)-11419 for FAA. AD-367328L.
6. Martin, Arnold W.; Kostin, Leonard C.; and Millstone, Sidney D.: Dynamic Distortion at the Exit of a Subsonic Diffuser of a Mixed Compression Inlet. NASA CR-1644, 1970.
7. Martin, Arnold W.; Beaulieu, Warren D.; and Kostin, Leonard C.: Analysis and Correlation of Inlet Unsteady Flow Data. NA-71-1146, North American Rockwell Corp., 1971.
8. Wasserbauer, Joseph F.: Dynamic Response of a Mach 2.5 Axisymmetric Inlet with Engine or Cold Pipe and Utilizing 60 Percent Supersonic Internal Area Contraction. NASA TN D-5338, 1969.
9. Neiner, George H.; Crosby, Michael J.; and Cole, Gary L.: Experimental and Analytical Investigation of Fast Normal Shock Position Controls for a Mach 2.5 Mixed-Compression Inlet. NASA TN D-6382, 1971.
10. Cole, Gary L.; Neiner, George H.; and Crosby, Michael J.: An Automatic Restart Control System for an Axisymmetric Mixed-Compression Inlet. NASA TN D-5590, 1969.

11. Baumbick, Robert J.; Neiner, George H.; and Cole, Gary L.: Experimental Dynamic Response of a Two-Dimensional, Mach 2.7, Mixed-Compression Inlet. NASA TN D-6957, 1972.
12. Cole, Gary L.; Neiner, George H.; and Baumbick, Robert J.: Terminal Shock Position and Restart Control of a Mach 2.7, Two-Dimensional, Twin-Duct Mixed-Compression Inlet. NASA TM X-2818, 1973.
13. Baumbick, Robert J.; Wallhagen, Robert E.; Neiner, George H.; and Batterton, Peter G.: Dynamic Response of Mach 2.5 Axisymmetric Inlet with 40 Percent Supersonic Internal Area Contraction. NASA TM X-2833, 1973.
14. Batterton, P. G.; Arpasi, D. J.; and Baumbick, R. J.: Digital Integrated Control of a Mach 2.5 Mixed-Compression Inlet and an Augmented Mixed-Flow Turbofan Engine. NASA TM X-3075, 1974.
15. Cole, Gary L.: Atmospheric Effects on Inlets for Supersonic Cruise Aircraft. AIAA Paper 77-874, July 1977.
16. Cole, Gary L.; Cwynar, David S.; and Geyser, Lucille C.: Wind-Tunnel Evaluation of the Response of a YF-12 Aircraft Flight Inlet to Internal Airflow Perturbations by Frequency-Response Testing. NASA TM X-3141, 1974.
17. Neiner, George H.; Arpasi, Dale J.; and Dustin, Miles O.: Wind-Tunnel Evaluation of YF-12 Aircraft Inlet Control System by Frequency-Response and Transient Testing. NASA TM X-3142, 1975.
18. Arpasi, Dale J.; Zeller, John R.; and Batterton, Peter G.: A General Purpose Digital System for On-Line Control of Air-breathing Propulsion Systems. NASA TM X-2168, 1971.
19. Reukauf, Paul J.; Burcham, Frank W., Jr.; and Holzman, Jon K.: Status of a Digital Integrated Propulsion/Flight Control System for the YF-12 Airplane. AIAA paper 75-1180, Sep. 1975.
20. Seidel, Robert C.; and Lehtinen, Bruce: Control System Design Using Frequency Domain Models and Parameter Optimization, With Application to Supersonic Inlet Controls. NASA TM X-3108, 1974.
21. Neiner, George H.; Seidel, Robert C.; and Arpasi, Dale J.: Wind-Tunnel Evaluation of Experimental Controls on YF-12 Aircraft Flight Inlet by Frequency-Response and Transient Testing. NASA TM X-3143, 1975.
22. Cubbison, Robert W.: Wind-Tunnel Performance of an Isolated, Full-Scale, YF-12 Aircraft Inlet at Mach Numbers Above 2.1. NASA TM X-3139, 1978.
23. Cubbison, Robert W.: Effects of Angle of Attack and Flow Bypass on Wind-Tunnel Performance of an Isolated, Full-Scale, YF-12 Aircraft Inlet at Mach Numbers Above 2.075. NASA TM X-3140, 1978.

24. Webb, John A., Jr.; Mehmed, Oral; and Hiller, Kirby, W.: Improved Design of a High Response Slotted Plate Overboard Bypass Valve for Supersonic Inlets. NASA TM X-2812, 1973.
25. Wind-Tunnel Installation of Full-Scale Flight Inlet of YF-12 Aircraft for Steady-State and Dynamic Evaluation. NASA TM X-3138, 1974.
26. Campbell, David H.: F-12 Series Aircraft Propulsion System Performance and Development. J. Aircr., vol. 11, no. 11, Nov. 1974, pp. 670-676.
27. Dustin, Miles O.; Cole, Gary L.; and Neiner, George H.: Continuous-Output Terminal-Shock-Position Sensor for Mixed-Compression Inlets Evaluated in Wind Tunnel Tests of YF-12 Aircraft Inlet. NASA TM X-3144, 1974.
28. Willoh, Ross G.: A Mathematical Analysis of Supersonic Inlet Dynamics. NASA TN D-4969, 1968.
29. Neiner, George H.; Cole, Gary L.; and Arpasi, Dale J.: Digital-Computer Normal Shock Position and Restart Control of a Mach 2.5 Axisymmetrix Mixed-Compression Inlet. NASA TN D-6880, 1972.
30. Zeller, John R.; et al.: Analytical and Experimental Performance of Optimal Controller Designs for a Supersonic Inlet. NASA TN D-7188, 1973.
31. Cole, Gary L.; Neiner, George H.; and Wallhagen, Robert E.: Coupled Supersonic Inlet-Engine Control Using Overboard Bypass Doors and Engine Speed to Control Normal Shock Position. NASA TN D-6019, 1970.
32. Paulovich, Francis J.; Neiner, George H.; and Hagedorn, Ralph E.: A Supersonic Inlet-Engine Control Using Engine Speed as a Primary Variable for Controlling Normal Shock Position. NASA TN D-6021, 1971.
33. Gilyard, Glenn B.; Berry, Donald T.; and Belte, Daumantes: Analysis of a Lateral-Directional Airframe/Propulsion System Interaction of a Mach 3 Cruise Aircraft. AIAA Paper 72-961, Sep. 1972.
34. Powers, Bruce G.: Phugoid Characteristics of a YF-12 Airplane with Variable-Geometry Inlets Obtained in Flight Tests at a Mach Number of 2.9. NASA TP-1107, 1977.

TABLE I. - DIGITAL SYSTEM CAPABILITIES

Digital computer

Magnetic core memory size, words	16 384
Word length, bits plus parity.	16
Memory cycle time, nsec.	750
Add time, μ sec	1.5
Multiply time, μ sec	4.5
Divide time, μ sec	8.25
Load time, μ sec	1.5
Indirect addressing	Infinite
Indexing	Total memory
Priority interrupts	28 separate levels
Index registers	2
Interval timers	2

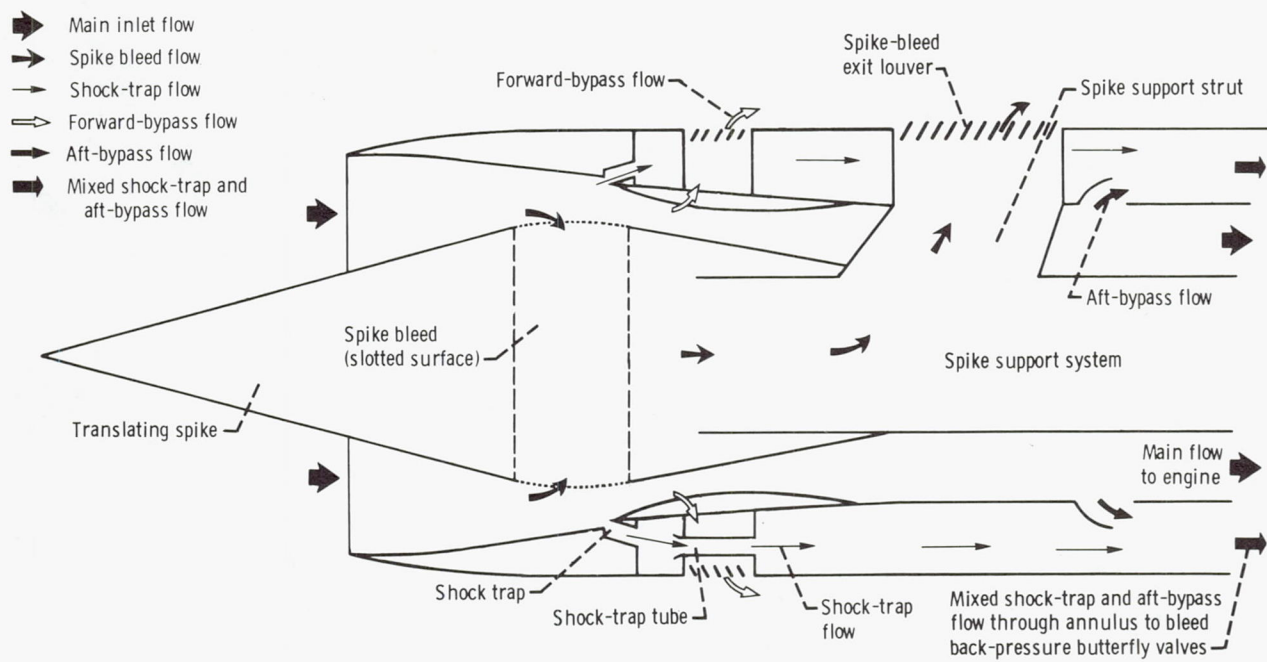


Figure 1. - Schematic diagram of inlet geometry and locations of bleeds and bypasses.

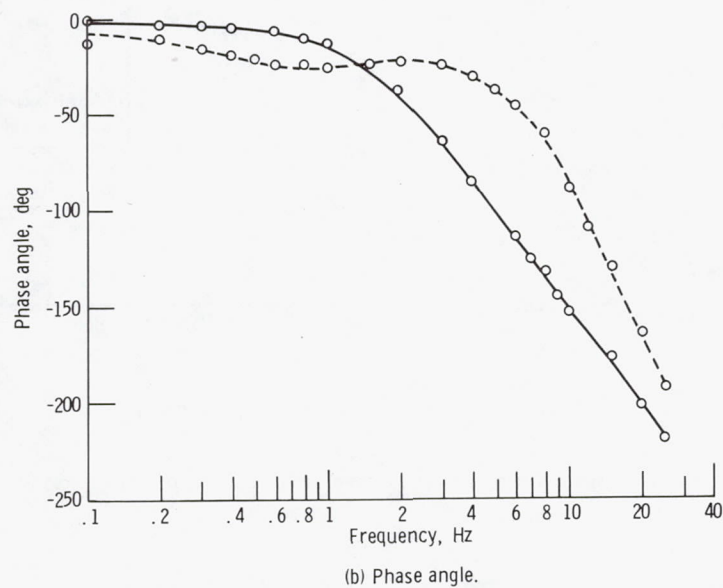
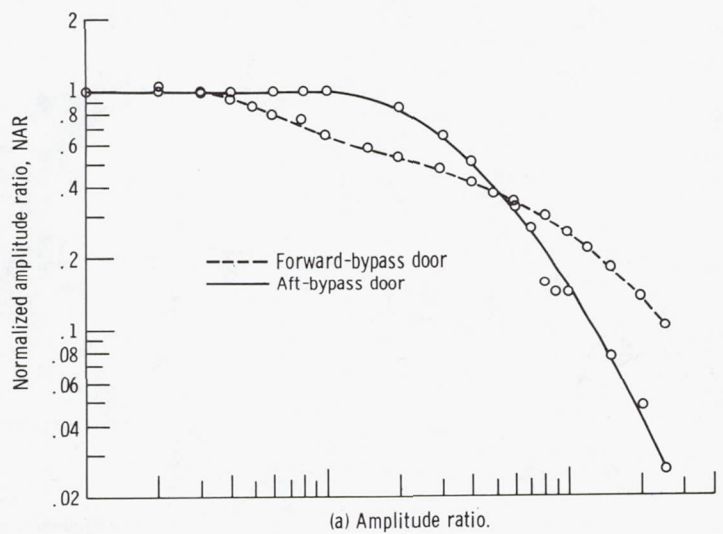


Figure 2. - Frequency response of forward- and aft-bypass position to command voltage. (Commanded peak-to-peak amplitude, 10 percent of maximum door area for forward-bypass and 20 percent for aft-bypass.)

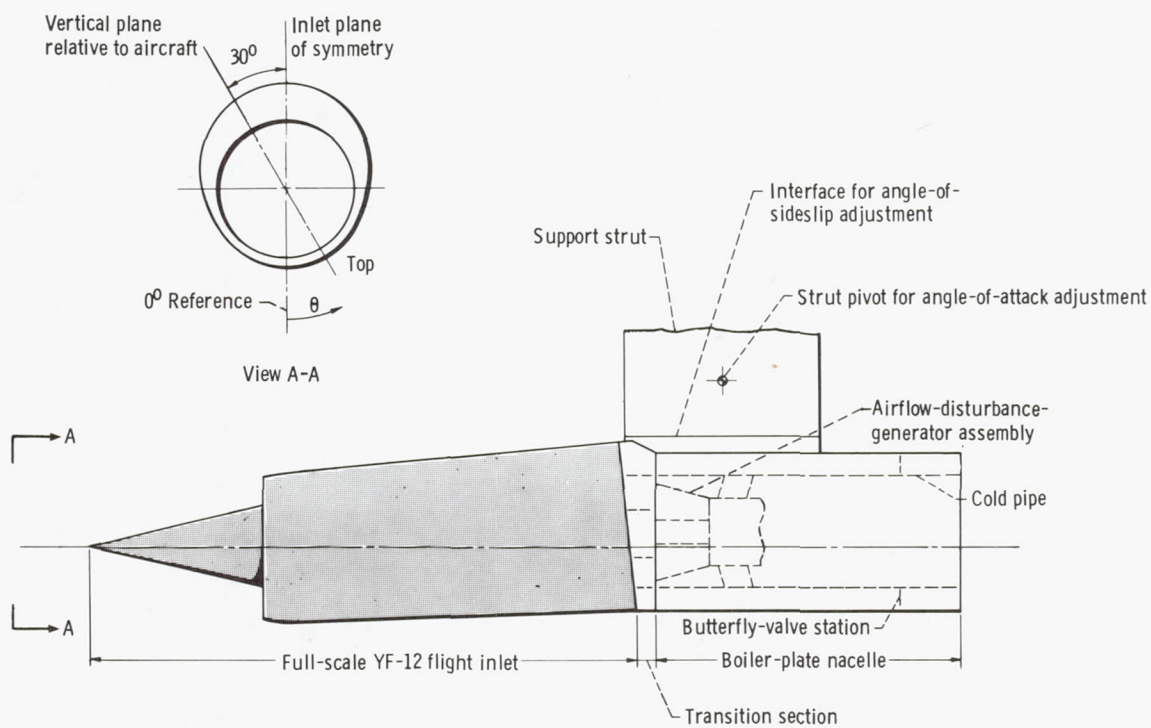


Figure 3. - Schematic diagram of inlet installation in test section of 10- by 10-Foot Supersonic Wind Tunnel.

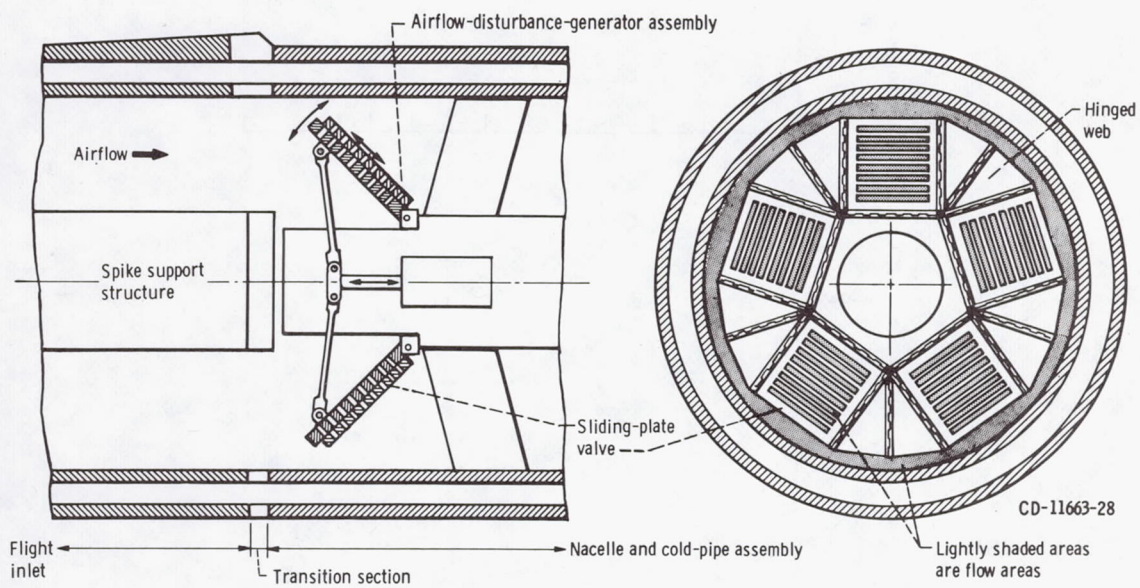


Figure 4. - Schematic diagram of airflow-disturbance generator.

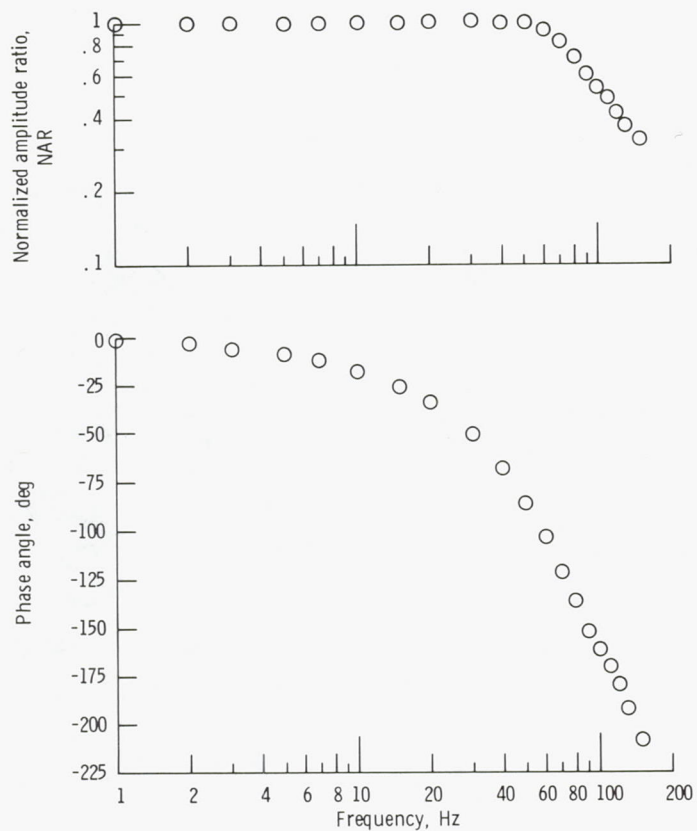


Figure 5. - Frequency response of airflow-disturbance-generator sliding-plate valve (disturbance door) position to position command voltage. (Commanded peak-to-peak amplitude, 10 percent of maximum valve area.)

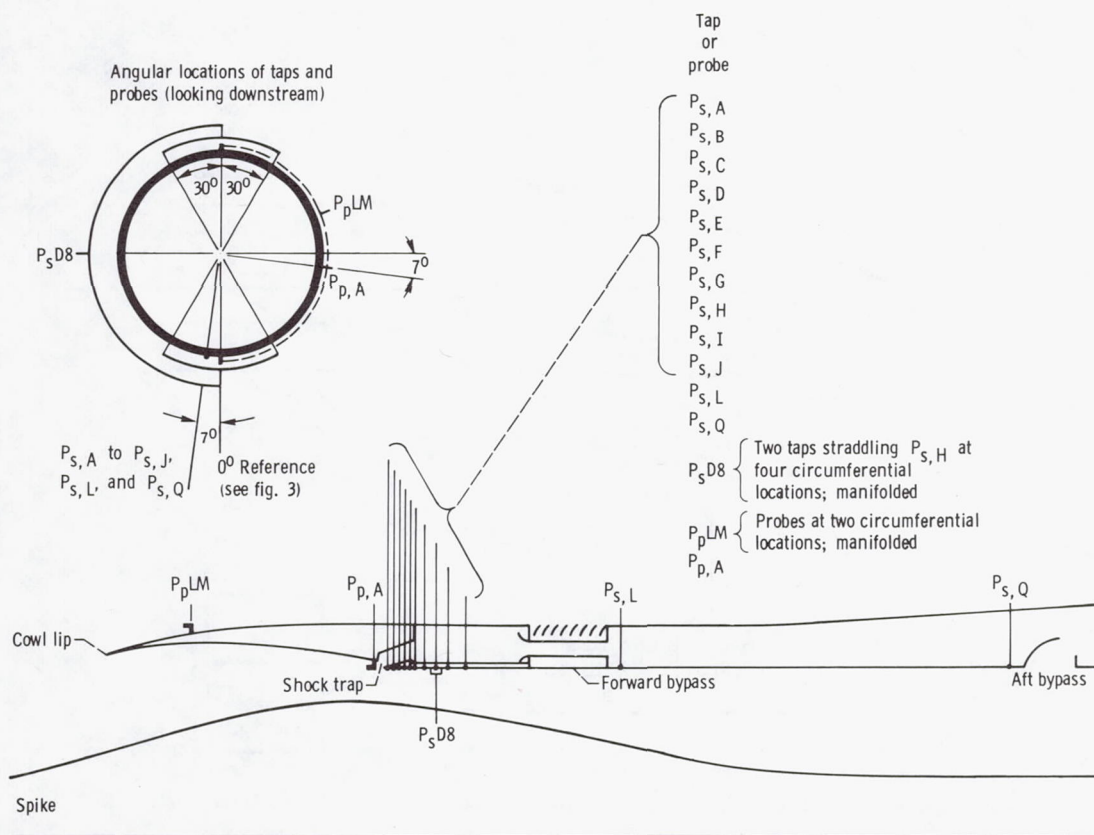


Figure 6. - Schematic diagram showing locations of static- and total-pressure measuring stations connected to high-response transducers.

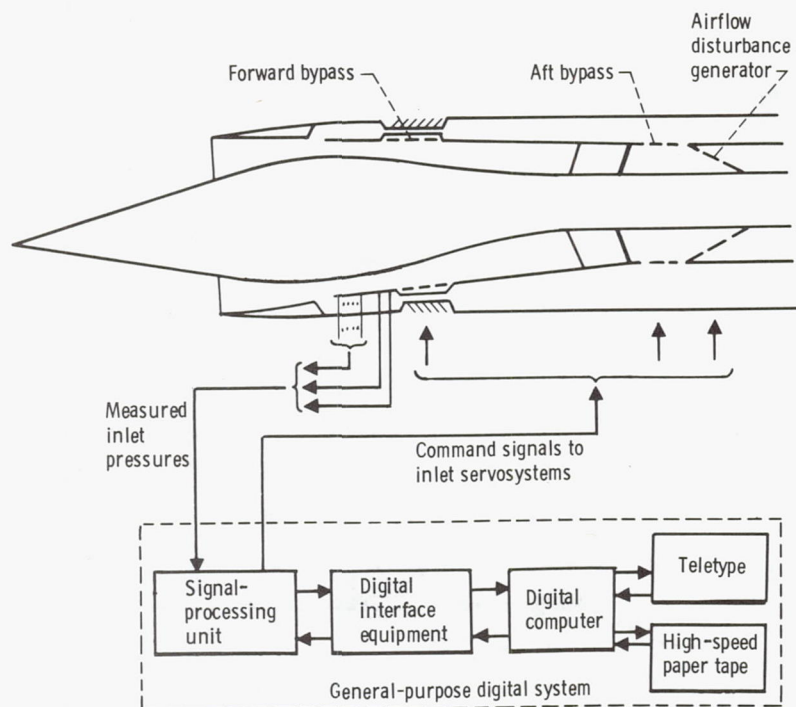


Figure 7. - Schematic representation of experimental setup in the 10- by 10-Foot Supersonic Wind Tunnel.

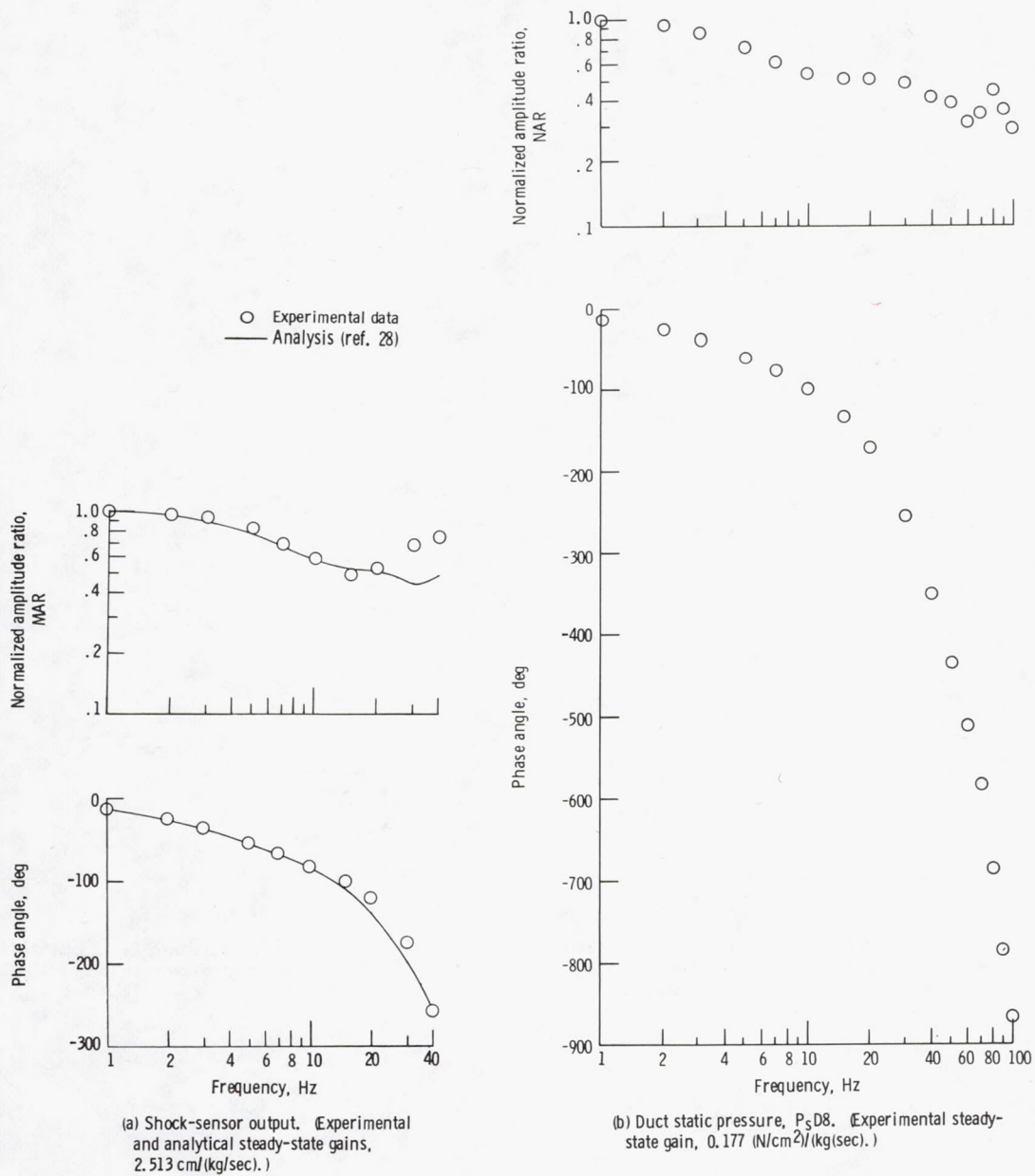
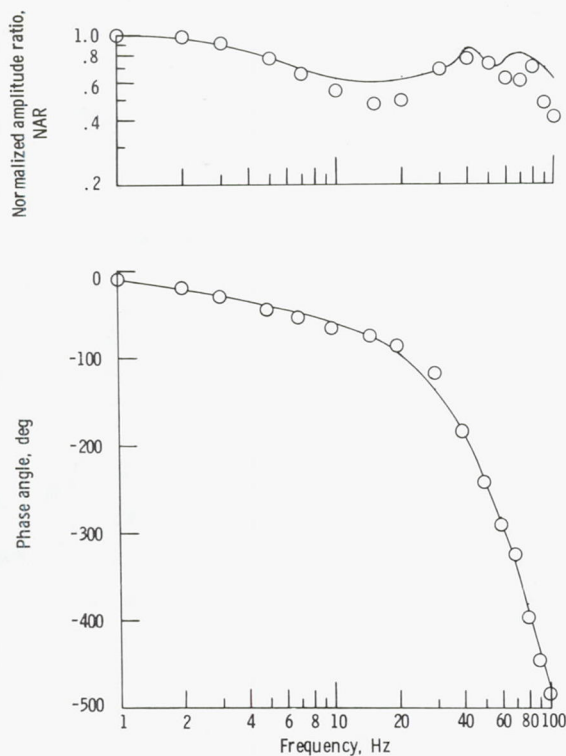
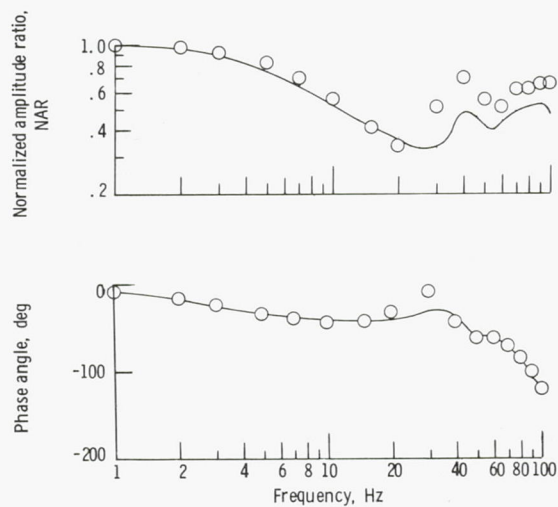


Figure 8. - Inlet signal responses to airflow-disturbance generator at Mach 2.956 conditions.



(c) Throat-exit static pressure, $P_{s, I}$. (Experimental steady-state gain, $0.104 \text{ (N/cm}^2\text{)/(kg/sec)}$; analytical steady-state gain, $0.066 \text{ (N/cm}^2\text{)/(kg/sec)}$.)



(d) Diffuser-exit static pressure, $P_{s, Q}$. (Experimental steady-state gain, $0.060 \text{ (N/cm}^2\text{)/(kg/sec)}$; analytical steady-state gain, $0.044 \text{ (N/cm}^2\text{)/(kg/sec)}$.)

Figure 8. - Concluded.

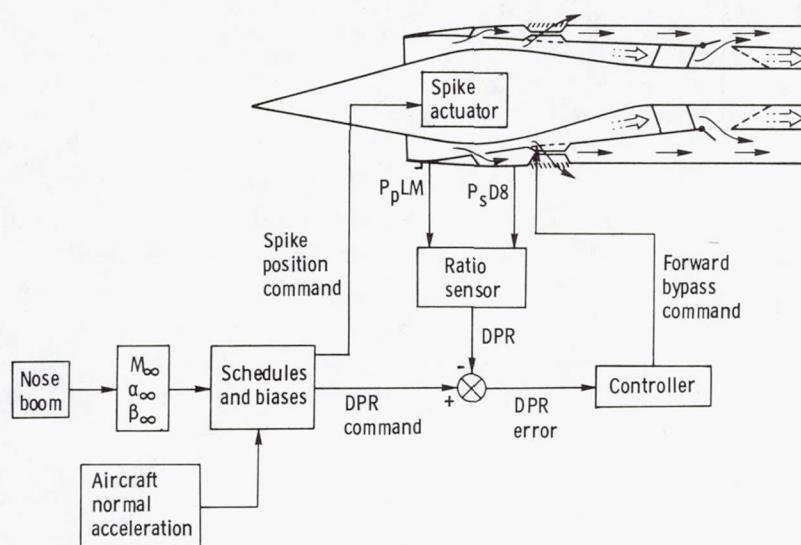


Figure 9. - Schematic of YF-12 aircraft inlet control system.

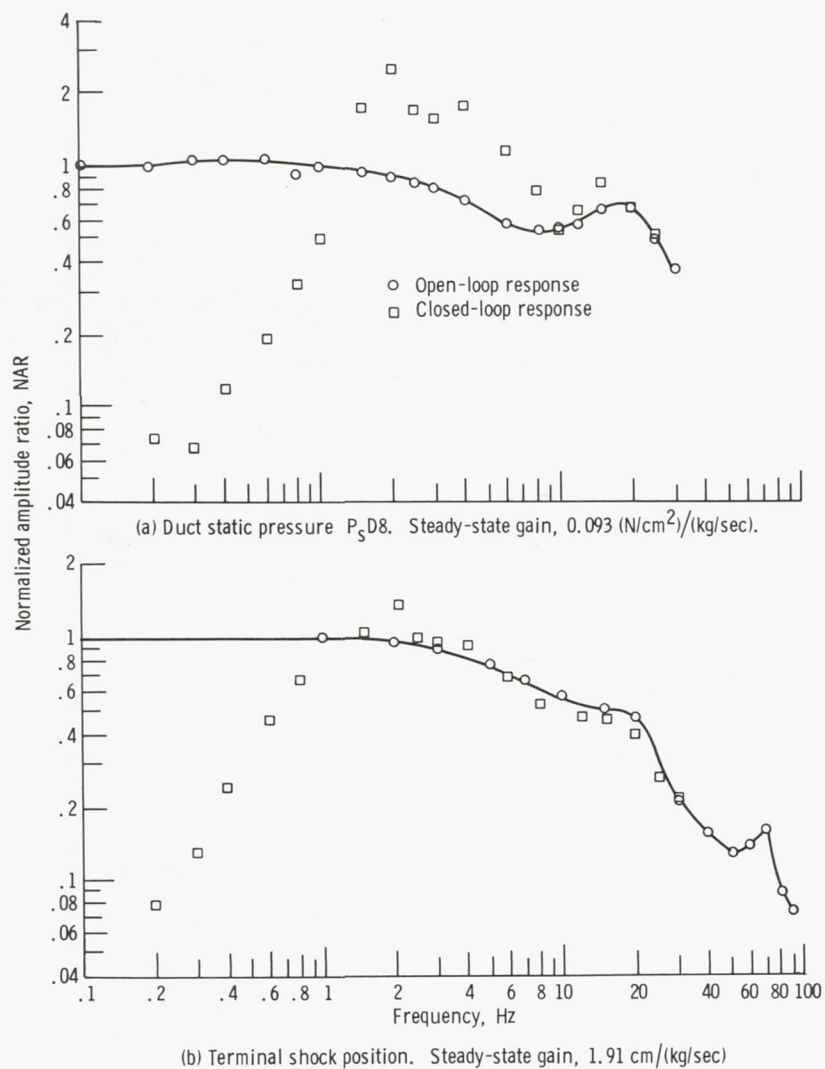
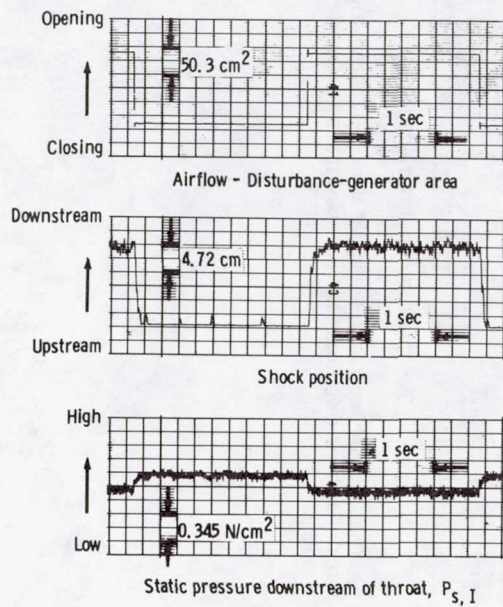
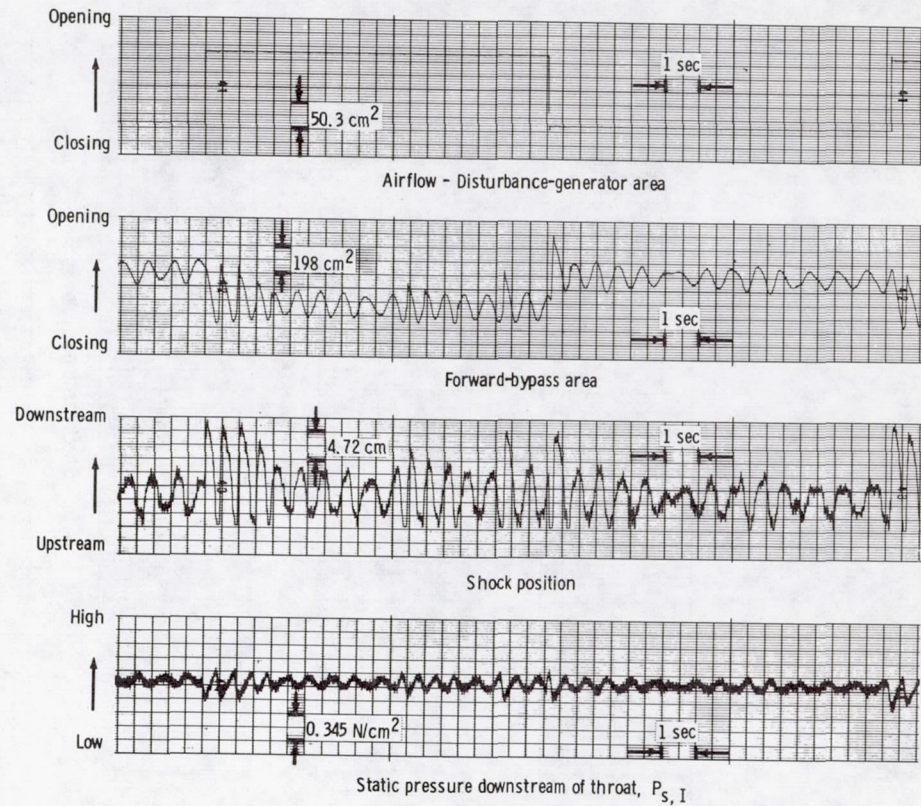


Figure 10. - Frequency responses of two inlet signals to airflow-disturbance generator, at Mach 2.474 conditions, with and without the duct-pressure-ratio control system of the aircraft.



(a) Open-loop responses.



(b) Closed-loop responses.

Figure 11. - Transient response of the duct-pressure-ratio control system of the YF-12 aircraft to the airflow-disturbance generator at Mach 2.474 conditions.

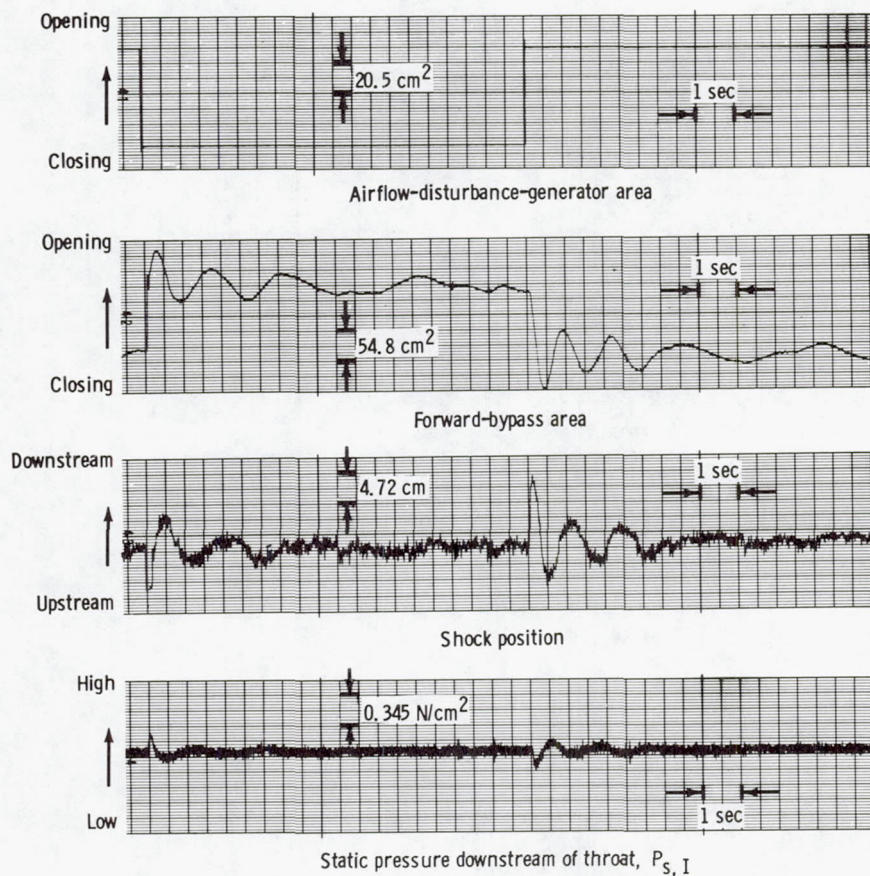


Figure 12. - Closed-loop transient responses of the YF-12 aircraft duct-pressure-ratio control system at reduced gain to the airflow-disturbance generator at Mach 2.474 conditions.

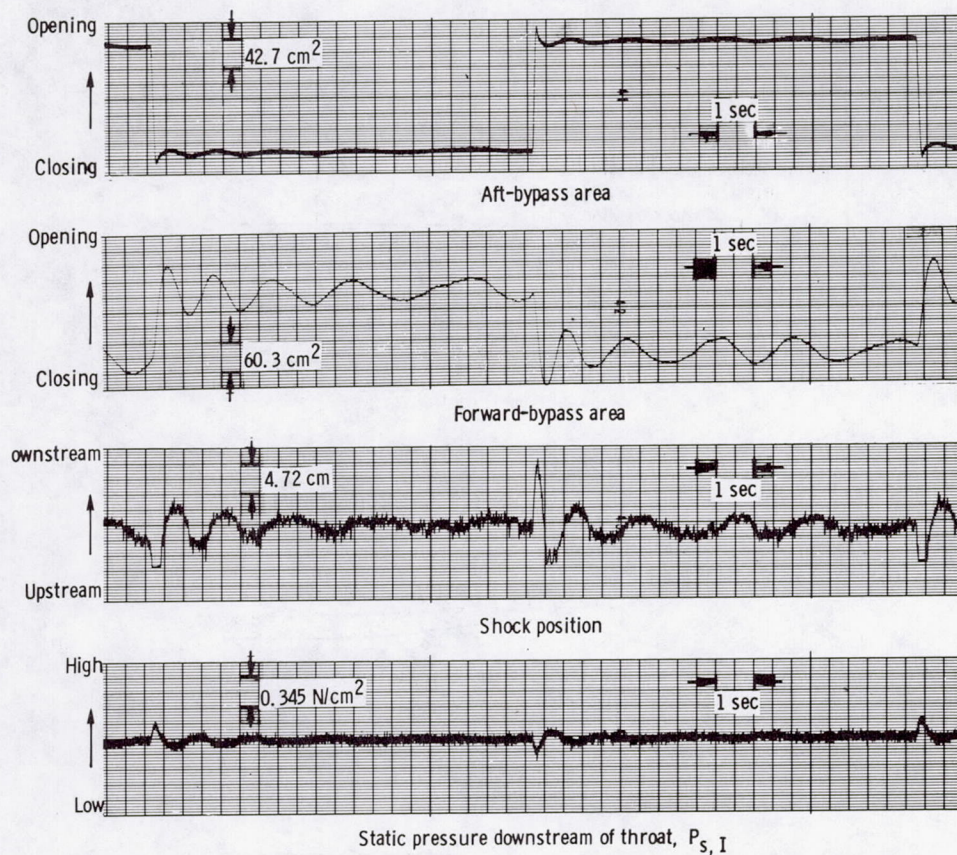


Figure 13. - Closed-loop transient responses of the YF-12 aircraft duct-pressure-ratio control system at reduced gain to an aft-bypass disturbance at Mach 2.474 conditions.

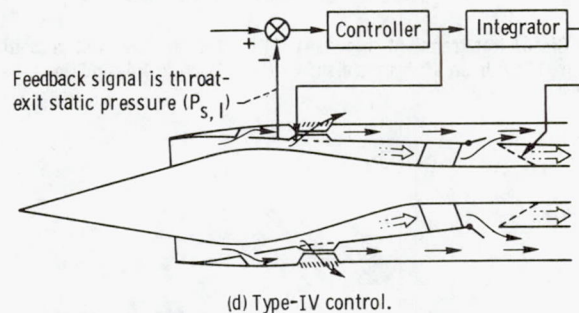
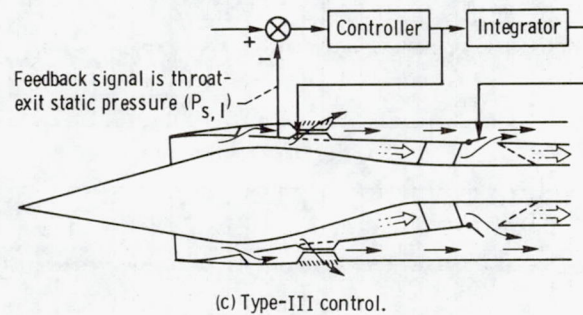
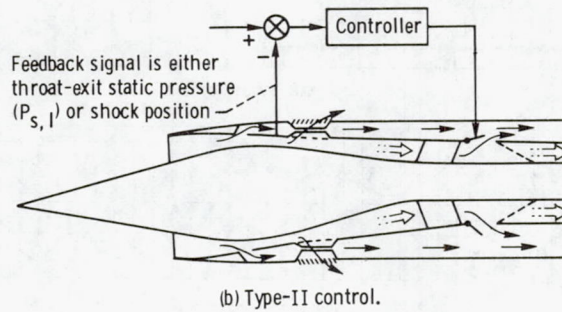
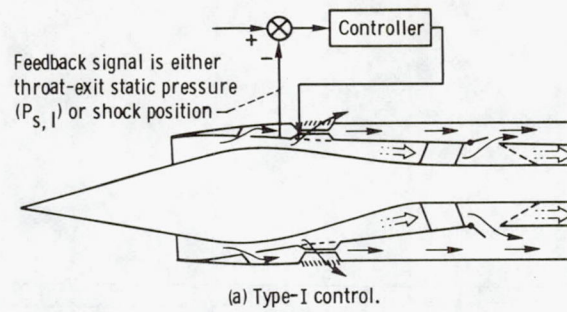


Figure 14. - Block diagrams of experimental, proportional-plus-integral, shock-position controls for YF-12 aircraft inlet.

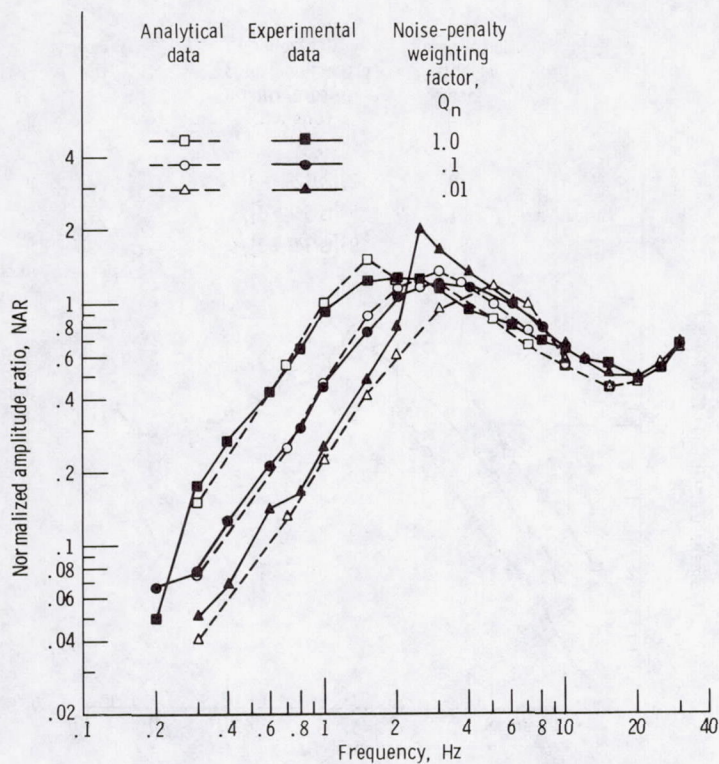


Figure 15. - Analytical and experimental closed-loop frequency responses of throat-exit static pressure $P_{s, I}$ for type-I controller with $P_{s, I}$ as feedback signal for various values of noise-penalty weighting factor Q_n . Mach 2.956 conditions.

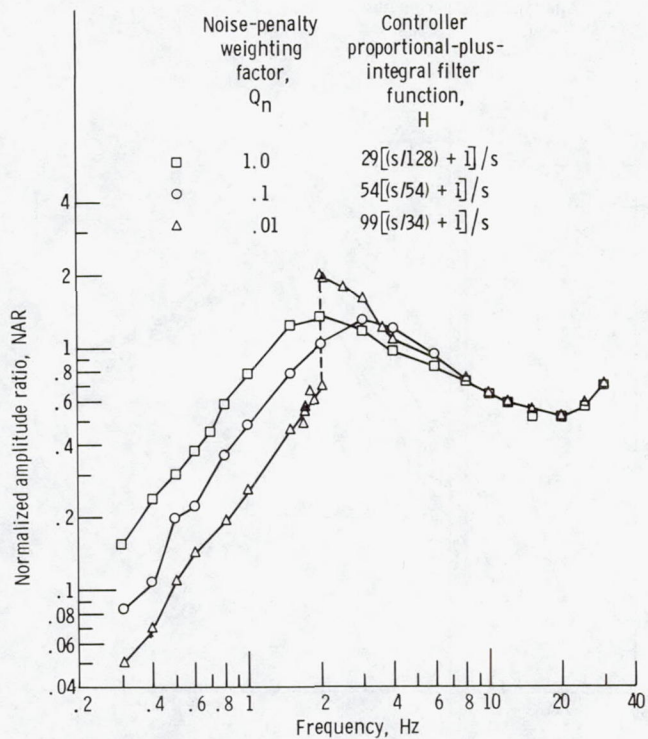


Figure 16. - Experimental closed-loop frequency responses of throat-exit static pressure $P_{s, I}$ for various values of noise-penalty weighting factor Q_n showing effect of non-linearity. Type-I control system. Mach 2.956 conditions.

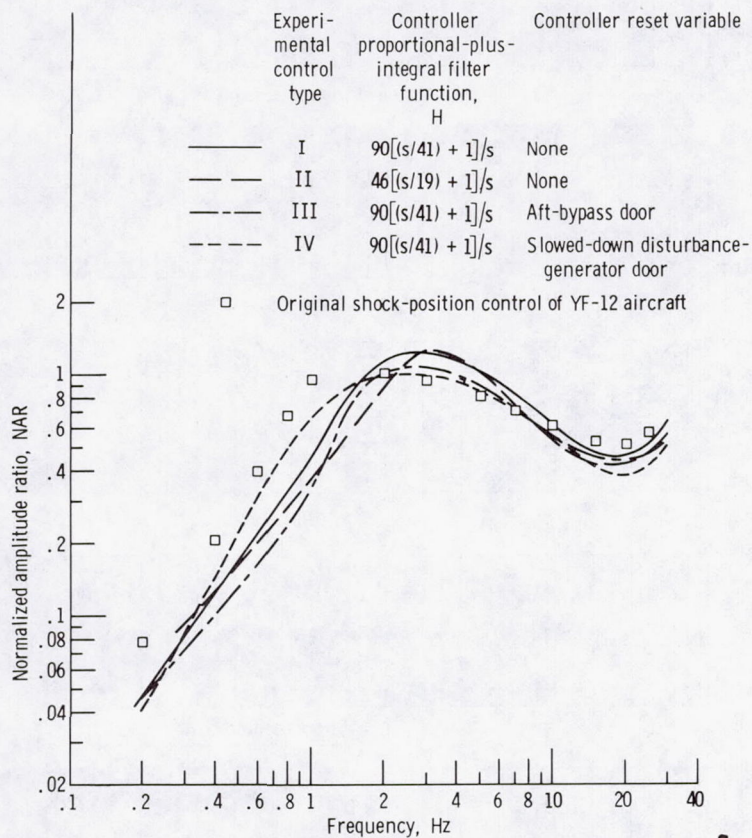


Figure 17. - Comparison of shock-position frequency responses of experimental controls with response of original shock control of YF-12 aircraft. Throat-exit static pressure $P_{s, I}$ used as feedback signal for experimental controls, and duct static pressure $P_{s, D8}$ used as feedback for shock control of aircraft. Noise-penalty weighting factor Q_n for experimental controls was 0.1. Airflow-disturbance generator used as disturbance. Mach 2.956 conditions.

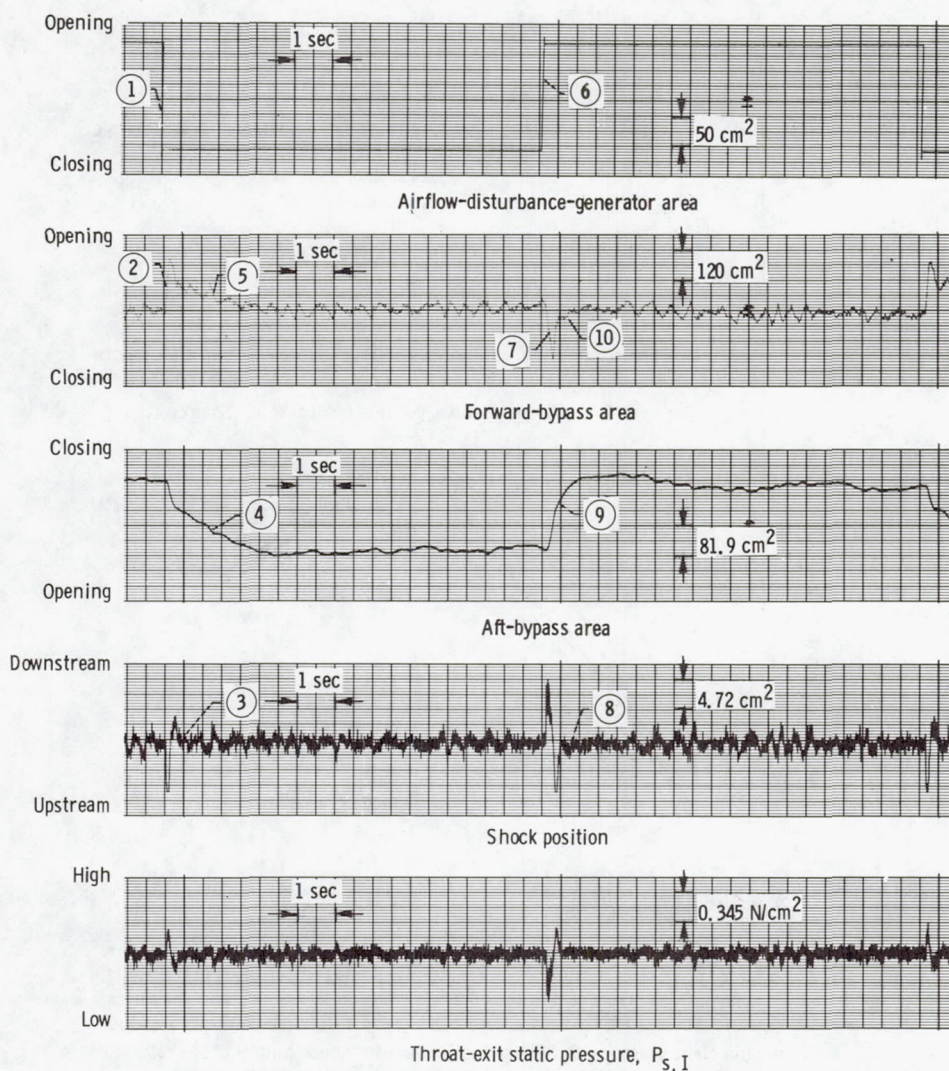


Figure 18. - Transient responses of type-III experimental shock-position control. Controller proportional-plus-integral filter function H was $90.4[(s/40.8) + 1]/s$. Mach 2.956 conditions.

FLIGHT-MEASURED TRANSIENTS RELATED TO
INLET PERFORMANCE ON THE YF-12 AIRPLANE

Paul J. Reukauf, Frank V. Olinger,
L. J. Ehernberger, and Craig Yanagidate
Dryden Flight Research Center

SUMMARY

As part of the YF-12 experiments program, the response of the inlet and inlet control system to transient phenomena was investigated in flight. A four-part study addressed characteristics associated with: (1) the pressure frequency response of the inlet, (2) the effects of compressor stalls, (3) the response to inlet unstarts, and (4) the effects of free stream turbulence.

Results from the first phase of the investigation revealed that the inlet duct has a lower open-loop frequency-response capability for sinusoidal inputs than does a full-scale wind tunnel model of the same inlet. Closed-loop frequency response, measured with the forward bypass doors active, also indicated that the inlet control system is less effective in controlling sinusoidal pressure inputs than is the full-scale wind tunnel model inlet control system.

Results from the second phase of the investigation indicated that the maximum overpressure induced by a compressor stall occurs at the location of the terminal normal shock wave with a magnitude that is a function of decreasing flow area.

The third phase of the investigation revealed that an unstarted inlet should be restarted as quickly as possible to minimize airplane performance loss. A quick inlet restart cycle could be accomplished using an active restart sensor.

The last phase of the investigation revealed that free stream turbulence does not have a significant effect on the internal static pressures of the YF-12 inlet. It also indicated that inlet unstart margins are not significantly affected by the turbulence.

WIND-TUNNEL PERFORMANCE OF A THROAT-BYPASS STABILITY SYSTEM FOR THE YF-12 INLET

Gary L. Cole, Miles O. Dustin, and George H. Neiner
Lewis Research Center

SUMMARY

The purpose of an inlet throat-bypass stability system is to allow higher performance of mixed-compression inlets while maintaining a substantial tolerance to internal and external flow-field disturbances. The objective of this program was to demonstrate the feasibility of a complete flight-hardware system. The basic concept has been demonstrated with wind-tunnel models. A YF-12 aircraft inlet was modified so that stability-bleed airflow could be removed through a porous cowl-bleed region just upstream of the inlet's shock trap. Bleed-plenum exit area was controlled by relief-type mechanical valves. The valves are designed for use in a high-Mach-number (3+) flight environment, and the system, with minor modifications, could be tested on a NASA YF-12 research aircraft. The valves provide their own reference pressure; hence, they do not respond to slowly varying disturbances that are handled by the inlet's control system. Wind-tunnel development of the stability-bleed pattern is discussed, and steady-state inlet and bleed performance data are presented. Transient performance of the unmodified inlet and the inlet with valves installed is presented for simulated engine corrected airflow disturbances. Transient performance data are presented for the inlet with valves installed for a rapid disturbance consisting of a change in both angle of attack and spike-tip Mach number. Results for slow angle-of-attack disturbances are also discussed. The results of this investigation show that (1) the stability system can absorb diffuser-exit airflow disturbances that are too fast for the inlet's control system and that the two systems complement each other; and (2) the stability system provides increased tolerance to transients in angle of attack and spike-tip Mach number and provides additional time for the inlet control system to respond. Some comments are made concerning the design of future stability systems.

FLIGHT TEST EXPERIENCE WITH A DIGITAL AIRFRAME/
PROPULSION CONTROL SYSTEM ON A YF-12 AIRPLANE

Paul J. Reukauf
Dryden Flight Research Center

SUMMARY

A YF-12 airplane with a digital air data system autopilot system, inlet control system, and autothrottle system is currently being flight tested at Dryden Flight Research Center. The first phase of the program consisted of programing the previously mentioned functions on a central digital computer and flight testing the resulting control laws to validate the digital system. Some of the problems which were encountered when converting the analog systems to digital systems are discussed. The second phase of the program was planned to address the problem of integrating the various systems with new control laws for flightpath and performance optimization.

SESSION VI: AERODYNAMICS

Chairman: Warner A. Robins, Langley Research Center

FLIGHT-MEASURED PRESSURE CHARACTERISTICS
OF AFT-FACING STEPS IN THICK BOUNDARY LAYER FLOW
FOR TRANSONIC AND SUPERSONIC MACH NUMBERS

Sheryll Goecke Powers
Dryden Flight Research Center

SUMMARY

Aft-facing step base pressure flight data were obtained for three step heights for nominal transonic Mach numbers of 0.80, 0.90, and 0.95, and for supersonic Mach numbers of 2.2, 2.5, and 2.8 with a Reynolds number, based on the fuselage length ahead of the step, of about 10^8 . Surface static pressures were measured ahead of the step, behind the step, and on the step face (base), and a boundary layer rake was used to obtain boundary layer reference conditions.

A comparison of the data from the present and previous experiments shows the same trend of increasing base pressure ratio (decreasing drag) with increasing values of momentum thickness to step height ratios. However, the absolute level of these data does not always agree at the supersonic Mach numbers. For momentum thickness to height ratios near 1.0, the differences in the base pressure ratios appear to be primarily a function of Reynolds number based on the momentum thickness. Thus, for Mach numbers above 2, the data analyzed show that the base pressure ratio decreases (drag increases) as Reynolds number based on momentum thickness increases for a given momentum thickness and step height.

INTRODUCTION

Aft-facing surface discontinuities such as those formed by wing trailing edges, panel trailing edges, lap joints, or other discontinuities are known to be a source of aircraft drag. Numerous theoretical and experimental studies (refs. 1 to 10) have been conducted for aft-facing steps immersed in turbulent-supersonic boundary layers. In the 1950's, theoretical flow models developed for predicting base pressures were usually simplified by assuming that the approaching boundary layer had either a zero thickness or a thickness approaching zero. For example, Korst's theory (ref. 1) and Chapman's flow model (ref. 2) used this assumption.

In the early 1950's, the data from supersonic experiments by Chapman, Wimbrow, and Kester (ref. 3) established a correlation that accounted for the effect of the approaching boundary layer thickness on the base pressure. In the mid 1960's, Hastings (ref. 4) extended the data base for supersonic flow to include boundary layers and momentum thicknesses that were relatively large compared to the step height (momentum thickness to step height ratio ≈ 2); however, the absolute thickness of the boundary layer, and hence the momentum thickness, was very small (momentum thickness < 0.05 cm). Two aft-facing step experiments (refs. 5 and 6) which had relatively large absolute values of momentum thickness and large values of momentum thickness to step height ratios (2.4 and 1.3, respectively) yielded a lower base pressure ratio (higher drag) than was obtained from the thin boundary layer data (ref. 4) for momentum thickness to step height ratios near 1. The base pressure ratio disagreement became more pronounced as Mach number increased above Mach 2. The reason for the disagreement between the thick and thin boundary layer data obtained at supersonic speeds is not fully understood, primarily because of the limited amount of experimental information. Therefore, the present study was undertaken to acquire additional experimental results to better analyze the differences between the thick and thin boundary layer data.

A YF-12 aircraft was used as a testbed for this study because of its ability to maintain given flight conditions from subsonic to triple-sonic speeds. The study provided thick boundary layer data for Reynolds number conditions that were different from the conditions obtained in the previous studies. This enabled additional insight to be gained into the effect of Reynolds number on aft-facing step drag.

This report presents base pressure data for three step heights at Mach numbers from approximately 0.80 to 0.95 and from approximately 2.2 to 2.8 for Reynolds numbers on the order of 10^8 based on a turbulent flow length of 21.53 meters. The ratio of momentum thickness to step height ranged from about 0.2 to 1.3. Surface static pressures ahead of and behind the step were also measured and are presented. A boundary layer rake was used to measure the local velocity profiles from which the local surface and boundary layer conditions were determined.

SYMBOLS

Physical quantities in this report are given in the International System of Units (SI); however, measurements were taken in U.S. Customary Units. Factors relating the two systems are provided in reference 11.

$$c_{p_b} \quad \text{base pressure coefficient, } \frac{p_b - p_r}{0.7 M_\infty^2 p_r}$$

D drag, N

h step height, cm

M	Mach number
p	static pressure, N
R_θ	Reynolds number based on momentum thickness, θ
u	flow velocity, m/sec
x	longitudinal distance from step (positions in front of the step are negative), cm
y	distance above surface (perpendicular to x), cm
δ	boundary layer thickness, cm
θ	momentum thickness, $\int_0^\delta \frac{\rho u}{\rho_e u_e} (1 - u/u_e) dy$, cm
ρ	air density, kg/m ³

Subscripts:

b	step face or base of aft-facing step
e	conditions at edge of boundary layer
r	local reference
∞	free stream

DESCRIPTION OF INSTRUMENTATION

The upper surface of the fuselage of a YF-12 aircraft was selected as the location for the experiment. A photograph showing the experiment location on the aircraft is provided in figure 1. In the area where the test was conducted, the fuselage diameter is 162.56 centimeters.

The test section was approximately 0.9 meter wide and 3.2 meters long. It consisted of a ramp region, a reference region, a recovery region, and two boundary layer rake complexes shown in figure 2(a). The ramp region had a slope of approximately 1.12° relative to the surface of the aircraft. This provided a gradual transition for the flow passing from the upper fuselage surface to the reference region height. Between flights, the step heights were changed by raising or lowering the recovery surface relative to the level of the reference region. A typical step installation is shown in figure 2(b). The step heights studied in this experiment were 0.33 centimeter, 0.63 centimeter, and 1.19 centimeters. The reference and recovery regions were parallel to within 0.67°.

Pressure orifices were located along the surfaces of the reference and recovery regions and the step face. These orifices can be seen in figure 2(c). The pressure measured from an orifice location 20.42 centimeters ahead of the step was used as the local reference pressure. An average base pressure was determined by manifolding the pressures from the three base pressure orifices.

A boundary-layer rake complex is shown in figure 3. One rake complex was located in the reference region 51 centimeters ahead of the step; the other was located 30 centimeters behind the step.

TEST CONFIGURATION AND CONDITIONS

Reference boundary-layer characteristics were determined both ahead of and behind the step (test) station. The reference characteristics behind the test station were obtained for a flush configuration. The forward rake was always removed for the flush configuration. These boundary layer data were used to define the momentum thickness used for the aft-facing step data analysis. Surface pressure measurements were also made ahead of and behind the step station for the flush configuration.

Aft-facing step base pressures and the surface pressure distributions were obtained with the forward rake removed for step heights of 0.33, 0.63, and 1.19 centimeters. Data were obtained at nominal Mach numbers of 0.80, 0.90, and 0.95 and at 2.2, 2.5, and 2.8 for each configuration studied.

For the Mach numbers used in the experiment, because of the length of the run to the test station, turbulent flow was assumed to originate at the aircraft nose. The turbulent run length was 21.01 meters for the forward rake station, 21.53 meters for the aft-facing step station, and 21.86 meters for the aft rake station. Momentum thickness for the aft-facing step station was considered to be the average of the values obtained from the forward and aft rakes. Analysis of the boundary layer rake and the Preston probe data indicated that the flow was not fully two-dimensional at the test section; therefore, it was treated as being quasi-two-dimensional. The method used to analyze the boundary layer rake and Preston probe data is provided in reference 8.

The base pressures, surface static pressures, and rake probe pressures were obtained using three 48-port multiplexing valves (scanivalves), each equipped with a differential pressure transducer referenced to a high-resolution, absolute-pressure transducer. Air data quantities, such as free stream values of Mach number and static pressure, were obtained from the airplane's air data system. A description of the air data system can be found in reference 12.

RESULTS AND DISCUSSION

Surface Pressure Distribution

Figures 4 and 5 present the surface static pressure distribution ahead of and

behind the step station. In these figures the ratio of surface pressure to local reference pressure is plotted as a function of the distance from the step for representative Mach numbers of 0.80 and 2.2. These data are included to demonstrate the uniform flow conditions that existed at the local reference pressure location and well upstream and well downstream of the step location. Although the curves show the pressure changes caused by the step, it is more convenient to compare the pressure changes for the different step heights by normalizing the distance from the step using the respective step height.

In figure 6, pressure ratio is plotted as a function of the normalized distance, x/h , ahead of and behind the step for each of the nominal Mach numbers used in this study. The pressure rise behind the step was found to occur at a normalized distance of approximately 4 for the transonic data. At Mach numbers equal to or greater than Mach 2.2, the pressure rise occurred at a normalized distance of about 2. Data from other sources are included for comparison in figures 6(a) to 6(c) and 6(e). The data from references 4, 6, and 13, and that shown later from reference 5, were obtained from two-dimensional shapes and were considered to have two-dimensional flow conditions. The trends of data from the various sources were much the same behind the step for all Mach numbers; however, at Mach 0.95, for x/h values below 12, the absolute values of the data from the present study and from reference 13 were significantly different. The larger differences appearing at this Mach number were not surprising because the base pressure could change rapidly for Mach numbers from 0.95 to 1.0 and, in addition, the differences in base pressure for these Mach numbers seemed to be a function of θ/h , as indicated by the results of the present study as well as references 6 and 13. The thicker boundary layer data, and the corresponding larger θ/h values, appeared to decrease the maximum change in base pressure. Further data relating the influence of θ/h on base pressure will be shown in following sections of this report.

Pressure influences caused by the step can be observed further downstream and in the region immediately ahead of the step location. The final pressure ratio recovery behind the step for the present study was slightly greater than 1 for the transonic data (see figs. 4 and 6(a) to 6(c)) and slightly less than 1 for the supersonic data (see figs. 5 and 6(d) to 6(f)).

The effect of step base pressure on the upstream reference region pressures can be seen in figures 4 and 6(a) to 6(c). As shown, the lower pressures in the base region propagated upstream and influenced the pressure region immediately ahead of the base. This did not occur at the supersonic flow conditions (figs. 5 and 6(d) to 6(f)).

Base Pressures

The base pressure ratio, p_b/p_r , for a given Mach number has been shown to be a function of θ/h , with p_b/p_r increasing (drag decreasing) as θ/h increases. A substantial amount of such base pressure data at supersonic Mach numbers exists for θ/h values less than 1.0, as indicated in references 9 and 10. However, corresponding data at transonic speeds for θ/h values greater than or equal to 1.0 are quite limited.

Base pressure results from the flight experiments of the present study and reference 6, and from the wind tunnel experiments of references 4 and 5, include data for θ/h values near 1.0. Base pressure ratio values from the present experiment, and from some previous experiments, are shown as a function of θ/h in figure 7. Tabulated data for the present experiment are also provided in table 1. The data shown in figure 7 established the expected trend of increasing base pressure ratio (decreasing drag) with increasing θ/h values. However, the absolute level of these data did not always agree at the supersonic Mach numbers for the θ/h values shown. For example, for values of θ/h near 1.0, the maximum spread in p_b/p_r increased with Mach number from less than 0.1 at about Mach 2.2 to 0.2 at about Mach 2.8. When the differences for Mach 2.8 shown in figure 7(f) were converted into drag penalties representative of discontinuities found on a supersonic cruise airplane, the results were as provided in the following table.

Drag penalty for a 30.5-meter, aft-facing step (lap joint) at a cruise altitude of 20,000 meters and with a step height of 2 millimeters.					
Data source	M	θ/h	R_θ	Drag, N	$\frac{D - D_{\text{ref. 4}}}{D_{\text{ref. 4}}}$, percent
Wind tunnel (ref. 4)	2.8	0.7	4.1×10^3	129	---
Flight (present study)	2.9	0.7	7.9×10^3	165	27
Wind tunnel (ref. 5)	2.8	0.7	4.3×10^5	205	59

Note that the difference between the step (lap joint) drag penalty of the present experiment and that reported in reference 4 amounts to 27 percent. The corresponding Reynolds numbers based on momentum thickness are 7.9×10^3 and 4.1×10^3 , respectively. Furthermore, the wind tunnel results from reference 5, with $R_\theta = 4.3 \times 10^5$, indicate a drag penalty 59 percent greater than that obtained from the results of reference 4. As indicated by the trend shown in the preceding table, these significant differences appear to be associated with the Reynolds number based on momentum thickness.

The variation of base pressure ratio with R_θ for a given θ/h value near 1.0 is shown in figures 8(a) and 8(b) for test Mach numbers above 2.4. The data from the various sources indicate that there is a relationship between base pressure ratio and R_θ for a given value of M and θ/h . A carefully controlled experiment covering a wide range of the important variables will be required to establish a firm relationship between the influencing variables and base pressure.

Data from the various experiments, in the form of base pressure ratio, p_b/p_r , as a function of θ/h have been shown to be effective for observing the degree to which Reynolds number, and hence viscosity, influences these pressures; however,

the method provides little direct information on the resulting drag. The base pressure coefficient, which is directly related to base drag, is plotted as a function of Mach number in figure 9. Results from this and other experiments, and from the incompressible semiempirical estimate of Hoerner (ref. 14), are shown in figure 9(a) for Mach numbers up to approximately 1.0. Hoerner's incompressible estimate uses θ/h to account for viscous effects. The incompressible estimates shown were based on θ/h values that correspond to the experimental data presented in figure 9(a).

In general, θ/h effects caused the vertical spread seen in the base pressure coefficient for a given Mach number, both for the various experimental data and for Hoerner's estimate. For Mach numbers less than 0.9, Hoerner's estimate adequately accounts for the magnitude of the vertical spread found in the experimental data, thus indicating that Hoerner's estimate adequately accounts for the viscous effects. Especially significant is the fact that, although Hoerner's expression was derived from relatively low Reynolds number water tunnel data, it appears to provide valid estimates of the viscous effects (though not necessarily the absolute levels) for

Reynolds numbers based on momentum thickness which are quite large (up to 10^5). When compared with the other data from the flight experiments, the absolute level of the results from reference 13, at Mach numbers below the point of the steep transonic rise, graphically illustrates the strong influence of θ/h on base pressure.

The variation of the base pressure coefficient with Mach number at supersonic speeds is shown in figure 9(b) for flight data from the present experiment and from reference 6. The effect of θ/h on the vertical spread of the data is about the same as for the transonic flight data and the incompressible estimate, both of which are presented in figure 9(a). A simple expression, $c_{p_b} = -0.7/M^2$, has been included in figure 9(b) as an approximation of the decay behavior of the base pressure coefficient with Mach number.

CONCLUDING REMARKS

Aft-facing step data for thick boundary layer, turbulent flow conditions were obtained from several flights of the YF-12 airplane at nominal Mach numbers of 0.80, 0.90, and 0.95 and 2.2, 2.5, and 2.8. The data were analyzed and compared with other flight and wind tunnel data and with an incompressible estimate. Analysis of the data showed the following results.

When distance from the step was expressed in terms of step height, the surface static pressure rise behind the step occurred at a normalized location of approximately 4 for all of the transonic data. The surface static pressure rise behind the step occurred at a normalized location of approximately 2 for all of the data above Mach 2.0.

The data from the present experiment and other experiments show the same trend of increasing base pressure ratio (decreasing drag) with increasing values of θ/h ; however, the absolute level of the data do not always agree at the supersonic Mach numbers for the momentum thickness to step height ratios presented. The differences in level of base pressure ratio or drag appear to be primarily a function of Reynolds

number based on momentum thickness, as shown by the data for momentum thickness to step height ratios near 1.0. For Mach numbers above 2.0, with a given momentum thickness and step height, the base pressure ratio decreases (drag increases) as Reynolds number based on momentum thickness increases.

For Mach numbers less than 0.9, the magnitude of the vertical spread in the base pressure coefficient for the experimental data is adequately accounted for by Hoerner's estimate. This indicates that Hoerner's estimate adequately accounts for viscous effects for values of Reynolds numbers, based on momentum thickness, up to 10^5 .

REFERENCES

1. Korst, H. H.: A Theory for Base Pressures in Transonic and Supersonic Flow. J. Appl. Mech., vol. 23, no. 4, Dec. 1956, pp. 593-600.
2. Chapman, Dean R.: An Analysis of Base Pressure at Supersonic Velocities and Comparison With Experiment. NACA Rept. 1051, 1951. (Supersedes NACA TN 2137.)
3. Chapman, Dean R.; Wimbrow, William R.; and Kester, Robert H: Experimental Investigation of Base Pressure on Blunt-Trailing-Edge Wings at Supersonic Velocities. NACA Rept. 1109, 1952. (Supersedes NACA TN 2611.)
4. Hastings, R. C.: Turbulent Flow Past Two-Dimensional Bases in Supersonic Streams. R. and M. No. 3401, British A.R.C., 1965.
5. Moore, D. R.: Drag Effects of Surface Roughness at High Reynolds Numbers, $M = 2.8$. Rept. No. 0-71000/4R-16, LTV Research Center, June 1964.
6. Goecke, Sheryll A.: Flight-Measured Base Pressure Coefficients for Thick Boundary-Layer Flow Over an Aft-Facing Step for Mach Numbers From 0.4 to 2.5. NASA TN D-7202, 1973.
7. Carpenter, P. W.; and Tabakoff, W.: Survey and Evaluation of Supersonic Base Flow Theories. NASA CR-97129, 1968.
8. Powers, Sheryll Goecke: Flight-Measured Pressure Characteristics of Aft-Facing Steps in High Reynolds Number Flow at Mach Numbers of 2.20, 2.50, and 2.80 and Comparison With Other Data. NASA TM-72855, 1978.
9. McDonald, H.: The Turbulent Supersonic Base Pressure Problems - A Comparison Between a Theory and Some Experimental Evidence. Rept. No. Ae 194, British Aircraft Corporation, Preston Div., Apr. 1965.
10. Nash, J. F.: An Analysis of Two-Dimensional Turbulent Base Flow, Including the Effect of the Approaching Boundary Layer. NPL Aero Rept. 1036, British A.R.C., July 30, 1962.
11. Mechtly, E. A.: The International System of Units - Physical Constants and Conversion Factors. Second Revision. NASA SP-7012, 1973.
12. Larson, Terry J.: Compensated and Uncompensated Nose Boom Static Pressures Measured From Two Air Data Systems on a Supersonic Airplane. NASA TM X-3132, 1974.
13. Nash, J. F.; Quincey, V. G.; and Callinan, J.: Experiments on Two-Dimensional Base Flow at Subsonic and Transonic Speeds. R. and M. No. 3427, British A.R.C., Jan. 21, 1963. (Supersedes NPL Aero Rept. 1070.)

14. Hoerner, Sighard F.: Fluid-Dynamic Drag. Publ. by the author
(148 Busteed Dr., Midland Park, N. J.), 1965.

TABLE 1.—STEP PARAMETERS

h , cm	M_∞	p_b/p_r	θ , cm	$R_\theta \times 10^4$
0.33	0.86	0.94	0.41	3.7
0.63	0.82	0.94		
1.19	0.83	0.93		
0.33	0.90	0.94	0.48	4.9
0.63	0.92	0.92		
1.19	0.92	0.92		
0.33	0.99	0.95	0.43	4.0
0.63	0.96	0.94		
1.19	0.98	0.92		
0.33	2.26	0.55	0.28	1.4
0.63	2.23	0.48		
1.19	2.23	0.45		
0.33	2.54	0.50	0.25	0.96
0.63	2.50	0.43		
1.19	2.50	0.38		
0.33	2.89	0.51	0.23	0.79
0.63	2.85	0.42		
1.19	2.81	0.34		

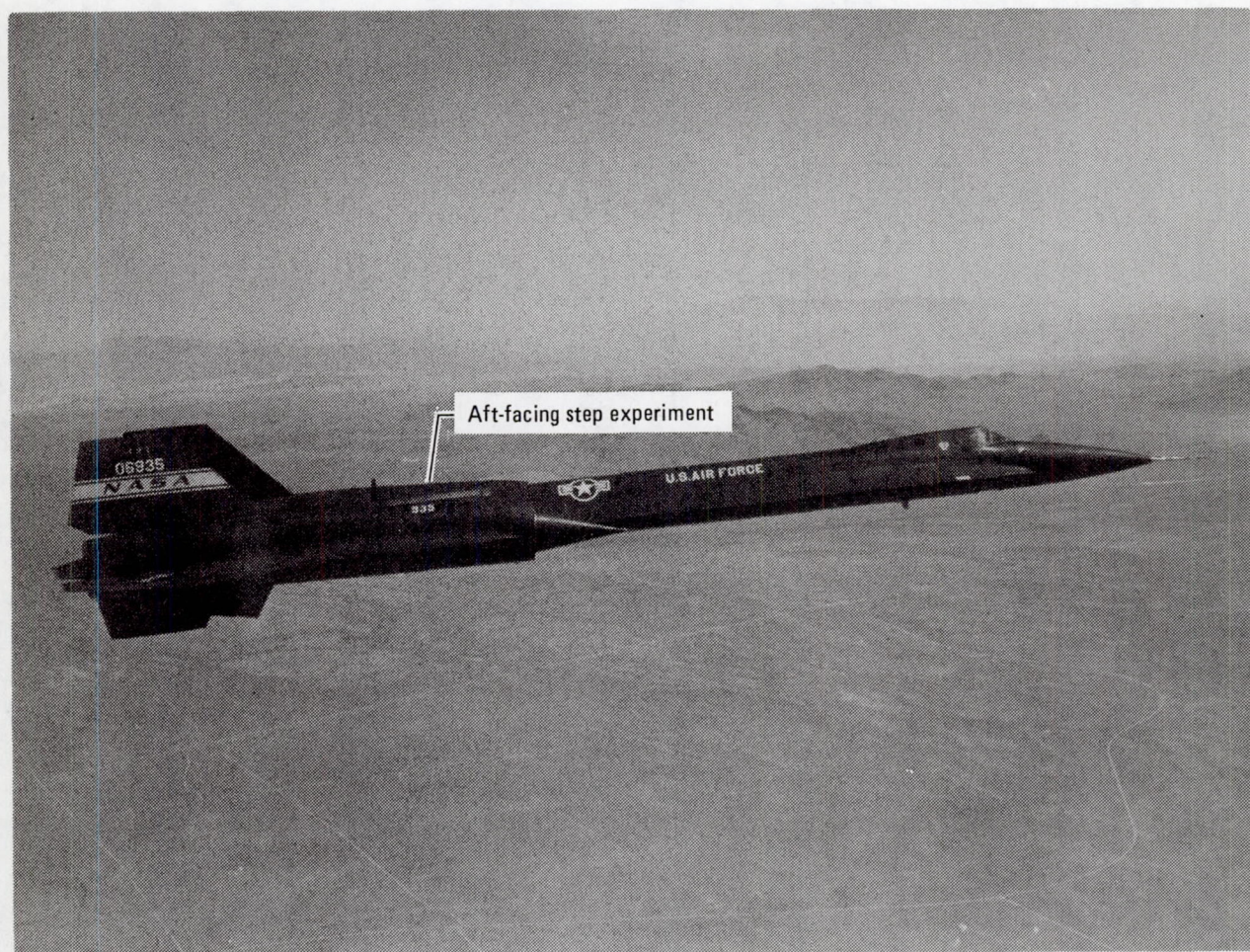
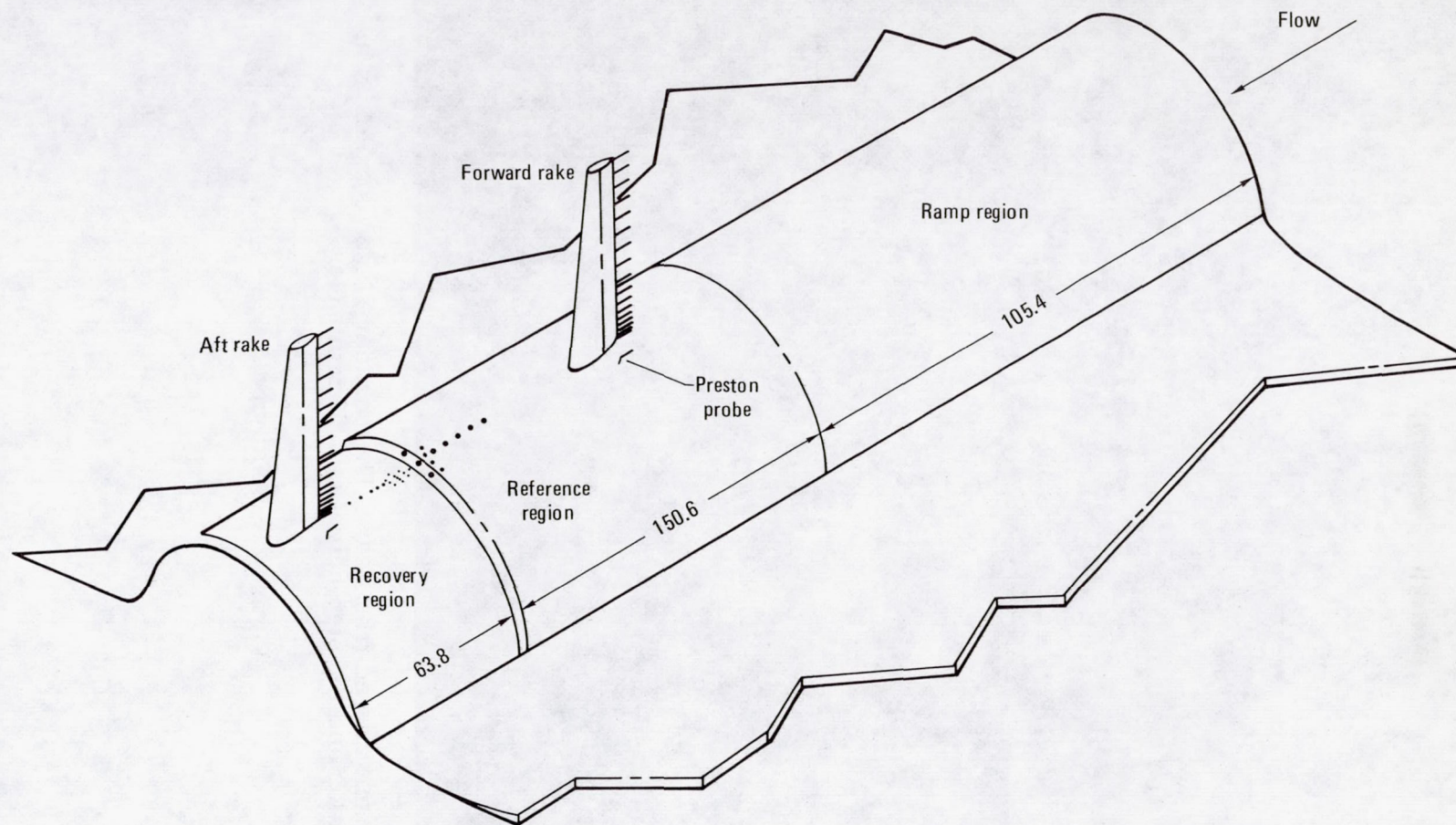
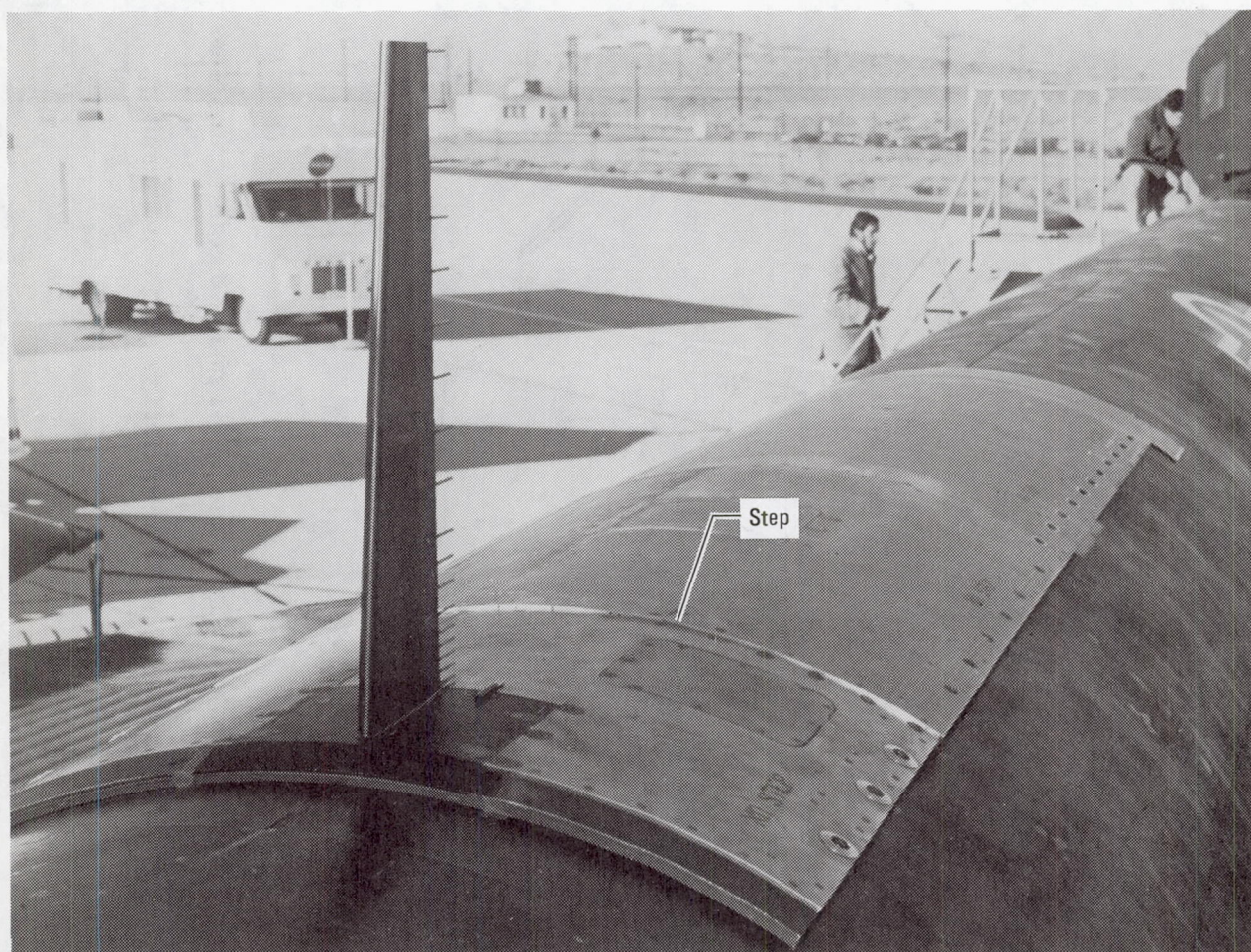


Figure 1.—YF-12 airplane in flight showing location of the aft-facing step experiment.



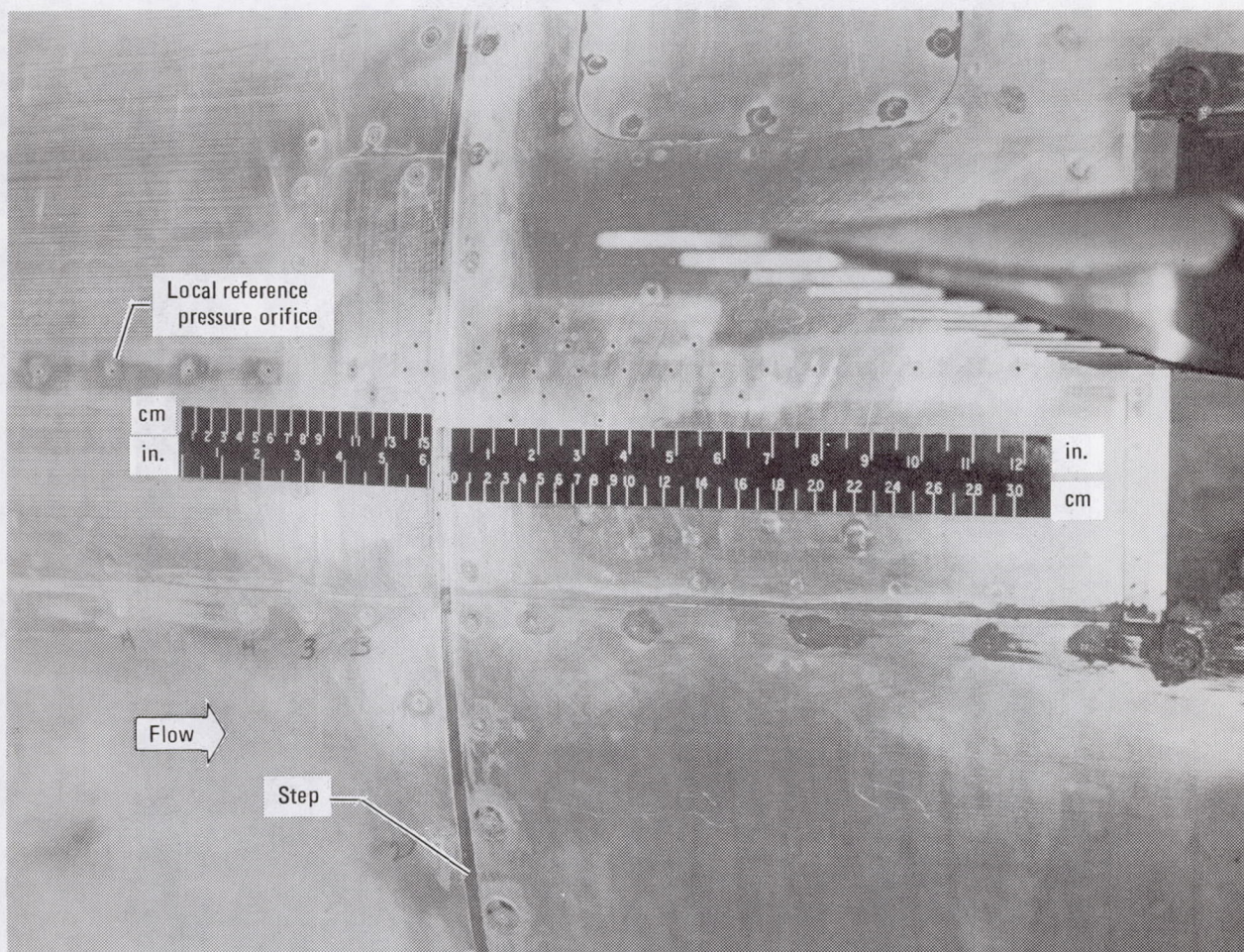
(a) Sketch showing relative location of components. Dimensions in centimeters.

Figure 2.—Sketch and photograph of the aft-facing step experiment.



(b) Experiment viewed from rear. The boundary layer complex is in the aft location and the step height is 0.63 centimeter.

Figure 2.—Continued.



(c) Top view of step region showing location of pressure orifices. Step height is 1.19 centimeters.

Figure 2.—Concluded.

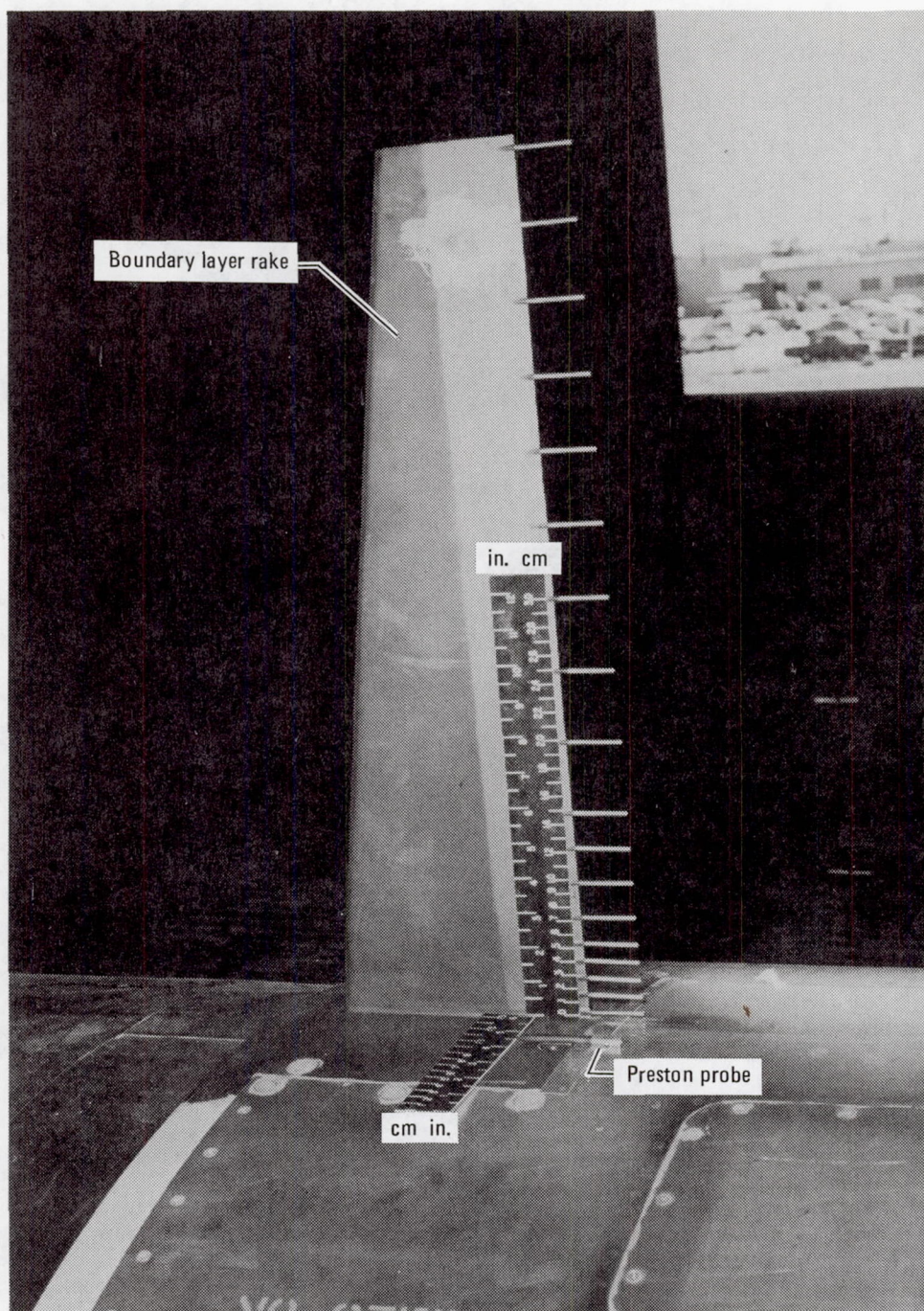


Figure 3.—A closeup view of a boundary layer rake complex.

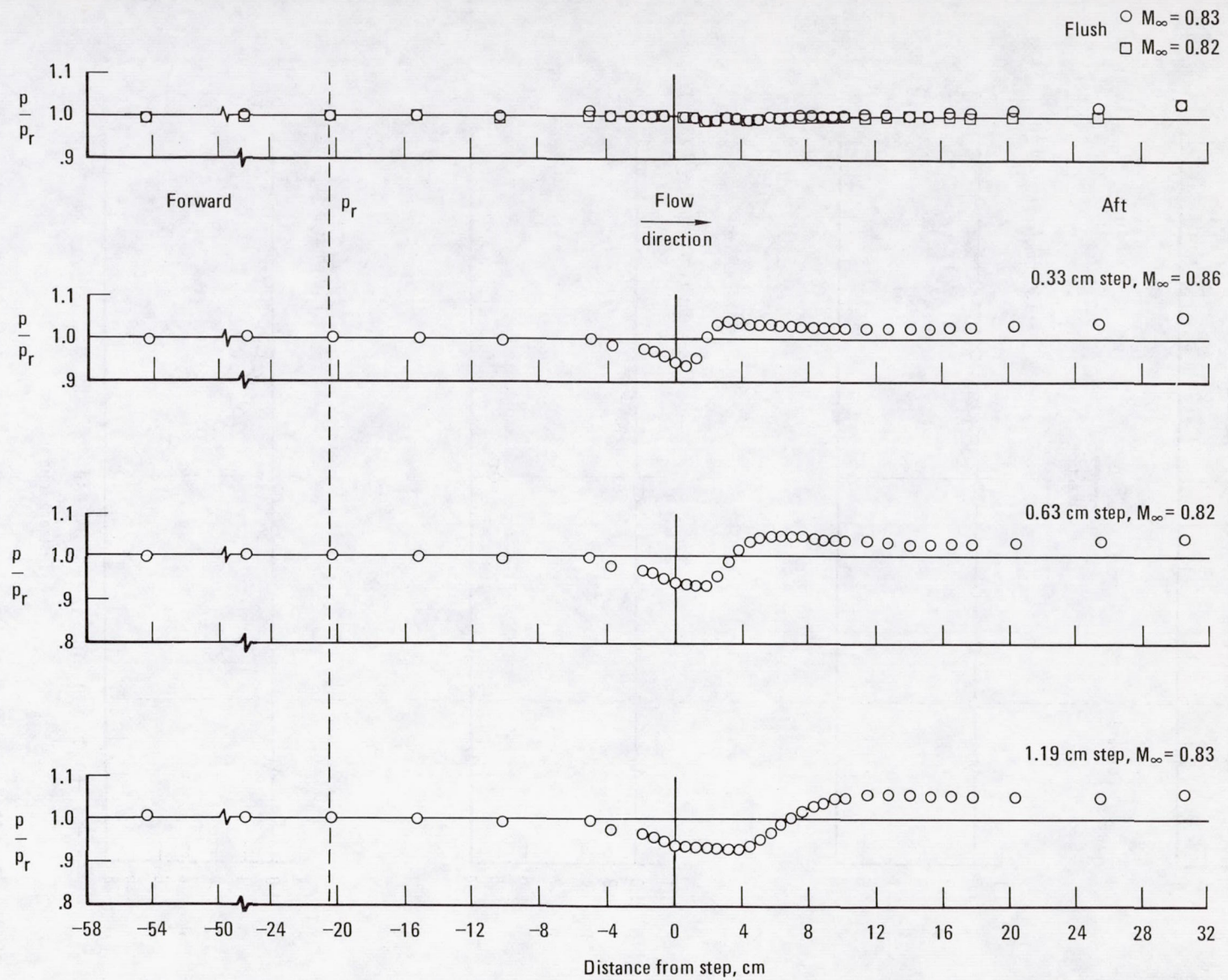


Figure 4.—Variation of the pressure ratio with distance from the step location. $M_\infty \approx 0.80$.

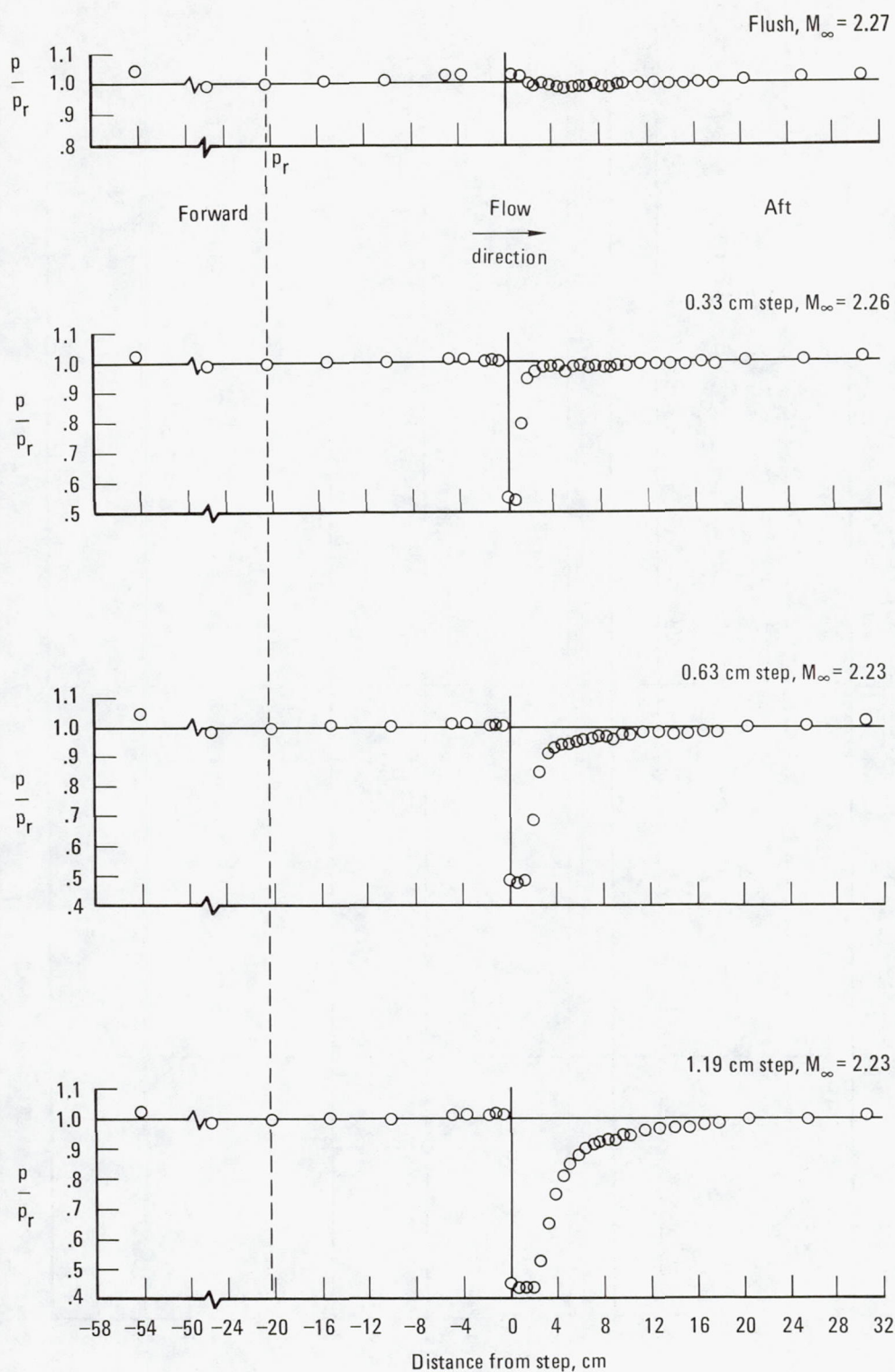
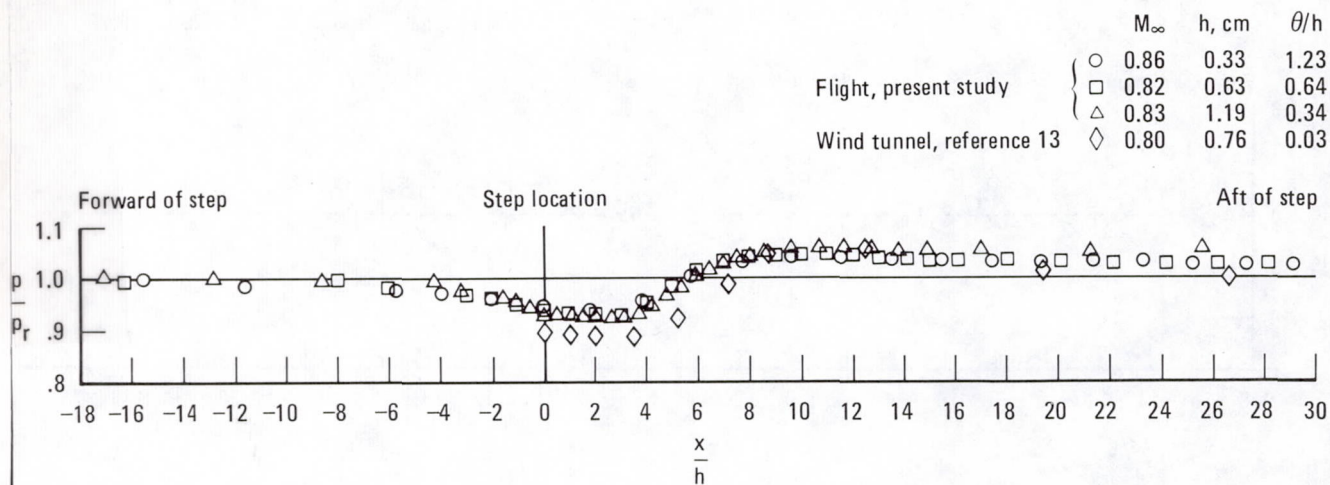
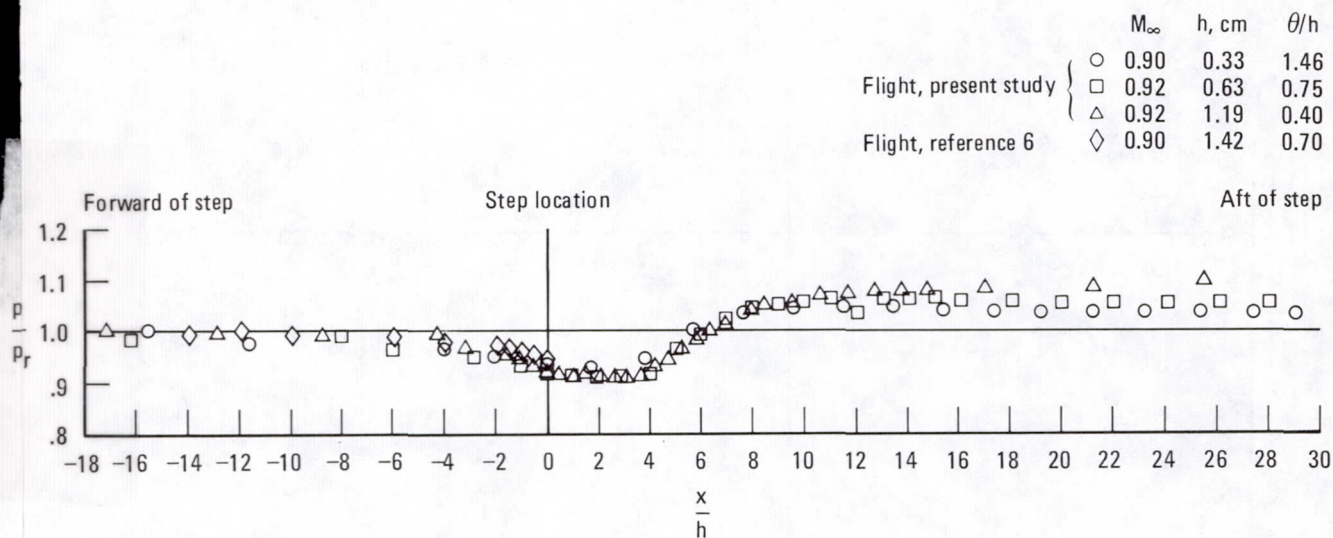


Figure 5.—Variation of the pressure ratio with distance from the step location. $M_\infty \approx 2.20$.

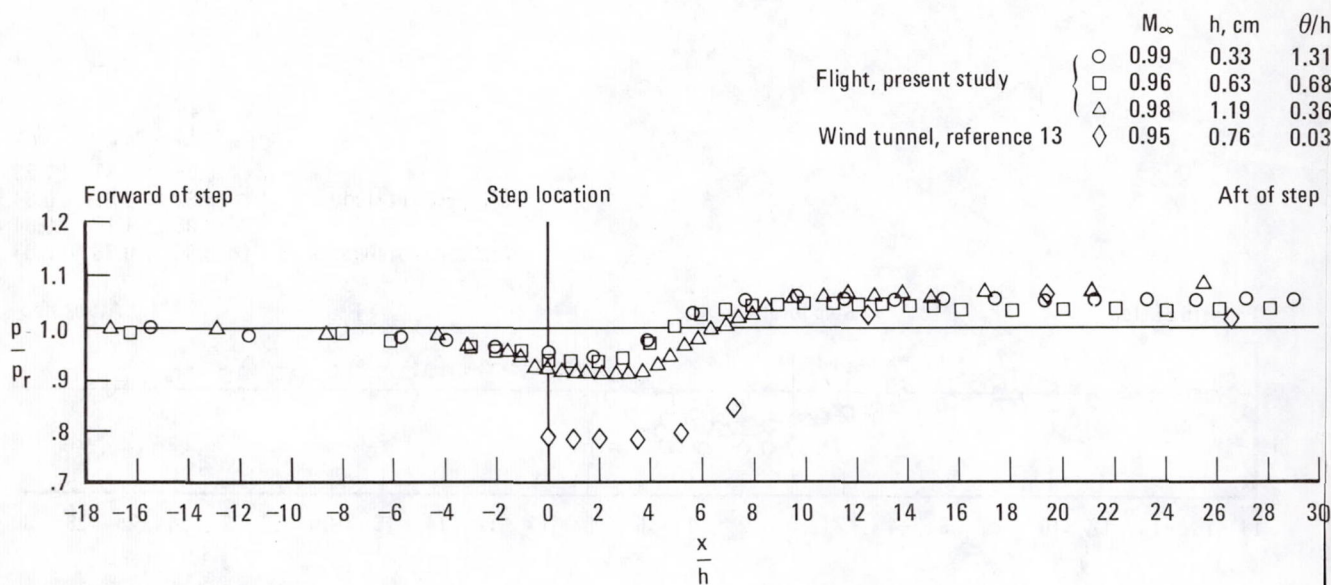


(a) Mach number near 0.80.

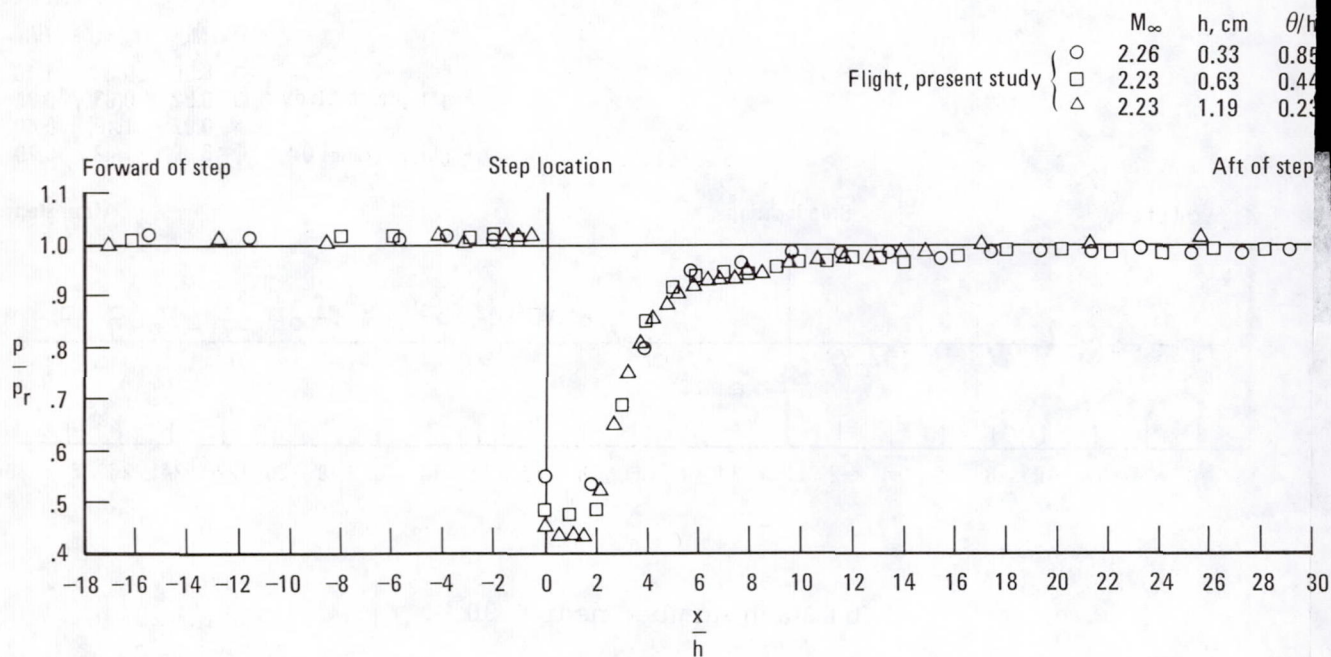


(b) Mach number near 0.90.

Figure 6.—Variation of the pressure ratio as a function of step height.



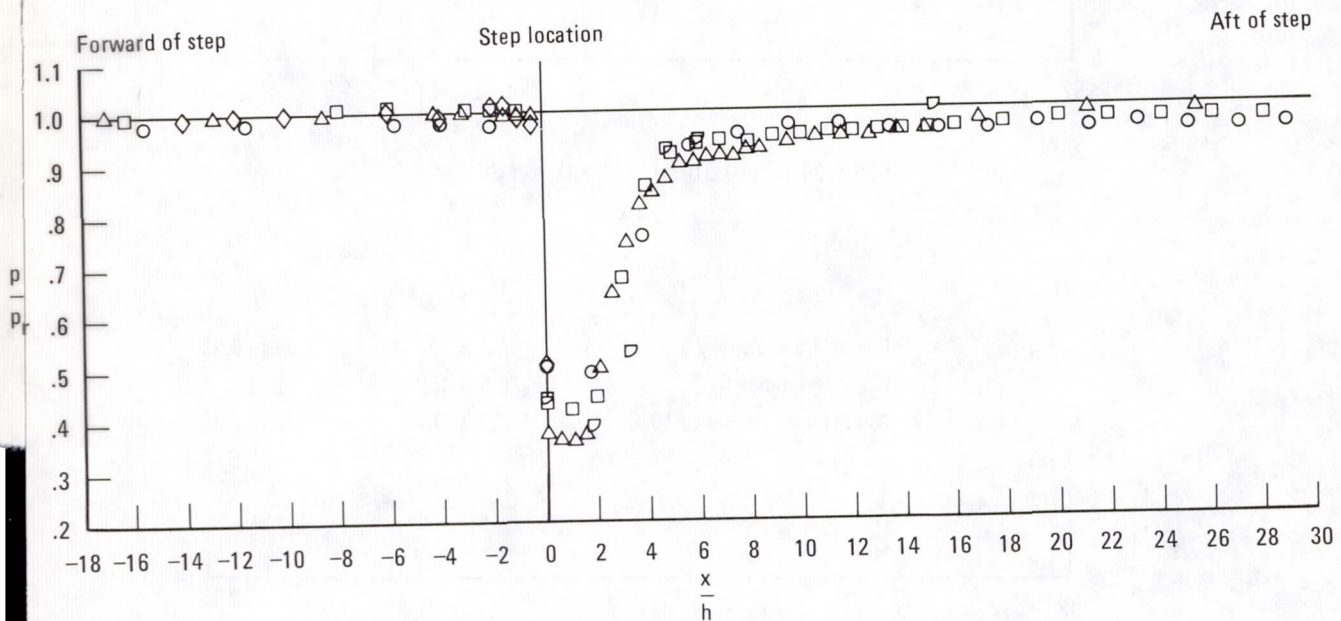
(c) Mach number near 0.95.



(d) Mach number near 2.20.

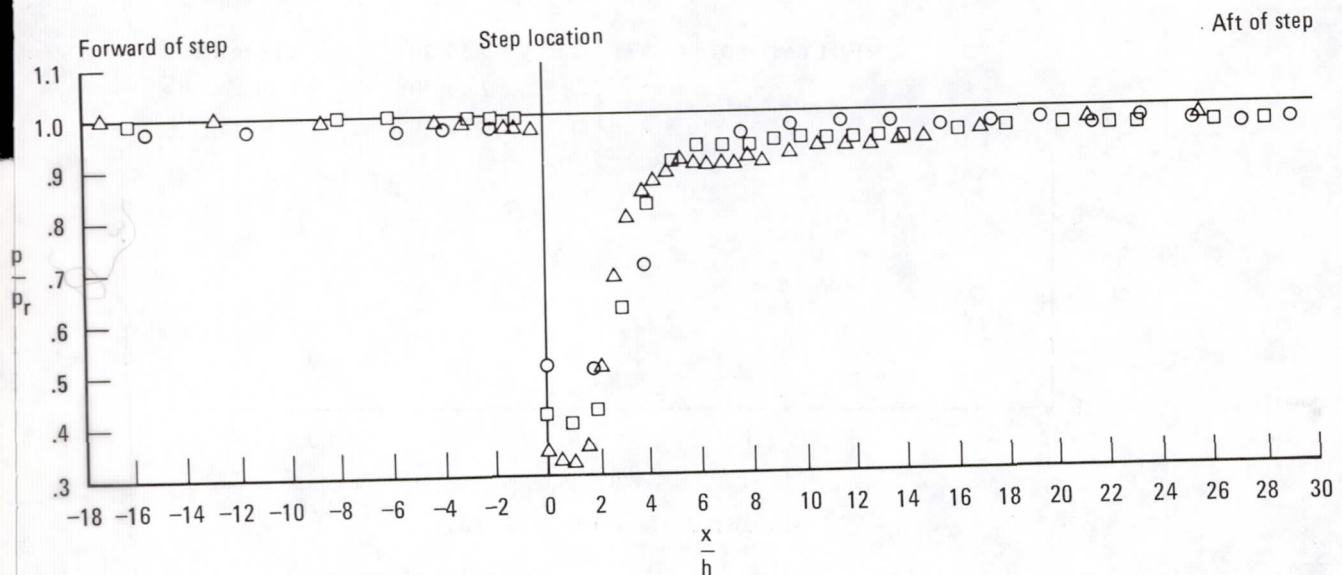
Figure 6.—Continued.

	M_∞	h , cm	θ/h
Flight, present study	○ 2.54	0.33	0.78
	□ 2.50	0.63	0.40
	△ 2.50	1.19	0.21
Flight, reference 6	◇ 2.46	1.42	1.16
Wind tunnel, reference 4	◻ 2.41	0.20	0.22



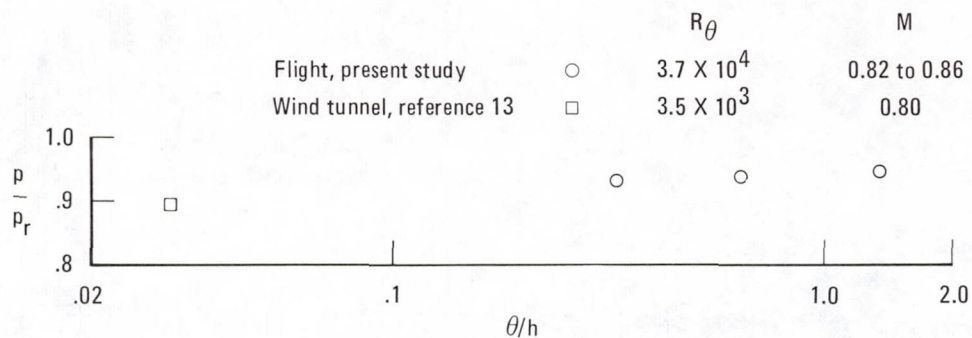
(e) Mach number near 2.50.

	M_∞	h , cm	θ/h
Flight, present study	○ 2.89	0.33	0.69
	□ 2.85	0.63	0.36
	△ 2.81	1.19	0.19

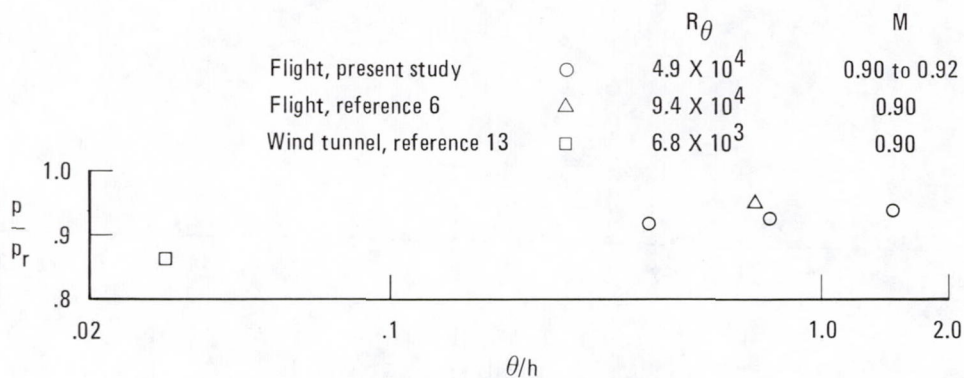


(f) Mach number near 2.80.

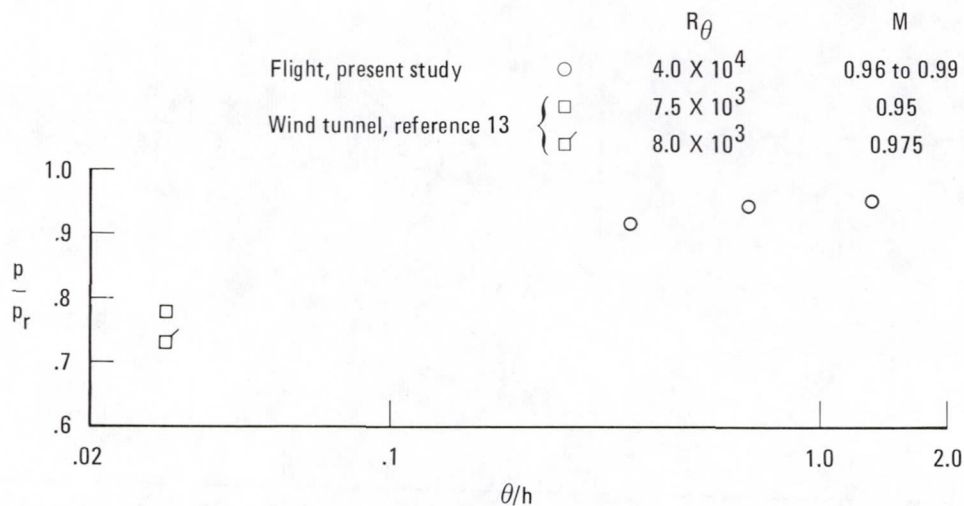
Figure 6.—Concluded.



(a) Mach number near 0.80.

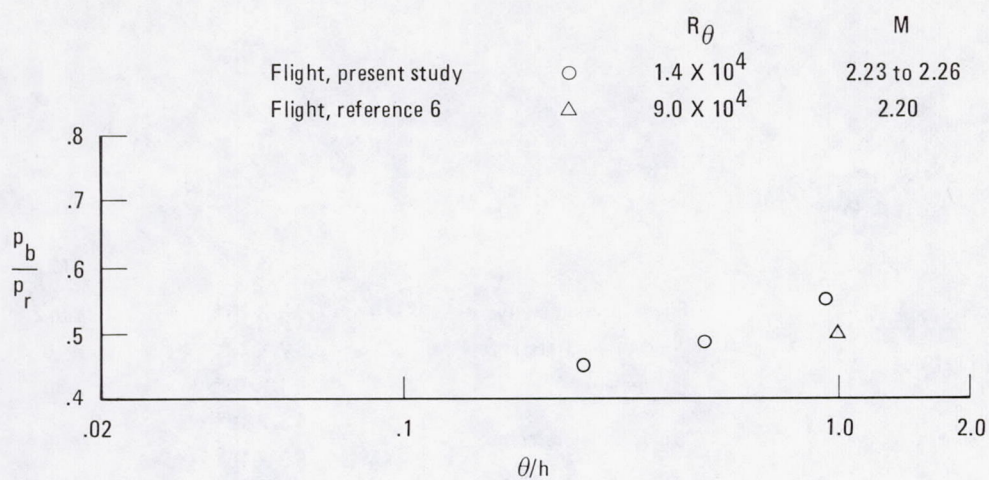


(b) Mach number near 0.90.

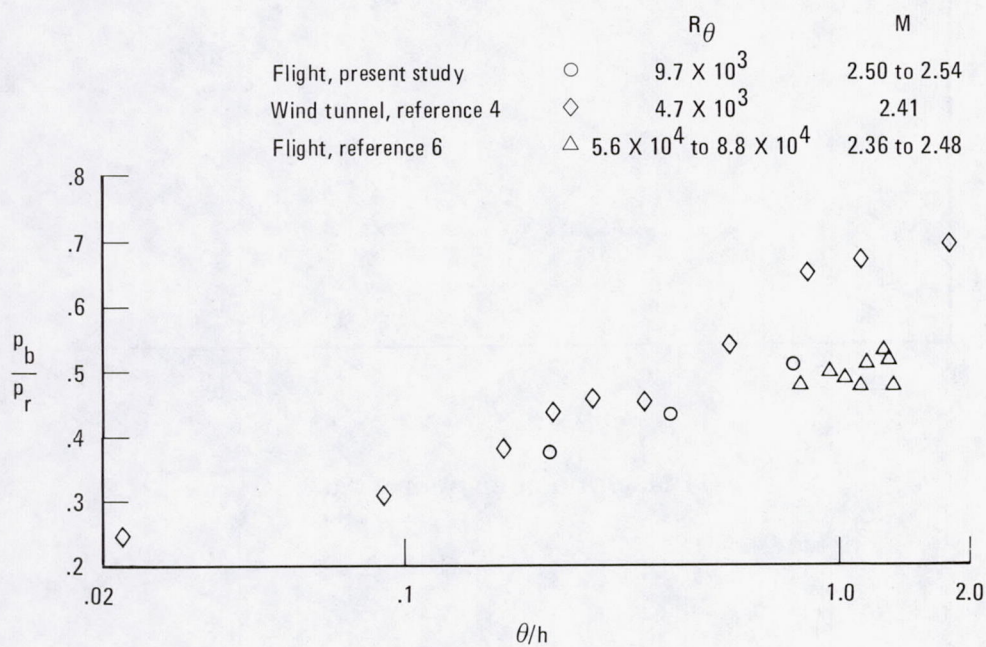


(c) Mach number near 0.95.

Figure 7.—Base pressure ratio as a function of momentum thickness and step height.

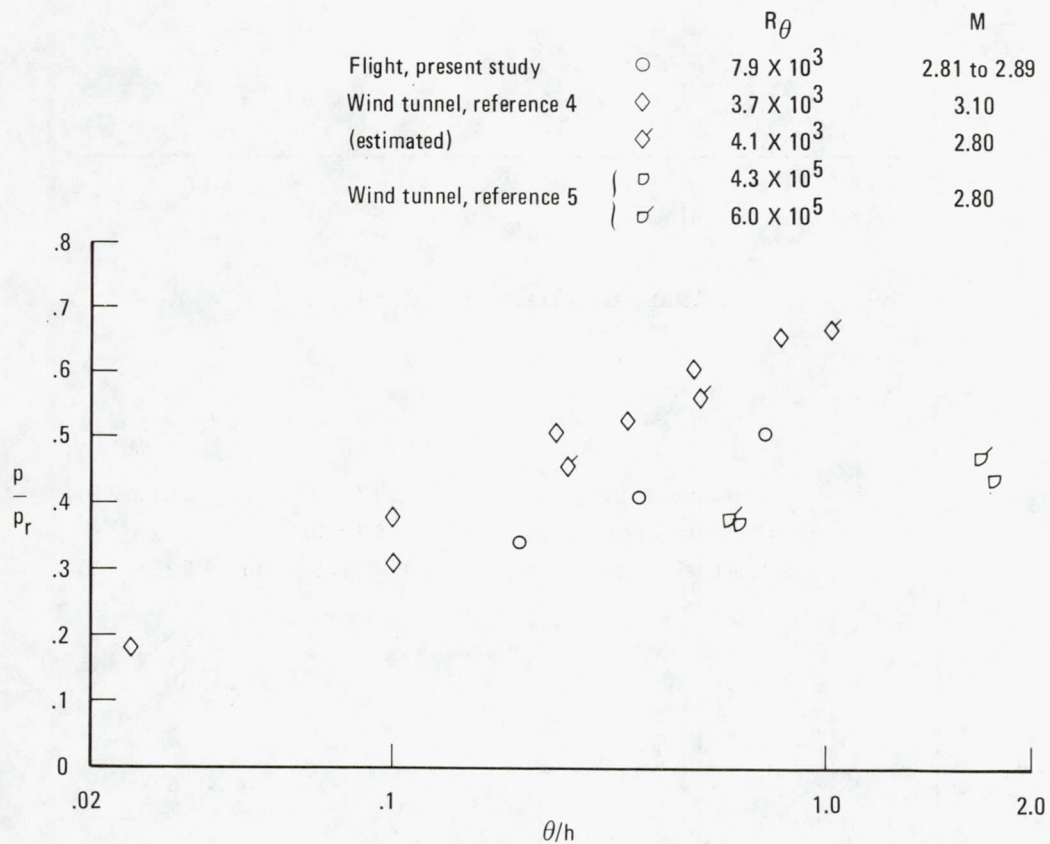


(d) Mach number near 2.20.



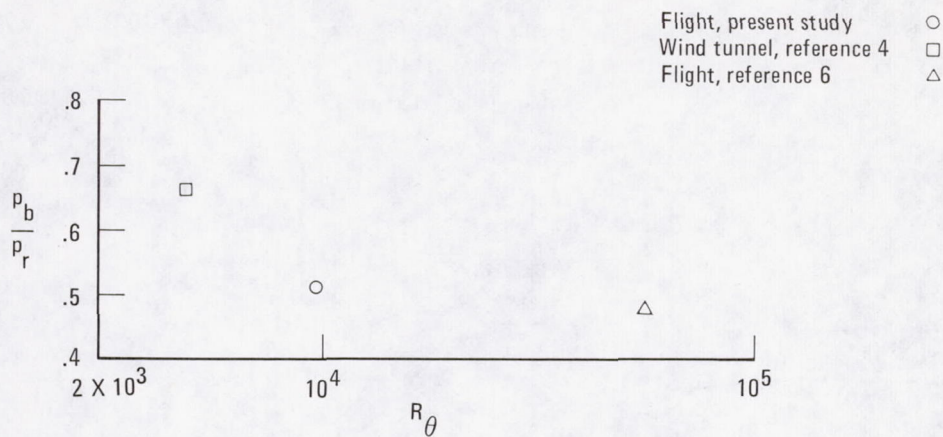
(e) Mach number near 2.50.

Figure 7.—Continued.

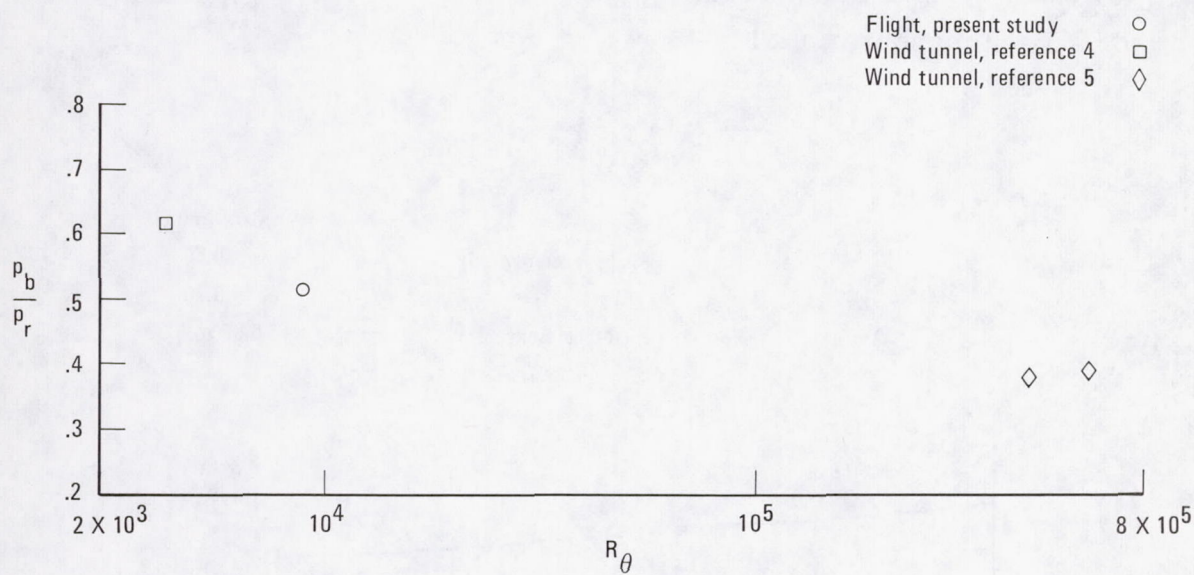


(f) Mach number near 2.80.

Figure 7.—Concluded.

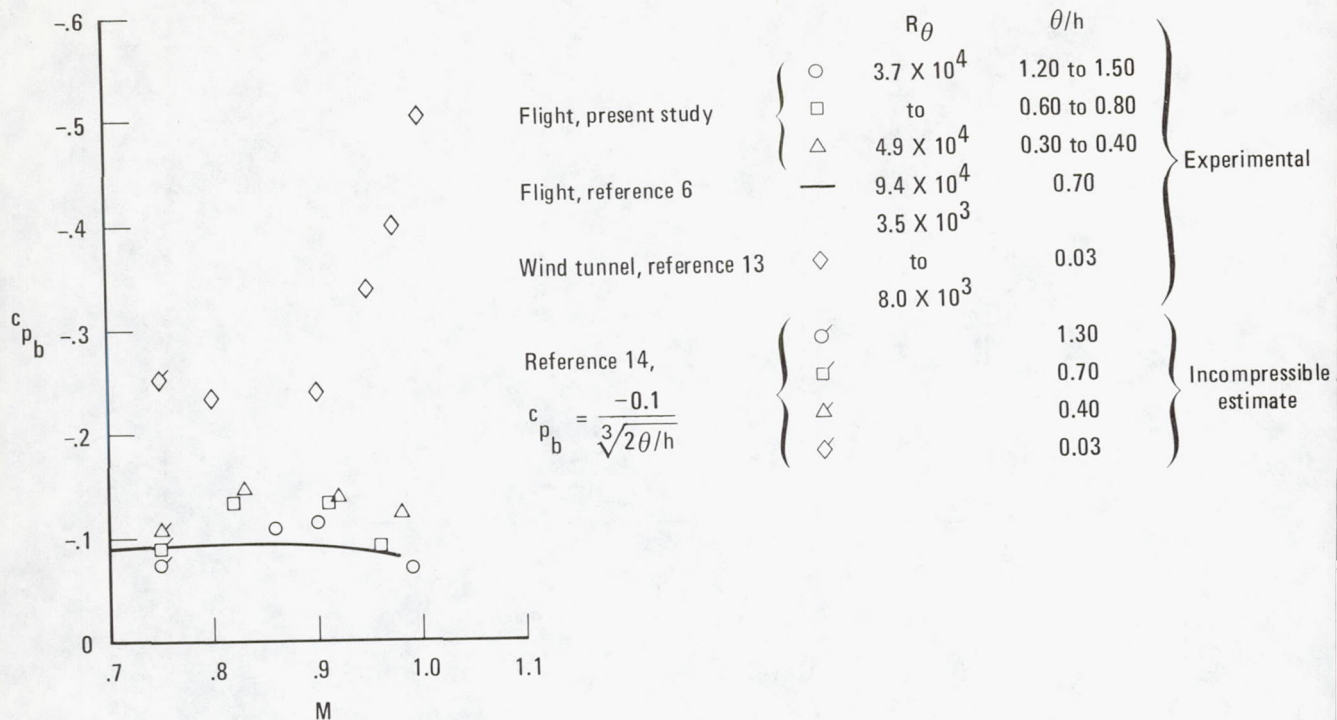


(a) $\theta/h = 0.80$, Mach number from 2.40 to 2.50.

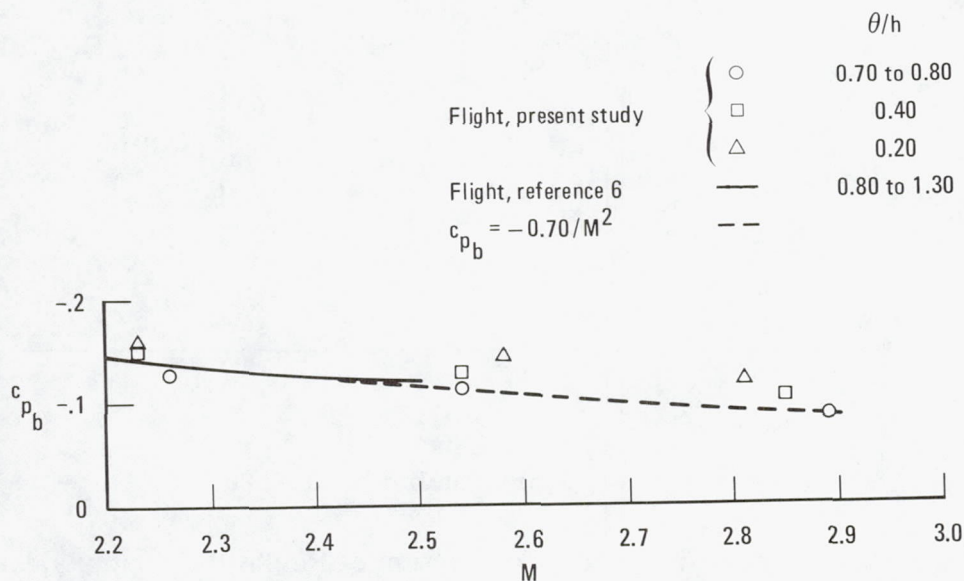


(b) $\theta/h = 0.70$, Mach number near 2.80.

Figure 8.—Base pressure ratio as a function of Reynolds number based on momentum thickness.



(a) Mach number below 1.00. R_θ and θ/h values of reference 6 are for a Mach number of 0.90.



(b) Mach numbers above 2.00.

Figure 9.—Variation of aft-facing step base pressure coefficient data with Mach number (including an incompressible estimate).

BOUNDARY LAYER, SKIN FRICTION, AND BOATTAIL PRESSURE
MEASUREMENTS FROM THE YF-12 AIRPLANE AT MACH NUMBERS UP TO 3

David F. Fisher
Dryden Flight Research Center

SUMMARY

In-flight measurements of boundary layer and skin friction data were made on YF-12 airplanes for Mach numbers between 2.0 and 3.0. Boattail pressures were also obtained for Mach numbers between 0.7 and 3.0 with Reynolds numbers up to 4×10^8 .

Boundary layer data measured along the lower fuselage centerline indicate local displacement and momentum thicknesses can be much larger than predicted, suggesting the need for careful consideration when integrating engine inlets and cooling air intakes into a supersonic cruise design.

Skin friction coefficients measured at two of five lower fuselage stations were significantly less than predicted by flat plate theory. Since other recent experiments have found local skin friction coefficients on the upper fuselage surface to be higher than predicted, it appears that the flat plate theory may not necessarily provide accurate, full-scale, localized skin friction predictions for supersonic cruise conditions. However, such compensating effects may be a forgiving factor when model to full-scale adjustments are made on the basis of the usual two-dimensional, flat plate relations.

The presence of large differences between measured boattail pressure drag and values calculated by a potential flow solution indicates the presence of vortex effects on the upper boattail surface. At both subsonic and supersonic speeds, pressure drag on the longer of two boattail configurations was equal to or less than the pressure drag on the shorter configuration. At subsonic and transonic speeds, the difference in C_D was on the order of 0.0008 to 0.0010. In the supersonic cruise range, the difference in C_D was on the order of 0.0002. Boattail drag coefficients are based on wing reference area.

INTRODUCTION

The economic feasibility of long range supersonic cruise airplanes, including current supersonic transports, is clearly dependent on design efficiency. Even slight increases in drag can cause large fuel penalties and substantially increase the overall operating costs of the airplane. Since the development of "second generation" supersonic transports is dependent on their ability to compete economically with current wide-bodied jets, designers of these airplanes must have both sufficient data and suitable analytical tools to accurately predict aerodynamic characteristics at supersonic cruise conditions. Unfortunately, in some cases, these needs are not adequately met.

For example, approximately one-third of the cruise drag of a typical supersonic transport airplane is attributed to skin friction; therefore, any prediction of flight performance must include an accurate accounting of full-scale, high Reynolds number, viscous flow characteristics. Since full-scale flow characteristics can differ significantly from those measured on small-scale models in a wind tunnel environment, correlation between the two is obtained by adjustments which primarily account for the Reynolds number differences. These adjustments are usually based on empirical data obtained for two-dimensional flow over smooth flat plates or on measurements taken along wind tunnel walls. However, recent studies indicate that these methods may not necessarily provide the accurate full-scale skin friction predictions that are essential for the development of efficient airplane designs.

Similar limitations are also found in fuselage closure or afterbody design. In this case, both predictive techniques and quantitative experimental data are lacking for the high Reynolds number, thick boundary layer conditions encountered in supersonic cruise flight, particularly when the possibility of afterbody flow separation exists. In wind tunnel tests, afterbody drag is usually estimated rather than measured because of the cost and complexity of the model, support structure, and data acquisition system needed to obtain accurate afterbody measurements. However, even when such needs are met, it is obvious that very thick boundary layer data cannot be obtained using models and existing supersonic wind tunnel facilities.

Although some data have been previously obtained in flight (refs. 1 to 3), suitable data are still lacking. Because of this, and because of limitations in present high Mach number predictive techniques, NASA initiated the flight experiments program using the YF-12A and YF-12C airplanes. As part of these experiments, skin friction and boundary layer data, as well as boattail pressures, were obtained for Reynolds numbers up to 4×10^8 and speeds up to Mach 3.0. Skin friction coefficients and boundary layer characteristics were measured on the lower fuselage centerline of the YF-12A airplane. Boattail pressures from two YF-12 afterbody configurations were obtained and analyzed to determine differences in pressure drag between the two configurations for both subsonic and supersonic flight conditions.

SYMBOLS

Physical quantities in this report are given in the International System of

Units (SI). Measurements were taken in U.S. Customary Units.

C_D	drag coefficient
C_f	local skin friction coefficient
C_p	pressure coefficient, $\frac{p - p_\infty}{q_\infty}$
L	fuselage length, m
M	Mach number
M_∞	free stream Mach number
p	local static pressure, N/m^2
p_∞	free stream static pressure, N/m^2
q_∞	free stream dynamic pressure, N/m^2
R_x	Reynolds number based on distance, x
R_θ	Reynolds number based on momentum thickness
T_1	static temperature at edge of boundary layer, K
T'	reference temperature (ref. 9), K
u/u_1	ratio of local velocity to boundary layer edge velocity
x	distance from nose apex, m
y	distance from surface to rake probe centerline, cm
α	wing angle of attack, deg
δ	boundary layer thickness, $u/u_1 = 0.99$, cm
δ^*	displacement thickness of boundary layer, cm
θ	momentum thickness of boundary layer, cm
μ_1	absolute viscosity based on edge temperature
μ'	absolute viscosity based on reference temperature

TEST DESCRIPTION

Boundary Layer Skin Friction Experiment

Measurements were taken at five boundary layer, skin friction stations on the lower fuselage of the YF-12A airplane. The stations were located 3.9, 7.3, 12.1, 18.6, and 24.1 meters aft of the nose apex to provide a history of the boundary layer flow along the lower fuselage surface. Tests were conducted with only one station mounted at a time. That station was instrumented with a boundary layer rake, a static pressure orifice, one to four Preston probes, and a skin surface thermocouple. A skin friction balance was also used at the two forward stations.

In order to provide an undisturbed flow over the lower fuselage, all upstream protrusions, bleeds, and vents were removed. This was accomplished by placing fairings over the nose vent and nose gear compartment vents and by rerouting the cooling air from the compartments out of an aft-facing vent on the upper surface of the left chine. In addition, a cooling air scoop on the right hand missile bay door was removed.

Boattail Drag Experiment

In flight, surface static pressures were measured on two boattail configurations of the YF-12 aircraft. Figure 3 provides a general view of the airplane showing the two boattail configurations and the radial locations of the static pressure orifices used on the YF-12A airplane. The YF-12C airplane does not have a lower centerline-mounted ventral fin; therefore, an additional row of static pressure orifices was installed along the lower fuselage centerline.

The YF-12A boattail had a fineness ratio of 4.6. The YF-12C boattail was 1.14 meters longer than the YF-12A configuration and had a fineness ratio of 5.3. Figure 4 provides detailed views of both configurations and indicates the fuselage stations at which the boattail begins on each of the two airplanes.

TEST CONDITIONS

The skin friction data were obtained at Mach numbers between 2.0 and 3.0 and at Reynolds numbers up to 2×10^8 , based on the run length. Boundary layer rake data were obtained at three nominal Mach numbers: 2.0, 2.5, and 3.0. Boattail pressures were measured from subsonic Mach numbers up to Mach 3.0 and at Reynolds numbers up to 4×10^8 , based on fuselage length. All data were obtained in stabilized level flight using a modified autopilot altitude hold mode which is described in reference 4. The use of the altitude hold mode enabled altitude to be held constant, thus minimizing lag effects.

The angle-of-attack range for the boundary layer skin friction experiment varied from 2.8° to 5.5° . For the boattail experiment, the angle of attack varied from 1.0° to 5.5° on the YF-12A airplane and from 2.0° to 5.5° on the YF-12C airplane.

INSTRUMENTATION

The two primary air data reference parameters, free stream Mach number, M_∞ , and free stream static pressure, p_∞ , were measured using identical pitot static probes (fig. 5) mounted on the nose boom on each aircraft. Descriptions of the probe and its flight calibration are presented in reference 5. Free stream total temperature was measured with a thermocouple-type total temperature probe mounted on the upper surface of the nose.

Pressures obtained from boundary layer rakes, Preston probes, and static pressure orifices were measured using several differential pressure transducers and scanning mechanisms. Transducer ranges were selected to optimize measurement accuracies, and each transducer was referenced to a closely monitored precise reference pressure. The skin friction force balance used in these tests was the same type as described in reference 6. All data were acquired by a nine bit pulse code modulated data system and recorded, in digital form, on magnetic tape.

RESULTS AND DISCUSSION

Boundary Layer Skin Friction Experiment

Velocity profiles for the five lower fuselage locations are presented in figure 6 for nominal Mach numbers of 2.0, 2.5, and 3.0. In general, the profiles have a logarithmic shape except for some distortion at station 2 and, to a lesser extent, at station 3. The distortion becomes most pronounced at Mach 3.

Figure 7 shows the growth of the boundary layer, δ , displacement thickness, δ^* , and momentum thickness, θ , as a function of fuselage length for each of the test Mach numbers. Figure 7(c) includes theoretical estimates of the displacement and momentum thickness computed using the finite difference method described in reference 7. At Mach 3.0 the theoretical predictions agree with the mean values of the flight measurements at stations 1 and 5; however, at stations 2, 3, and 4 the measured values of displacement and momentum thickness are much larger than predicted. For example, at station 2 the measured value exceeds the predicted value by a factor of about 2.8. The fact that thickness parameters may be significantly larger than predicted suggests that extra care must be taken in designing and locating engine inlets and cooling air intakes for supersonic cruise applications in order to prevent the ingestion of low energy boundary layer air.

At stations 1 and 2, local skin friction coefficients were measured using skin friction force balances and Preston probes. The Preston probes were calibrated using the technique described in reference 8. In figure 8 the friction coefficient values obtained using the Preston probes are plotted as a function of the corresponding values obtained using the friction force balance. The line of perfect agreement represents the locus of points for which the two techniques yield identical results. The root-mean-square value of the scatter about the line of perfect agreement for the Preston probe at station 1 was ± 2 percent. At station 2, the Preston probe results were biased about 5 percent high, and, the root-mean-square error was on the

order of ± 4 percent. The good agreement between the values confirms the findings of reference 1 which indicate that the Preston probes can provide reliable skin friction coefficients in the supersonic cruise environment. This is significant since the Preston probes are less expensive, easier to install and maintain, and less susceptible to damage. Also, unlike the force balance units, they do not require cooling at the higher Mach numbers, and they can be installed in locations where there is insufficient space beneath the skin to install a friction force balance.

In figure 9(a), the local friction coefficients obtained using the friction force balance at stations 1 and 2 are plotted as a function of Reynolds number based on run length, R_x . In figure 9(b), the same values are plotted as a function of Reynolds number based on momentum thickness, R_θ . In these plots the friction coefficients and Reynolds numbers have been normalized to a Mach number of 0 using the Sommer and Short *T-prime* method described in reference 9.

The local friction coefficients from station 1 agree reasonably well with the von Kármán-Schoenherr flat plate theory; however, for station 2, the skin friction coefficients plotted as a function of R_x are about 30 percent lower than predicted and those plotted as a function of R_θ are about 20 percent lower than predicted.

In figures 10(a) and 10(b), friction coefficients obtained by the Preston probe technique are plotted as functions of R_x and R_θ for all five stations. Most of the skin friction coefficients for stations 1, 4, and 5 fall near the von Kármán-Schoenherr theoretical values, tending to be slightly lower at the highest Reynolds numbers; however, the data from stations 2 and 3 are significantly lower than predicted. The differences at station 2 amount to about 30 percent for the R_x plot and about 20 percent for the R_θ plot. At station 3 the coefficients in the same two plots were about 35 to 25 percent lower, respectively. However, even though the skin friction at stations 2 and 3 was lower than predicted, it should not be concluded that the overall skin friction drag was lower. A limited number of skin friction measurements made on the upper centerline of the YF-12A airplane (ref. 10) indicate that local skin friction coefficients at those stations were 17 to 23 percent higher than predicted by flat plate theory. Similarly, local skin friction coefficients measured on the upper fuselage centerline of the XB-70 airplane (ref. 1) were approximately 25 percent higher than predicted for a Mach number range of 2.0 to 2.5. These findings suggest that flat plate theory extrapolations from low Reynolds number model measurements to high Reynolds number flight predictions are sometimes dependent upon compensating differences in skin friction effects over the various parts of the aircraft.

Because of the unusual boundary layer profiles and low skin friction coefficients obtained at station 2, additional tests and analyses were performed in an attempt to find an explanation for the anomalies observed in the data. It was first hypothesized that a strong adverse pressure gradient might have existed very near station 2. To investigate this possibility, pressure coefficient data from previously unpublished one-twelfth-scale model wind tunnel tests and in-flight data obtained from several local flush orifices were examined. Figure 11 presents the pressure coefficients measured along the lower fuselage centerline of the one-twelfth-scale model along with the in-flight measurements. Neither the wind tunnel nor the flight data provide

any indication that a strong adverse longitudinal pressure gradient exists at station 2.

Other possible causes could have been the presence of a pressure gradient through the boundary layer or the presence of crossflow conditions near station 2. To investigate these possibilities, additional instrumentation was added to the air-plane; however, subsequent tests detected only very slight gradients and crossflow conditions which were insufficient to cause the anomalies at station 2.

While the unexpected shape of the boundary layer and the increased thickness parameters cannot be explained at present, they represent real and repeatable flow conditions over a three-dimensional shape with practical surface construction, lifting surfaces, and three-dimensional flow.

Boattail Drag Experiment

Figure 12 provides boattail pressure coefficients for both the YF-12A and YF-12C configurations for several representative Mach numbers. At a Mach number of 0.7 (fig. 12(a)), the upper surface pressure coefficients for the YF-12C configuration are significantly more positive than those for the YF-12A configuration at normalized fuselage locations, x/L , of 0.80 to 0.93. Similar characteristics can be noted along the lower surface for values of x/L from 0.90 to 0.98. The more positive pressures indicate that the YF-12C boattail configuration offers less subsonic pressure drag at a Mach number of 0.7.

In figure 12(b), a similar comparison of boattail pressure coefficients at Mach 0.96 shows significantly more positive values for nearly the entire upper boattail region of the YF-12C configuration as well as for x/L values from 0.90 to 0.98 on the lower surface.

Fewer apparent differences are present at a Mach number of 1.12 (fig. 12(c)) except for a local region between x/L locations of about 0.80 to 0.85 on the upper surfaces and at x/L locations greater than 0.93 on the lower surfaces. The pressure coefficients for the YF-12C configuration become positive aft of about an x/L location of 0.97 on both the upper and lower surfaces. A fuel dump nozzle on the YF-12A airplane prevented the installation of static pressure orifices on the aft-most portion of the boattail; therefore, it is uncertain if positive pressure coefficients were present at these locations on the YF-12A configuration. It is suspected that the additional 1.14 meters length of the YF-12C boattail may extend through a region of influence from the engine exhaust flow field. Further flight tests are planned to determine if engine power settings influence the YF-12C boattail pressures.

Pressure distributions for Mach numbers of 2.0 and 3.0 are presented in figures 12(d) and 12(e), respectively. Although the YF-12C airplane has higher upper surface pressure coefficients in these speed ranges, there are compensating effects in favor of the YF-12A configuration over parts of the lower boattail surfaces. When the pressure coefficients are integrated to determine the overall boattail pressure drag for the two configurations, it is found that the YF-12C configuration has a slight advantage at Mach 2.0. However, this slight advantage becomes significant if the vehicle must cruise at this speed for extended periods of time.

A version of the Woodward-Carmichael computer program (ref. 11) was used to estimate the potential pressure distribution of the YF-12 wing planform. The afterbodies were modeled as wing thicknesses. The program provides a reasonably accurate analytical estimate of the pressure distribution under potential, attached, and inviscid flow conditions at both subsonic and supersonic Mach numbers. The presence of large differences between analytical results and flight measurements affords a method for identifying nonpotential flow such as can exist when vortex interactions, separated flow conditions, large viscous effects, or transonic flow anomalies are present. It has been postulated that at low speeds the upper surfaces of the YF-12 airplanes are affected by vortex flow. This postulate is supported by the large differences between the analytical results and the flight measurements shown in figure 13(a). However, such an interpretation is inappropriate for the supersonic data shown in figures 13(b) and 13(c) where the differences are too small to be conclusive.

Figure 14 shows the overall boattail pressure drag results obtained for the entire Mach number range studied. Pressure coefficients for both configurations have been integrated over the respective projected areas of the aft-sloping surfaces, and the wing reference area has been used to compute the boattail drag coefficients. This plot shows that the longer boattail configuration on the YF-12C airplane has significantly less boattail pressure drag up to a Mach number of 1.2, and slightly less boattail pressure drag from Mach 2.0 to Mach 2.5. The longer length and higher fineness ratio of the YF-12C configuration caused the boattail pressure drag coefficient to peak at Mach 1.2 instead of at Mach 1.05 as for the YF-12A configuration. Subsonically, the pressure drag coefficients for the YF-12C configuration are 8 to 10 counts (1 count = $0.0001 C_D$) less than those for the YF-12A configuration. At Mach 1.05 the reduction in the pressure drag coefficients is on the order of 9.5 counts, and in the Mach number range from 2.0 to 2.5, the YF-12C boattail pressure coefficients are about 2 counts less.

It should be noted that the apparent advantage in boattail pressure drag due to the higher fineness ratio on the YF-12C airplane may not provide the same increment of drag improvement when applied to a specific airplane. A longer boattail can be expected to result in increased friction, weight, and volume, and it could result in more or less trim drag, depending on the specific aircraft configuration. However, assuming the same values of thrust, weight, volume, and trim drag, the reduced pressure drag could offer a significant advantage in transonic acceleration. On the YF-12C airplane the improvement amounts to about $0.01g$ or an equivalent thrust increase of about 2 percent.

While these pressure drag differences may seem insignificant on the YF-12 airplanes because of their large excess thrust, they could become significant on a supersonic transport aircraft operated in a competitive commercial environment. For a 200 to 250 passenger supersonic transport aircraft, fuel savings could amount to about 900 kilograms per hour at subsonic loiter, about 1100 kilograms per hour at subsonic cruise, and about 600 kilograms per hour at a supersonic cruise Mach number of 2.3.

CONCLUDING REMARKS

Boundary layer, skin friction, and boattail pressure distribution data have been obtained in flight using the YF-12 airplanes. The boundary layer data were obtained for Mach numbers between 2.0 and 3.0 and the boattail pressure data were measured from Mach 0.7 to Mach 3.0 at Reynolds numbers up to 4×10^8 .

Boundary layer data measured along the lower fuselage centerline of the YF-12A airplane indicate that local displacement and momentum thickness parameters can be much larger than predicted. The possibility of larger momentum thicknesses should be a consideration in the design and integration of engine inlets and cooling air scoops for supersonic cruise vehicles.

It was determined that local skin friction coefficients at two of five lower fuselage centerline stations were significantly less than predicted by flat plate theory. However, flight results from other experiments have shown local friction coefficients on upper surface locations to be higher than predicted (refs. 1 and 10). Such compensating effects may be a forgiving factor when model to full-scale flight friction drag adjustments are made using the usual flat plate, two-dimensional Reynolds number and drag relationships.

Large differences between measured boattail pressures and values calculated by the Woodward-Carmichael potential flow solution suggest the presence of vortex flow effects on the upper surfaces of the YF-12 boattail at subsonic speeds.

At subsonic speeds the pressure drag coefficients of the longer boattail configuration of the YF-12C were 8 to 10 counts less than the coefficients for the shorter YF-12A configuration. At Mach numbers from 2.0 to 2.5, pressure drag coefficients of the longer configuration were approximately 2 counts less. These same values, if projected for a supersonic transport aircraft of about 200 to 250 passenger capacity, could result in a fuel savings of about 900 kilograms per hour at subsonic loiter, about 1100 kilograms per hour at subsonic cruise, and about 600 kilograms per hour at a supersonic cruise Mach number of 2.3.

REFERENCES

1. Fisher, David F.; and Saltzman, Edwin J.: Local Skin Friction Coefficients and Boundary-Layer Profiles Obtained in Flight From the XB-70-1 Airplane at Mach Numbers up to 2.5. NASA TN D-7220, 1973.
2. Saltzman, Edwin J.; and Fisher, David F.: Some Turbulent Boundary-Layer Measurements Obtained From the Forebody of an Airplane at Mach Numbers up to 1.72. NASA TN D-5838, 1970.
3. Erlich, E.: Sondage de la Couche Limite en Vol Supersonique sur L'Avion "Mirage IV." O.N.E.R.A. Paper Presented at 3^e Colloque Aerodynamique de l'A. F.I.T.A.E., Marseille, France, Nov. 8-10, 1966.
4. Gilyard, Glenn B.; and Smith, John W.: Flight Experience With Altitude Hold and Mach Hold Autopilots on the YF-12 Aircraft at Mach 3. Proceedings of YF-12 Experiments Symposium, NASA CP-2054, Vol. 1, 1978.
5. Larson, Terry J.: Compensated and Uncompensated Nose Boom Static Pressures Measured From Two Air Data Systems on a Supersonic Airplane. NASA TM X-3132, 1974.
6. Garringer, Darwin J.; and Saltzman, Edwin J.: Flight Demonstration of a Skin-Friction Gage to a Local Mach Number of 4.9. NASA TN D-3830, 1967.
7. Albers, James A.; and Gregg, John L.: Computer Program for Calculating Laminar, Transitional, and Turbulent Boundary Layers for a Compressible Axisymmetric Flow. NASA TN D-7521, 1974.
8. Hopkins, Edward J.; and Keener, Earl R.: Study of Surface Pitots for Measuring Turbulent Skin Friction at Supersonic Mach Numbers — Adiabatic Wall. NASA TN D-3478, 1966.
9. Sommer, Simon C.; and Short, Barbara J.: Free-Flight Measurements of Turbulent-Boundary-Layer Skin Friction in the Presence of Severe Aerodynamic Heating at Mach Numbers From 2.8 to 7.0. NACA TN-3391, 1955.
10. Powers, Sheryll Goecke: Flight-Measured Pressure Characteristics of Aft-Facing Steps in High Reynolds Number Flow at Mach Numbers of 2.20, 2.50, and 2.80 and Comparison With Other Data. NASA TM-72855, 1978.
11. Woodward, Frank A.: Analysis and Design of Wing-Body Combinations at Subsonic and Supersonic Speeds. J. Aircraft, vol. 5, no. 6, Dec. 1968, pp. 528-534.

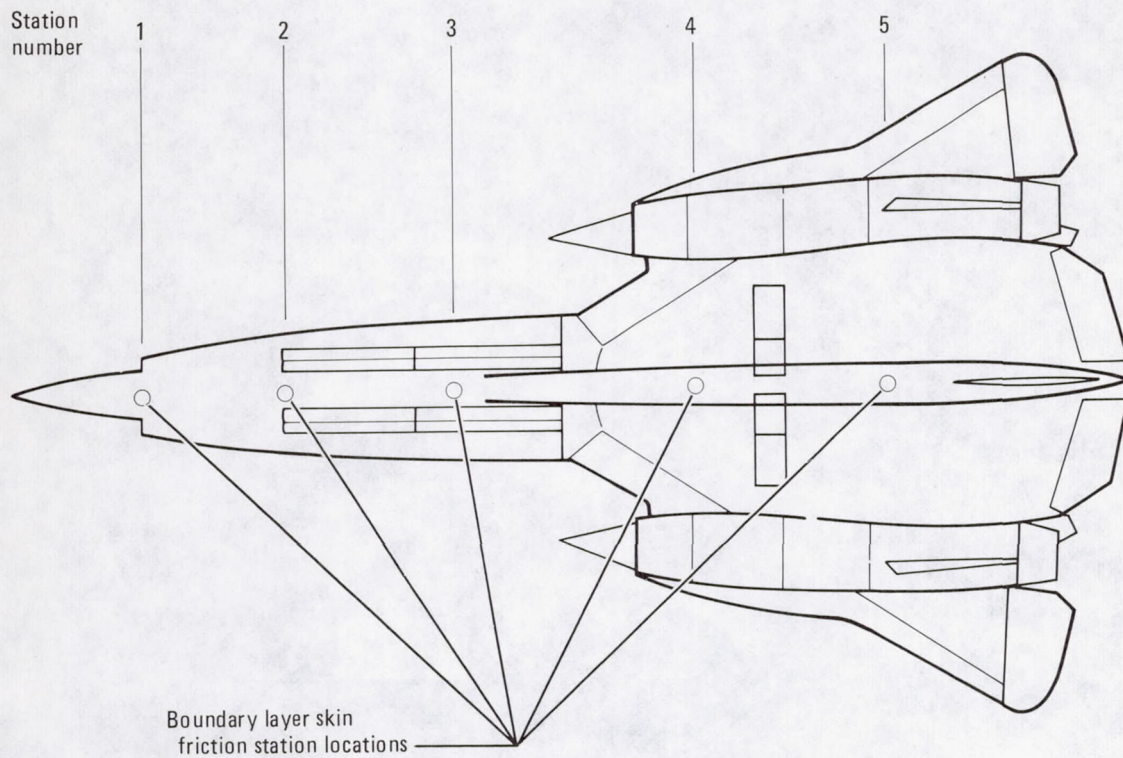


Figure 1.—Bottom view of YF-12A airplane showing locations of boundary layer skin friction stations.

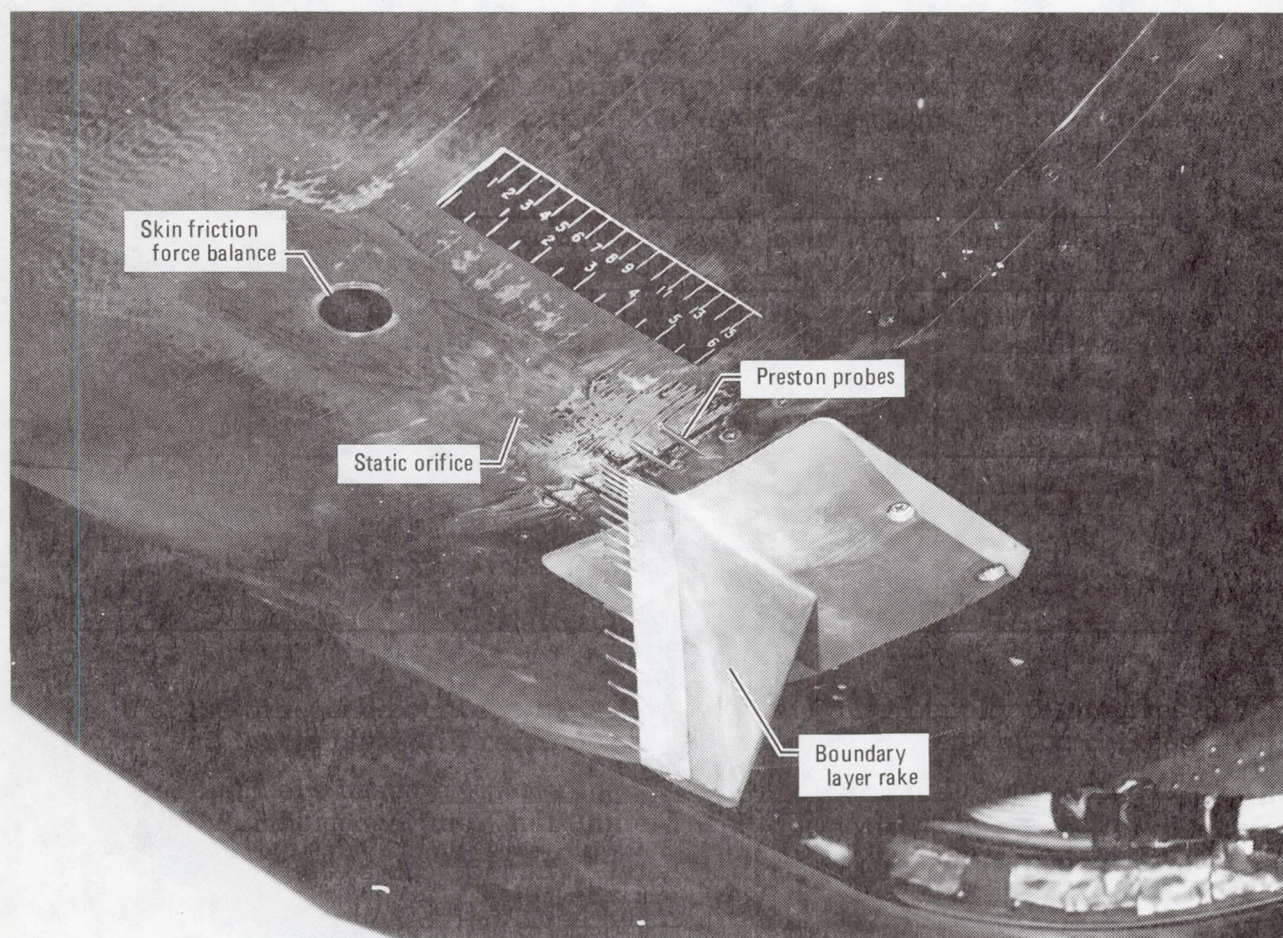


Figure 2.—Photo of typical boundary layer skin friction station showing the boundary layer rake, Preston probes, skin friction force balance, and static orifice.

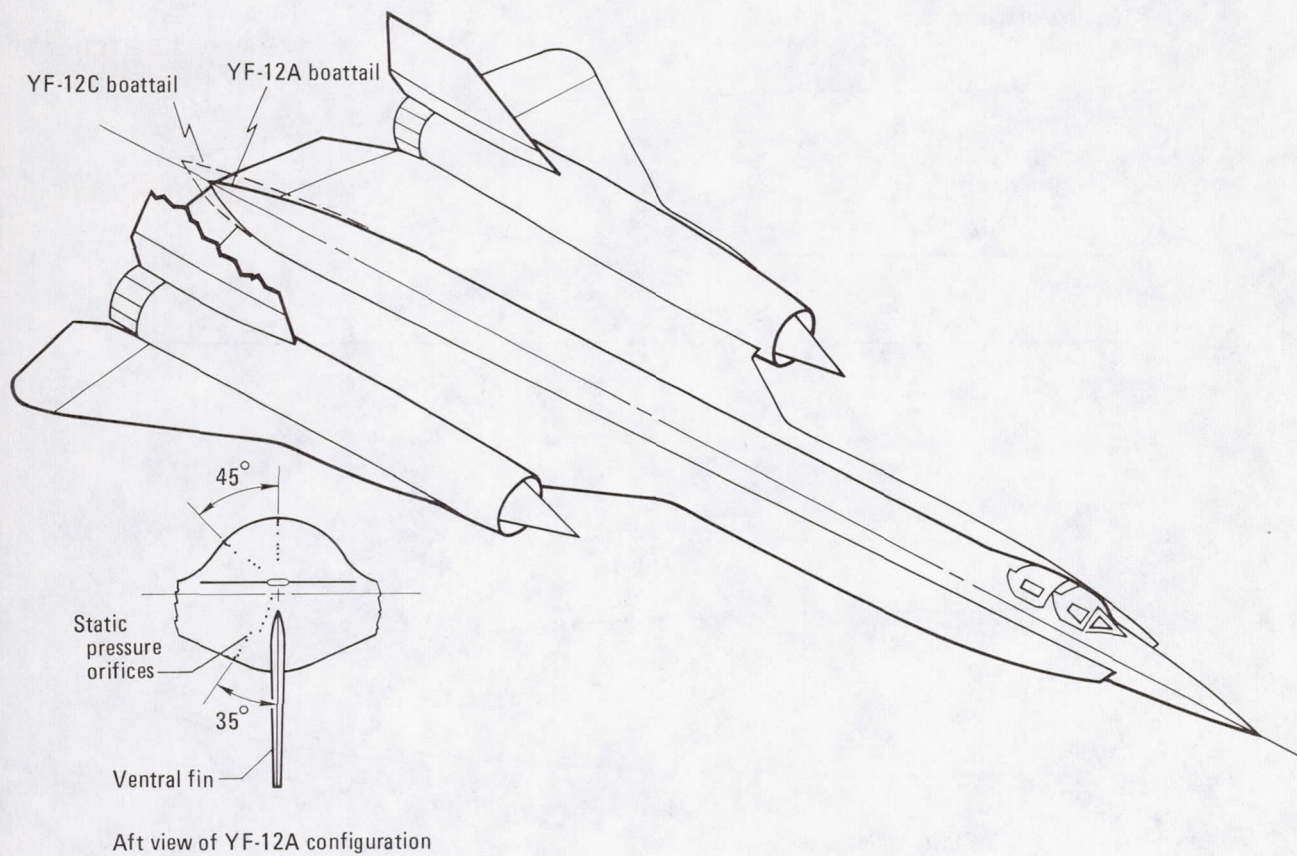
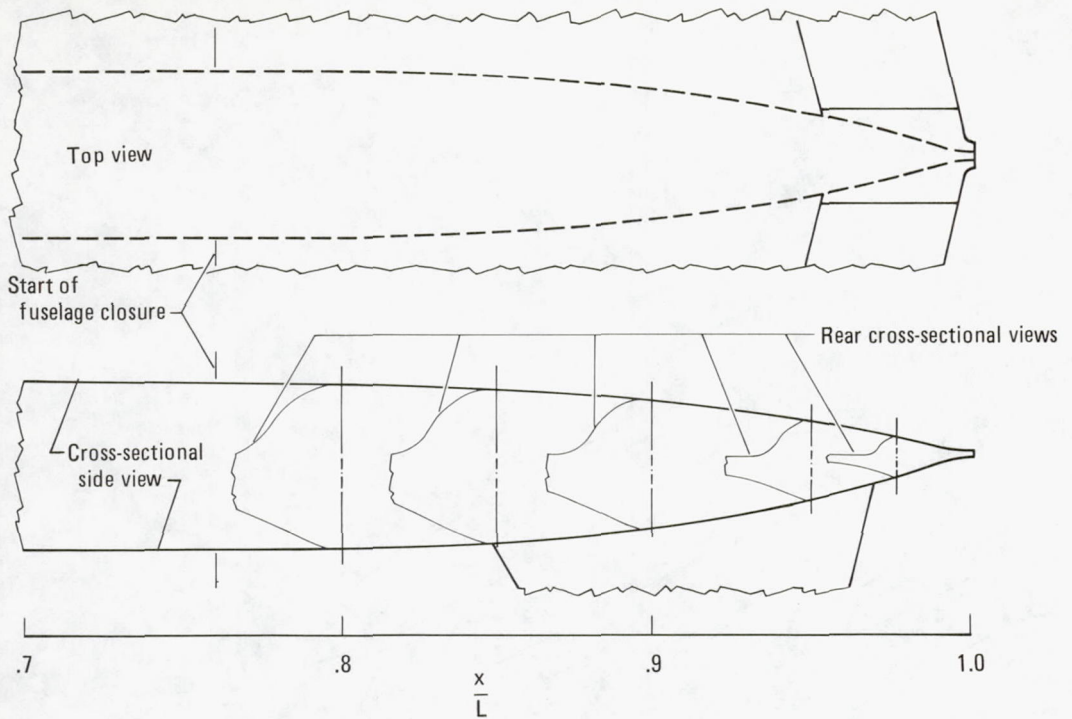


Figure 3.—General view of YF-12 airplane showing the two boattail configurations and radial location of static pressure orifices on configuration A.

YF-12A boattail configuration



YF-12C boattail configuration

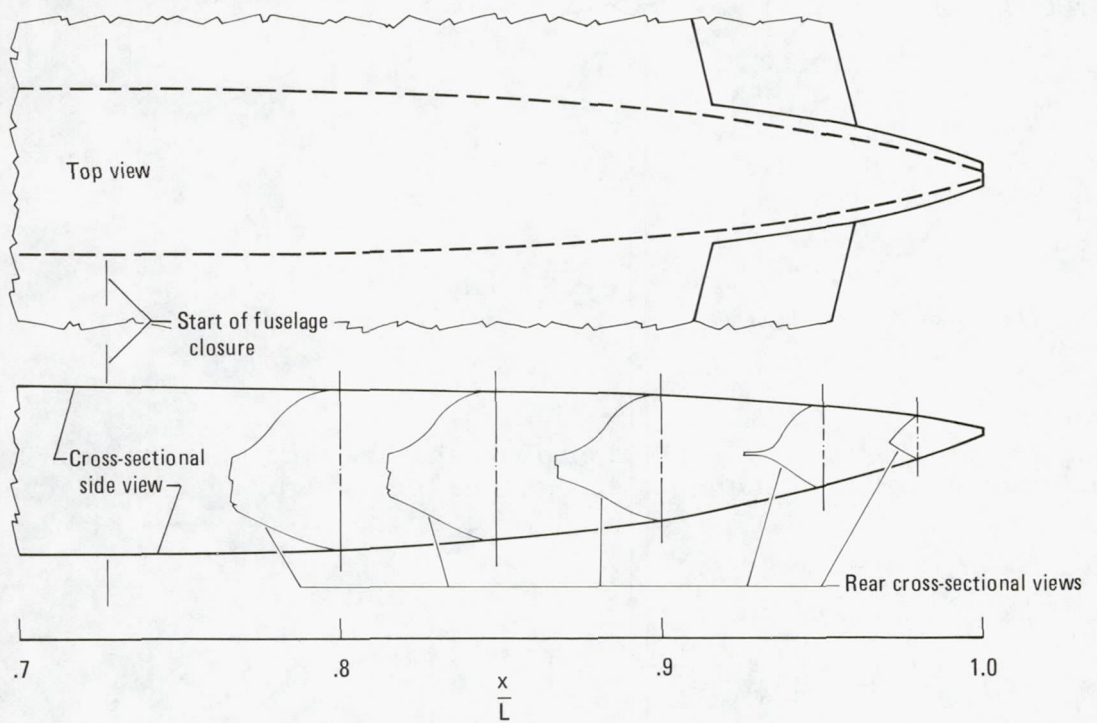


Figure 4.—Views of YF-12 boattails, configurations A and C.

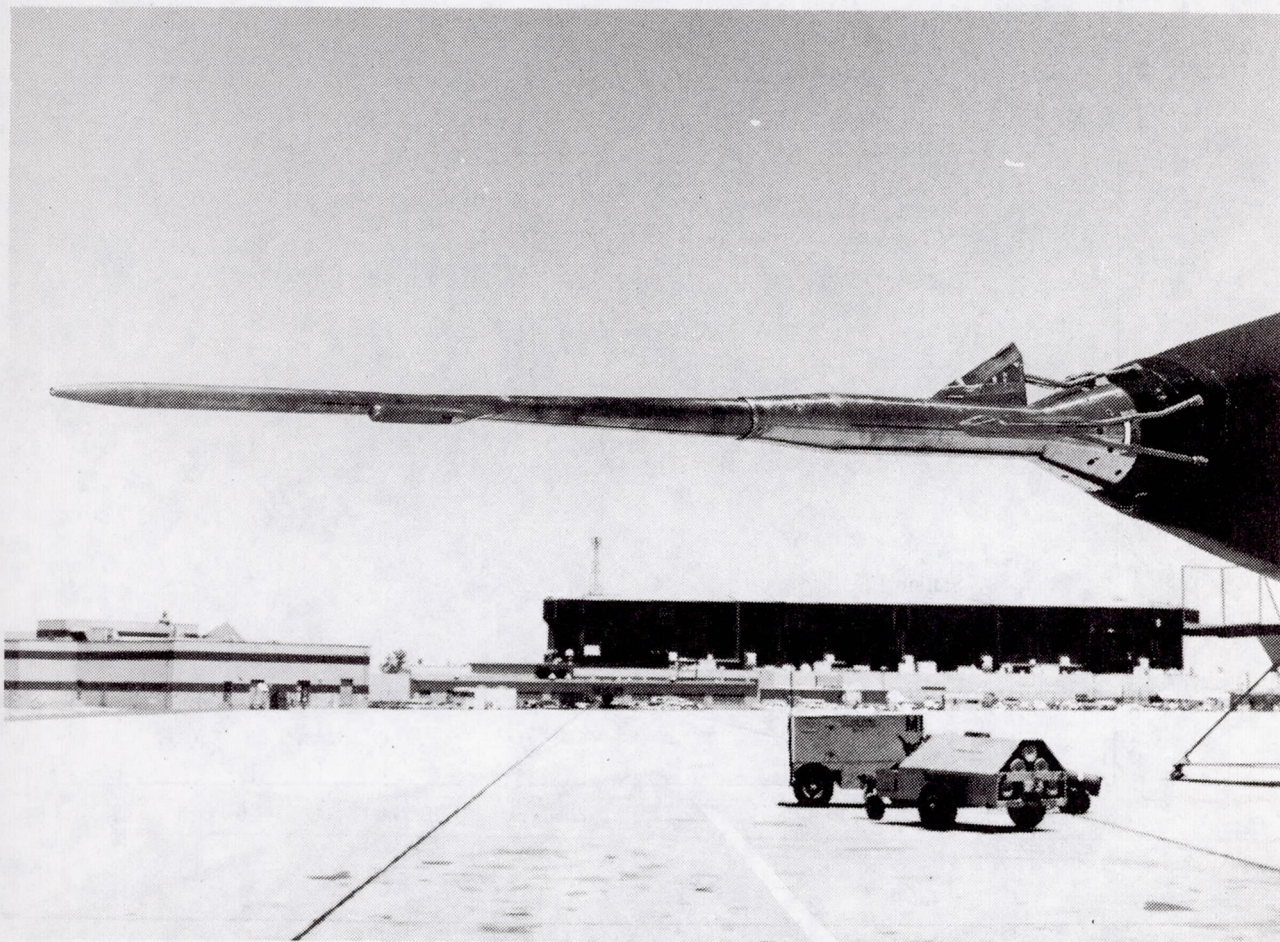
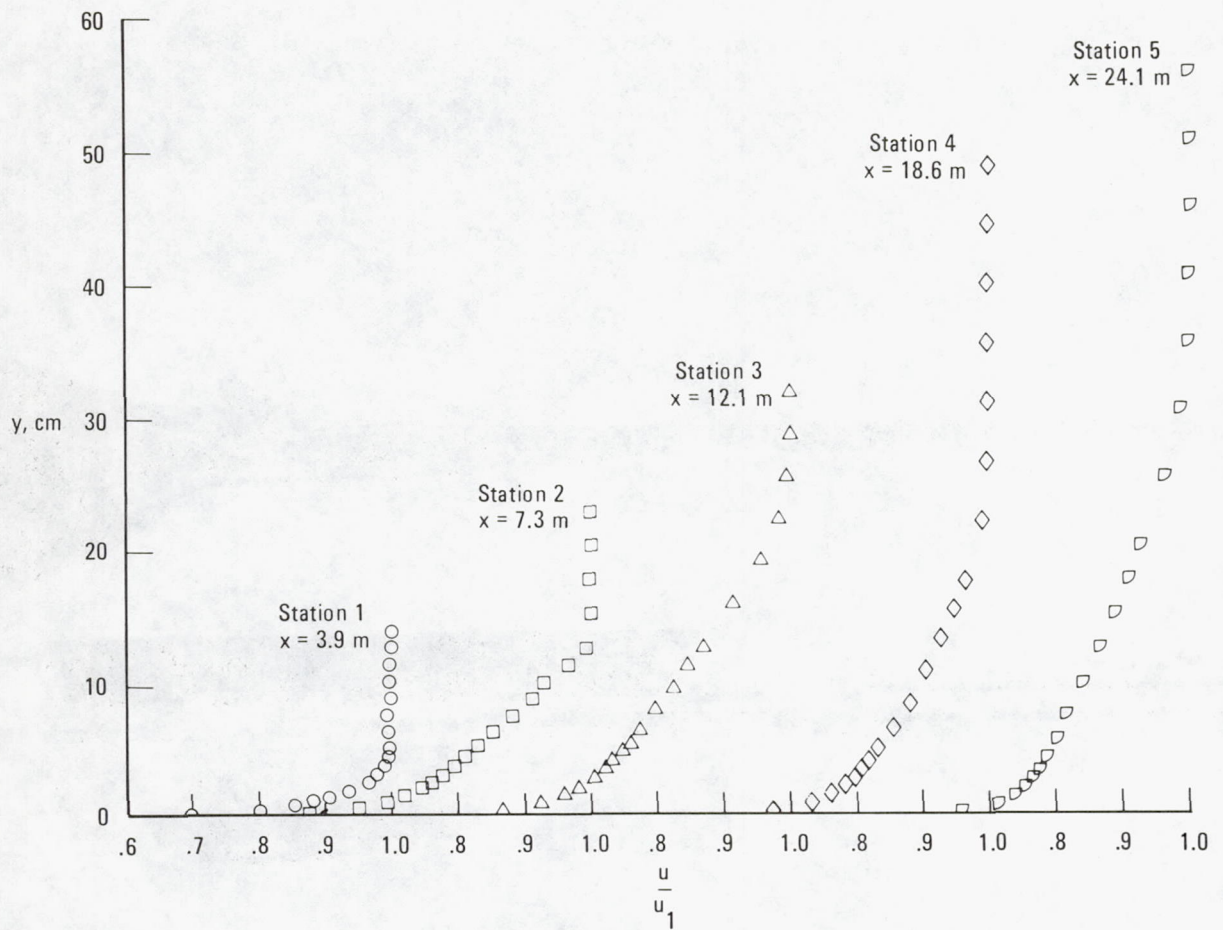
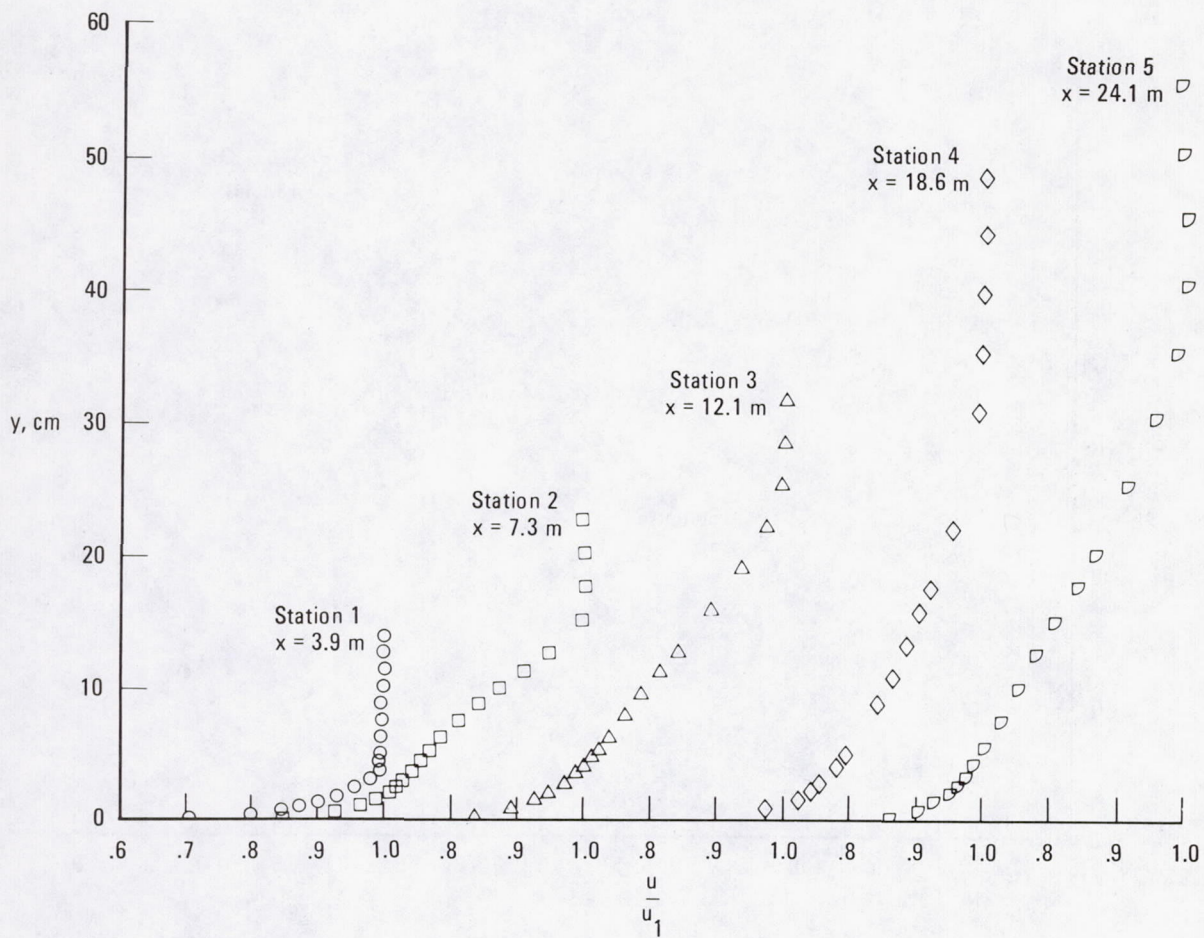


Figure 5.—Photo of airspeed probe.



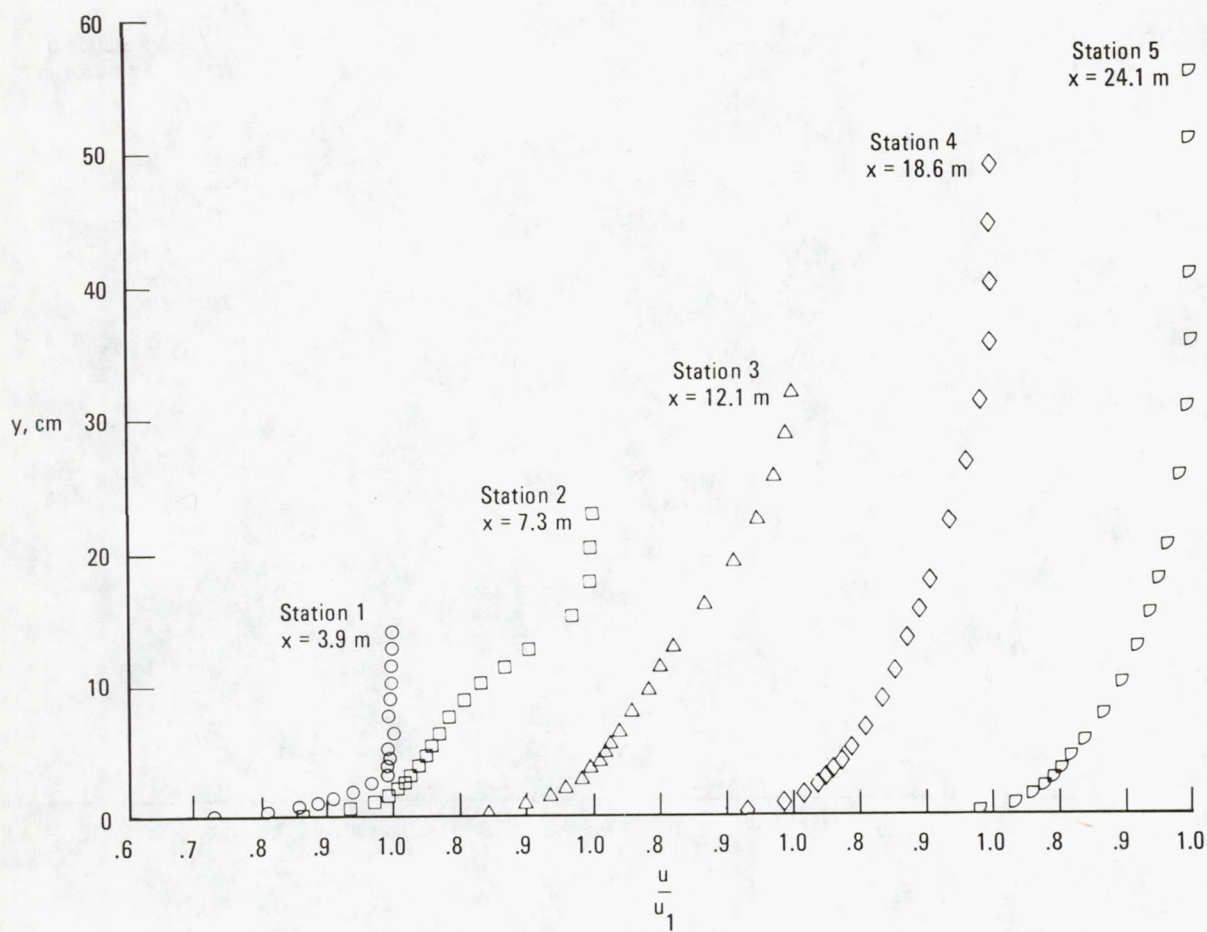
(a) $M \approx 2.0$.

Figure 6.—Boundary layer velocity profiles from five stations along the lower fuselage centerline of the YF-12A.



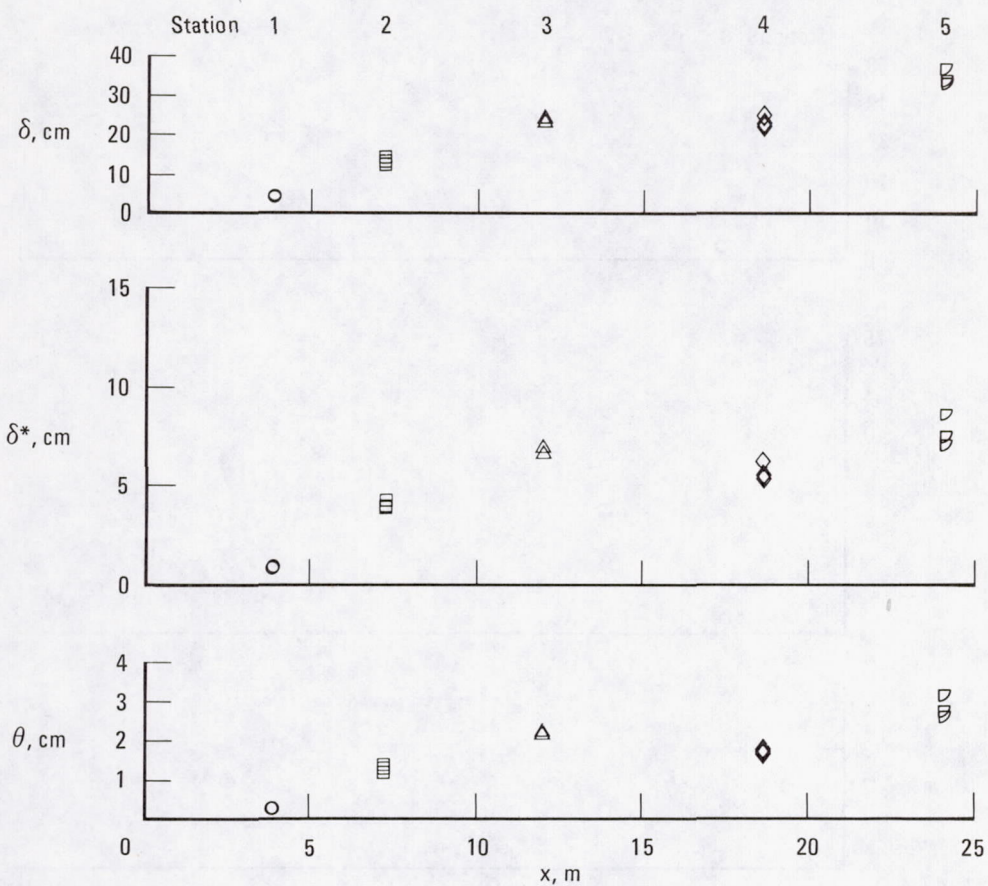
(b) $M \approx 2.5$.

Figure 6.—Continued.



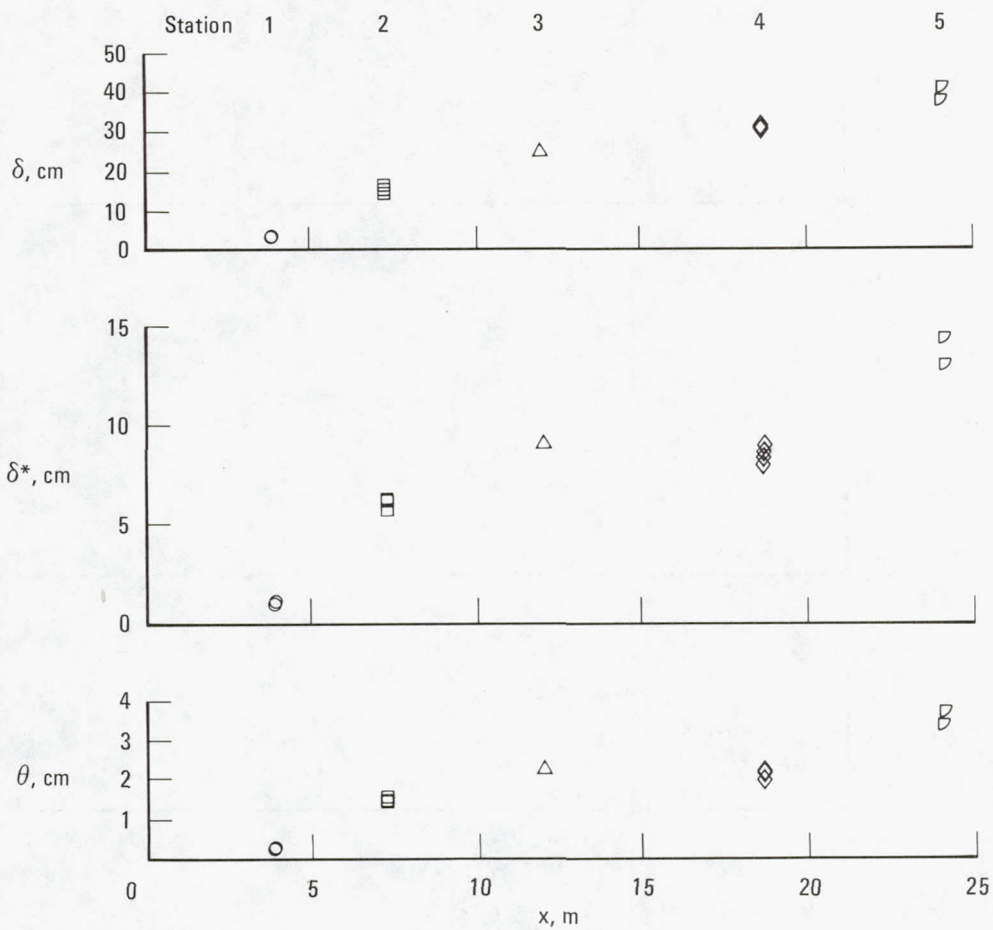
(c) $M \approx 3.0$.

Figure 6.—Concluded.



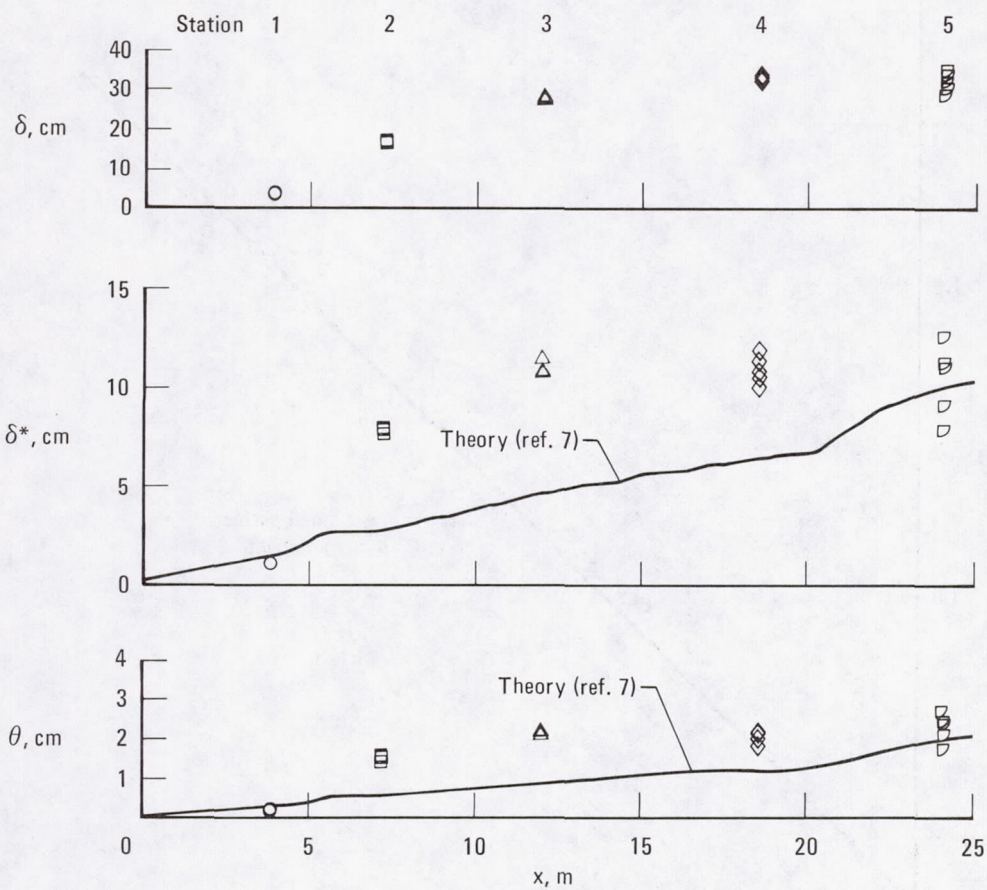
(a) $M \approx 2.0$.

Figure 7.—Variation of boundary layer thickness, δ , displacement thickness, δ^* , and momentum thickness, θ , as a function of run length, x .



(b) $M \approx 2.5$.

Figure 7.—Continued.



(c) $M \approx 3.0$.

Figure 7.—Concluded.

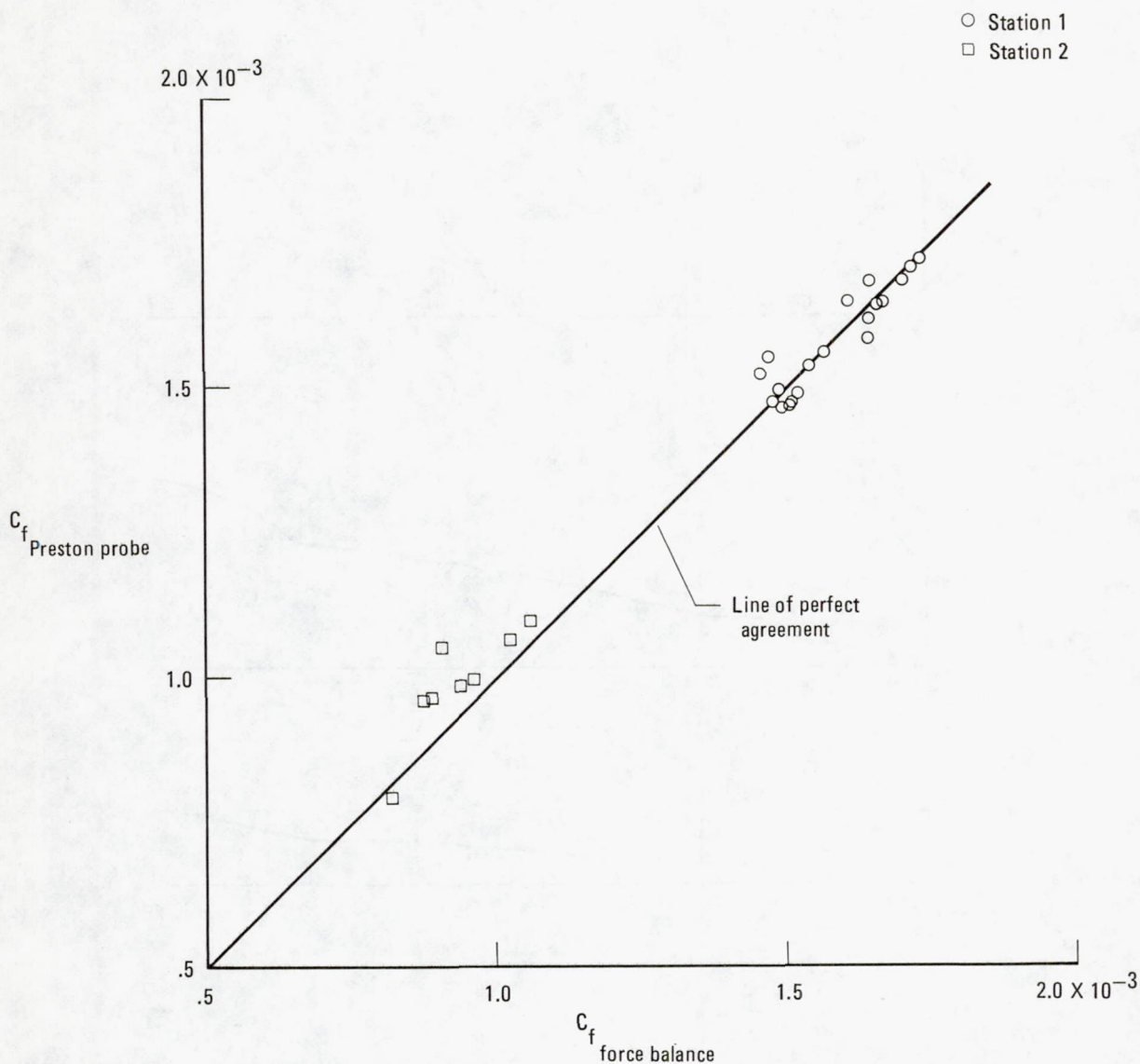
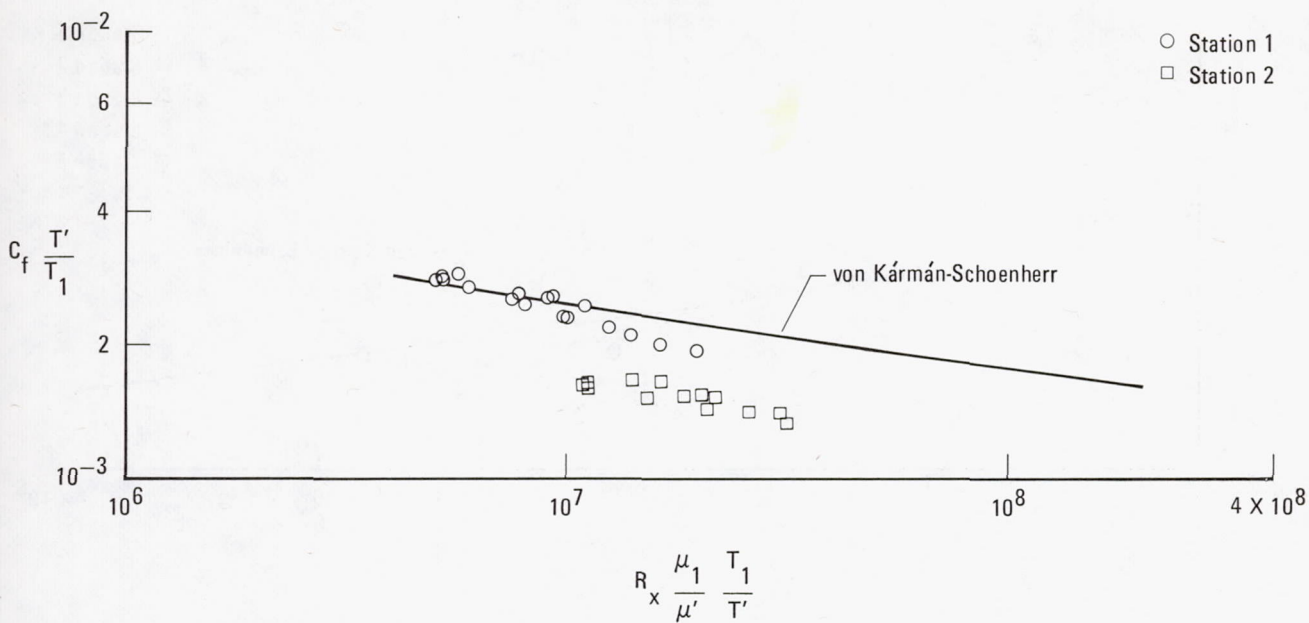
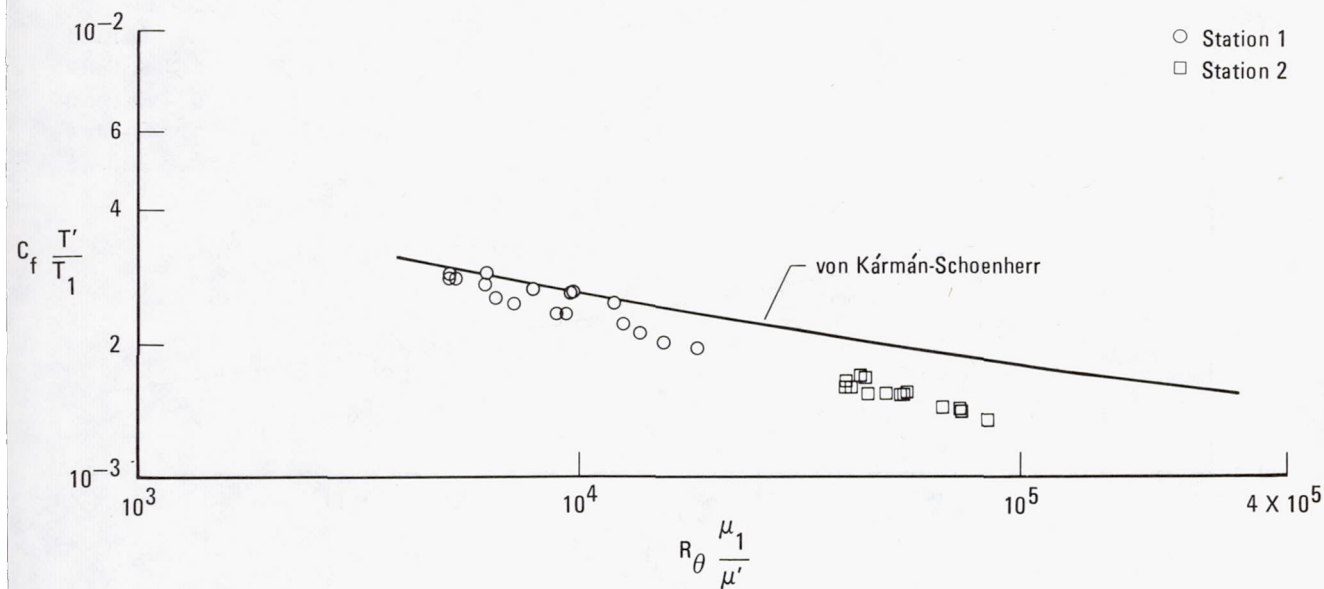


Figure 8.—Comparison of Preston probe skin friction coefficients determined by the Hopkins-Keener calibration with the skin friction coefficients obtained by the force balance technique.

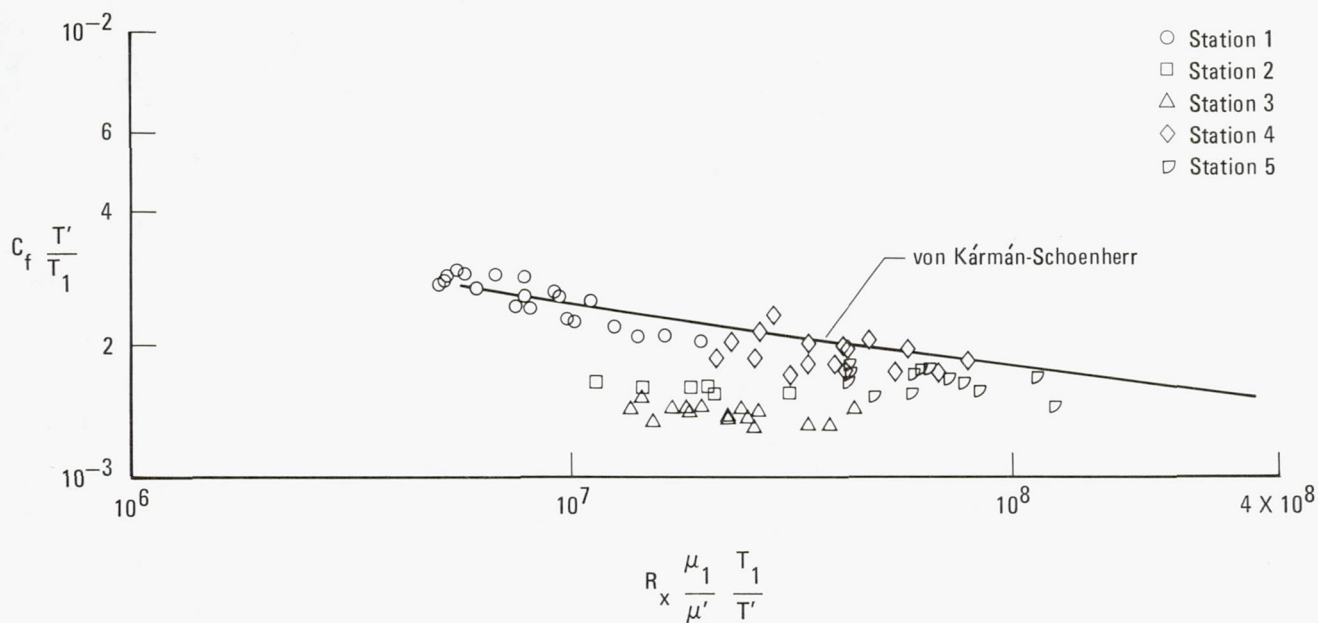


(a) Reynolds number based on x , distance from nose apex.

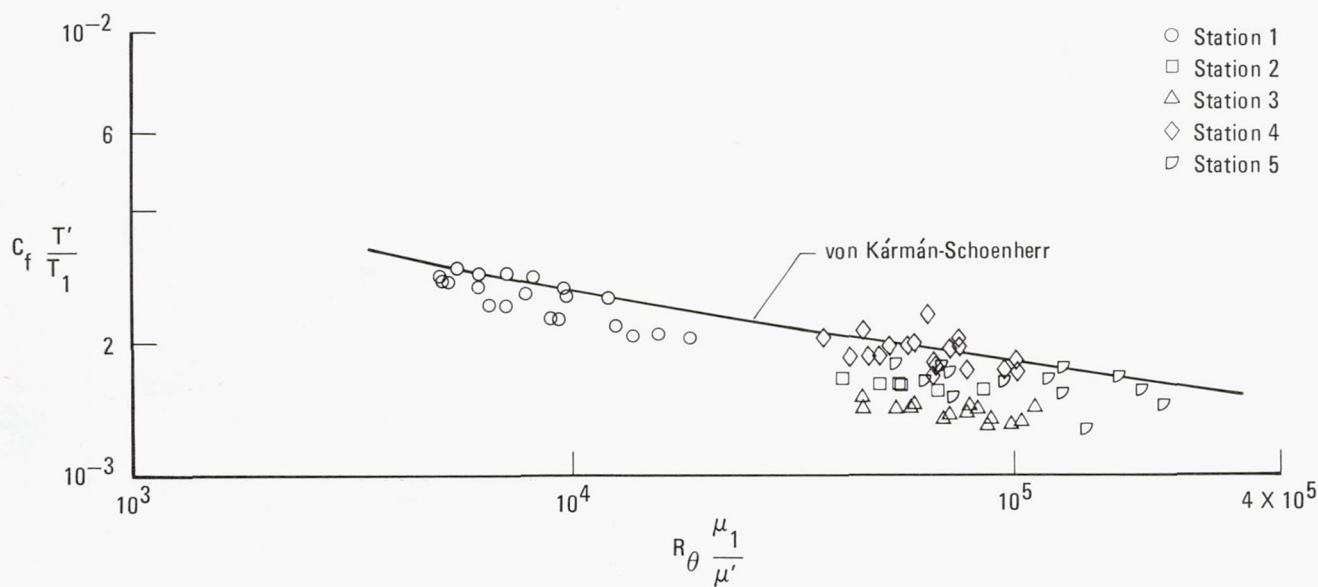


(b) Reynolds number based on θ , momentum thickness.

Figure 9.—Variation of local skin friction coefficient from the friction force balance as a function of Reynolds number.



(a) Reynolds number based on x , distance from nose apex.



(b) Reynolds number based on θ , momentum thickness.

Figure 10.—Variation of local skin friction coefficient from the Preston probe as a function of Reynolds number.

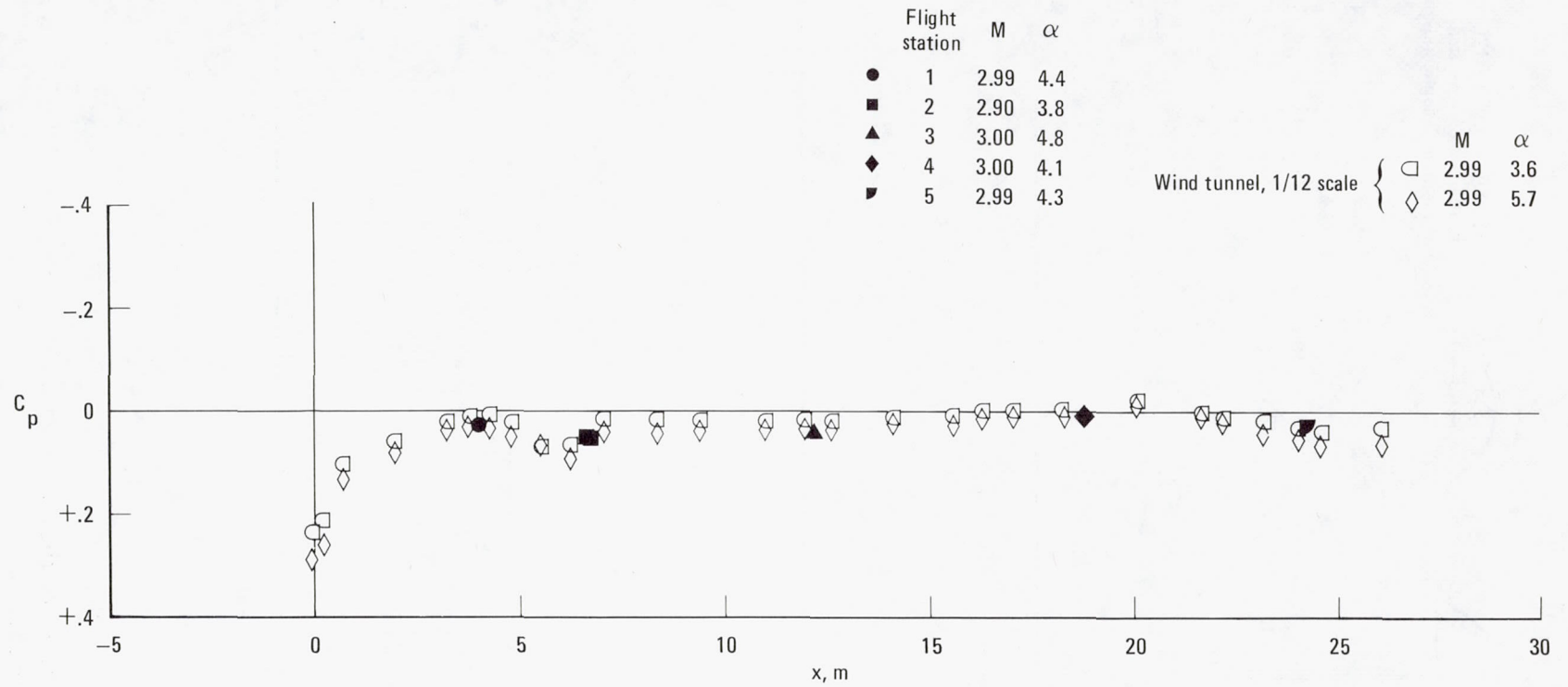
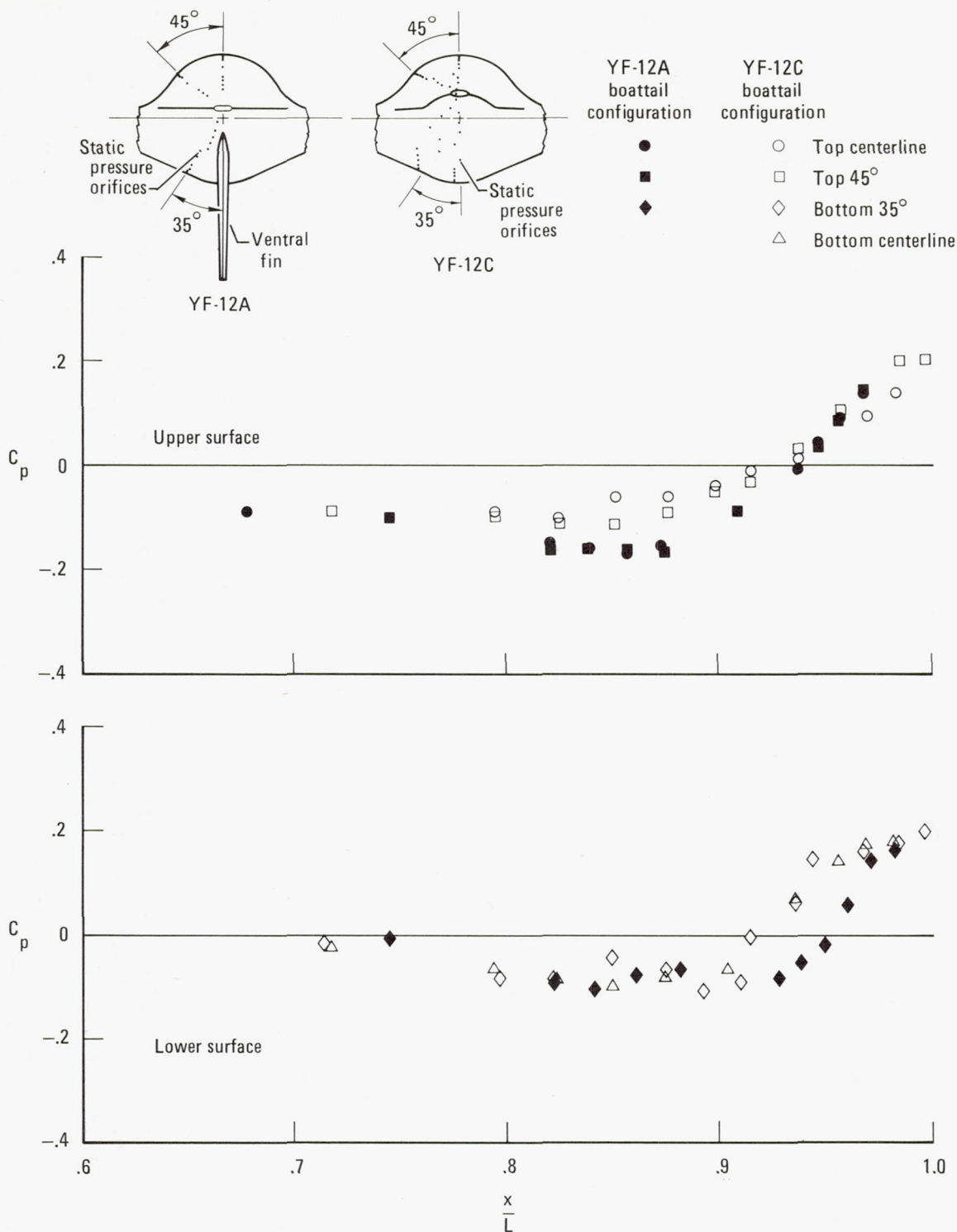
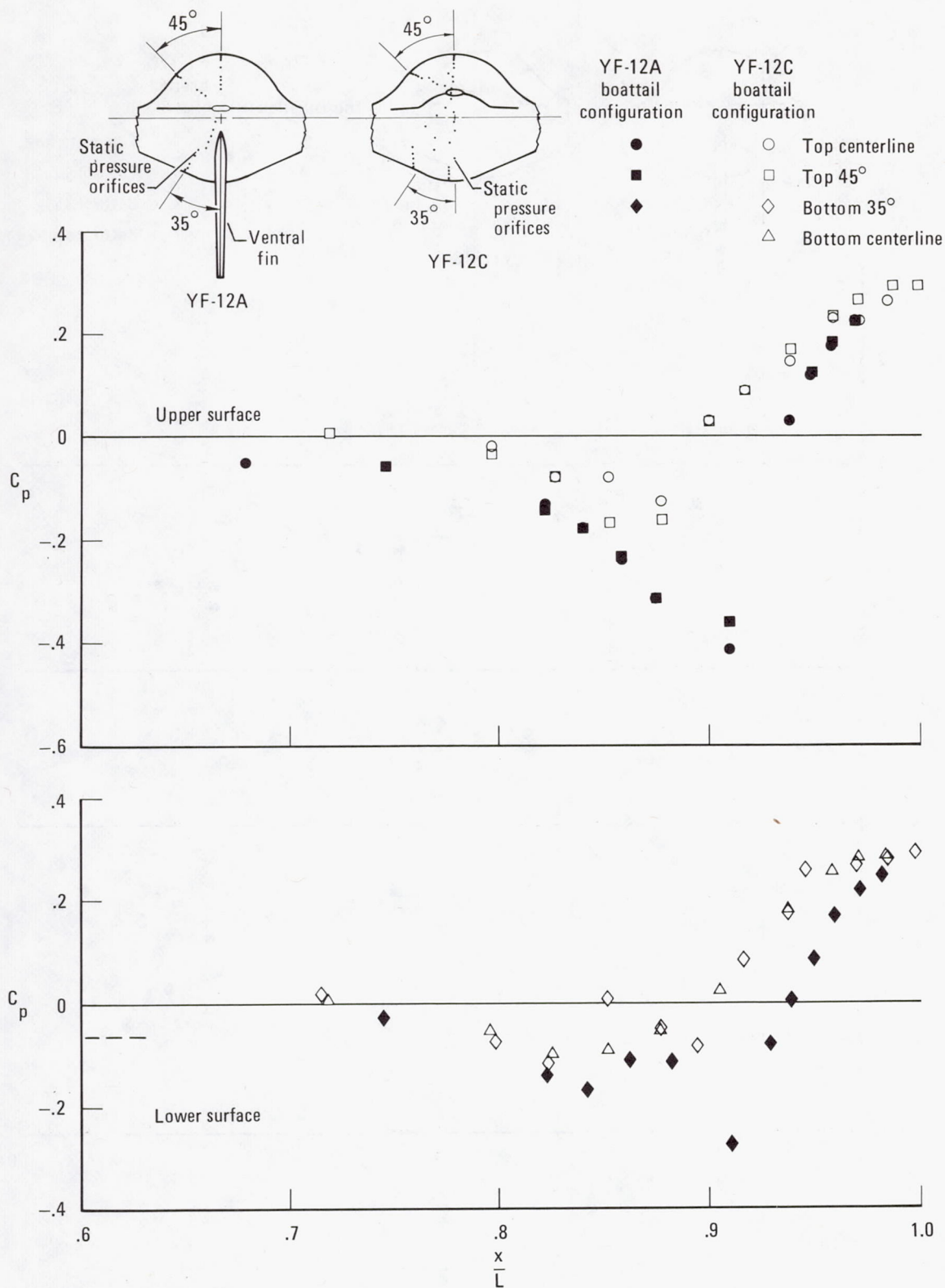


Figure 11.—Flight-measured pressure coefficients along the lower fuselage centerline of the YF-12 airplane and corresponding pressure coefficients from a 1/12-scale model.



(a) $M \approx 0.7$.

Figure 12.—Pressure distribution on the boattails of the YF-12A and YF-12C airplanes.



(b) $M \approx 0.96$.

Figure 12.—Continued.

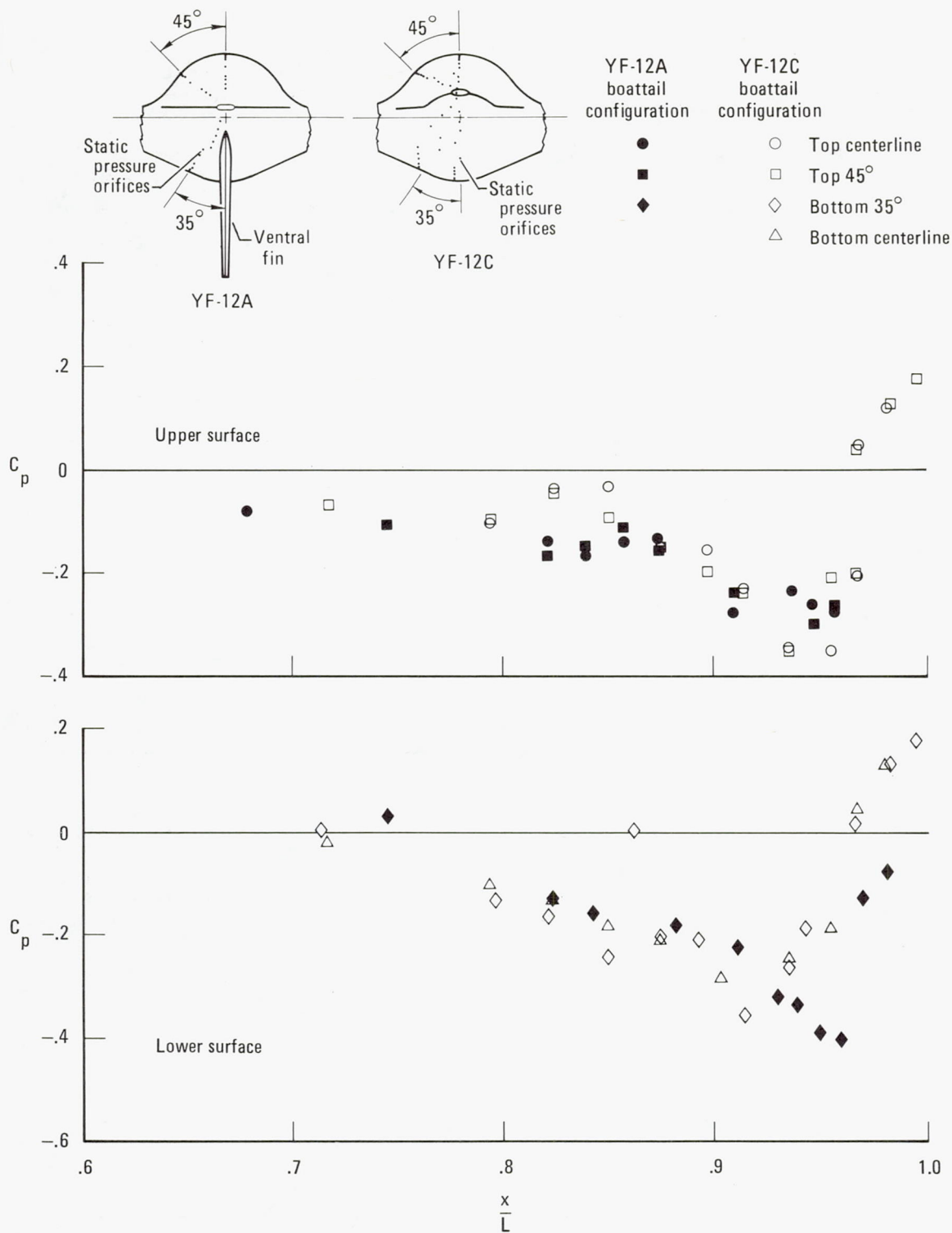
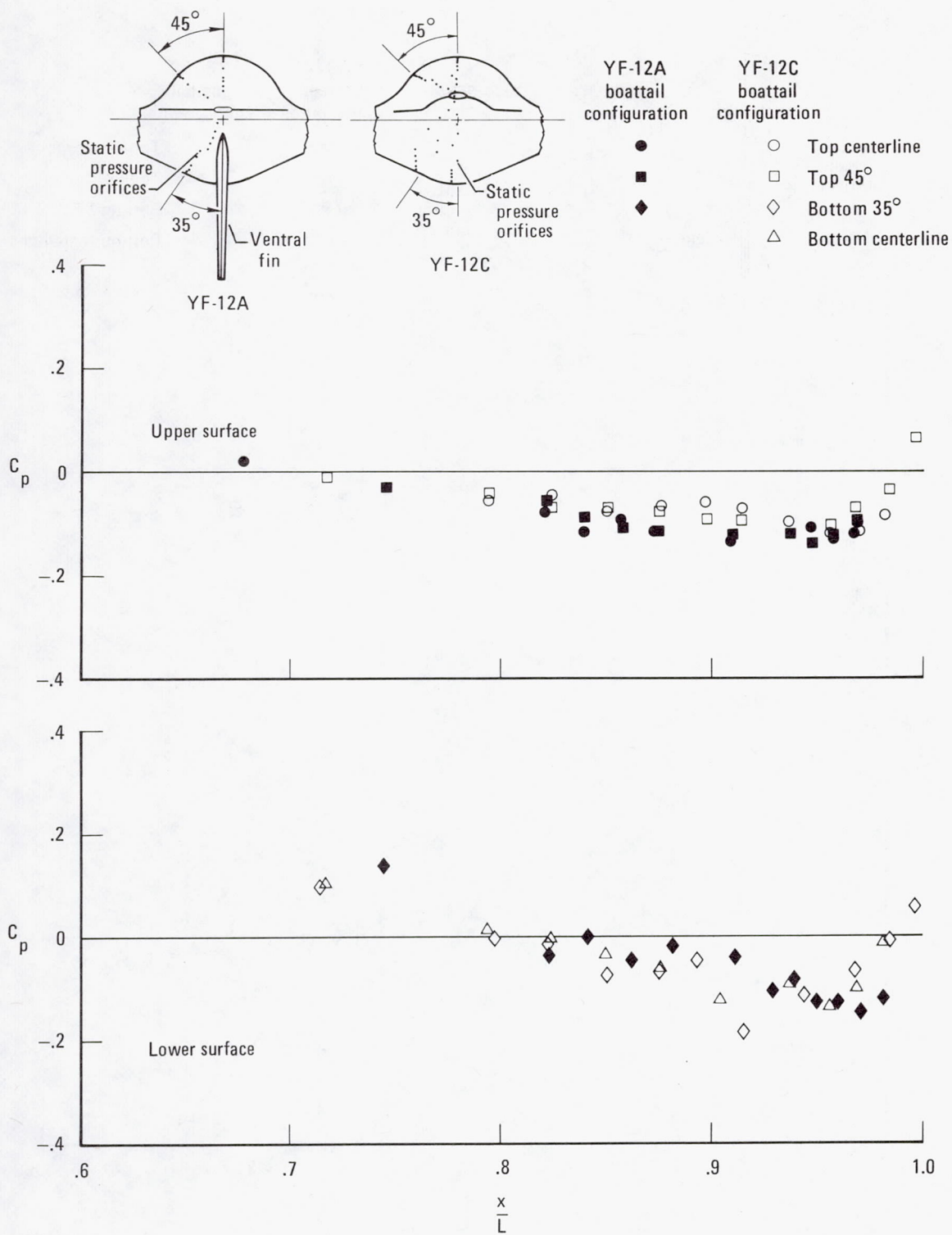
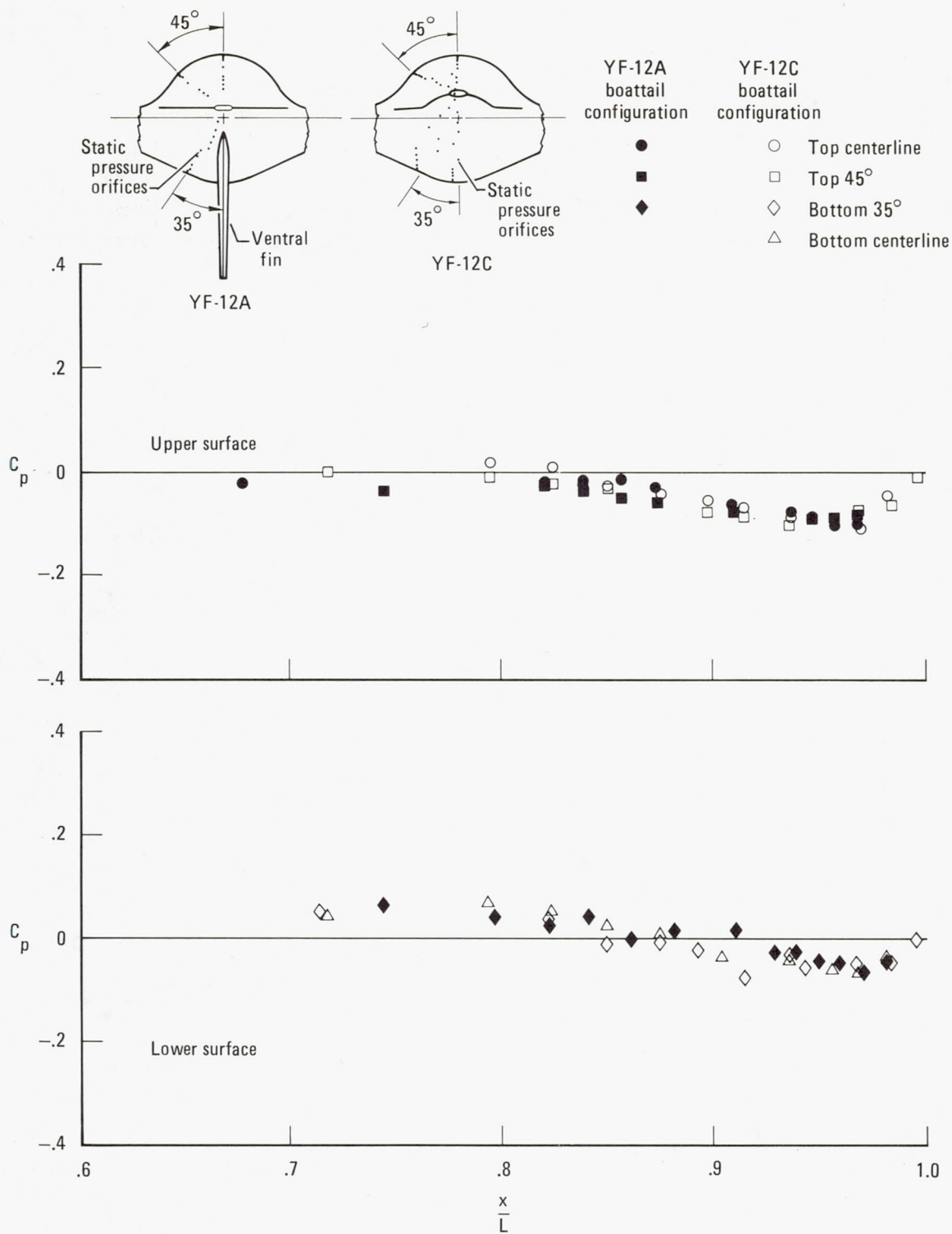


Figure 12.—Continued.



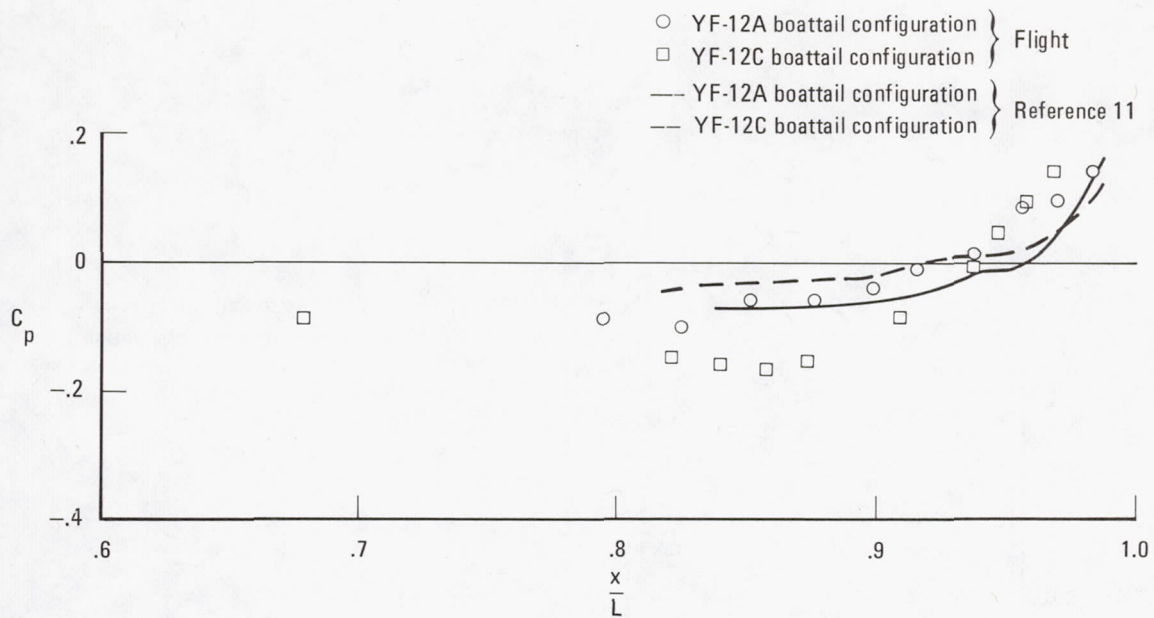
(d) $M \approx 2.0$.

Figure 12.—Continued.

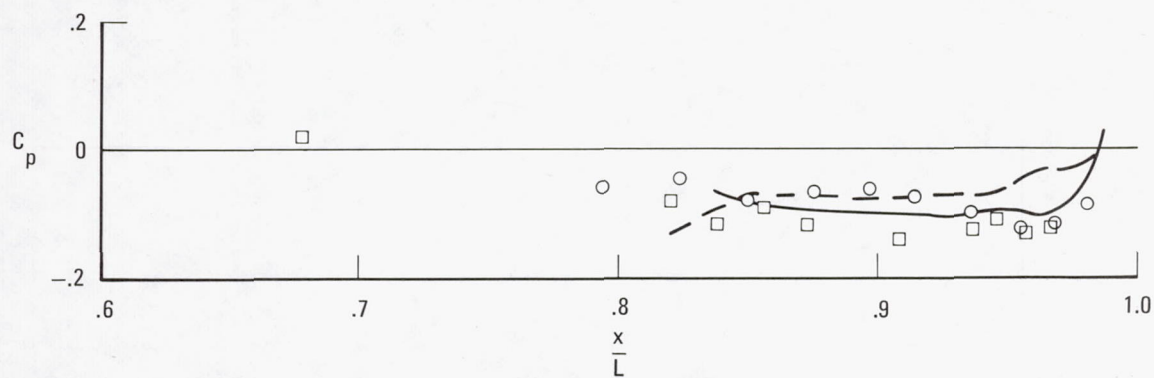


(e) $M \approx 3.0$.

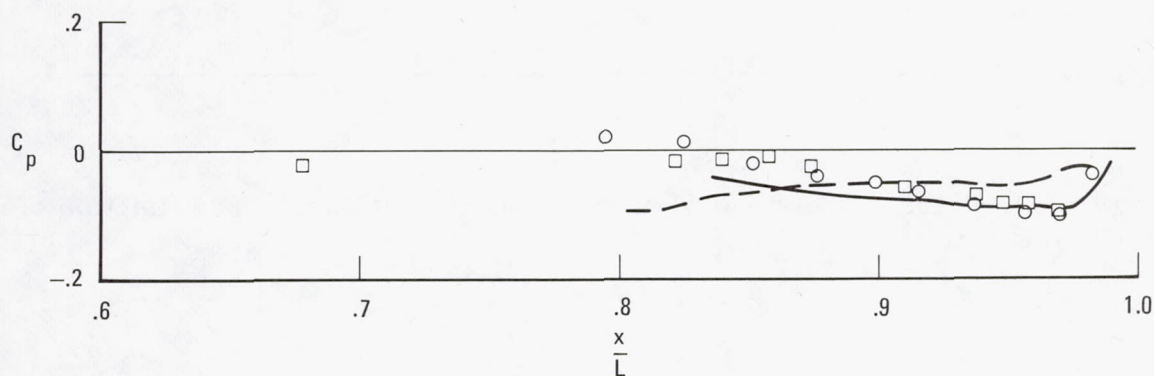
Figure 12.—Concluded.



(a) $M \approx 0.7$.



(b) $M \approx 2.0$.



(c) $M \approx 3.0$.

Figure 13.—Comparison of top centerline boattail pressure coefficients for YF-12A and YF-12C configurations with the predictions obtained using the techniques of reference 10.

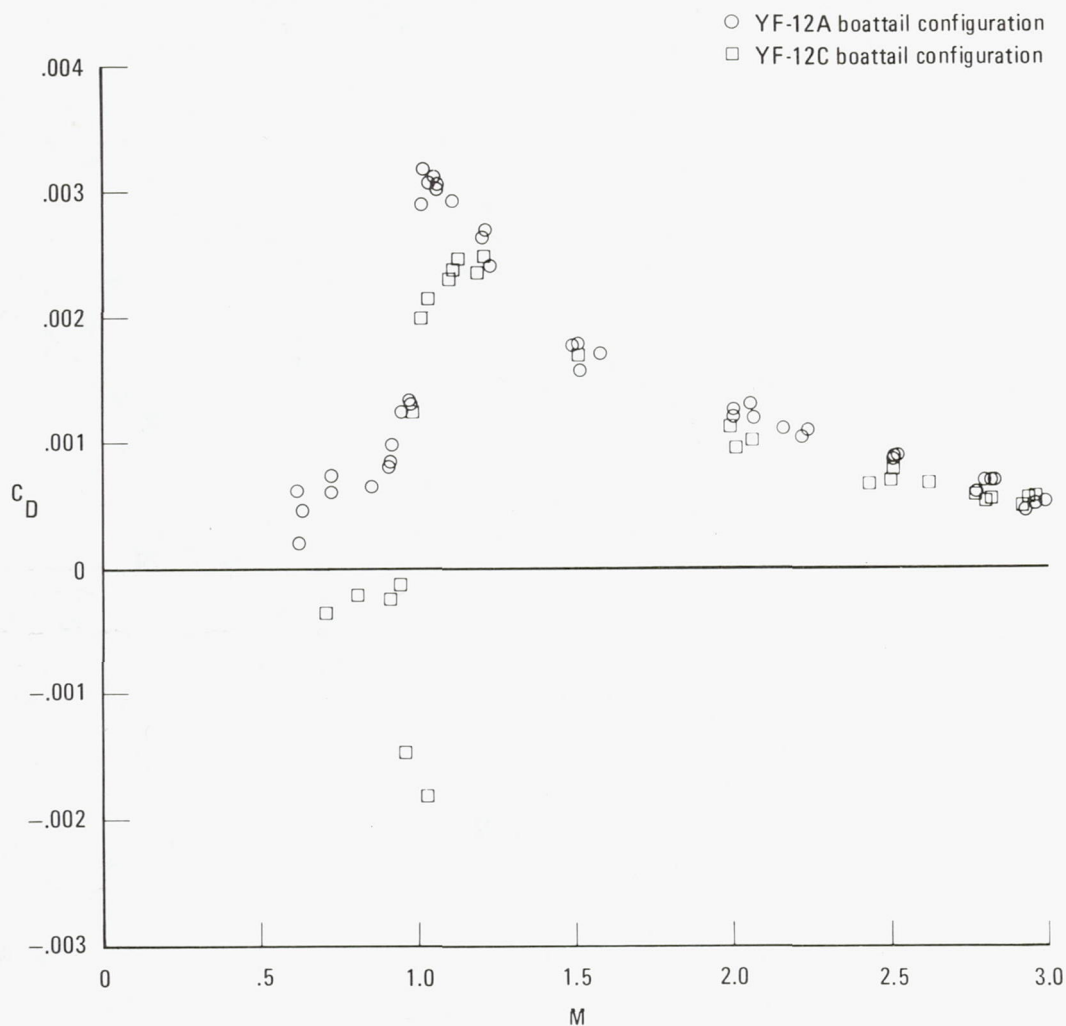


Figure 14.—Variation of boattail pressure drag coefficients as a function of Mach number.

IN-FLIGHT COMPRESSIBLE TURBULENT BOUNDARY LAYER
MEASUREMENTS ON A HOLLOW CYLINDER AT
A MACH NUMBER OF 3.0

Robert D. Quinn and Leslie Gong
Dryden Flight Research Center

SUMMARY

Skin temperatures, shearing forces, surface static pressures, and boundary layer pitot pressures and total temperatures were measured on a hollow cylinder 3.04 meters long and 0.437 meter in diameter mounted beneath the fuselage of the YF-12A airplane. The data were obtained at a nominal free stream Mach number of 3.0 and at wall-to-recovery temperature ratios of 0.66 to 0.91.

The free stream Reynolds number had a nominal value of 4.2×10^6 per meter. Heat transfer coefficients and skin friction coefficients were derived from skin temperature time histories and shear force measurements, respectively. Also, boundary layer velocity profiles were derived from pitot pressure measurements, and a Reynolds analogy factor of 1.11 was obtained from the measured heat transfer and skin friction data.

Skin friction, calculated by the theory of van Driest, by Eckert's reference enthalpy method, and by the Spalding and Chi method, was compared with the measured data. The skin friction coefficients predicted by the theory of van Driest were in excellent agreement with the measurements. Theoretical heat transfer coefficients, in the form of Stanton numbers calculated by using a modified Reynolds analogy between skin friction and heat transfer, were compared with measured values. The theory of van Driest, together with the experimentally determined Reynolds analogy factor of 1.11, predicted heat transfer coefficients that were in excellent agreement with the measured data. The measured velocity profiles were compared to Coles' incompressible law-of-the-wall profile by transforming the compressible measured data to their incompressible values. The transformation methods of van Driest and Eckert both gave good correlation.

INTRODUCTION

Accurate calculations of turbulent skin friction and heat transfer are required

for the efficient and safe design of high-speed aircraft. A large number of empirical and semiempirical theories are available which can be used to predict skin friction and heat transfer. However, values predicted by the various theories usually differ substantially; therefore, experiments must be performed to determine the validity of the theories. A large amount of experimental skin friction and heat transfer data has been obtained in the wind tunnel (refs. 1 and 2). Unfortunately, the wind tunnel tests have shown conflicting results (refs. 3 and 4). Data obtained from flight have also differed from the wind tunnel results (refs. 5 and 6). This lack of agreement in results obtained from the various experimental tests has hampered the evaluation of turbulent boundary layer theories and clearly indicates the need for further study.

The YF-12A airplane with its Mach 3 cruise capability offered an excellent test bed for compressible turbulent boundary layer measurements. Consequently, an instrumented hollow cylinder 3.04 meters in length was installed beneath the fuselage of the YF-12A airplane to obtain flight-measured turbulent boundary layer data that could be used to evaluate the various turbulent predicting methods. In addition, the size of the hollow cylinder would allow the same cylinder with the same instrumentation to be tested in the wind tunnel so that flight and wind tunnel measurements could be directly compared.

This paper presents flight data that were obtained on a hollow cylinder during two YF-12 flights designated flights A and B. During flight A, skin friction and boundary layer profile data were obtained at a local Mach number of 2.9, at a wall-to-recovery temperature ratio of 0.91, and at a momentum thickness Reynolds number of 8664. During flight B, heat transfer and skin friction data were obtained at a local Mach number of 2.92, at wall-to-recovery temperatures of 0.66 to 0.71 and at a local Reynolds number of 4.17×10^6 per meter. The measured data are compared to values calculated by various predicting methods. In addition, boundary layer transition determined from measured temperatures and measured heat transfer are presented.

SYMBOLS

Physical quantities in this report are given in the International System of Units (SI).

C_f local skin friction coefficient

F_c transformation function for skin friction, $\frac{\bar{C}_f}{C_f}$

F_x transformation function for length Reynolds number,
 $\frac{\bar{Re}_x}{Re_x}$ or $\frac{\bar{Re}_L}{Re_L}$

h	altitude, m
h_H	local heat transfer coefficient based on enthalpy, $\text{kg/m}^2\text{-sec}$
L	length of turbulent flow, m
M	Mach number
P	pressure, N/m^2
Re	unit Reynolds number, $\frac{\rho U}{\mu}$, m^{-1}
Re_L	Reynolds number based on length of turbulent boundary layer flow, $\frac{\rho_\delta U_\delta L}{\mu_\delta}$
Re_x	Reynolds number based on distance from the leading edge, $\frac{\rho_\delta U_\delta x}{\mu_\delta}$
Re_θ	Reynolds number based on momentum thickness, $\frac{\rho_\delta U_\delta \theta}{\mu_\delta}$
St	local Stanton number, $\frac{h_H}{\rho_\delta U_\delta}$
s	Reynolds analogy factor
T	temperature, K
T_R	boundary layer recovery temperature, K
U	velocity, m/sec
U_τ	friction velocity, $\sqrt{\frac{\tau}{\rho}}$
x	distance from leading edge, m
y	distance normal to surface of cylinder, cm
α	angle of attack, deg
β	angle of sideslip, deg
δ	total boundary layer thickness, cm

θ	boundary layer momentum thickness, cm
μ	dynamic viscosity, N-sec/m ²
ν	kinematic viscosity, m ² /sec
ρ	density of air, kg/m ³
τ	shearing stress, N/m ²

Subscripts:

t	total conditions
w	wall or skin
δ	boundary layer edge conditions
∞	free stream

Superscripts:

$(-)$	incompressible variable or a variable that has been transformed to the equivalent constant property case
-------	--

DESCRIPTION OF EQUIPMENT

A hollow cylinder, 3.04 meters in length and 0.437 meter in outside diameter, was installed on the lower fuselage of the YF-12A airplane, as shown in figure 1. The cylinder was attached to a pylon which was mounted to hard points on the aircraft. The pylon provided a vertical separation distance of 0.46 meter between the aircraft fuselage and the hollow cylinder. A photograph of the airplane with the cylinder installed is shown in figure 2. The cylinder skin was 0.127 centimeter thick and had a sharp leading edge with a radius of 0.0127 centimeter. A complete description of the airplane can be found in reference 7.

INSTRUMENTATION

As shown in figure 3, the cylinder was instrumented with 123 thermocouples, 34 static pressure orifices, a skin friction balance, a pitot pressure rake, and a total temperature boundary-layer rake. The thermocouples were 30-gage chromel-alumel wires spot welded to the inside surface of the skin. The pressure orifices were tubing with an inside diameter of 0.32 centimeter installed flush with the outside surface of the skin. The skin friction gage was a commercially developed, liquid-cooled force balance installed flush with the surface of the cylinder at the location shown in figure 3. A detailed description of the skin friction gage is given in reference 8. The pitot pressure rake and the total temperature rake were installed

274.12 centimeters aft of the leading edge, and, as shown in figure 3, the pitot pressure rake was installed on the lower surface centerline and the total temperature rake was located on the lower surface at an angular displacement of 16.25° from the vertical centerline. The outermost probe on the pressure rake was a 20° half angle conical probe used to measure flow angles needed to insure that the cylinder was aligned with the local flow.

The primary boundary layer measurements were made on the lower centerline of the cylinder. Data presented in this paper were obtained from these measurements. The surface static pressure measurements and the skin temperature measurements made at the other locations were used to detect any anomalies in the flow field on the cylinder.

TEST CONDITIONS

In order to obtain meaningful boundary layer measurements, the hollow cylinder had to be installed at a location on the YF-12A airplane where the local flow was uniform. Consequently, before the aircraft installation was made, flow-field surveys were conducted on a 1/25-scale model of the YF-12A airplane in the Langley Unitary Plan Wind Tunnel (ref. 9) and on the YF-12A airplane in flight. These tests confirmed that the local flow field below the airplane was uniform in the area where the cylinder was to be located.

Two configurations of the cylinder were used in the experiment. The first configuration, tested during flight A, is shown in figure 4. With this configuration the wall or skin temperature is always at or near radiation equilibrium temperature and, consequently, heat transfer data were not obtained during flight A. The second configuration, tested during flight B, is shown in figure 5. In this configuration the cylinder was insulated with a frangible cover which was used to provide low initial wall temperatures. Prior to takeoff, to insure that the measurements were obtained at cold surface temperatures, the cylinder was cooled to a temperature of 211 K using gaseous nitrogen. When the airplane reached the desired test conditions, the insulation was removed within 50 milliseconds and the test data were obtained.

Time histories of free stream Mach number, altitude, and angle of attack for flights A and B are shown in figures 6(a) and 6(b), respectively. Also shown in each figure is a typical skin-temperature time history. The shaded portion of these flight profiles indicates the time during which the boundary layer data of this experiment were obtained. Also shown in figure 6(b) is the time at which the insulation was removed. As can be seen, once the insulation was removed, the skin temperature increased at a rapid rate. It was during this period of high heating rates that the heat transfer and other boundary layer data were obtained. The free stream conditions at which the data presented in this paper were obtained are given in table 1. The local (cylinder) test conditions at which the data were obtained are given in table 2.

It should be noted that the boundary layer edge static pressure given in table 2 was actually measured on the surface of the cylinder. The usual assumption was made that the static pressure through the boundary layer was constant. Also, the wall-to-recovery temperature ratio given in table 2 for flight A is based on the wall

temperature measured on the lower centerline of the cylinder at the skin friction balance location, and is slightly lower than the wall-to-recovery temperature ratios on the cylinder forward of this location.

RESULTS AND DISCUSSION

Surface Static Pressures

The surface static pressures measured on the lower centerline of the cylinder are shown in figure 7. Figure 7(a) shows the data obtained during flight A, and figure 7(b) shows the data obtained during flight B. The solid lines in these figures are straight line fairings of the data. The pressures were constant and equal to 4943 N/m^2 for flight A and 4413 N/m^2 for flight B.

Boundary Layer Profiles

The Mach number and velocity profiles derived from the data measured during flight A are tabulated in table 3. Also given in table 3 are the boundary layer temperature distribution, the momentum thickness, and the pertinent boundary layer edge conditions. As previously noted, boundary layer profiles were not obtained during flight B.

Measured total temperature ratios obtained during flight A are plotted in figure 8 as a function of the velocity ratio squared. Also shown for comparison purposes is the quadratic profile calculated by the method given in reference 3. The figure shows that the measured data are in excellent agreement with the quadratic distribution.

The boundary layer velocity distribution, calculated from the measured data obtained during flight A, is presented in figure 9. Also shown is the velocity profile predicted by the power law. When a power law exponent of 8 was used, excellent agreement was obtained between the power law velocity profile and the measured data.

Boundary Layer Thickness

A problem often encountered when trying to evaluate the various turbulent skin friction and heat transfer theories is that of determining the virtual origin of turbulent flow. Unless turbulent flow originates at or near the leading edge of the test specimen, the determination of the virtual origin is somewhat arbitrary. This problem can be eliminated if the comparisons of measured data with calculated data are based on momentum thickness Reynolds number. Consequently, one of the primary purposes of the boundary layer surveys was to determine the momentum thickness. However, in order to evaluate the momentum thickness, the total thickness must be determined. In the present investigation the total boundary layer thickness was computed by the method developed in reference 10, which yielded a thickness value of 3.05 centimeters.

Law-of-the-Wall Velocity Profiles

The use of the Clauser technique to obtain skin friction from velocity profiles is well known and is described in reference 11. However, when applying this technique, especially to compressible turbulent boundary layers, there is the inherent problem that the accuracy of the skin friction obtained by this procedure depends on the accuracy of the compressible theory used to predict the law-of-the-wall velocity profile. Therefore, before accurate skin friction can be obtained from velocity profiles, the accuracy of the various theories must be determined.

Comparison of measured and calculated law-of-the-wall velocity profiles are shown in figures 10(a) to 10(c). The solid curve in these figures represents Coles' incompressible values as given in reference 12. The flight data in these figures are the measured compressible boundary layer velocities that have been reduced to their incompressible values by the indicated theory using the shearing stress that was measured by the skin friction balance. In this form the data should agree with the solid line if the theory used to transform the data is correct. The three transformation methods used are the theory of van Driest (ref. 13) shown in figure 10(a), the reference enthalpy method of Eckert (ref. 14), shown in figure 10(b), and the wall reference temperature method as applied in reference 15, shown in figure 10(c). Both the theory of van Driest and Eckert's reference enthalpy method yield good correlation between the measured profiles and Coles' incompressible curve. However, as shown in figure 10(c), the data transformed by the wall reference temperature method are in poor agreement with the incompressible curve.

SKIN FRICTION

Skin friction data were obtained directly from the skin friction balance measurements during flights A and B and indirectly from heat transfer measurements obtained during flight B. The measured skin friction data in the form of shearing force, obtained during flight A, are shown in figure 11. Also shown for comparison and evaluation are the values predicted by the theory of van Driest (ref. 16), the Spalding and Chi method (ref. 17), and Eckert's reference enthalpy method (ref. 14). Values predicted by the theory of van Driest and the method of Spalding and Chi are in excellent agreement with the measured data. However, Eckert's reference enthalpy method underpredicts the measured data by approximately 10 percent.

Origin of turbulence.—All of the calculated values shown in figure 11 were based on momentum thickness Reynolds number. However, because the momentum thickness was not available for the test conditions of flight B, the virtual origin of turbulent flow had to be determined in order to correlate and compare the measured skin friction coefficients obtained from both flights A and B with theoretical predicted values. The first step in determining the virtual origin was to look at the boundary layer transition. If the transition data showed that turbulent flow existed at or near the leading edge of the test specimen, then there was no need to determine a virtual origin because, in this case, the virtual origin could be assumed to be the leading edge.

Figures 12 and 13 show boundary layer transition data obtained on the lower centerline of the cylinder during flights A and B, respectively. In figure 12 the transition data are shown in the form of measured wall temperature as a function of distance from the leading edge. As shown, the beginning of transition occurs at a distance of 0.76 meter and a Reynolds number of 3.4 million, and the end of transition occurs at approximately 1.22 meters and a Reynolds number of 5.5 million. It is obvious from this data that the leading edge is not the origin of turbulent flow and a virtual origin must be determined. Fortunately, the momentum thickness Reynolds number is known for flight A. Consequently, equivalent length Reynolds numbers were determined for each theory that yielded the same results as obtained when using the momentum thickness Reynolds number. The distance from the leading edge determined from these equivalent Reynolds numbers was interpreted as being the virtual origin for the particular theory used. The virtual origins obtained by this procedure are shown in figure 12. Figure 13 shows transition data obtained during flight B. The data are in the form of heat transfer coefficients as a function of distance from the leading edge. It is obvious from these data that transition occurs so close to the leading edge that turbulent flow can be assumed to exist from the leading edge.¹ Consequently, for flight B the length of turbulent flow, L , and the distance from the leading edge, x , are considered to be equal.

Evaluation of compressible transformation theories.—Comparison between measured skin friction coefficients and values predicted by Eckert's reference enthalpy method, the Spalding and Chi method, and the theory of van Driest are shown in figures 14(a), 14(b), and 14(c), respectively. The solid line in these figures represents the incompressible skin friction coefficients predicted by the von Kármán-Schoenherr equation, and the symbols represent the measured data that have been transformed to their incompressible values by the indicated compressible theory. In this form the transformed measured data should agree with the solid line if the theory used to transform the data is correct. The open symbols in figure 14 represent skin friction coefficients that were obtained from the measured heat transfer data using the experimentally determined Reynolds analogy factor of 1.11. The procedure used to determine the experimental Reynolds analogy factor is discussed in the following section of this report. The solid circle symbol represents the skin friction coefficients obtained from the skin friction balance measurements during flight B, and the solid square symbol represents the skin friction balance data obtained during flight A. As can be seen, all three theories do a good job of correlating the skin friction coefficients with Reynolds number. However, the level of skin friction predicted by each transformation theory differs substantially. As can be seen in figure 14(a), the data transformed by Eckert's reference enthalpy method are approximately 10 percent higher than the von Kármán-Schoenherr curve, and this is considered to be fair agreement. Figure 14(b) shows that the measured data are about 7 percent higher than the incompressible values when the Spalding and Chi method is used to transform the data. The agreement shown in this figure is considered to be good. However, as shown in figure 14(c), the measured data transformed by the theory

¹ The fact that the boundary layer transition occurred much closer to the leading edge during flight B than during flight A was not expected, since it is normally assumed that the boundary layer becomes more stable at the lower wall temperatures. The reason for the early transition during flight B has not been determined at this time.

of van Driest are within ± 2 percent of the von Kármán-Schoenherr incompressible values and the agreement is considered to be excellent.

Reynolds Analogy Factor

Most turbulent heat transfer methods are based on some form of Reynolds analogy between skin friction and heat transfer. Consequently, once a skin friction equation is selected, a Reynolds analogy factor is needed to calculate heat transfer coefficients. The determination of a Reynolds analogy factor has been the subject of considerable investigation but has still not been resolved (ref. 18). Therefore, heat transfer and skin friction were measured simultaneously during this investigation, and by using the relationship $s = 2St/C_f$, an experimental Reynolds analogy factor was determined, thus eliminating the necessity of estimating a Reynolds analogy factor when making the heat transfer calculation. The Reynolds analogy factor determined from the measured skin friction and heat transfer was 1.11.

Heat Transfer

Figure 15 shows the comparison between the measured heat transfer coefficients, in the form of Stanton numbers, and the theoretical values predicted by the theory of van Driest using an experimental Reynolds analogy factor of 1.11. The dashed line represents the laminar Stanton numbers predicted by Eckert's reference enthalpy method. The values predicted by the theory of van Driest are represented by two solid lines. The upper line represents the Stanton numbers that were calculated using a wall-to-recovery temperature ratio of 0.66 and the lower line represents values computed using a temperature ratio of 0.71. As shown, the Stanton numbers predicted by the theory of van Driest are in excellent agreement with the measured heat transfer data.

CONCLUSIONS

Flight-measured turbulent skin friction, heat transfer, and boundary layer velocity profiles were measured on the lower centerline of a hollow cylinder 3.04 meters in length at a nominal free stream Mach number of 3.0, at wall-to-recovery temperature ratios of 0.66 to 0.91 and at local Reynolds numbers of 1 to 12 million. Skin friction coefficients were obtained directly from measurements made by a skin friction force balance and indirectly from heat transfer measurements using a Reynolds analogy factor derived from the force balance and heat transfer data. The results of this investigation led to the following conclusions:

1. The theory of van Driest predicted skin friction coefficients that were in excellent (± 2 percent) agreement with the measured data. The Spalding and Chi method predicted skin friction coefficients that were 7 percent lower than the measured coefficients, and the values predicted by Eckert's reference enthalpy method were 10 percent lower than the measured skin friction coefficients.

2. A measured Reynolds analogy factor of 1.11 was derived from the skin friction and heat transfer data.

3. Heat transfer coefficients predicted by the theory of van Driest, using the measured Reynolds analogy factor, were in excellent agreement with the measured heat transfer coefficients.

4. Measured velocity profiles transformed by the theory of van Driest and Eckert's reference enthalpy method were in good agreement with Coles' incompressible law-of-the-wall velocity profile.

REFERENCES

1. Hopkins, Edward J.; Rubesen, Morris W.; Inouye, Mamou; Keener, Earl R.; Mateer, George C.; and Polek, Thomas E.: Summary and Correlation of Skin-Friction and Heat-Transfer Data for a Hypersonic Turbulent Boundary Layer on Simple Shapes. NASA TN D-5089, 1969.
2. Peterson, John B., Jr.: A Comparison of Experimental and Theoretical Results for the Compressible Turbulent-Boundary-Layer Skin Friction With Zero Pressure Gradient. NASA TN D-1795, 1963.
3. Samuels, Richard D.; Peterson, John B., Jr.; and Adcock, Jerry B.: Experimental Investigation of the Turbulent Boundary Layer at a Mach Number of 6 With Heat Transfer at High Reynolds Numbers. NASA TN D-3856, 1967.
4. Hopkins, Edward J.; Keener, Earl R.; and Louie, Pearl T.: Direct Measurements of Turbulent Skin Friction on a Nonadiabatic Flat Plate at Mach Number 6.5 and Comparison With Eight Theories. NASA TN D-5675, 1970.
5. Quinn, Robert D.; and Olinger, Frank V.: Heat-Transfer Measurements Obtained on the X-15 Airplane Including Correlation With Wind-Tunnel Results. NASA TM X-1705, 1969.
6. Banner, Richard D.; Kuhl, Albert E.; and Quinn, Robert D.: Preliminary Results of Aerodynamic Heating Studies on the X-15 Airplane. NASA TM X-638, 1962.
7. NASA YF-12 Flight Loads Program. NASA TM X-3061, 1974.
8. Garringer, Darwin J.; and Saltzman, Edwin J.: Flight Demonstration of a Skin-Friction Gage to a Local Mach Number of 4.9. NASA TN D-3830, 1967.
9. Lamb, Milton; Stallings, Robert L., Jr.; and Richardson, Celia S.: Aerodynamic Characteristics of 1/25-Scale Model of YF-12 Airplane at Mach 1.80 to 2.96 With and Without External Instrument Packages and Flow-Field Surveys at Mach 2.96. NASA TM X-2524, 1972.
10. Peterson, John B., Jr.: Boundary-Layer Velocity Profiles Down Stream of Three-Dimensional Transition Trips on a Flat Plate at Mach 3 and 4. NASA TN D-5523, 1969.
11. Winter, K. G.: An Outline of the Techniques Available for the Measurement of Skin Friction in Turbulent Boundary Layers. Tech. Memo. Aero., 1956, Royal Aircraft Establishment, 1975.
12. Coles, Donald: Measurements in the Boundary Layer on a Smooth Flat Plate in Supersonic Flow. Part I. The Problem of a Turbulent Boundary Layer, Rept. 20-69, Jet Propulsion Lab., Calif. Inst. of Technology, June 1953.

13. van Driest, E. R.: Turbulent Boundary Layer in Compressible Fluids. IAS J., vol. 18, no. 3, Mar. 1951, pp. 145-160, 216.
14. Eckert, Ernest R. G.: Survey of Boundary Layer Heat Transfer at High Velocities and High Temperatures. WADC Tech. Rep. 59-624, Wright Air Dev. Center, U.S. Air Force, Apr. 1960. (Available from ASTIA as 238292.)
15. Keener, Earl R.; and Hopkins, Edward J.: Turbulent Boundary-Layer Velocity Profiles on a Nonadiabatic Flat Plate at Mach Number 6.5. NASA TN D-6907, 1972.
16. van Driest, E. R.: The Problem of Aerodynamic Heating. Aero. Eng. Rev., vol. 15, no. 10, Oct. 1956, pp. 26-41.
17. Spalding, D. B.; and Chi, S. W.: The Drag of a Compressible Turbulent Boundary Layer on a Smooth Flat Plate With and Without Heat Transfer. J. Fluid Mech., vol. 18, part I, Jan. 1964, pp. 117-143.
18. Cary, Aubrey M., Jr.: Summary of Available Information on Reynolds Analogy for Zero-Pressure-Gradient, Compressible, Turbulent-Boundary-Layer Flow. NASA TN D-5560, 1970.

TABLE 1.—FREE STREAM CONDITIONS

Flight	M_∞	P_∞ , N/m ²	T_∞ , K	α , wing, deg	β , deg	Re_∞/m , per m
A	3.02	4178	218	3.9	0	4.28×10^6
B	2.98	4092	217	3.8	0	4.07×10^6

TABLE 2.—LOCAL (CYLINDER) CONDITIONS

Flight	M_δ	T_w/T_R	P_δ , N/m ²	T_δ , K	α , deg	β , deg	Re_δ/m , per m	Re_θ
A	2.90	0.91	4943	229	0 ± 0.05	0 ± 0.10	4.49×10^6	8664
B	2.92	0.66 to 0.77	4413	222	0 ± 0.05	0 ± 0.10	4.17×10^6	--- ^a

^a Boundary-layer velocity profiles were not obtained during flight B. Consequently, the experimental momentum thickness Reynolds number was not available for this flight; however, sufficient data were obtained from the pitot pressure rake to determine the boundary-edge Mach number.

TABLE 3.—BOUNDARY LAYER MACH NUMBER AND
VELOCITY DISTRIBUTIONS

Flight A

$$x = 274 \text{ cm}; \theta = 0.193 \text{ cm}; M_{\delta} = 2.90;$$

$$T_{\delta} = 229 \text{ K}; U_{\delta} = 880 \text{ m/sec}; P_{\delta} = 4943 \text{ N/m}^2; \delta = 3.05 \text{ cm}$$

$y,$ cm	$\frac{y}{\delta}$	$\frac{M}{M_{\delta}}$	$\frac{T}{T_{\delta}}$	$\frac{U}{U_{\delta}}$
0.254	0.083	0.566	1.64	0.724
0.432	0.142	0.617	1.55	0.769
0.610	0.200	0.666	1.46	0.805
0.787	0.258	0.700	1.41	0.833
0.965	0.316	0.734	1.36	0.857
1.321	0.433	0.797	1.27	0.896
1.956	0.641	0.903	1.12	0.956
2.591	0.849	0.979	1.02	0.990
3.226	1.058	1.000	1.00	1.000
3.861	1.266	1.003	1.00	1.003
4.496	1.474	1.003	1.00	1.003

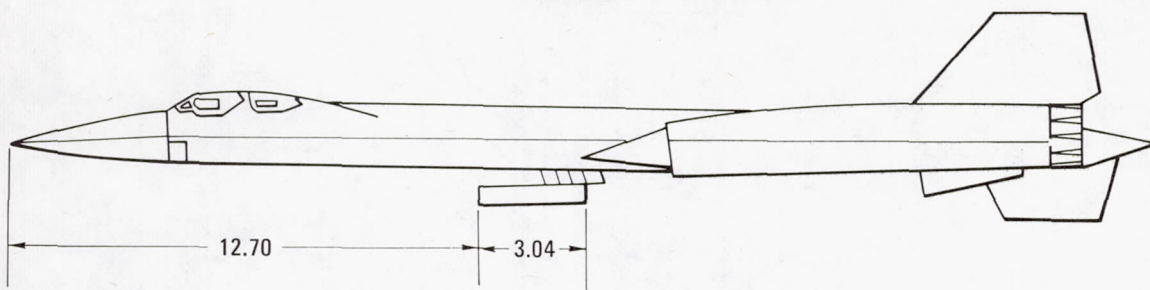


Figure 1.—YF-12A airplane showing location of hollow cylinder. Dimensions in meters.

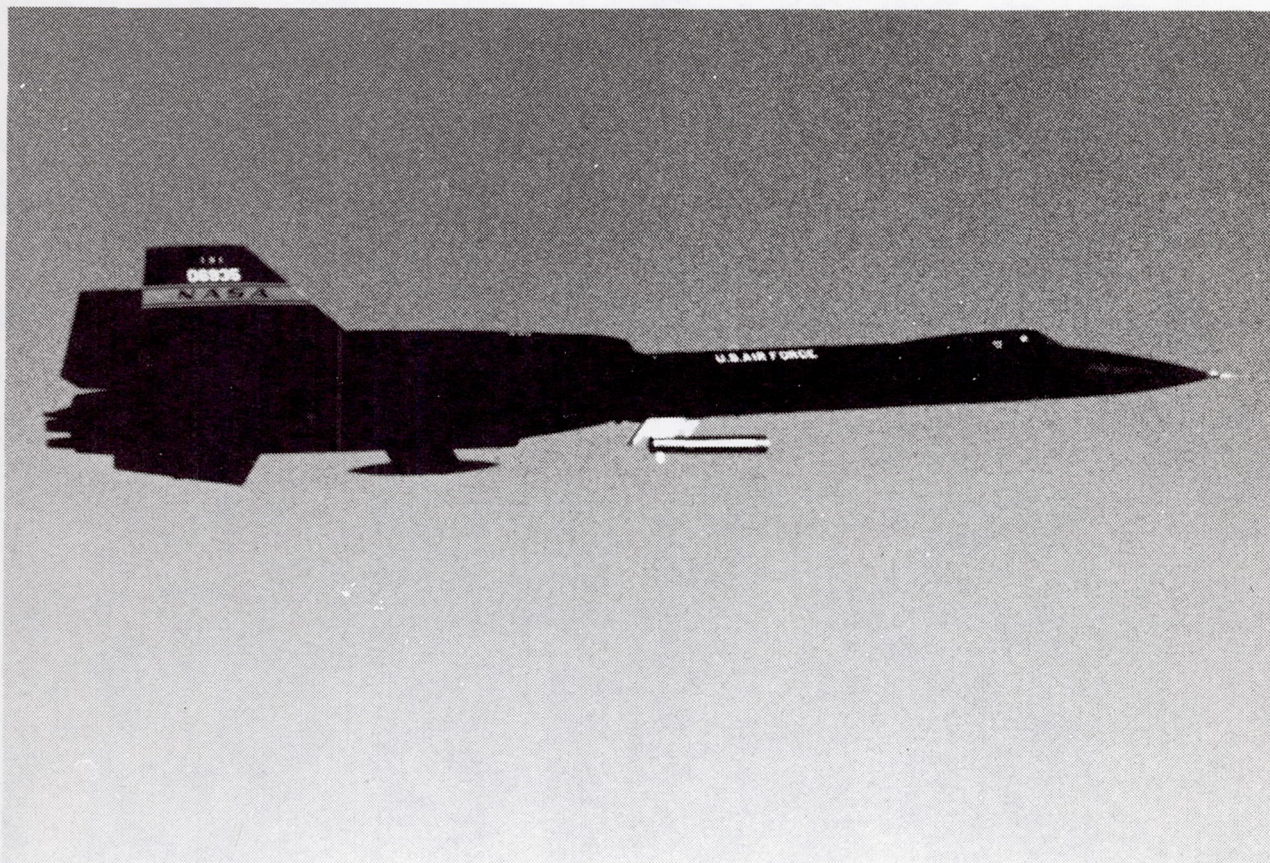


Figure 2.—YF-12A airplane with hollow cylinder attached.

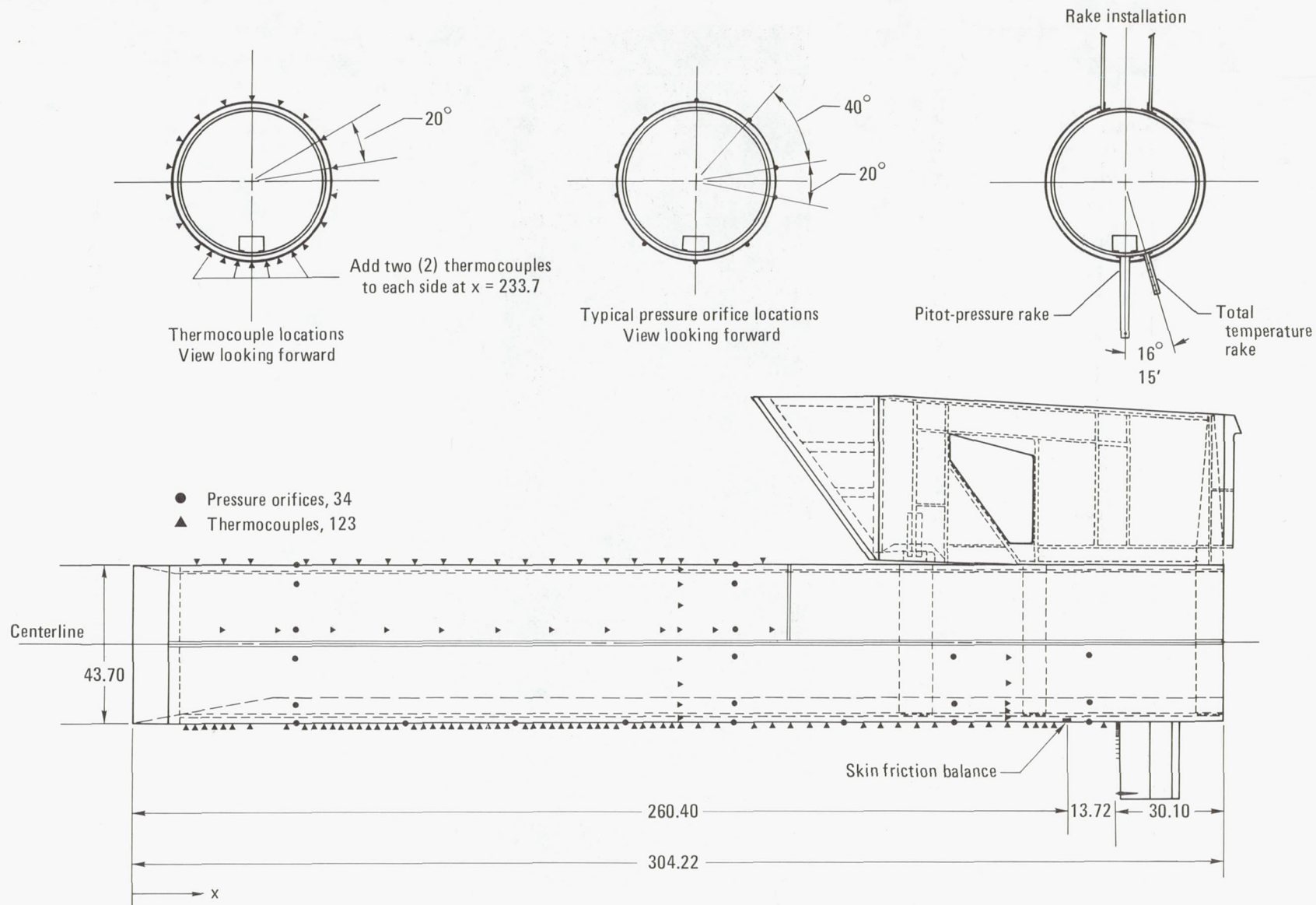


Figure 3.—Location of instrumentation on hollow cylinder. Dimensions in centimeters.

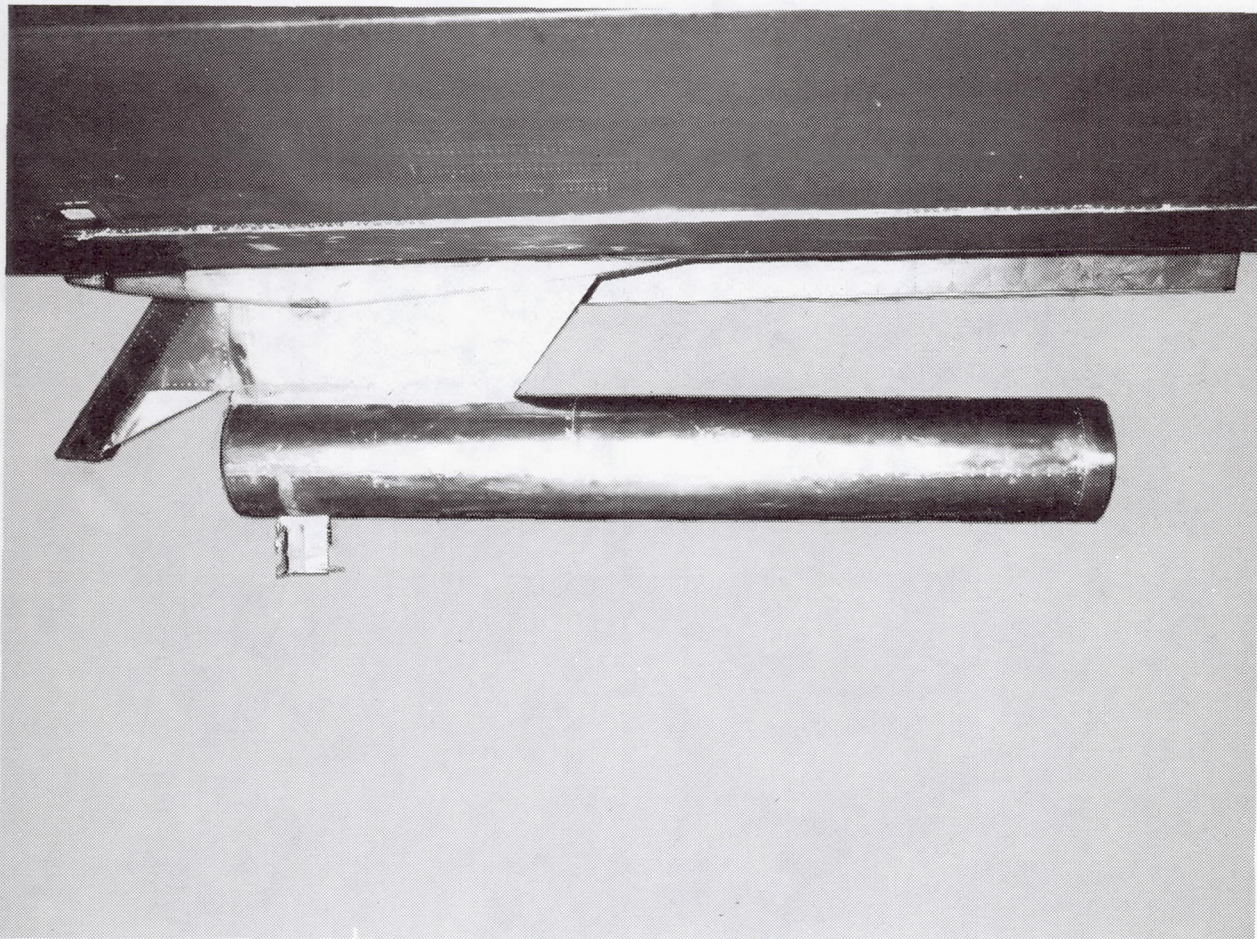


Figure 4.—Hollow cylinder (flight A).

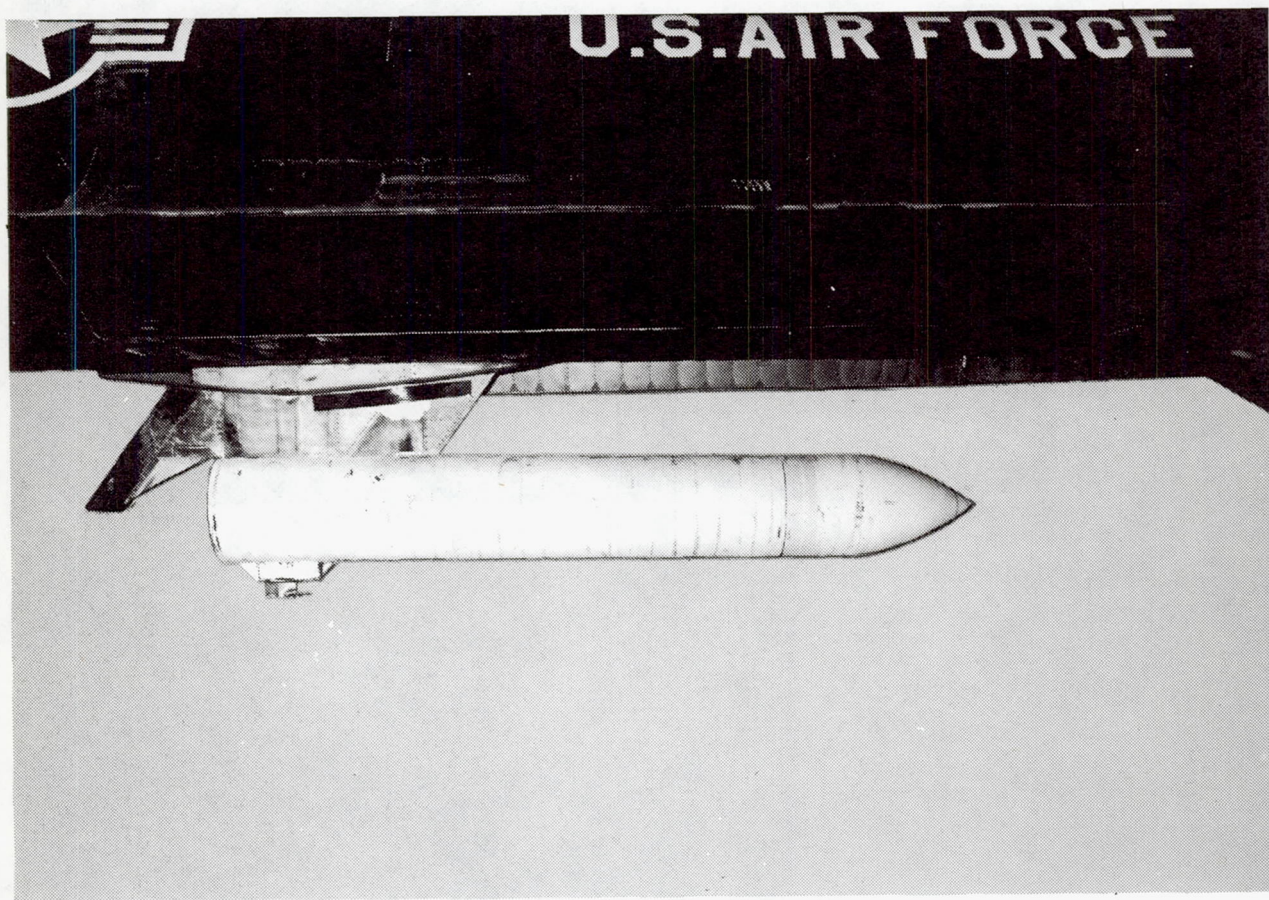
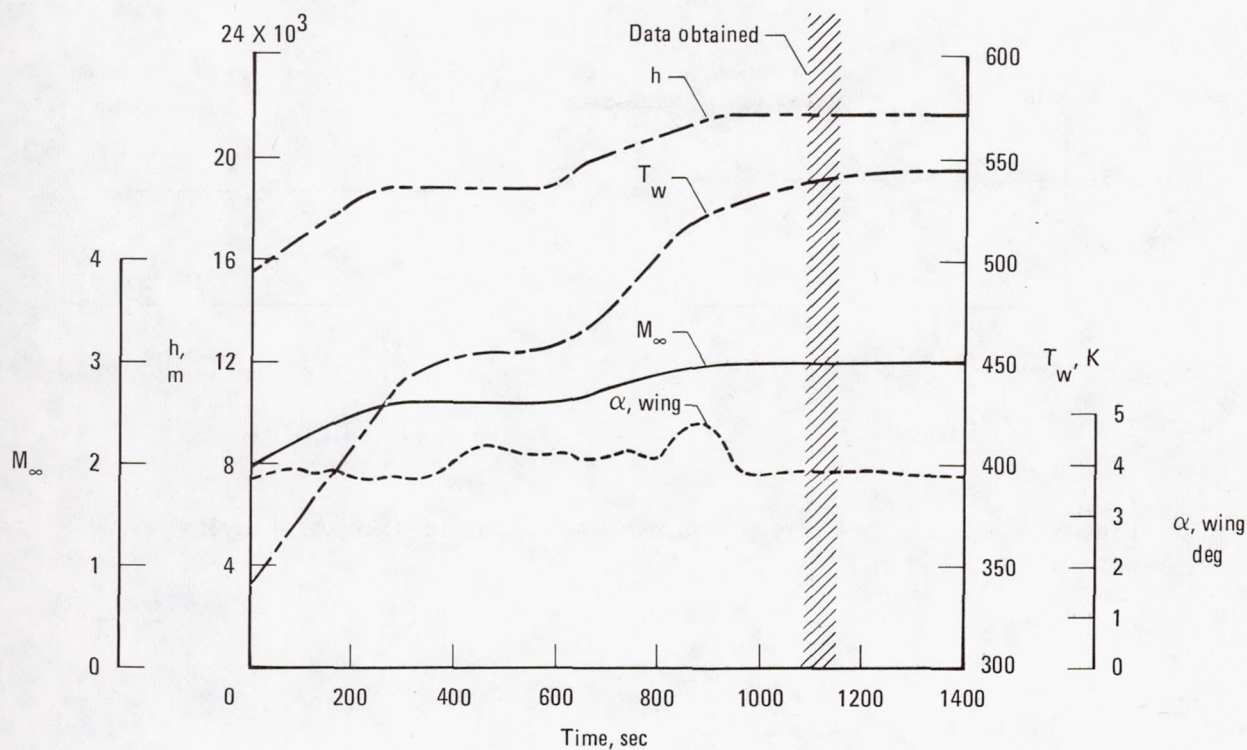
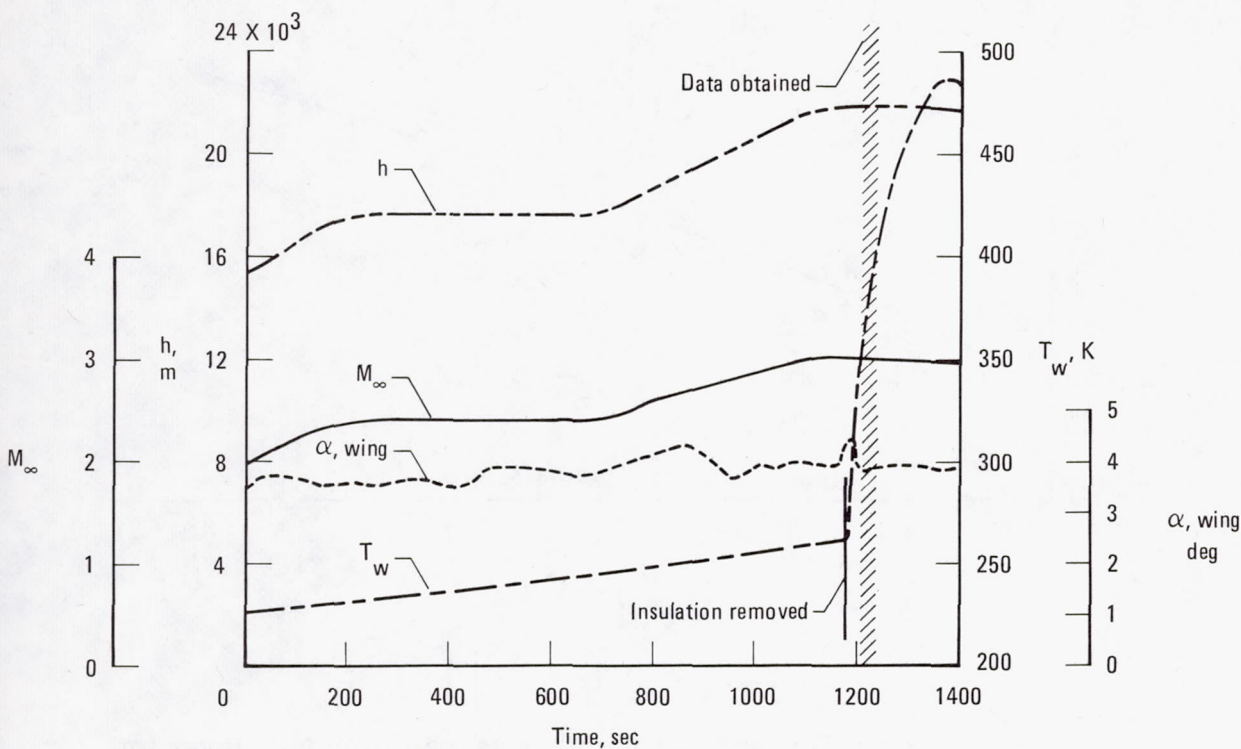


Figure 5.—Hollow cylinder with insulating cover (flight B).

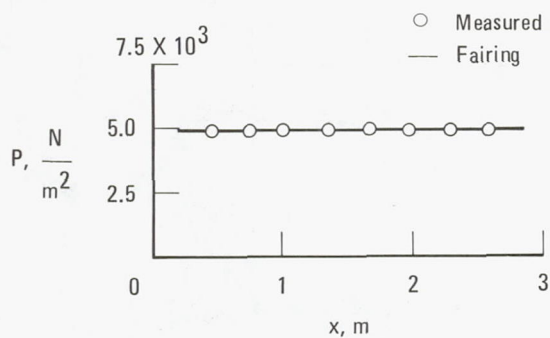


(a) Flight A.

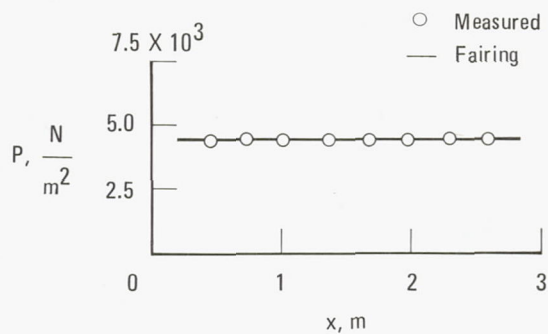


(b) Flight B.

Figure 6.—Time history of flight parameters and typical skin temperatures.



(a) Flight A.



(b) Flight B.

Figure 7.—Surface static pressures measured on the lower cylinder centerline.

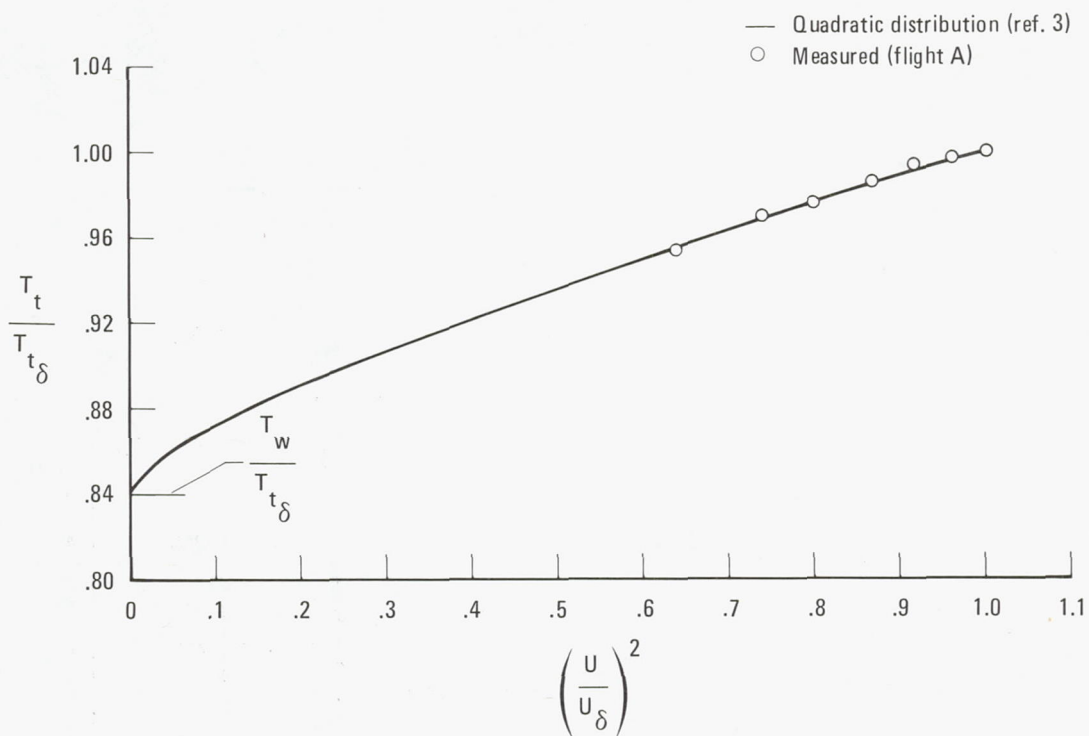


Figure 8.—Comparison of theoretical and measured boundary layer total temperature ratios.

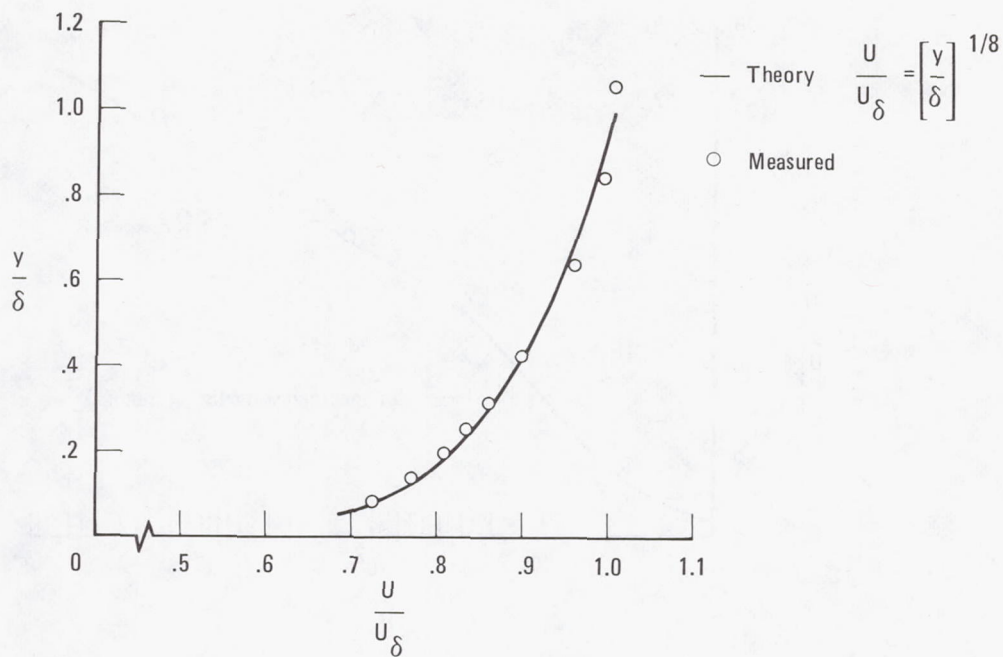
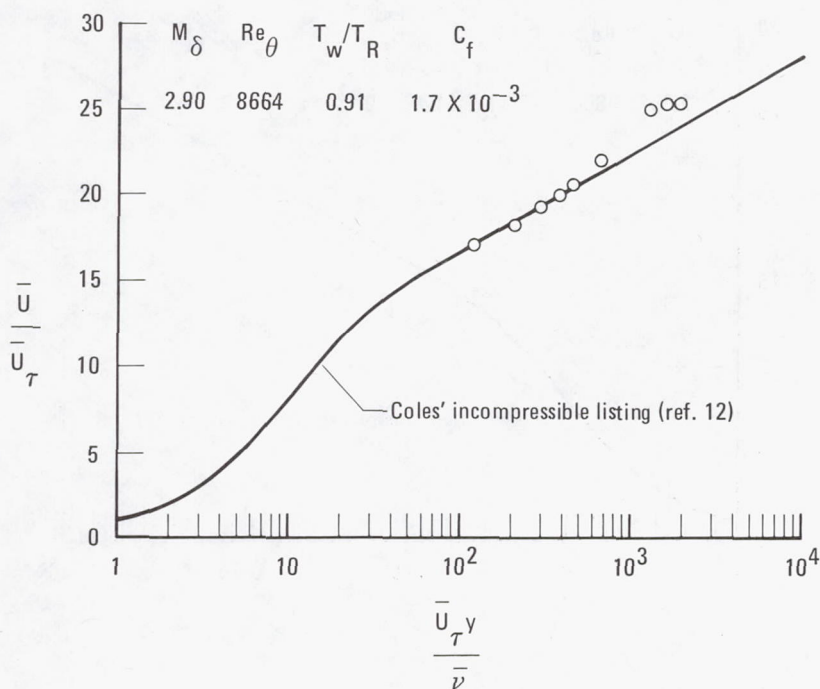
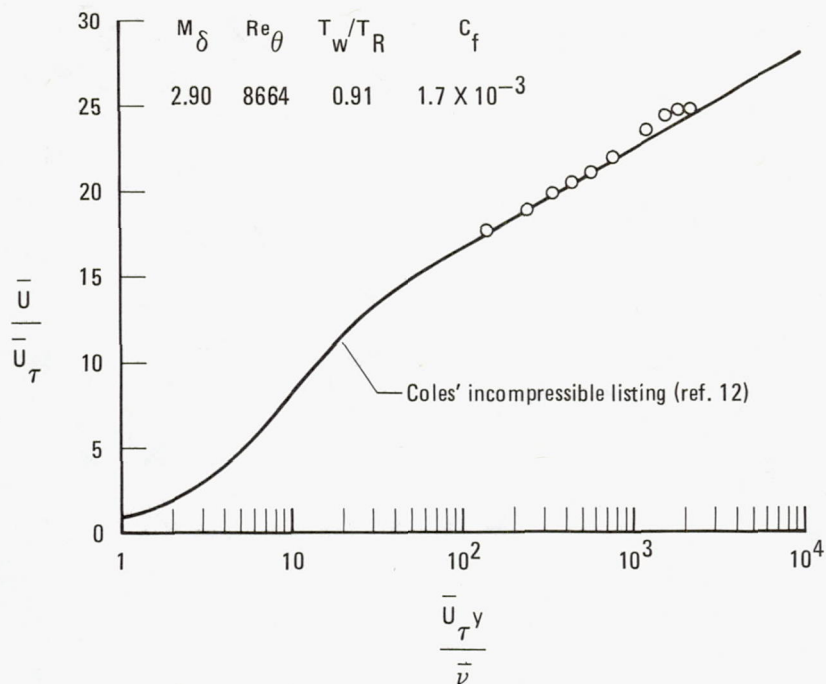


Figure 9.—Boundary layer velocity profile for flight A. $M_\delta = 2.90$, $Re_\theta = 8664$, $\delta = 3.05$ cm.

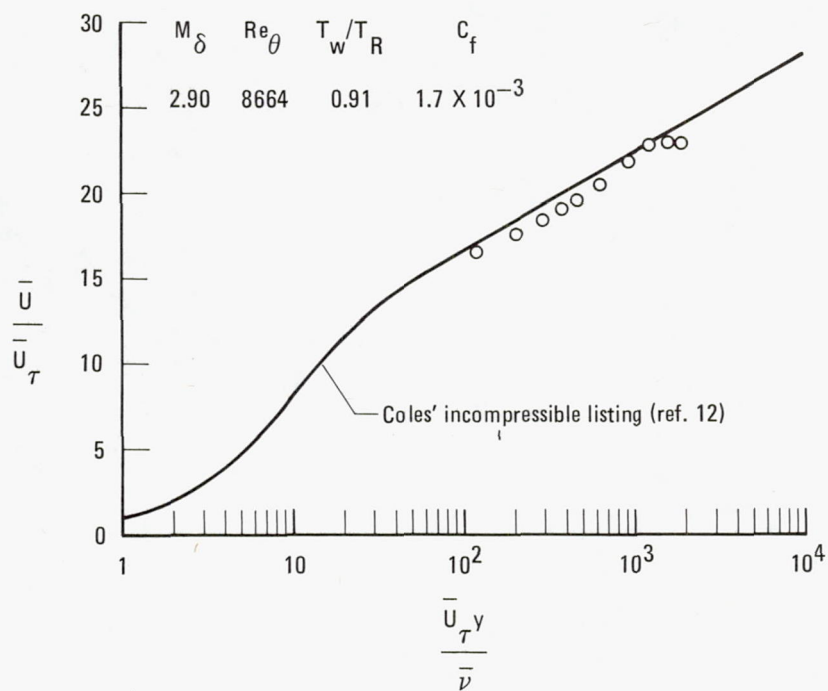


(a) Mixing length transformation of van Driest.

Figure 10.—Law-of-the-wall velocity profiles for flight A.



(b) Eckert's reference enthalpy transformation.



(c) Wall reference temperature transformation.

Figure 10.—Concluded.

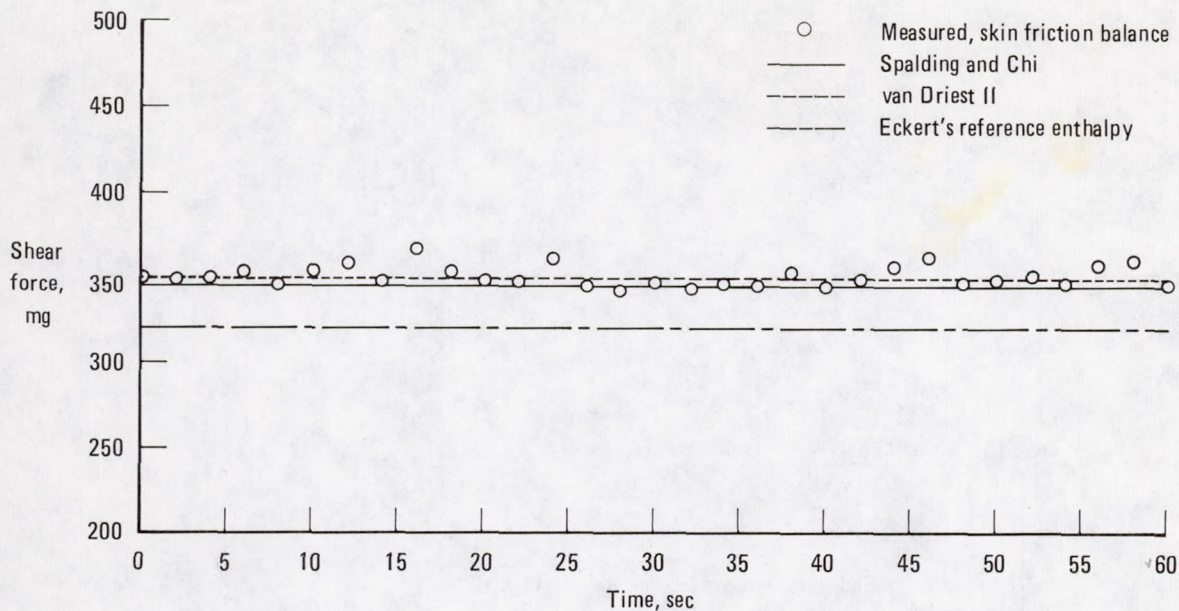


Figure 11.—Comparison of measured and calculated skin friction for flight A.
 $M_\delta = 2.90$, $Re_\theta = 8664$, $T_w/T_R = 0.91$.

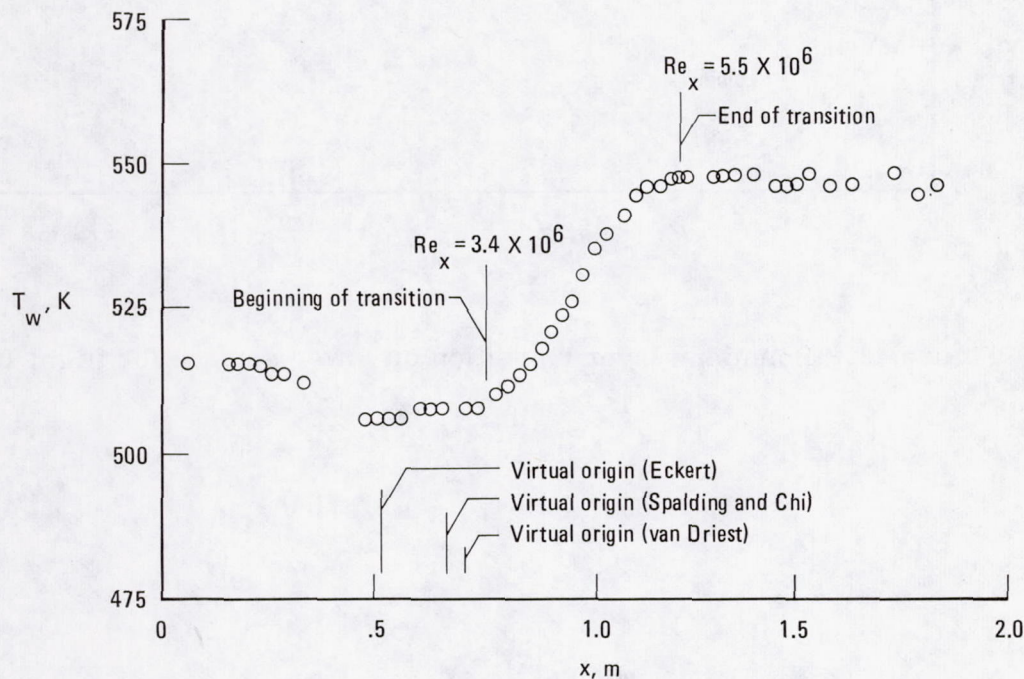


Figure 12.—Boundary layer transition on lower surface for flight A.

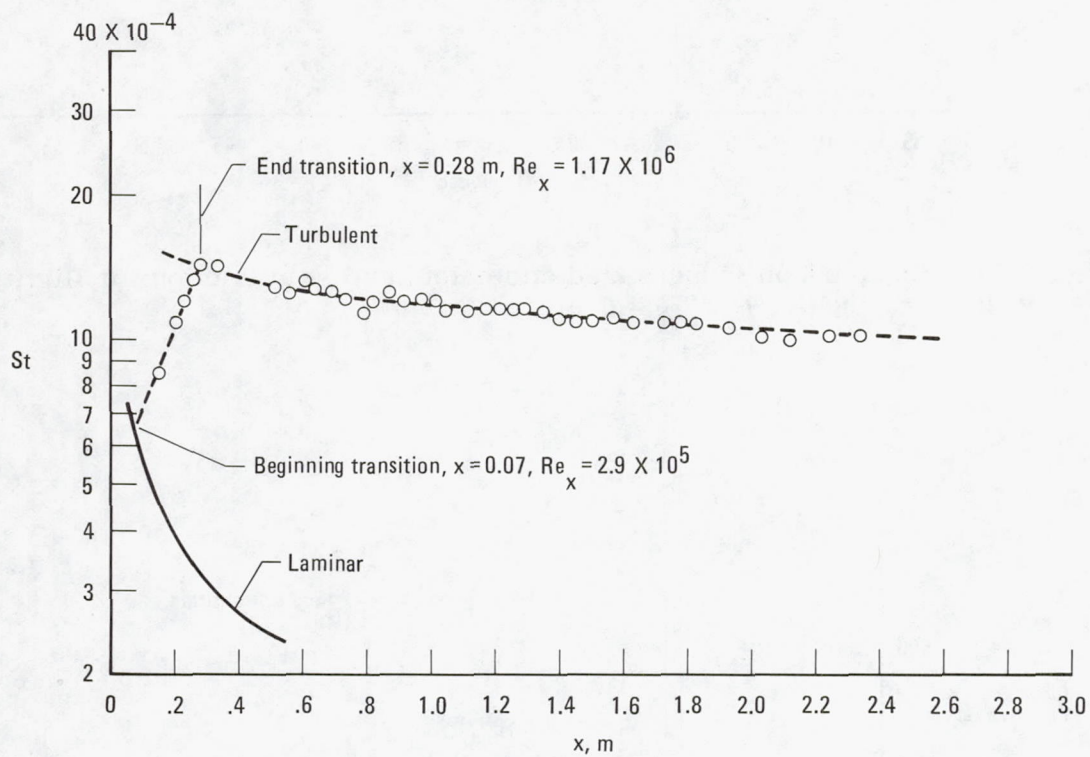
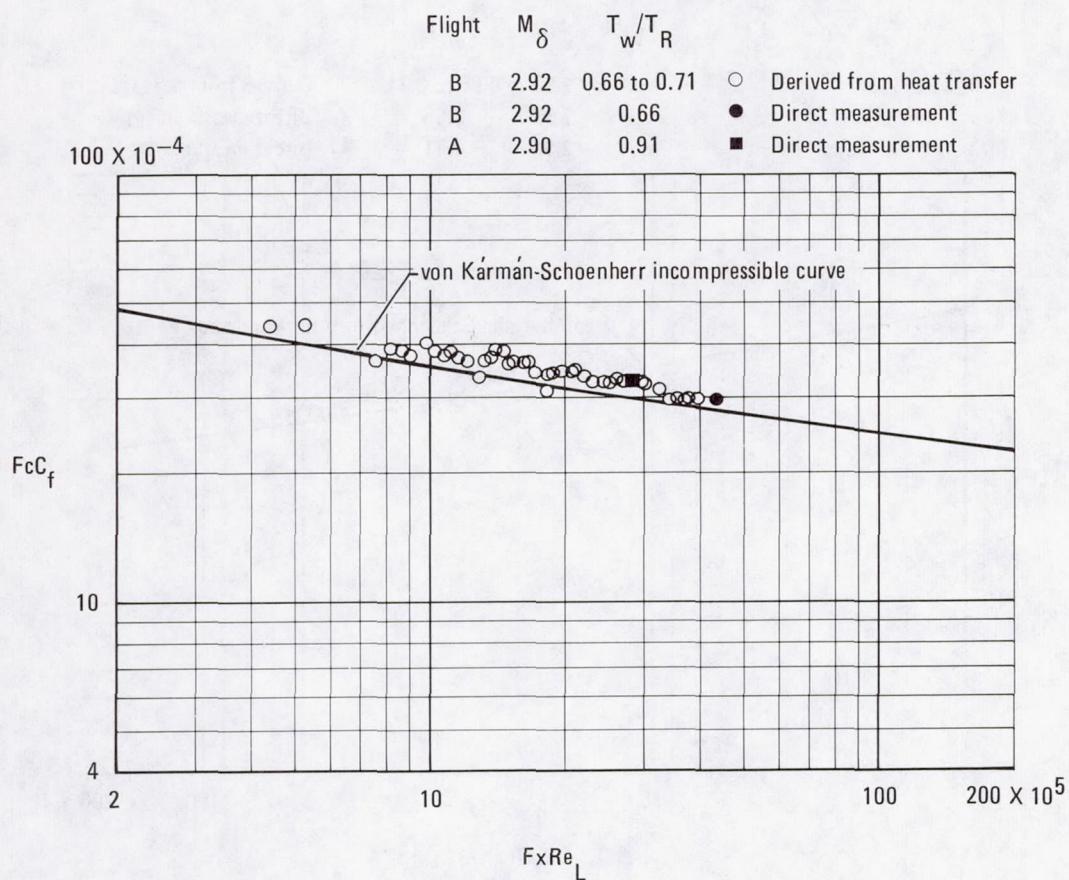
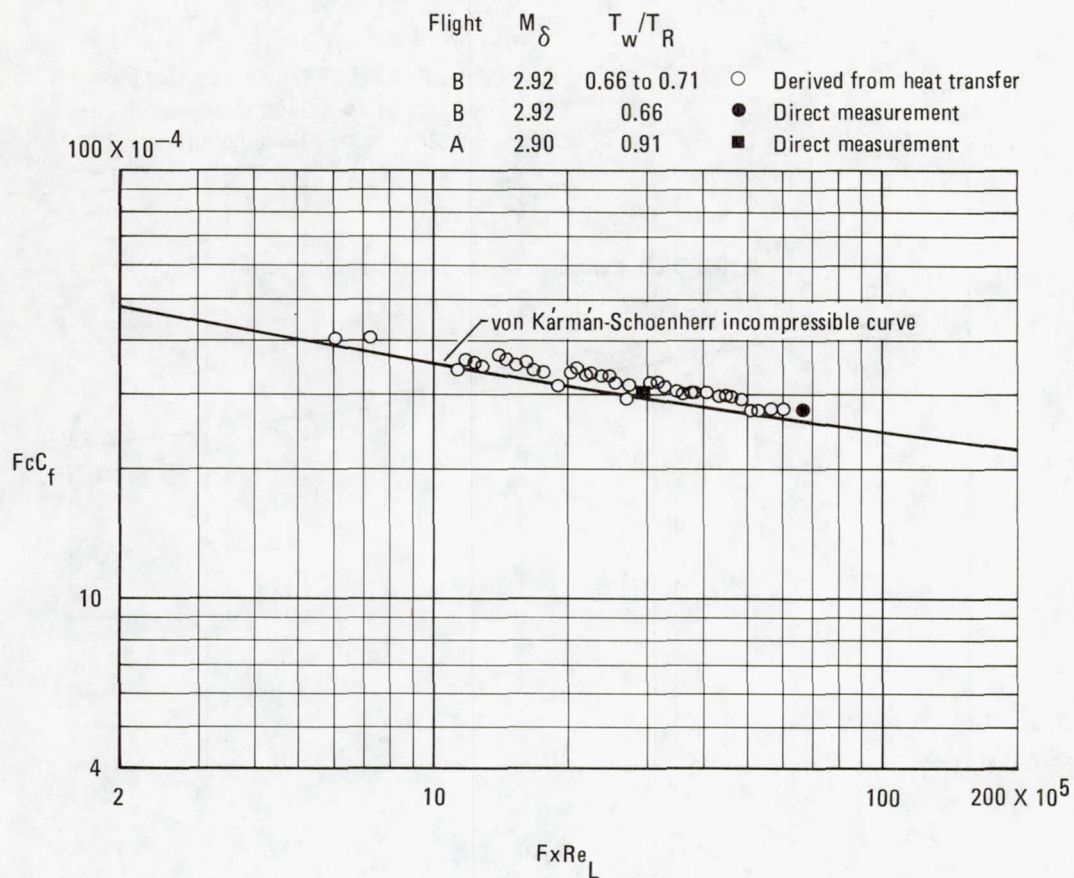


Figure 13.—Boundary layer transition on lower surface for flight B.



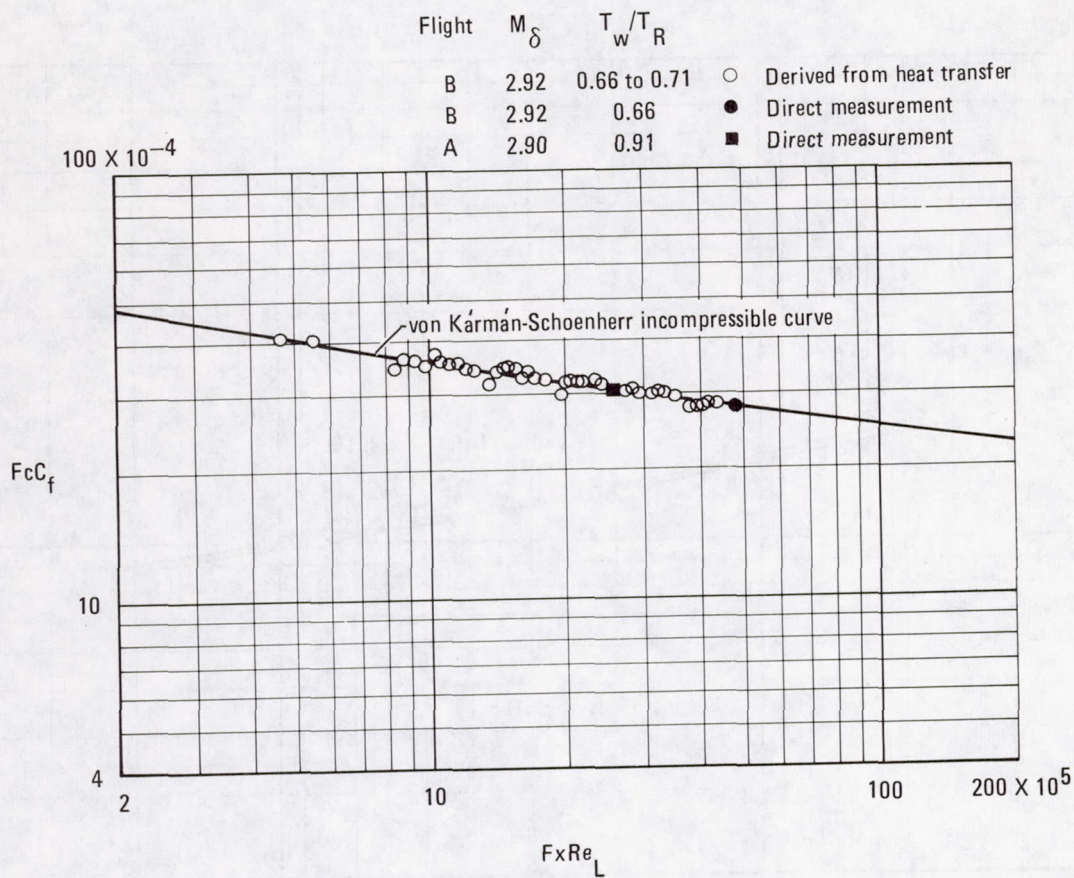
(a) Eckert's reference enthalpy.

Figure 14.—Evaluation of three compressible turbulent skin friction theories.



(b) Spaulding and Chi.

Figure 14.—Continued.



(c) van Driest II.

Figure 14.—Concluded.

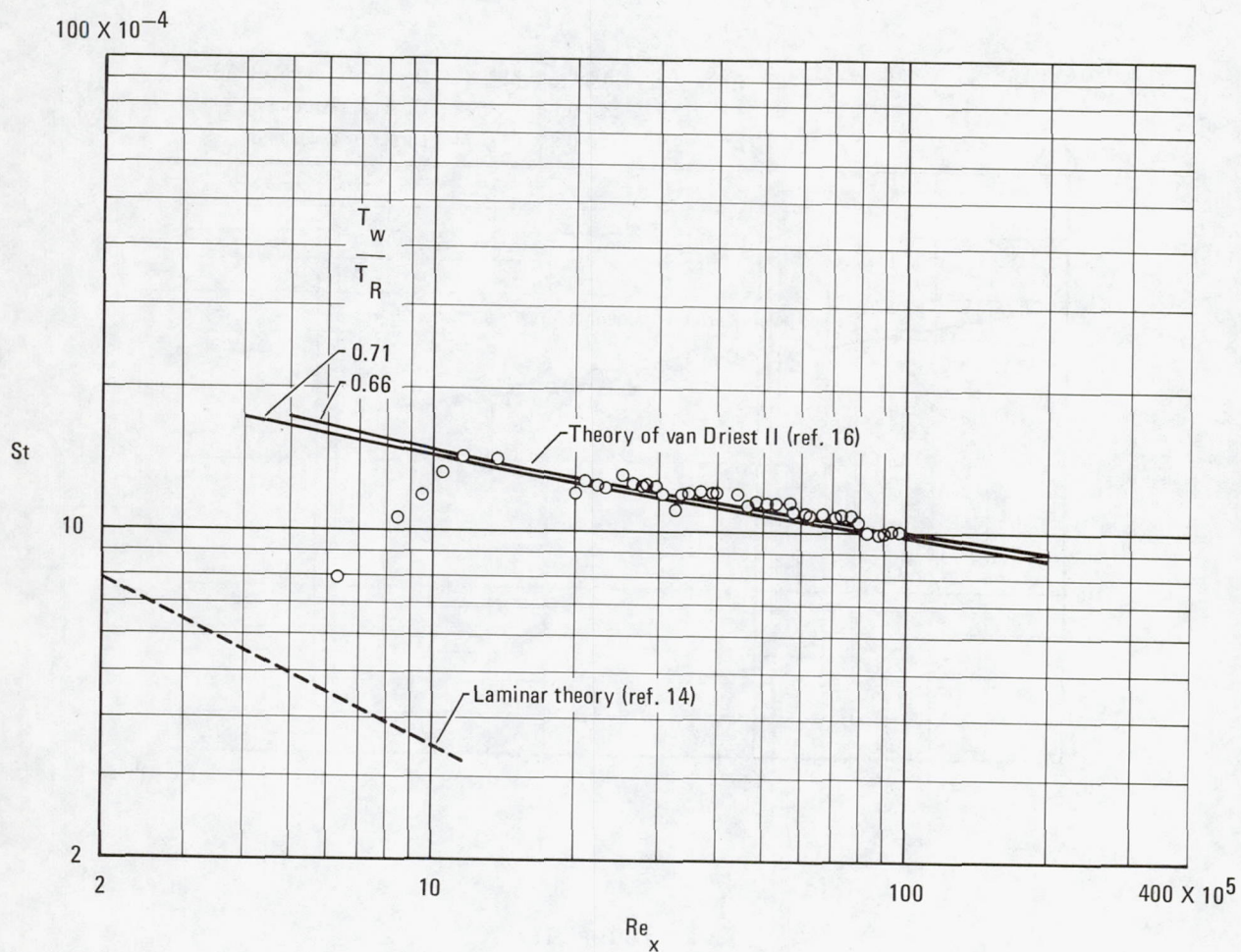


Figure 15.—Comparison of measured and calculated heat transfer for flight B.

PREDICTED AND MEASURED FLOW FIELDS UPSTREAM
OF THE YF-12 INLET AND INLET INTERNAL FLOW SOLUTIONS

L. Presley, P. Kutler, and R. Sorenson
Ames Research Center

SUMMARY

Flow field solutions have been obtained for the YF-12 forebody at various Mach numbers and angles of attack using a three-dimensional shock-capturing technique. These results are compared to wind tunnel data wherein the flow field at two radii in the plane of the cowl lip were surveyed. Good qualitative agreement between the data and the computational results were obtained. Output of the forebody computational code was used to define the upstream flow conditions for a subsequent inlet internal flow solution. The inlet flow solutions were obtained using a three-dimensional shock-capturing technique.

A PERFORMANCE MODEL OF THE YF-12C AIRPLANE

Paul C. Redin
Dryden Flight Research Center

SUMMARY

A performance modeling technique previously developed for an F-104G airplane with a fixed-geometry inlet was modified and applied to a YF-12C airplane with a variable-geometry inlet. Flight test data from level accelerations, climbing accelerations, and constant-Mach-number climbs flown at maximum afterburning power were used to develop and validate the model. After the model was corrected for nonstandard operating conditions, predicted propulsion and drag data were found to be in error by as much as 20 percent over a significant portion of the Mach number range considered. After the propulsion and drag data were adjusted, the model-predicted performance data fell to within 6 percent or less of the measured flight values.

